Electronic Processes in Organic Optoelectronics: Insights Gained Through Modeling and Magnetic Field Effects
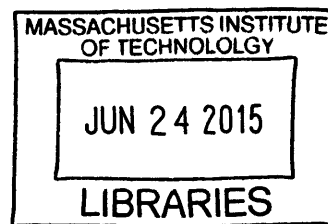
by

Eric Richard Hontz

Submitted to the Department of Chemistry

in partial fulfillment of the requirements for the degree of

Doctor of Philosophy in Physical Chemistry

at the

MASSACHUSETTS INSTITUTE OF TECHNOLOGY

June 2015

© Massachusetts Institute of Technology 2015. All rights reserved.

Author . . . .

Signature redacted

Department of Chemistry
May 18, 2015

Certified by. . . . .

Signature redacted

Troy Van Voorhis
Professor
Thesis Supervisor

Accepted by . . . .

Signature redacted

Robert W. Field
Chairman, Departmental Committee on Graduate Students

This doctoral thesis has been examined by a Committee of the
Department of Chemistry as follows:

Professor Jianshu Cao . . **Signature redacted**
        Chairman, Thesis Committee
        Professor of Chemistry

Professor Troy Van Voorhis . . **Signature redacted**
        Thesis Supervisor
        Professor of Chemistry

Professor Moungi Bawendi . . . **Signature redacted**
        Member, Thesis Committee
        Professor of Chemistry

Electronic Processes in Organic Optoelectronics:

Insights Gained Through Modeling and Magnetic Field Effects

by

Eric Richard Hontz

Submitted to the Department of Chemistry
on May 18, 2015, in partial fulfillment of the
requirements for the degree of
Doctor of Philosophy in Physical Chemistry

Abstract

Organic photovoltaics (OPVs) and organic light-emitting diodes (LEDs) are organic optoelectronics offering a number of unique benefits that may play an important role in the future of clean energy generation and efficient energy consumption. In this thesis, we explore key electronic processes in OPVs and OLEDs, with a major focus on quantum-mechanical kinetic modeling of magnetic field effects (MFEs) that probe underlying subprocesses.

Certain organics are capable of dividing excited states in a process termed singlet fission, which can increase the maximum theoretical efficiency of an OPV by a factor of nearly 1/3. The MFEs on photocurrent measurements from our collaborators are combined with theoretical models to determine optimal device architectures for singlet fission OPVs, allowing us to exceed the conventional limit of one electron per photon. We also use MFEs to determine the spin of charge transfer states most efficient at generating photocurrent and demonstrate microscopic insight into the mechanism of their diffusion, offering new design principles for the engineering of donor-acceptor interfaces in OPVs.

Thermally activated delayed fluorescence (TADF) is becoming an increasingly important OLED technology that extracts light from non-emissive triplet states via reverse intersystem crossing (RISC) to the bright singlet state. We use MFEs to prove a rather surprising finding that in TADF materials composed of donor-acceptor bends, the electron-hole distance fluctuates as a function of time, resulting in spontaneous cycling between states that are advantageous to fluorescence at one moment and then advantageous to RISC at another.

Combined with additional topics in the fields of metal organic frameworks and reaction pathfinding methods, the work in this thesis provides insight into how to achieve optimal performance in OPV and OLED devices, which may serve an important role in the future of our energy landscape.

5

Thesis Supervisor: Troy Van Voorhis
Title: Professor

Acknowledgments

During my five years at MIT, I've had the pleasure of meeting amazing people and scientists. I've learned more than I could have imagined, and they helped me get through the tough spots. I would like to thank them for all they've done.

I would first like to thank my thesis advisor, Troy Van Voorhis, for all of his research and life guidance. He taught me so much about science and how to navigate the community successfully. He helped calm me down and get through stressful situations. I've been very fortunate to have an advisor that understands work/life balance and puts his students' well being above everything else.

I would like to thank Shane Yost for being a great friend and colleague. He helped me get up to speed on a lot of science in the beginning of my PhD, and he made me laugh more times than I could ever count.

I would like to thank Marc Baldo, Nicholas Thompson, Daniel Congreve, Wendi Chang, Tony Wu, Jiye Lee, Priya Jadhav, Matthias Bahlke, Phil Reusswig, and the rest of the Baldo group for our many successful collaborations. Much of the work in this thesis would not have been possible without their top-notch experimental work and our fruitful discussions.

I would like to thank my parents, Jill and Larry Hontz, for all their support and love. They've been there for me every step of the way and never put pressure on me. They've done everything possible to make my life easier, especially during their visits to Boston, when they've gone shopping for me and even cleaned my apartment.

Finally, I would like to thank my beautiful and absolutely amazing wife, Casandra Cox. She is my best friend and makes me happy every minute I am with her. She's helped me get through the tough times and made the good times so much brighter. She is my world, and will love her forever.

THIS PAGE INTENTIONALLY LEFT BLANK

Contents

THIS PAGE INTENTIONALLY LEFT BLANK

List of Figures

14

17

THIS PAGE INTENTIONALLY LEFT BLANK

List of Tables

THIS PAGE INTENTIONALLY LEFT BLANK

Chapter 1

Introduction and background

With projections of a world population increase of 3 billion people by the end of 2050 and a correlated 56% increase in energy consumption,[20,21] the need for a major change in the way energy is sourced and consumed is hardly an debatable topic. As majority of these projected population and energy increases expected to take place in emerging markets, where economic development will likely take precedence over environmental impact,[22] it may be shockingly more difficult to decrease fossil fuel dependence from the already overwhelming current value of 86%.[23,24] As long as the consequences of these realities remain years in the future, however, changes in consumption habits may not take place without a reordering of the costs of renewable energy technologies and fossil fuels. Significant advancements in clean-energy-related fields are therefore a necessity.

Solar energy is the most abundant source of clean energy, with enough of the sun's energy reaching earth's surface over the course of one hour to sustain energy demands for one year.[25] In fact, even 10%-efficient solar cells would net the requisite energy figures with a land-mass coverage of 0.1%.[26,27] Therefore, solar energy remains one of the most promising renewable energy options. As stated, however, economics will likely the distance future, and the present 3× greater price of utilizing solar power motivates the exploration of new approaches to harnessing the potential of solar

energy.[28]

In addition to seeking clean, renewable sources for energy, it is important to also continually improve the efficiency of devices that consume energy. Lighting constitutes a substantial use of energy, particularly in the commercial sector, where it was estimated to constitute over 10% of electricity consumption in 2013.[20] Light-emitting diode (LED) bulbs already offer efficiencies 48% greater than compact fluorescent bulbs and 560% greater than traditional incandescent bulbs.[29] Widespread adoption of LED lighting, however, will require competitive pricing and comparable or better light output quality.

1.1 Organic semiconductors

Organic optoelectronics offer potential solutions to the problems currently faced in the fields of solar energy capture and solid-state lighting. Organic photovoltaics (OPVs) and organic LEDs (OLEDs) are new technologies that utilize organic semiconductor (OSC) materials, in place of the inorganic materials used in traditional electronics. OSC materials are composed of organic molecules that are bound by relatively weak Van der Walls interactions. As a result of the weak intermolecular interactions and the low dielectric screening of electron interactions, the fundamental excited states in OSCs are highly localized, Coulombically-bound electron-hole pairs, known as excitons (see Figure 1.1b).[30–32]

The localized nature of excitons results in a number of unique benefits in OSCs. For instance, localization makes OSC materials robust to disorder in the molecular packing structure,[33] allowing for cheap and easy processing of OLEDs that even have the potential to be flexible.[29] Additionally, the unique property of distinct spin-substates enables efficient multiplication of excited states, which increases the maximum theoretical solar conversion efficiency. Localization also gives rise to unique physics, as well as obstacles, that necessitate certain approaches to design of OPVs and OLEDs.

1.1.1 The fundamental electronic states

The electrons of OSCs are typically envisaged and modeled within the valence-orbital approximation, in which only the highest occupied and lowest unoccupied molecular orbitals (HOMO and LUMO) of each molecule are considered; the tightly-bound core electrons are usually ignored. The term "hole" is used to refer to an unpaired electron occupying a HOMO orbital of molecule a, with wavefunction $\phi_{HOMO,a}$, while the "electron" is occupies a LUMO orbital of molecule b, with wavefunction $\phi_{LUMO,b}$. While far from quantitative, this electronic description serves as a reasonable zeroth-order approximation, due to the weak intermolecular interactions in OSCs. The discussions of this section will be framed around zeroth-order approximations commonly used in traditional organic materials; higher-order corrections will be discussed and incorporated as needed in specific cases.
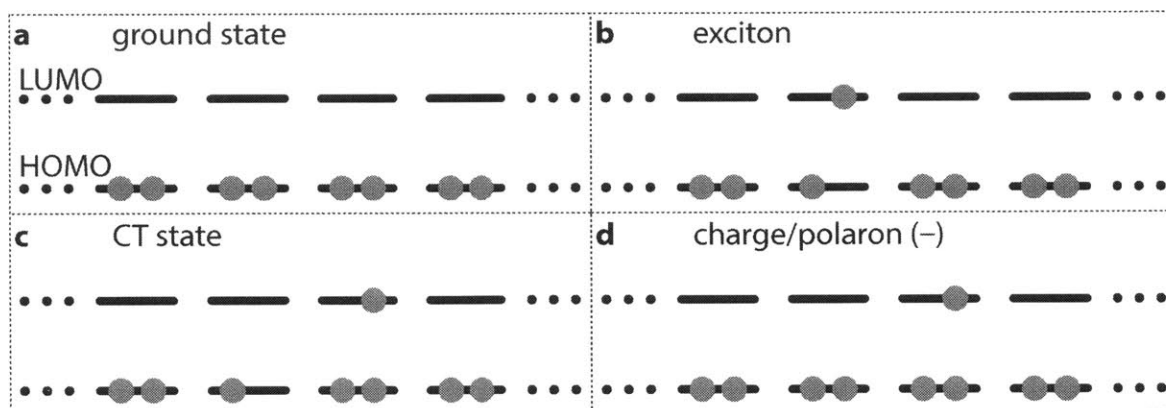
Figure 1.1: Fundamental electronic states in OSCs illustrated in the context of a 1-dimensional chain of molecules. Each pair of HOMO and LUMO lines corresponds the valence orbitals of a molecule. Grey circles represent electrons occupying the molecular orbitals.

The fundamental electronic states in OSCs are illustrated in Figure 1.1. In the ground state (Figure 1.1a), the HOMO is doubly occupied and the LUMO is unoccupied. In an exciton (Figure 1.1b), the HOMO and LUMO of the same molecule are singly occupied. A charge transfer (CT) state consists of a singly occupied HOMO on one molecule and additional electron in the LUMO of a neighboring molecule (Figure 1.1c). CT states can also be described as an overall-neutral state composed of positive

and negative (Figure 1.1d) charges on neighboring molecules. Some systems have CT states that can undergo radiative relaxation directly from the CT state to the ground state; this type of CT state is referred to as an exciplex.

Charges in OSCs are often referred to as polarons. Polarons are quasiparticles consisting of a charge and the dielectric polarization of its surroundings. Polarization of the surrounds is the distortion of positive and negative densities in the surroundings in response to the unbalanced charge.
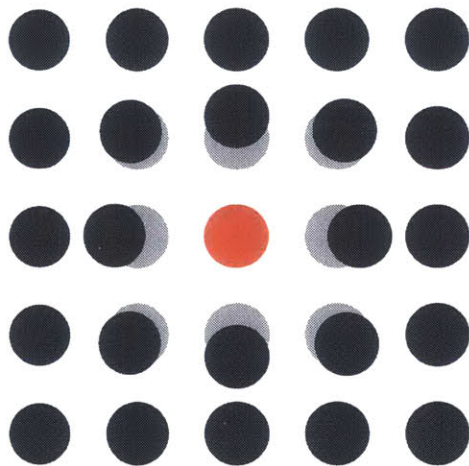
Figure 1.2: Illustration of a polaron. The charge (red) induces distortions (polarization) in the surrounding molecules.

1.1.2 Singlet and triplet spin substates

Electrons have intrinsic spin angular momentum of $S = 1/2$. Within the zeroth order approximations of the current discussion, the electronic spatial $\mathbf{r}$ and spin σ degrees of freedom are uncoupled. Therefore, total electronic wavefunctions will be products of spatial and spin components:

$$\Psi = \phi(\{\mathbf{r}\})\chi(\{\sigma\}). \tag{1.1}$$

The spin statistics theorem the total wavefunction of a system of identical, half-integer-spin particles must change sign when two particles are swapped—the total

34

a

$$\Psi_{S_1} = \frac{1}{\sqrt{2}} \begin{bmatrix} \phi_{\text{HOMO}}(\mathbf{r}_1)\phi_{\text{LUMO}}(\mathbf{r}_2) \\ +\phi_{\text{HOMO}}(\mathbf{r}_2)\phi_{\text{LUMO}}(\mathbf{r}_1) \end{bmatrix} \times \begin{bmatrix} \alpha(\sigma_1)\beta(\sigma_2) \\ -\alpha(\sigma_2)\beta(\sigma_1) \end{bmatrix}$$

(symmetric)   (antisymmetric)

b

$$\Psi_{T_+} = \frac{1}{\sqrt{2}} \begin{bmatrix} \phi_{\text{HOMO}}(\mathbf{r}_1)\phi_{\text{LUMO}}(\mathbf{r}_2) \\ -\phi_{\text{HOMO}}(\mathbf{r}_2)\phi_{\text{LUMO}}(\mathbf{r}_1) \end{bmatrix} \times \begin{bmatrix} \alpha(\sigma_1)\alpha(\sigma_2) \end{bmatrix}$$

(antisymmetric)   (symmetric)

c

$$\Psi_{T_0} = \frac{1}{\sqrt{2}} \begin{bmatrix} \phi_{\text{HOMO}}(\mathbf{r}_1)\phi_{\text{LUMO}}(\mathbf{r}_2) \\ -\phi_{\text{HOMO}}(\mathbf{r}_2)\phi_{\text{LUMO}}(\mathbf{r}_1) \end{bmatrix} \times \begin{bmatrix} \alpha(\sigma_1)\beta(\sigma_2) \\ +\alpha(\sigma_2)\beta(\sigma_1) \end{bmatrix}$$

(antisymmetric)   (symmetric)

d

$$\Psi_{T_-} = \frac{1}{\sqrt{2}} \begin{bmatrix} \phi_{\text{HOMO}}(\mathbf{r}_1)\phi_{\text{LUMO}}(\mathbf{r}_2) \\ -\phi_{\text{HOMO}}(\mathbf{r}_2)\phi_{\text{LUMO}}(\mathbf{r}_1) \end{bmatrix} \times \begin{bmatrix} \beta(\sigma_1)\beta(\sigma_2) \end{bmatrix}$$

(antisymmetric)   (symmetric)

e

$$\Psi_{S_0} = \frac{1}{\sqrt{2}} \begin{bmatrix} \phi_{\text{HOMO}}(\mathbf{r}_1)\phi_{\text{HOMO}}(\mathbf{r}_2) \end{bmatrix} \times \begin{bmatrix} \alpha(\sigma_1)\beta(\sigma_2) \\ -\alpha(\sigma_2)\beta(\sigma_1) \end{bmatrix}$$

(symmetric)   (antisymmetric)

Figure 1.3: Ground (**e**) and first excited singlet (**a**) and triplet states (**b**, **c**, **d**) of a two-electron system in the HOMO-LUMO basis. The orbital digram representations are shown in the left column, with the bottom level representing the HOMO and the top level the LUMO. The wavefunctions are given to the right, with exchange symmetry of the spatial and spin components labeled in blue. Note: For simplicity, a general triplet exciton is commonly illustrated using the orbital diagrams of either **b** or **d**.

wavefunction must be antisymmetric under exchange. For the product wavefunction of Equation (1.1), this requires either ϕ or χ to be antisymmetric and the other to be symmetric. For a two-electron system in the HOMO-LUMO basis, this results in the ground and single-excitation wavefunctions given in Figure 1.3.

35

In the notation used for the total wavefunctions Ψ in Figure 1.3, the capital letter of the subscript indicates the total spin: $S \leftrightarrow S_{\text{tot}} = 0$, $T \leftrightarrow S_{\text{tot}} = 1$. $S_{\text{tot}} = 0$ states are referred to as singlets, because they have spin multiplicity $S_{\text{tot}}(S_{\text{tot}} + 1) = 1$. $S_{\text{tot}} = 1$ states are referred to as triplets, because they have spin multiplicity $S_{\text{tot}}(S_{\text{tot}} + 1) = 3$, and the subscripts of T_-, T_0, T_+ indicates the magnetic quantum number $m_S = -1$, $m_S = 0$, and $m_S = +1$, respectively. As singlets all have $m_S = 0$, their spin quantum number is omitted from the notation. Instead, the S_0 is used denote the ground state (always a singlet in typical organics, and S_1 is used to denote the first excited singlet state.

The electron-electron interaction energy,

$$E_{\text{e-e}} = \iint \Psi(\mathbf{r}_1, \mathbf{r}_2)^* \frac{1}{|\mathbf{r}_1 - \mathbf{r}_2|} \Psi(\mathbf{r}_1, \mathbf{r}_2) \, d^3\mathbf{r}_1 d^3\mathbf{r}_2,$$

is composed of a Coulomb energy and an exchange energy. For the excited (exciton) states of Figure 1.3, the Coulomb energy is given by

$$C = \iint |\phi_{\text{HOMO}}(\mathbf{r}_1)|^2 \frac{1}{|\mathbf{r}_1 - \mathbf{r}_2|} |\phi_{\text{LUMO}}(\mathbf{r}_2)|^2 \, d^3\mathbf{r}_1 d^3\mathbf{r}_2,$$

and is analogous to the Coulombic repulsion of the electron and hole densities. The exchange energy is given by

$$J = \iint \phi_{\text{HOMO}}^*(\mathbf{r}_1) \phi_{\text{LUMO}}(\mathbf{r}_1) \frac{1}{|\mathbf{r}_1 - \mathbf{r}_2|} \phi_{\text{HOMO}}^*(\mathbf{r}_2) \phi_{\text{LUMO}}(\mathbf{r}_2) \, d^3\mathbf{r}_1 d^3\mathbf{r}_2, \qquad (1.2)$$

and, despite being completely quantum mechanical in nature, can be conceptualized as the Coulomb repulsion of the electron and hole within the overlapping region of ϕ_{HOMO} and ϕ_{LUMO}. The exchange energy will therefore depend on the spatial overlap of ϕ_{HOMO} and ϕ_{LUMO}:

$$J \propto |\langle \phi_{\text{HOMO}} | \phi_{\text{LUMO}} \rangle|^2$$

Due to the symmetry of the S_1 spatial component,

$$E_{\text{e-e}}(S_1) = C + J.$$

The antisymmetry of the spatial components of the triplets, on the other hand, results in

$$E_{\text{e-e}}(T_-) = E_{\text{e-e}}(T_0) = E_{\text{e-e}}(T_+) = C - J.$$

Therefore, the exited singlet is $2J$ higher in energy than the triplet states:

$$\Delta E_{\text{ST}} = E(S_1) - E\left(T_{\{-,+,0\}}\right) = 2J \tag{1.3}$$

This singlet-triplet exchange splitting is brought to light by considering a system of two indistinguishable electrons in an infinite 1-dimensional well of length L. The eigenstates of this system are the familiar particle-in-a-box eigenfunctions,

$$\phi_n(x) = \sqrt{\frac{2}{L}} \sin\left(\frac{n\pi x}{L}\right), \quad n = 1, 2, \ldots$$

The spatial components of the first excited singlet and triplet wavefunctions are

$$\text{singlet:} \ [\phi_1(x_1)\,\phi_2(x_2) + \phi_1(x_2)\,\phi_2(x_1)], \tag{1.4}$$

$$\text{triplet:} \ [\phi_1(x_1)\,\phi_2(x_2) - \phi_1(x_2)\,\phi_2(x_1)]. \tag{1.5}$$

The probability densities of these spatial components are plotted in Figure 1.4. In the singlet state, the particles are most likely to be found at the same point in the box (at coordinates $\{0.3L, 0.3L\}$ and $\{0.7L, 0.7L\}$). In the triplet state, the particles are most likely to be found toward opposite sides of the box (at coordinates $\{0.3L, 0.7L\}$ and $\{0.7L, 0.3L\}$). The electrons are, therefore, better correlated in the triplet state, resulting in it a lower energy than the singlet.

The effects of confinement are also displayed in Figure 1.4. As the box size is increased from $L = 1$ to $L = 2$, the differences in correlation between the singlet and triplet are

diminished, which decreases the effect of the exchange splitting.
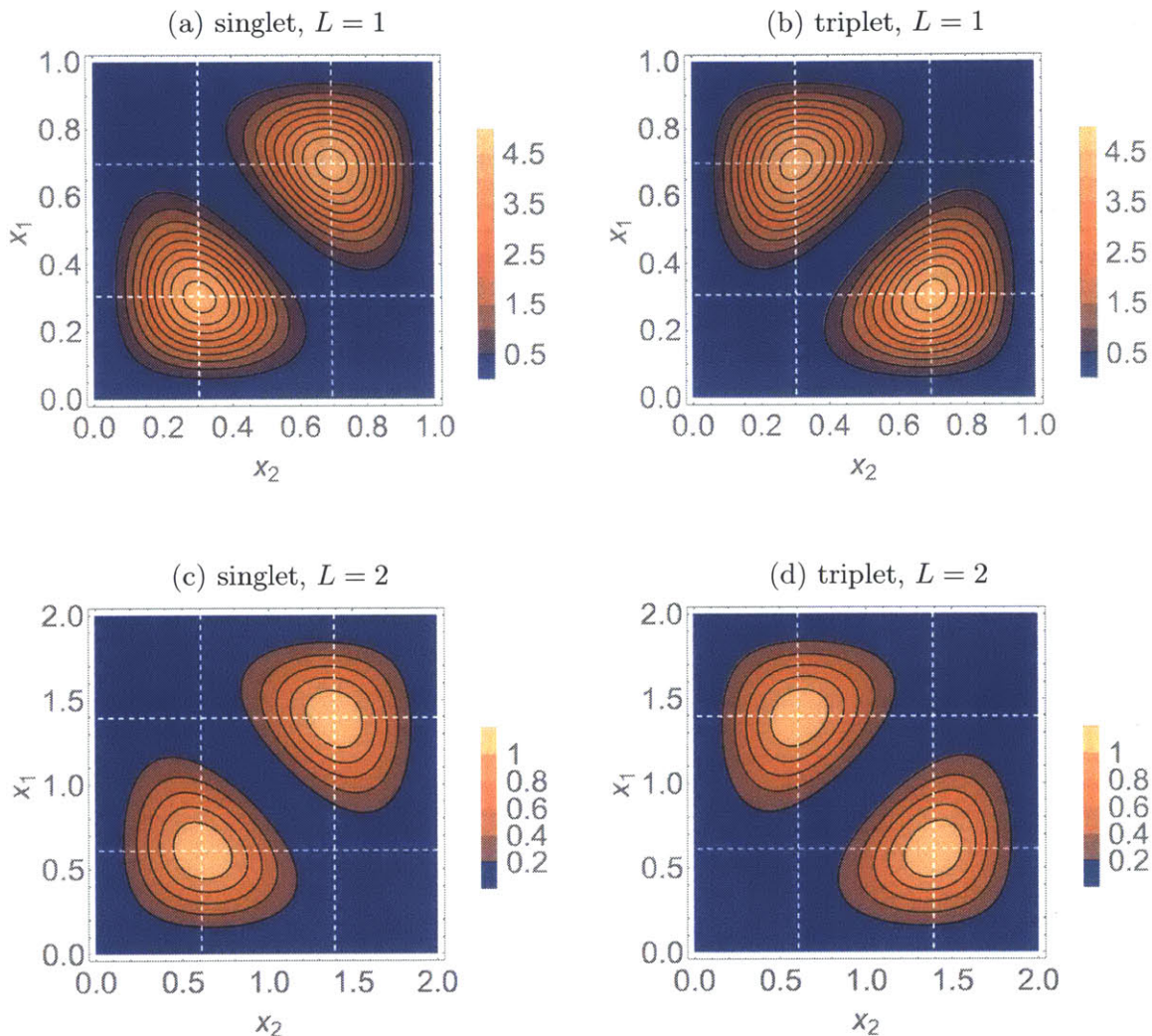
Figure 1.4: Probability density for the singlet and triplet and spatial components of the wavefunction for two particles in a box of length L with quantum numbers $n_1 = 1$, $n_2 = 2$ [see Equations (1.4) and (1.5)]. In the singlet state, the particles are most likely to be found at the same point in the box (at coordinates $\{0.3L, 0.3L\}$ and $\{0.7L, 0.7L\}$). In the triplet state, the particles are most likely to be found toward opposite sides of the box (at coordinates $\{0.3L, 0.7L\}$ and $\{0.7L, 0.3L\}$). Increasing the box size spreads out the joint probability, decreasing the effects of exchange.

Confinement of the electron and hole as an exciton or CT state in OSCs results in a substantial overlap of ϕ_{HOMO} and ϕ_{LUMO} (i.e. the HOMO and LUMO are of the same or neighboring molecules) and a potentially large exchange energy, as large as

several hundred meV.[34] Therefore, the singlet and triplet substates of excited states in OSCs often behave as distinct states, and a number of consequences result.

One of the most important properties of singlet and triplet states is orthogonality:

$$\langle \Psi_S \mid \Psi_T \rangle = 0,$$

which results from orthogonality of the different spin components $\chi(\{\sigma\})$. This results in spin-forbidden transitions between the excited singlet and triplet substates. Also, due to the ground state being a singlet, photoexcitation results in only singlet excitons, and only singlet excitons are able to radiatively relax to the ground state. Triplet excitons are, therefore, dark states in traditional OSCs.

1.2 Organic photovoltaics

1.2.1 Fundamental electronic processes

Solar energy harvesting requires conversion of absorbed photon energy into a separated charges that are collected at opposite electrodes. The fundamental processes in
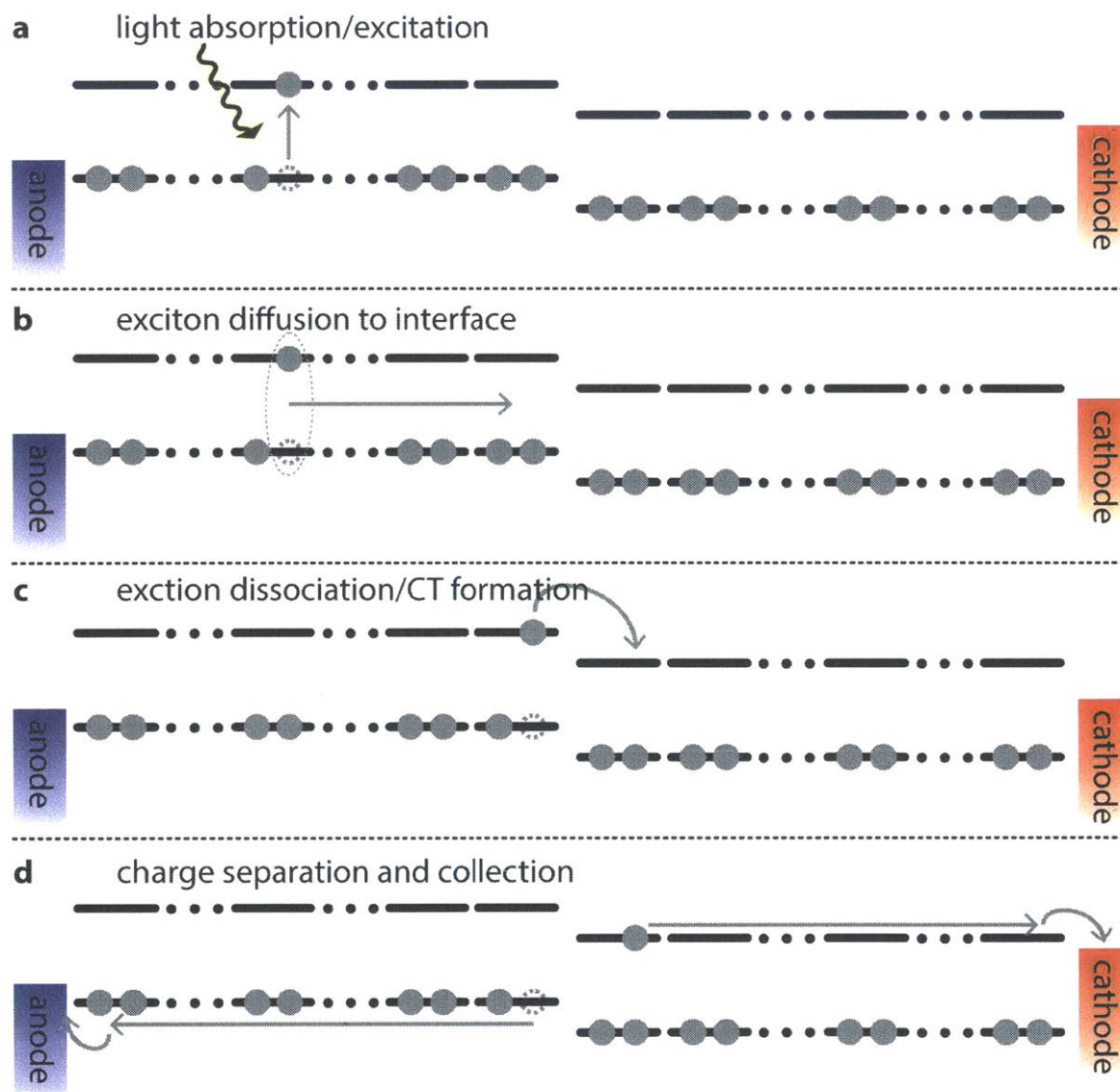
Figure 1.5: Illustrations of the fundamental processes in an OPV device. Grey circles represent electrons, and grey, dashed circle outlines are used here to denote the empty occupation resulting from the initial excition process in **b**. The acceptor valence orbitals are lower than the donor's, which drives exciton dissociation at the interface.

OPVs are illustrated in Figure 1.5. Photon absorption produces an excition (Figure 1.5a). The exciton binding energy is $\gg k_{\mathrm{B}}T$, preventing spontaneous dissociation at room temperature.[31] Instead, exciton dissociation requires the exciton to diffuse (Figure 1.5b) to an interface between two OSC materials with correct offset of their HOMO and LUMO levels to induce a CT state, as show in Figure 1.5c. Finally, charge separation from the CT state must occur, followed by diffusion and extraction of the charges to opposite electrodes (Figure 1.5d).

1.2.2 Architectures and morphologies
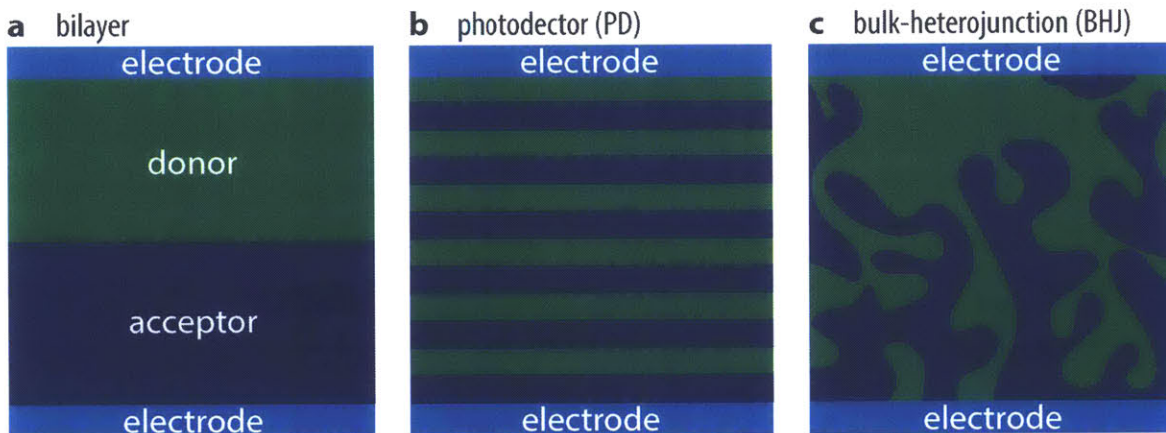
Figure 1.6: Illustration of the three OPV device architectures used in studies found in §2 and §3.

The donor/acceptor interface required for excition dissociation can be realized using a number of different OPV architectures. Figure 1.6 contains illustrations of the three OPV device architectures used in the studies throughout §2 and §3. The most basic architecture is a bilayer OPV (Figure 1.6a), where single layers of the donor and acceptor materials are sandwiched between the two electrodes. A problem arrises in bilayer OPVs if either layer is made thicker than the exciton diffussion length ($\sim$ nm for singlet excitons[35]), in which case a number of relaxation processes may occur prior to exciton diffusion to the interface, wasting energy as heat. Photodetectors (PDs) (Figure 1.6b) are similar to bilayer OPVs, but contain a number of thin donor and acceptor films layered in series between the two electrodes. They can be made thicker

41

and absorb more photons while avoiding exciton diffusion limitations, and are useful for scientific studies under reverse-bias conditions, which ensures high charge extraction yield.[36,37] PDs are akin to a nanostructured version of a bulk-heterojunction (BHJ) OPV (1.6c), which contain a blend of donor and acceptor materials. The morphology of the blend layer of a BHJ can vary significantly depending on the materials and preparation technique.

Metal organic frameworks

One class of materials that allows exquisite control over the intermolecular distances and angles between organic molecules is metal-organic frameworks (MOFs). These are crystalline hybrid materials made from inorganic and organic building blocks whose topologies, and implicitly the intermolecular distances between various building blocks, can be controlled by design using the principles of reticular chemistry. Although MOFs have traditionally been used for gas separation and storage, their highly ordered nature has also made them attractive targets for studying photophysical phenomena related to energy transfer[38-40] for light harvesting and luminescence for sensing.[41-45] One idea is that blends of donor and acceptor OSC materials could be incorporated within the empty space a MOF with a highly conductive framework component, allowing for rapid and efficient transport of charges formed within the embedded OSC blends.

1.2.3 Efficiency and the Shockley-Queisser limit

Understanding the factors limiting current-day solar conversion efficiencies is fundamental to achieving performance increases. The power generated by a solar cell is equal to the product of its voltage and current. The maximum voltage is set by the bandgap ($E(S_1$ in OVPs), because photons below are not absorbed, and the energy of photons above is wasted as heat through rapid vibrational relaxation. Because the solar spectrum is composed of photons at wide range of energies at varying intensities,

there is a maximum theoretical efficiency for a singlet-junction solar cell of 33.7%, known as the Shockley-Queisser limit.[46]

Multiple exciton generation

Splitting the excited state generated after the absorption of high energy photons presents one pathway beyond the single junction efficiency limit. Instead of harvesting a single electron, several charges can be obtained by dissociating the child excitons. For example, so-called multiple exciton generation mechanisms have been used to produce an average of more than one electron from an ultraviolet photon with energy four times the bandgap.[47] Multiple exciton generation thus recaptures wasted energy by generating and additional exciton using the excess vibrational energy before it is converted to heat.

1.2.4 Singlet fission

Singlet exciton fission is a type of multiple exciton generation mechanism found in organic semiconductors, whereby a singlet excited state (S_1) splits into two triplets (T_1) of $E(T_1) \lesssim \frac{1}{2}E(S_1)$ on neighboring molecules; see Figure 1.7.[48,49] It is notable because spin conservation disallows the usual competing loss process: thermal relaxation of the high-energy exciton into a single low-energy exciton (i.e. thermal relaxation from S_1 to T_1 is spin-forbidden). In fission, the low energy exciton is a dark state, inaccessible by a direct transition from either the high energy exciton or the ground state. Only the evolution of the high-energy state into two triplet excitons is spin-allowed, as discussed below. Consequently, prior studies have suggested that singlet fission can be efficient even in the visible spectrum, harnessing photons of just twice the energy of the child excitons.[50–55]

There is a side effect of spin in singlet fission, however. The dark exciton controls the electrical properties of the cell. These are decoupled from the optical absorption, which is controlled by the bright, high-energy exciton. Thus, fission does not itself
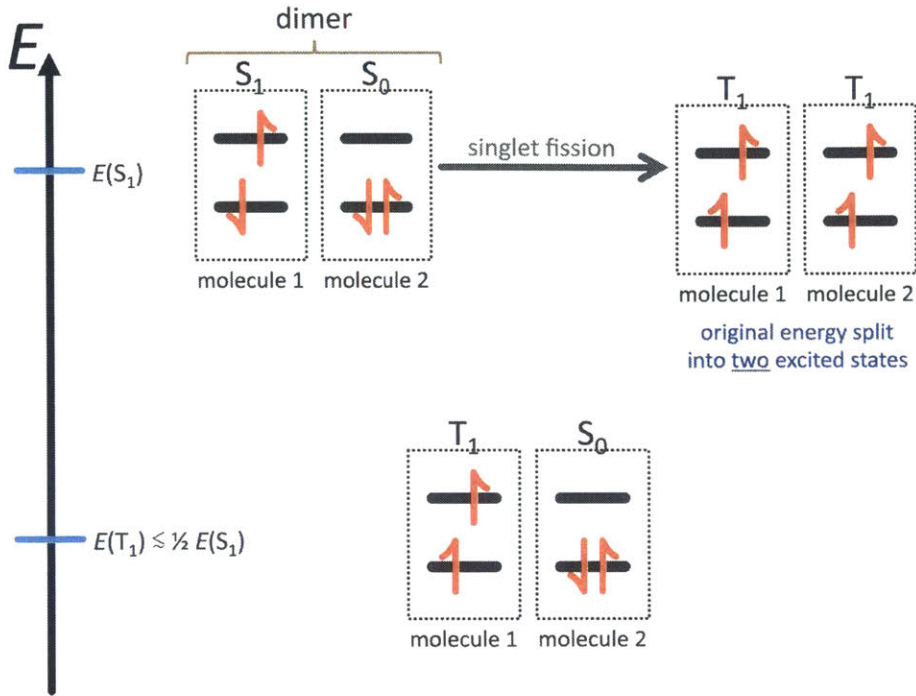
Figure 1.7: Illustration of the singlet fission process. A singlet excited state (S_1) splits into two triplets (T_1) of $E(T_1) \lesssim \frac{1}{2}E(S_1)$ on neighboring molecules.

increase the power efficiency of a solar cell. It potentially doubles the photocurrent at the cost of losing at least half the open circuit voltage. To overcome the Shockley-Queisser limit, solar cells must combine fission with a conventional material that fills in the absorption spectrum above the dark exciton.[1,56–59] Therefore, in addition to demonstrating singlet fission can break the conventional barrier of one electron per photon, it is necessary to provide proof of concept device designs that also incorporate a material that absorbs energy between $E(T_1)$ and $E(S_1)$, which has to potential to raise the maximum device efficiency to 44.4%.[60].

1.2.5   Triplet-charge annihilation

Singlet fission introduces a large number of triplet excitons, which would otherwise not be present in a typical OPV. The presence of triplet excitons in and charges in an OPV results in an important and characteristic loss mechanism in singlet-fission-based solar cells: triplet-charge annihilation (TCA). TCA is the process of destroying

$$T_1 + C^+ \longrightarrow C^+ + S_0$$
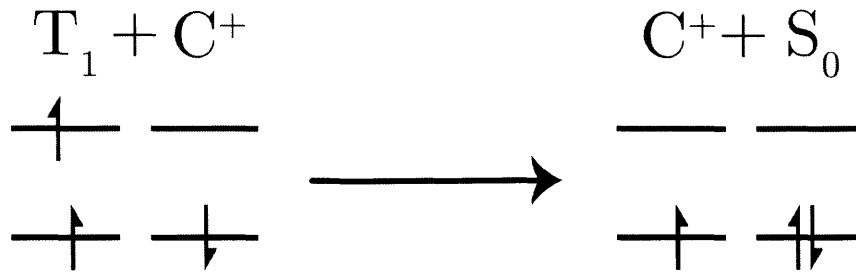
Figure 1.8: Orbital diagram illustrating the process of triplet-charge annihilation.

a triplet exciton during its interaction with a charge (see Figure 1.8). As the triplet destroyed in a TCA event was a potential source of photocurrent, it is crucial to design devices that minimize TCA, in order to preserve the benefits of singlet fission.

1.3 Organic light-emitting diodes

1.3.1 Fundamental electronic processes
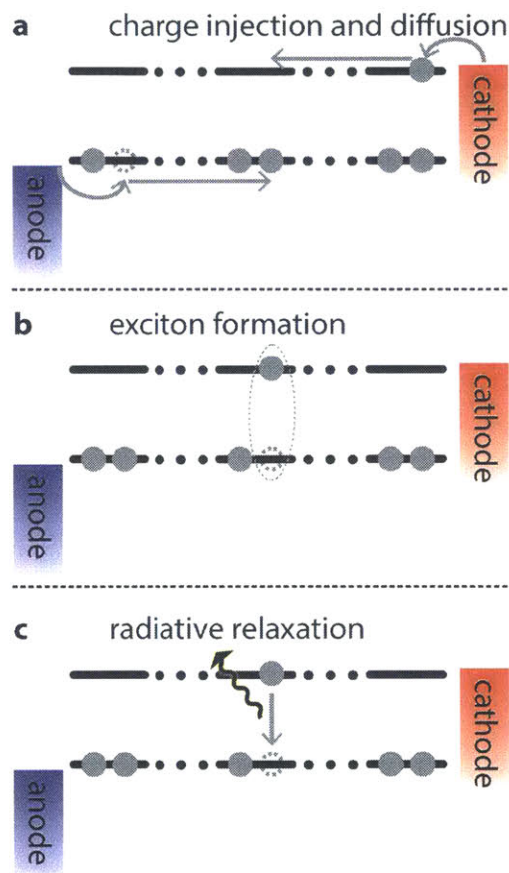
Figure 1.9: Illustrations of the fundamental processes in an OLED device.

The operation of OLEDs is similar to reverse of the processes in OPVs. Whereas light is converted into electrical power in OPVs, electrical power converted into light in OLEDs. The fundamental processes in OLEDs are illustrated in Figure 1.9. Charges (electrons and holes) injected at opposite electrodes diffuse and eventually come within the radius at which they are attracted through their mutual Coulomb interaction (Figure 1.9a). Under influence of the Coulomb attraction the charges form an exciton (Figure 1.9b). The exciton then may undergo radiative relaxation to the ground state, emitting a photon (Figure 1.9c).

1.3.2 Efficiency and the impact of exciton spin substates
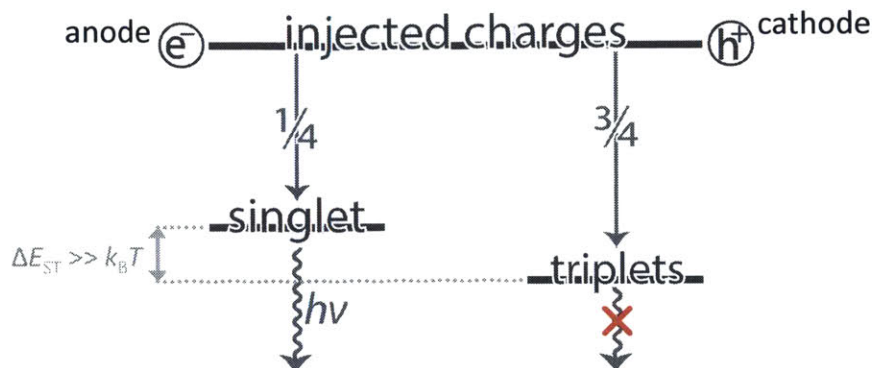
Figure 1.10: Diagram of the result of the operation of an OLED based on typical hydrocarbon OSCs. Injected charges have random spins, and 3/4 of the excitons formed are dark triplet states. The maximum efficiency in such a device is 25%.

The spin of the injected charges are completely random and, therefore, combine to form excitons with equal probability for forming each of the four spin substates discussed in §1.1.2. This results in a major fundamental limitation for OLEDs composed of traditional semiconductor materials: 75% of the excitons formed are non-emissive, dark triplet states (see Figure 1.10), resulting a maximum efficiency of 25%.
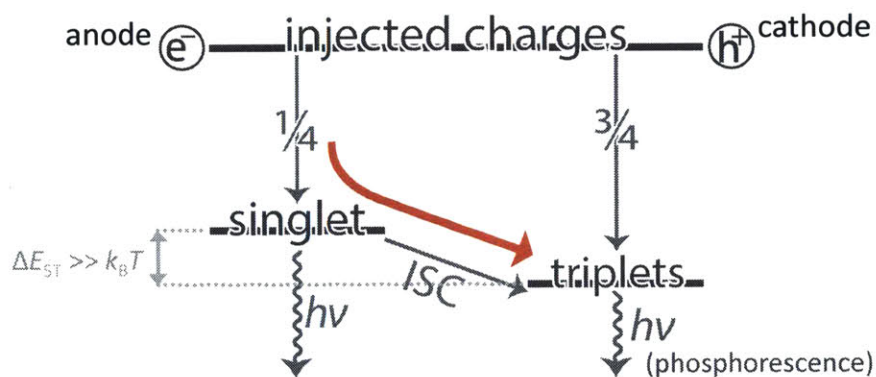
Figure 1.11: Diagram of the result of the operation of an OLED incorporating phosphorescent organometallic emitters. Nearly all of the injected charges end up in the triplet states, from which phosphorescence may take place. The maximum efficiency in such a device is 100%.

Current state-of-the-art OLEDS incorporate organometallic complexes containing heavy metal atoms that provide high amounts of spin-orbit coupling (SOC).[61–63] SOC causes mixing between the singlet and triplet excited states, relaxing the spin-selection

rule for transitions between the singlet and triplet excited states and allowing efficient phosphorescence from the triplet states. The majority of singlet excitons in these systems undergo intersystem crossing ISC to form triplet excitons, so the majority of the emission comes from phosphorescence.

Unfortunately, in addition to the high cost associated with the precious metals found in many of these organometallic complexes, empirical evidence suggests there is a practical lower limit to the phosphorescence lifetime of commonly used phosphors, which has stagnated somewhere in the vicinity of 1 microsecond.[64] This limit imposes a major roadblock to device design, because as the charge injection rate is increased to drive the OLED brighter, long lived excitons result in substantial energy build-up in the device, which ultimately leads to bimolecular annihilation processes and lower efficiency—a phenomenon often referred to as "roll-off."[65–67] In addition, the energy released during such bimolecular recombination events is believed generate structural defects through chemical reactions, resulting in degradation of OLED devices over time.[29,68]
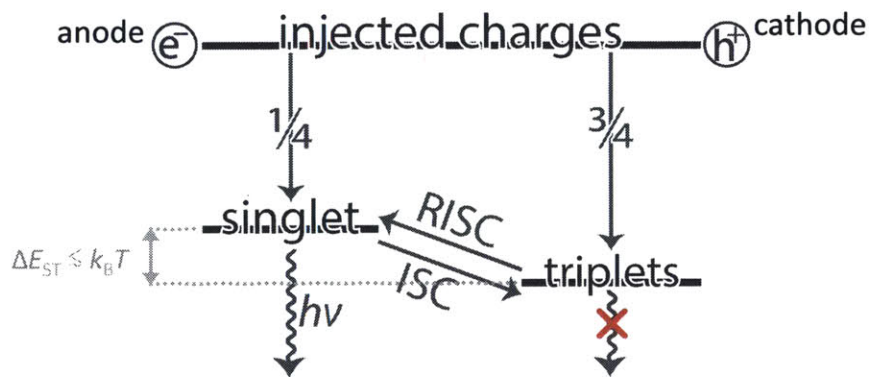
Figure 1.12: Diagram of the result of the operation of an OLED incorporating TADF emitters. By minimizing the ΔE_{ST}, excited triplets may be thermally upconverted to S_1 and undergo ensuing fluorescence. The maximum efficiency in such a device is 100%.

To obtain high-efficiency, low-cost OLEDs for applications in solid-state lighting, recent work has proposed thermally assisted delayed fluorescence (TADF) as an alternative mechanism to phosphorescence for harvesting triplet excitons.[69–71] TADF relies on efficient thermal upconversion from the dark triplet state to an emissive sin-

glet state,[72] a process termed reverse intersystem crossing (RISC); see Figure 1.12. TADF emitters are designed based on achieving a small overlap between the HOMO and LUMO orbitals, which as discussed in §1.1.2, decreases the exchange interaction energy. Because typical fluorescence rates are on the order of nanoseconds, TADF devices could achieve better roll-off characteristics and longevity, if the RISC lifetime can be made comparable to the fluorescence lifetime. Indeed, the maximum efficiency of a TADF-based device is also 100%.

1.4 Theoretical tools

1.4.1 Quantum master equations

Whereas wave functions are used when a system is known to be in a single, quantum state, density operators and matricies are used for any of the following conditions:

1. Only the probability of a system being in a certain state is known (i.e. there is some uncertainty regarding the state of the system).

2. There is an ensemble of systems that may be in a different states at a given moment.

3. The generation or interaction of two or more subsystems results in entanglement of their states.

The density operator ρ of an for a system existing in a possibility of N states is expressed as

$$\rho = \sum_{i}^{N} p_i \left| \psi_i \right\rangle \left\langle \psi_i \right|, \tag{1.6}$$

where p_i is the probability of finding the system in the state $\left| \psi_i \right\rangle$ and must sum to one: $\sum p_i = 1$. Note: The states in Equation (1.6) do not to be orthogonal. The elements of the density matrix corresponding to ρ in a basis of states $\{ \left| u_m \right\rangle \}$ are given

49

by

$$\rho_{mn} = \langle u_m | \rho | u_n \rangle = \sum_i^N p_i \langle u_m | \psi_i \rangle \langle \psi_i | u_n \rangle, \qquad (1.7)$$

where it is recognized that the probability of finding the system in state $|u_m\rangle$ is the diagonal element ρ_{mm}.

When the system is known to be in state $|\psi_j\rangle$ (a pure ensemple) its density operator is simply

$$\rho = |\psi_j\rangle \langle \psi_j|, \qquad (1.8)$$

while a system whose state is completely random or uncertain has the diagonal density matrix proportional to the $N \times N$ identity matrix $\mathbf{1}_N$:

$$\rho = \frac{1}{N}\mathbf{1}_N = \begin{pmatrix} N^{-1} & & \\ & \ddots & \\ & & N^{-1} \end{pmatrix}, \qquad (1.9)$$

where N is the number of states in the sum of Equation (1.6).

Some other useful properties of the density matrix are:

- The ensemble average expectation value of the observable with operator A: $\langle A \rangle = \mathrm{Tr}\{A\rho\}$.

- The probability of finding the system in state $|\psi\rangle$: $\mathrm{Tr}\{|\psi\rangle \langle \psi| \rho\}$

Lindblad form of quantum master equations

The time dependence of the system density matrix is given by the Liouville-von Neumann equation:

$$\frac{d\rho}{dt} = -\frac{i}{\hbar}[H, \rho], \qquad (1.10)$$

where H is the Hamiltonian of the system. Often, one is only interested in the behavior of a subset of the system. This is often the case when thermal fluctuations (i.e. phonons, in the solid state) are involved in irreversible (incoherent) transitions

50

of the subsystem. Rather than calculating the unitary (coherent) evolution of the entire system using Equation (1.10), a partial trace can be used to isolate a reduced description for the behavior of the subsystem under the influence of its environment. This process represents an approximation that assumes the time scale of the environmental fluctuations causing the irreversible transition are short with respect to the transition they cause.[73] The irreversible transition is then said to be stochastic, due to the uncertainty in the state of the environment. The time evolution of the reduced density matrix—referred to as ρ from here on—is then governed by what is termed a "quantum master equation" (QME).

The most general form for a QME is the Lindblad form[73–75]:

$$\frac{d\rho}{dt} = -\frac{i}{\hbar}\left[H, \rho\right] + \sum_n \left(\Gamma_n \rho \Gamma_n^\dagger - \frac{1}{2}\left\{\Gamma_n^\dagger \Gamma_n, \rho\right\}\right), \tag{1.11}$$

where where $\{A, B\} = AB + BA$ is the anticommutator. The first hand on the right-hand side of Equation (1.11) corresponds the the right-hand side of Equation (1.10), except H is the Hamiltonian of the *subsystem*, and describes the unitary evolution of the subsystem. The second term on the right-hand side of Equation (1.11) describes the stochastic, irreversible transitions between the states of subsystem. The Γ operators are known as "Lindblad operators," or "quantum jump operators."[75] Each one corresponds to an irreversible transition between states of of the subsystem induced by interactions with the environment, or "bath." For example, the Lindblad operator corresponding to a transition from state $|\psi_i\rangle$ of the subsystem to state $|\psi_j\rangle$ of the subsystem can be represented as

$$\Gamma_{j\leftarrow i} = \sqrt{k_{j\leftarrow i}}\,|\psi_j\rangle\,\langle\psi_i|\,, \tag{1.12}$$

where $k_{j\leftarrow i}$ is the rate constant quantifying the transition rate.

The effect of the Γ operators can be seen by considering the Equation (1.11) in the case that $H = 0$. For a subsystem with two possible states, $|a\rangle$ and $|b\rangle$, and one Lindblad operator, $\Gamma_{a\leftarrow b} = \sqrt{k_{a\leftarrow b}}\,|a\rangle\,\langle b|$. The two terms of the sum in Equation

(1.11) are

$$\Gamma_{a\leftarrow b}\rho\Gamma_{a\leftarrow b}^{\dagger} = k_{b\leftarrow a}\,|a\rangle\,\langle b|\,\rho\,|b\rangle\,\langle a| = k_{a\leftarrow b}\rho_{bb}\,|a\rangle\,\langle a|\,,$$

and

$$-\frac{1}{2}\left\{\Gamma_{a\leftarrow b}^{\dagger}\Gamma_{a\leftarrow b}, \rho\right\} = -\frac{k_{a\leftarrow b}}{2}\left(|b\rangle\,\langle b|\,\rho + \rho\,|b\rangle\,\langle b|\right).$$

This yields the system of equations rate equations

$$\frac{d}{dt}\begin{pmatrix} \rho_{aa} & \rho_{ab} \\ \rho_{ba} & \rho_{bb} \end{pmatrix} = k_{a\leftarrow b}\begin{pmatrix} \rho_{bb} & \rho_{ab}/2 \\ -\rho_{ba}/2 & -\rho_{bb} \end{pmatrix}$$

Therefore, we can see there is transfer of probability from ρ_{bb} to ρ_{aa} with rate constant $k_{a\leftarrow b}$, and the off-diagonal coherence elements decay with rate constant $k_{a\leftarrow b}/2$. The decay of the coherences is due to the loss of phase information (dephasing) that results from an irreversible transition.[76]

Extending the Lindblad form with annihilation and source operators

The sum over Lindblad operator transitions in Equation (1.11) preserves the total population of states in the subsystem and the trace of the subsystem density matrix $\text{Tr}\,\{\rho\}$,[73–75,77] as the two are equivalent. This is because the Lindblad operators only produce population transfer between states of the subsystem and dephasing. When population can be exchanged between the subsystem and bath, creating or destroying population of subsystem states, Equation (1.11) can be extended by adding annihilation and source operators Λ and Φ:[78]

$$\frac{d\rho}{dt} = -\frac{i}{\hbar}\,[H, \rho] + \sum_{n}\left(\Gamma_n\rho\Gamma_n^{\dagger} - \frac{1}{2}\left\{\Gamma_n^{\dagger}\Gamma_n, \rho\right\}\right) - \frac{1}{2}\left\{\Lambda, \rho\right\} + \Phi. \tag{1.13}$$

The annihilation operator Λ is the sum over individual operators for the population-decreasing transitions. For example, if states $|a\rangle$ and $|b\rangle$ decay with rate constants k_a and k_b, then

$$\Lambda = k_a\,|a\rangle\,\langle a| + k_b\,|b\rangle\,\langle b|.$$

The creation operator is the sum over individual operators for the the growth rate of each state. For example, if $|a\rangle$ and $|b\rangle$ are generated at the *rates* ϕ_a and ϕ_b, then

$$\Phi = \phi_a |a\rangle \langle a| + \phi_b |b\rangle \langle b|.$$

Analytical solutions

The time dependent solution for ρ can be obtained analytically by rewriting Equation 1.13) as a superoperator equation in Liouville space:

$$\frac{d}{dt} |\rho) = \mathcal{M} |\rho) + \text{vec}\,(\Phi). \qquad (1.14)$$

In Equation (1.14), the $N \times N$ density matrix ρ is vectorized to obtain an $N^2 \times 1$ super vector $|\rho)$ composed by stacking the columns of ρ:

$$\text{vec}(\rho) = |\rho) = \begin{pmatrix} \rho_{1,1} \\ \vdots \\ \rho_{N,1} \\ \rho_{1,2} \\ \vdots \\ \rho_{N,2} \\ \vdots \\ \rho_{1,N} \\ \vdots \\ \rho_{N,N} \end{pmatrix}. \qquad (1.15)$$

Similarly, $\text{vec}\,(\Phi)$ is the vectorized source matrix Φ. $\mathcal{M}$ in Equation (1.14) is a $N^2 \times N^2$ superoperator matrix. An analytical expression for $\mathcal{M}$ may be obtained using the vectorization relation for the multiplication of general $N \times N$ matrices A, B, and C:

$$\text{vec}\,(ABC) = \left(C^\mathsf{T} \otimes A\right) \text{vec}\,(B), \qquad (1.16)$$

where we recognize $\mathrm{vec}(B)$ as $|\rho)$. Using Equation (1.16), we can vectorize Equation (1.13):

$$
\begin{aligned}
\mathrm{vec}\left(\frac{d\rho}{dt}\right) &= \mathrm{vec}\left(-\frac{i}{\hbar}\left[H,\rho\right] + \sum_n \left[\Gamma_n \rho \Gamma_n^\dagger - \frac{1}{2}\left\{\Gamma_n^\dagger \Gamma_n, \rho\right\}\right] - \frac{1}{2}\left\{\Lambda, \rho\right\} + \Phi\right) \\
&= \left(\begin{array}{l}
-\dfrac{i}{\hbar}\left[\mathbf{1}_N \otimes H - H^\top \otimes \mathbf{1}_N\right] \\[2mm]
+\displaystyle\sum_n \left[\Gamma_n^* \otimes \Gamma_n - \frac{1}{2}\left(\mathbf{1}_N \otimes \Gamma_n^\dagger \Gamma_n + \Gamma_n^\top \Gamma_n^* \otimes \mathbf{1}_N\right)\right] \\[2mm]
-\dfrac{1}{2}\left[\mathbf{1}_N \otimes \Lambda + \Lambda^\top \otimes \mathbf{1}_N\right]
\end{array}\right) \mathrm{vec}\left(\rho\right) + \mathrm{vec}\left(\Phi\right) \\
&= \mathcal{M}\,|\rho) + \mathrm{vec}\left(\Phi\right).
\end{aligned}
\tag{1.17}
$$

Transient decay   Transient decay experiments are represented by defining an initial density matrix $\rho(t=0) = \rho(0)$ and have no source term (i.e. $\Phi = 0$). Solving the differential equation of Equation (1.17), the solution for $|\rho)$ at time t is

$$
|\rho(t)) = e^{\mathcal{M}t}\,|\rho(0)) .
\tag{1.18}
$$

The matrix exponential of Equation (1.18) can be solved easily on a computer using the eigendecomposition of $\mathcal{M}$, $\mathcal{M} = ULU^{-1}$:

$$
|\rho(t)) = e^{\mathcal{M}t}\,|\rho(0)) = Ue^{Lt}U^{-1}\,|\rho(0)) ,
\tag{1.19}
$$

where e^{Lt} represents the diagonal matrix with elements

$$
(e^{Lt})_{ii} = e^{L_{ii}t}.
$$

Steady-state (continuous illumination)   Continuous illumination experiments are represented by defining a source term Φ, and we are interested in the solution of Equation (1.17) at steady-state (i.e. $\frac{d}{dt}|\rho) = 0$). Solving Equation (1.17) under these

conditions yields the steady state solution

$$|\rho(\infty)\rangle = -\mathcal{M}^{-1}\text{vec}(\Phi),\qquad(1.20)$$

which is easily solved on a computer by computing the matrix inverse $\mathcal{M}^{-1}$.

1.4.2 Magnetic field modulation of the rate of singlet-fission

Singlet fission is a spin-allowed process, because the overall process of going from a singlet to two spatially separated, takes place through 9 spin-coupled "triplet-pair" energy-eigenstate intermediates, $(TT)^{l=1,\dots,9}$.[48,78–81] We represent this kinetically as

$$S_0 + S_1 \underset{k_{-1}}{\overset{k_1}{\rightleftharpoons}} \{(TT)^l\} \overset{k_2}{\longrightarrow} T_1 + T_1$$

with $\gamma_{\text{fis}}(B)$ spanning from $S_0 + S_1$ to $T_1 + T_1$,
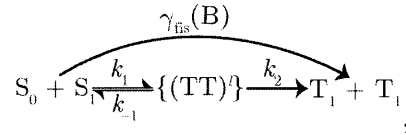
where the k_1 and k_{-1} processes represent spin-conserving electronic transitions, the k_2 process represents the spatial separation of the triplets by exciton diffusion, and $\gamma_{\text{fis}}(\mathbf{B})$ is the (magnetic field dependent) effective rate constant for the overall process of going from a singlet to an uncorrelated triplet pair. For convenience in later sections, we define the magnetic modulation factor $\chi(\mathbf{B})$:

$$\gamma_{\text{fis}}(\mathbf{B}) = \chi(\mathbf{B})\,\gamma_{\text{fis}}(\mathbf{B}=0) = \chi(\mathbf{B})\,\gamma_{\text{fis}}^0.\qquad(1.21)$$

The $\{(TT)^l\}$ states are mixtures of one singlet, three triplet, and five quintet eigenfunctions of the total spin operator $\mathbf{S}_{\text{tot}}^2 = \mathbf{S}_1^2 + \mathbf{S}_2^2$, where $\mathbf{S}_1^2$ and $\mathbf{S}_2^2$ are the spin vector operators of the two triplets. Spin must be conserved during the k_1 transition, so the initially generated pair is a singlet coherent superposition of the 9 (TT) eigenstates. This singlet state is, in general, not a stationary state, because it's zero-field

splitting spin Hamiltonian[80]

$$H_{\text{zfs}} = D\left(S_{z_1}{}^2 + S_{z_2}{}^2\right) + E\left(S_{x_1}{}^2 + S_{x_2}{}^2 - S_{y_1}{}^2 - S_{y_2}{}^2\right), \qquad (1.22)$$

does not commute with the total spin of the pair (i.e. $[H_{\text{zfs}}, \mathbf{S}_{\text{tot}}{}^2] \neq 0$).[1] The singlet admixture of the (TT) states will, therefore, vary with time. This changes the effective rate of the spin conserving k_{-1} transition back to the singlet and, therefore, affects the competition with the spin-agnostic k_2 triplet diffusion process.

By applying an external magnetic field, we have the ability to change the (TT) Hamiltonian through the Zeeman effect:

$$H = g\mu_{\text{B}}\mathbf{B} \cdot (\mathbf{S}_1 + \mathbf{S}_2) + H_{\text{zfs}}, \qquad (1.23)$$

where $g = 2.002$ is the electron g-factor, $\mu_{\text{B}} = 5.788 \times 10^{-5}$ eV $\cdot$ T is the Bohr magneton, and $\mathbf{B}$ is the external magnetic field. By varying the strength of the magnetic field, we can affect the spin-mixing in the (TT) manifold, and as a result, the effective rate of fission. We must emphasize that while the direct rate from S_1 to the (TT) manifold (which always has total singlet admixture equal to 1) is not magnetic field dependent,[83] the overall rate of going from the singlet to two separated/spin-decoupled individual triplets, $T_1 + T_1$, is magnetic field dependent. This is because the magnetic field dependent mixing of singlet character affects the number of (TT) pairs that successfully separate/decouple versus those that return to S_1. This competition is strongly dependent on the branching ratio, k_{-1}/k_2, which influences the magnetic field modulation of γ_{fis} as a result.[48,84,85] The rate constant, k_1, only determines the zero-field value, $\gamma_{\text{fis}}(0)$, by determining the attempt rate of the overall singlet fission process $S_1 \xrightarrow{\gamma_{\text{fis}}} T_1 + T_1$.

To obtain an analytical expression for the overall rate γ_{fis} at steady-state (i.e. under continuous illumination/generation of singlet excitons), we use a we start with the

---

[1]In Equation (1.22) the spin operators are labeled by the triplet (1 or 2) of the pair, and D and E are the triplet excitonic zero-field-splitting parameters that are averaged over the inequivalent molecules of the unit cell.[80,82]

QME for the (TT) density operator ρ of the form

$$\frac{d\rho}{dt} = -\frac{i}{\hbar}[H, \rho] - \frac{1}{2}\{\Lambda, \rho\} + \Phi, \tag{1.24}$$

where H is Equation (1.23),

$$\Lambda = k_2 I + k_{-1}|\text{S}\rangle\langle\text{S}| \tag{1.25}$$

$$\Phi = [\text{S}_1] k_1 |\text{S}\rangle\langle\text{S}|, \tag{1.26}$$

and $[\text{S}_1]$ is the concentration rate of singlet excitons. Equation (1.24) can be solved for ρ exactly using Equation (1.20).

Taking the trace of ρ gives the population of (TT) states:

$$\frac{d}{dt}\text{Tr}\{\rho\} = -k_2\text{Tr}\{\rho\} - \text{Tr}\{\Lambda\rho\} + [\text{S}_1]k_1 I, \tag{1.27}$$

where we recognize the first term on the right hand side of Equation (1.27) as the rate of disappearance of singlets due to fission.[78] Thus,

$$\gamma_{\text{fis}}[\text{S}_1] = k_2\text{Tr}\{\rho\}. \tag{1.28}$$

In the eigenbasis of H, the matrix elements of ρ are given by

$$\left(i\frac{E_m - E_n}{\hbar k_2} + 1\right)\rho_{mn} = \frac{k_1}{k_2}[\text{S}_1]\mathcal{S}_m^*\mathcal{S}_n - \frac{1}{2}\frac{k_{-1}}{k_2}\sum_{l=1}^{9}(\mathcal{S}_m^*\mathcal{S}_l\rho_{ln} + \mathcal{S}_l^*\mathcal{S}_n\rho_{ml}), \tag{1.29}$$

where the E_m are the eigenvalues of H and The $\mathcal{S}_m$ are overlap factors of the mth energy eigenstate of H, $|m\rangle$, with the singlet-spin eigenstate of S^2_{total} (i.e. $S^2|\text{S}\rangle = 0|\text{S}\rangle$):

$$\mathcal{S}_m = \langle\text{S}|0\rangle. \tag{1.30}$$

Both E_m and $\mathcal{S}_m$ change with the field strength, influencing the fission rate through Equations (1.29) and (1.28) by changing the oscillation frequency and singlet admix-
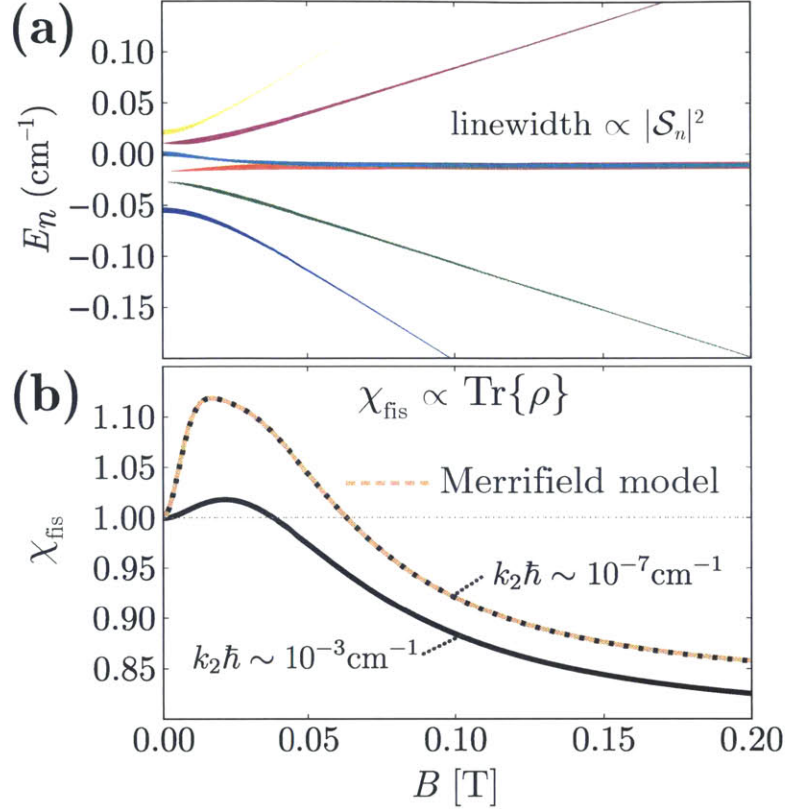
Figure 1.13: Density matrix (Johnson and Merrifield model) MFE calculations. (a) Magnetic field changes the E_m and $\mathcal{S}_m$, which (b) affects χ_{fis}. In the long-lifetime limit ($|E_m - E_n| \gg \hbar k_2$), the MFE is nearly identical to that calculated with the simplified Merrifield model.

tures (see Figure 1.13).

The density matrix treatment discussed so far has become known as the "Johnson and Merrifield model," and has been shown to accurately reproduce experimental singlet fission magnetic field effects (MFEs).[48,81] The simpler and more widely used "Merrifield model,"[79] while not as quantitative, has a more intuitive interpretation. In the long-lifetime limit ($|E_m - E_n| \gg \hbar k_2$; see Figure 1.13c), Equation (1.29) simplifies to to a diagonal matrix and yields

$$\gamma_{\text{fis}} = k_1 \sum_{l=1}^{9} \frac{|\mathcal{S}_l|^2}{1 + \frac{k_{-1}}{k_2}|\mathcal{S}_l|^2} \tag{1.31}$$

58
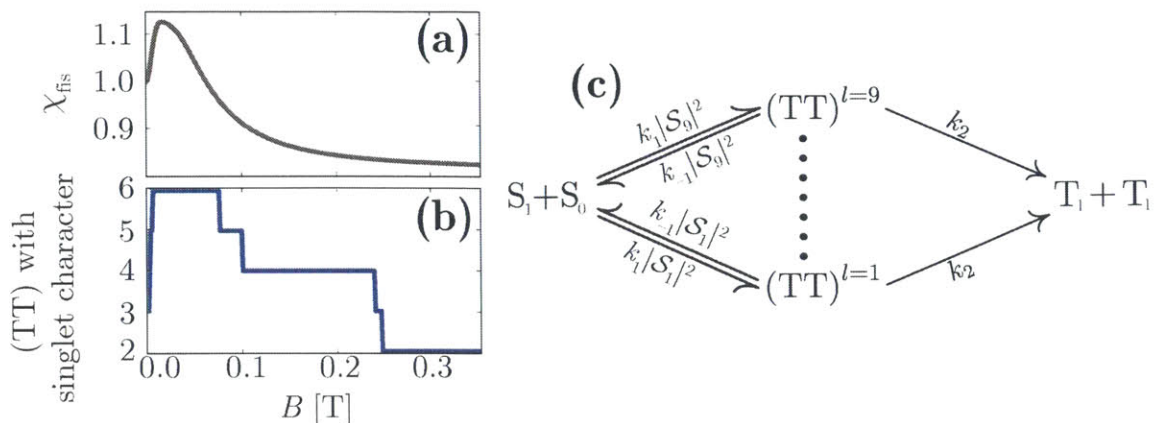
Figure 1.14: Merrifield model MFEs, in which coherence within the (TT) manifold are ingnored. (a) The singlet fission modulation is proportional to the number of (TT) states with substantial singlet character. (b) The magnetic field redistributes the singlet character over the (TT) eigenstates. (c) Classical kinetic scheme for the Merrifield model. The rates k_1 and k_{-1} are scaled by the singlet character of the respective (TT) state.

where the salient feature is that γ_{fis} increases with the number of (TT) states with substantial $|\mathcal{S}_l|^2$ (i.e. the number of states with appreciable singlet amplitude), which varies with magnetic field, from 3 states at zero-field to 6 states at low-field $[\lesssim 50 \text{ mT}]$ (for crystalline materials; up to 9 for disordered materials) and 2 states at high-field $[\gtrsim 100 \text{ mT}]$ (see Figure 1.14).[80] The model can be depicted as classical kinetic scheme, where the rates k_1 and k_{-1} are scaled by the singlet character of the respective (TT) state, as shown in Figure 1.14c, and an alternative derivation of Equation (1.31) will be shown in §2.1.[7] Importantly, both models predict the unique, non-monotonic MFE line shape observed in singlet fission materials,[81,86] though the coherence effects on the low-field enhancement are more in line with experimental results.[1,49,56]

1.4.3 Magnetic field modulation of the rate of triplet-charge annihilation

Similar to singlet fission, TCA is a spin-allowed process, because it takes place through 6 spin-coupled triplet-charge intermediate states, $(TC)^{l=1,\cdots,6}$, which have fractional doublet-character.[78,87] We represent this kinetically in Figure 2.12c, where the red-colored transition between the spin-coupled (TC) state to a single charge (rate constant k_4) is spin conserving and, in a similar manner to singlet fission, depends on the amount of doublet character in a given pair state.

The TCA rate constant (i.e. the rate constant for the overall process, $T_1 + C^{\pm} \xrightarrow{\gamma_{TCA}} C^{\pm}$) is given by[78]

$$\gamma_{TCA} = \frac{k_4}{[T_1][C^{\pm}]} \sum_{m=1}^{6} \sum_{n=1}^{6} \rho_{mn} \left(\mathcal{D}_n^{+*} \mathcal{D}_m^{+} + \mathcal{D}_n^{-*} \mathcal{D}_m^{-} \right) \tag{1.32}$$

where ρ is the spin density-matrix 6×6 matrix of the intermediate $(TC)^l$ manifold of states, and

$$\mathcal{D}_m^{\pm} = \langle D^{\pm}|m \rangle \tag{1.33}$$

is the doublet character, or overlap of mth eigenstate of the triplet-doublet Hamiltonian with the up/down-doublet-spin eigenstate of S_{total}^2 (i.e. $S_{\text{total}}^2 |D^{\pm}\rangle = \pm\frac{1}{2}|D^{\pm}\rangle$). These overlap factors change with the magnetic field strength due to modification of the spin Hamiltonian.

The spin Hamiltonian of the triplet-doublet pair state is[78]

$$H = g\beta \mathbf{B} \cdot (\boldsymbol{\sigma} + \mathbf{S}) + D S_z^2 + E \left(S_x^2 - S_y^2 \right) \tag{1.34}$$

where $\boldsymbol{\sigma}$ and $\mathbf{S}$ are the spin operators for the doublet and triplet exciton, respectively, and S_x, S_y, and S_z are the spin projection operators of the triplet. The remaining terms have been defined above for Equations (1.22) and (1.23).

The steady-state (TC) density matrix, ρ in Equation (1.32), is determined by an

equation analogous to Equation (1.29)[78]

$$\left(i\frac{E_m - E_n}{\hbar k_{-3}} + 1 \right) \rho_{mn} = \frac{1}{6} \left[\text{T}_1 \right] \left[\text{C}^\pm \right] \frac{k_3}{k_{-3}} \delta_{mn}$$

$$- \frac{1}{2} \frac{k_4}{k_{-3}} \sum_{l=1}^{6} \left[\left(\mathcal{D}_m^{+\,*} \mathcal{D}_l^+ + \mathcal{D}_m^{-\,*} \mathcal{D}_l^- \right) \rho_{ln} + \left(\mathcal{D}_l^{+\,*} \mathcal{D}_n^+ + \mathcal{D}_l^{-\,*} \mathcal{D}_n^- \right) \rho_{ml} \right] \quad (1.35)$$

We note that the quantity

$$\frac{1}{6} \left[\text{T}_1 \right] \left[\text{C}^\pm \right] \frac{k_3}{k_{-3}}$$

does not influence the value of γ_{TCA}, and the prefactor

$$\frac{k_4}{\left[\text{T}_1 \right] \left[\text{C}^\pm \right]}$$

in Equation (1.32) cancels out when we calculate the normalized MFE of the magnetic field TCA rate.

In contrast to singlet fission, the number of (TC) spin states with doublet character monotonically decreases from six at zero magnetic field to four under a large magnetic field.[78] As a result, the modulation factor

$$\chi_{\text{TCA}} = \frac{\gamma_{\text{TCA}}(B)}{\gamma_{\text{TCA}}(0)} \quad (1.36)$$

displays a monotonic decease with field strength (see Figure 2.15), in stark contrast to the unique line shape of the singlet fission MFE (compare with Figures 1.13b and 1.14a). The characteristic dependences of γ_{fis} and γ_{TCA} with varying magnetic field are distinct, allowing for unique determination of the two processes.

THIS PAGE INTENTIONALLY LEFT BLANK

Chapter 2

Magnetic field effects as a tool for studying singlet-fission-based organic photovoltaics

2.1 Determining the singlet-fission layer thickness necessary for maximum triplet yield

Singlet exciton fission in photovoltaic devices is complicated by the presence of additional important loss pathways, such as singlet exciton dissociation into charge;[55,81] see Figure 2.1.[7] Singlet exciton dissociation losses occur when singlet excitons are generated close enough to the donor-acceptor interface that the exciton dissociation rate is comparable to the rate of singlet fission. Consequently, it is necessary to determine the singlet-fission layer thickness necessary to ensure singlet excitons are generated far enough from the interface and have the necessary time to undergo fission.

Due to the potentially significant internal loss mechanism of singlet exciton dissociation, it is typically insufficient to measure fission rates in of stand-alone materials. Practical applications require measurements of the triplet yield (also referred to as

the singlet fission yield or fission yield)–the average number of triplets generated per excited singlet–in actual operating devices devices. A lower limit is defined by the internal quantum efficiency (IQE)–the ratio of charges generated by the solar cell to the number of photons *absorbed*. Due to the inherent error introduced by the optical modeling necessary to estimate the number of photons absorbed the IQE is often met with sceptism.[88,89] Much more concrete evidence is provided by measuring the number of charges generated per *incident* photon, referred to as the external quantum efficiency (EQE). An EQE greater than 100% is the gold-standard for proving the caliber of an MEG material. However, simultaneously optimizing a device's triplet yield and it's the numerous factors contributing the the EQE is far from ideal, and could lead to obscurement of an excellent singlet fission candidate.

In this section we discuss how MFEs can be used to quantify triplet yields and provide independent conformation of IQE evaluations. By determining the triplet yield of devices with different thicknesses of the singlet fission material, the minimum thickness required to prevent singlet exciton dissociation can be determined. Combined with the device's EQE or IQE, triplet exciton diffusion limitations can also be factored into determining the optimal layer thickness.

2.1.1 Pentacene-C_{60} devices

The best understood fission material to date is pentacene, an acene with five rings. Its dynamics are illustrated in Figure 2.1. Optical excitation generates a delocalized spin-0, or singlet, exciton. Within about 80 fs,[50-55] the pentacene singlet exciton splits into a pair of triplet excitons. Although triplet excitons are dark states, energy may be extracted from them if they are dissociated into charge. This is possible at a junction between pentacene and the fullerene C60 when the pentacene is oriented approximately perpendicular to the interface.[1]

The structure of the pentacene-based solar cell designed by the our collaborators is shown in Figure 2.2.[7] In order to demonstrate singlet fission can break the con-
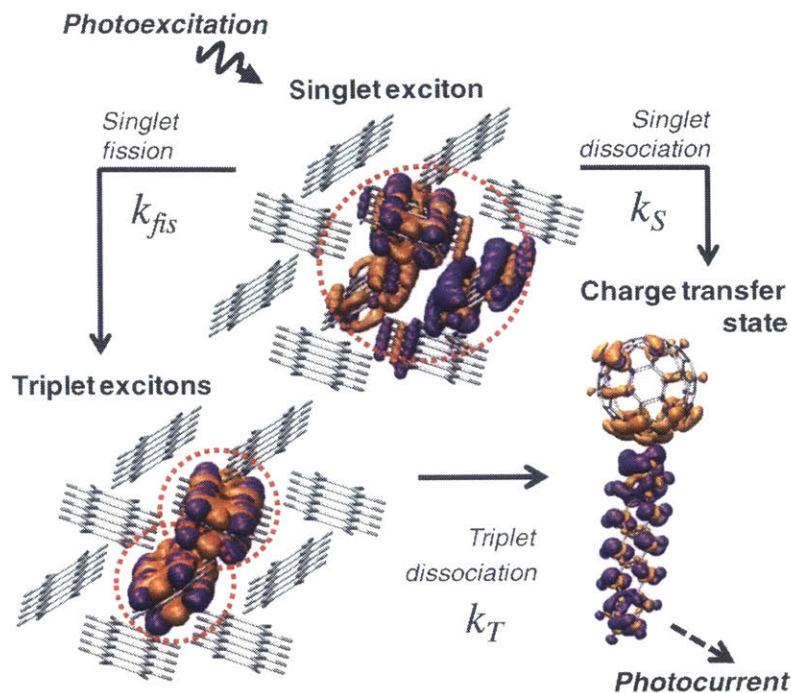
Figure 2.1: A kinetic scheme of singlet exciton fission in pentacene, based on calculations of the singlet and triplet excitons and charge transfer states at the pentacene/fullerene interface, with the purple (orange) density indicating where less (more) electron density is found in the excited state. The delocalized singlet exciton and two localized triplet excitons are circled in red. The loss pathway for singlet excitons is direct dissociation into charge before singlet exciton fission. Each process is labeled with a corresponding rate constant.

ventional barrier of one electron per photon, they went through great lengths to minimize losses unrelated to the singlet fission process itself. They incorporated a poly(3-hexylthiophene) (P3HT) layer, which increases the device efficiency by confining pentacene triplet excitons away from the anode and helps extract holes from pentacene that are generated from exciton dissociation, approximately doubling the highest IQE previously reported for pentacene.[2,7] Despite an IQE of $(160 \pm 10)\%$, the EQE of their device was only $(82 \pm 1)\%$, owing to the low absorption yield of pentacene.[7] By employ a light-trapping scheme, they were finally able to increase the EQE to $(109 \pm 1)\%$,[7] still considerably less than the IQE they determined.

To provide independent conformation of the high IQE, we developed a model to analyze the photocurrent modulation under a magnetic field. The crucial rates are identified in Figure 2.1. The singlet exciton can either directly dissociate into a single
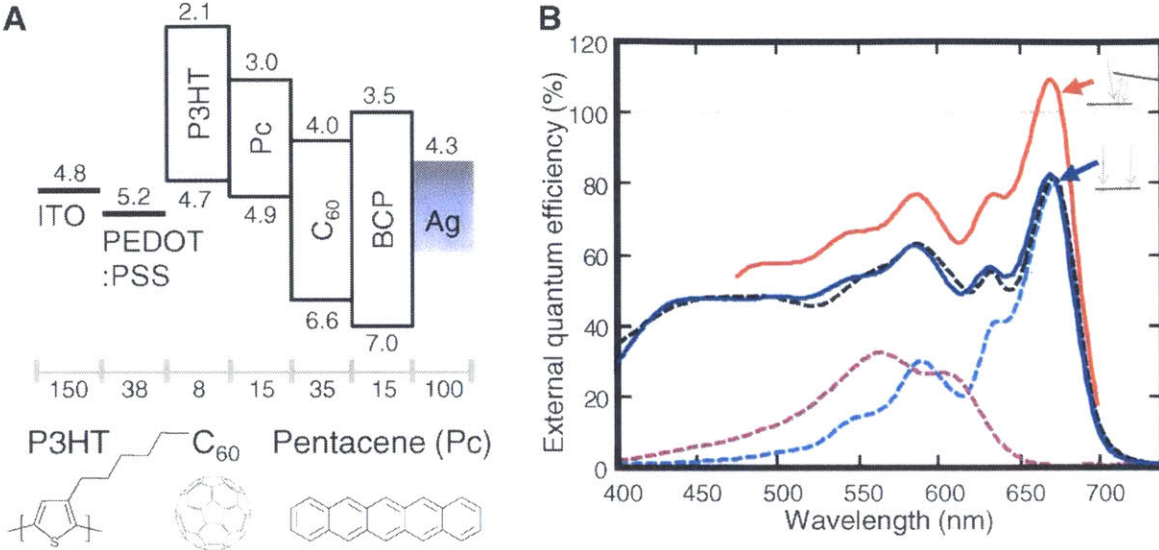
Figure 2.2: (A) Chemical structures and architecture of the solar cell with the thickness of each layer in nanometers and energy levels of the lowest unoccupied and highest occupied molecular orbitals in electron volts.[1-6] The anode is composed of indium tin oxide (ITO) and poly(3, 4-ethylenedioxythiophene) poly(styrenesulfonate) (PEDOT:PSS). The cathode employs bathocuproine (BCP) and a silver cap. (B) External quantum efficiency of devices without optical trapping (blue line), and device measured with light incident at 10° from normal with an external mirror reflecting the residual pump light (red line). Optical fits from IQE modeling are shown with dashed lines: modeled pentacene EQE (blue dashes), modeled P3HT EQE (purple dashes), and modeled device EQE (black dashes) for comparison to the measured device efficiency without optical trapping.

electron-hole pair, k_S, or undergo fission resulting in the generation of two electron-hole pairs, $k_{fis}(B)$ (only a different notation from $\gamma_{fis}(B)$ in §1.4.2). In absence of a magnetic field, three out of nine triplet-pair states have singlet character. Under a high magnetic field (B > 0.2 T), the number of triplet-triplet pairs with singlet character reduces to two, reducing the singlet fission rate, $k_{fis}(B)$. The photocurrent yield changes if there is effective competition between fission and the dissociation of the singlet exciton. It is not possible to generate a magnetic field effect on the photocurrent yield unless there is a singlet loss mechanism that competes with the fission process.

We used the following kinetic scheme, which includes the rates essential to Merrifield's theory of singlet fission, to explain the magnetic field dependence of photocurrent.

66
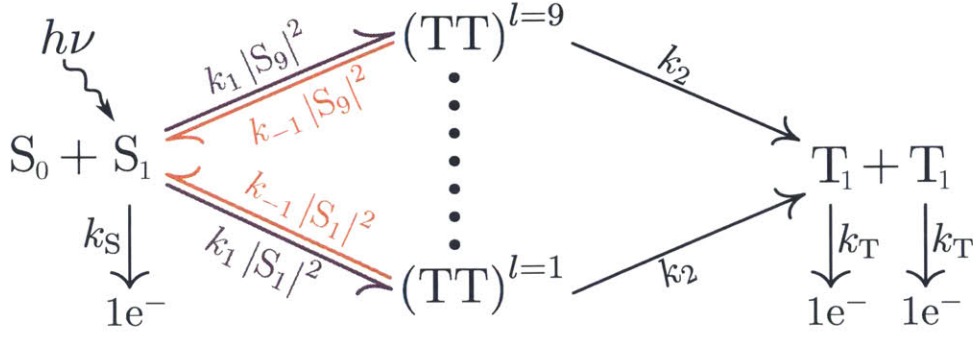
Figure 2.3: Detailed kinetic scheme of singlet fission. k_1 is the conversion of a singlet exciton into a triplet-triplet pair. k_{-1} represents the reverse process, i.e. recombination of the triplet-triplet pair to a singlet excited state. A triplet-triplet pair is separated into two free triplets (k_2), which dissociate to charge (k_T). The singlet exciton can directly dissociate into a single electron-hole pair, k_S.

In Merrifield's theory, a singlet fission event takes place by way of one of nine spin-coupled triplets $(\text{TT})^l$, where $l = 1, \ldots, 9$ designates the quantum spin state. The factor $|S^l|^2$ is the singlet character of the spin state of $(\text{TT})^l$ and changes under a magnetic field. We do not include backward recombination of the free triplets, i.e. $T_1 + T_1 \rightarrow (\text{TT})^l$, because such a process is endothermic by ~ 0.1 eV; there are no reports of delayed fluorescence in pentacene.

Under steady-state conditions, the concentrations of all species are constant, leading to the following equations:

$$\frac{d\,[\text{S}_1]}{dt} = \phi + \sum_{l=1}^{9} k_{-1}|S_l|^2 \left[(\text{TT})^l\right] - \sum_{l=1}^{9} k_1|S_l|^2\,[\text{S}_1] - k_\text{S}\,[\text{S}_1] = 0 \qquad (2.1)$$

$$\frac{d\left[(\text{TT})^l\right]}{dt} = k_1|S_l|^2\,[\text{S}_1] - k_{-1}|S_l|^2\left[(\text{TT})^l\right] - k_2\left[(\text{TT})^l\right] = 0 \qquad (2.2)$$

$$\frac{d\,[\text{T}_1]}{dt} = 2\sum_{l=1}^{9} k_2\left[(\text{TT})^l\right] - k_\text{T}\,[\text{T}_1] = 0 \qquad (2.3)$$

$$\frac{d\,[\text{e}^-]}{dt} = k_\text{S}\,[\text{S}_1] + k_\text{T}\,[\text{T}_1] - k_\text{out}\left[\text{e}^-\right] = 0 \qquad (2.4)$$

$$(2.5)$$

where ϕ is the rate of singlet generation, and k_out is the rate constant for charge extraction.

Solving Equation (2.2) for $[(TT)^l]$, substituting into Equations (2.1) and (2.3), and simplifying gives

$$\frac{d\,[\mathrm{S_1}]}{dt} = \phi + \sum_{l=1}^{9} k_{-1}|S_l|^2 \frac{k_1|S_l|^2}{k_{-1}|S_l|^2 + k_2}\,[\mathrm{S_1}] - \sum_{l=1}^{9} k_1|S_l|^2\,[\mathrm{S_1}] - k_\mathrm{S}\,[\mathrm{S_1}]$$

$$= \phi - k_1 \sum_{l=1}^{9} \frac{|S_l|^2}{\frac{k_{-1}}{k_2}|S_l|^2 + 1}\,[\mathrm{S_1}] - k_\mathrm{S}\,[\mathrm{S_1}]$$

$$= \phi - k_\mathrm{fis}\,(B)\,[\mathrm{S_1}] - k_\mathrm{S}\,[\mathrm{S_1}] = 0$$

$$(2.6)$$

and

$$\frac{d\,[\mathrm{T_1}]}{dt} = 2\sum_{l=1}^{9} k_2 \left[(TT)^l\right] - k_\mathrm{T}\,[\mathrm{T_1}]$$

$$= 2k_1 \sum_{l=1}^{9} \frac{|S_l|^2}{\frac{k_{-1}}{k_2}|S_l|^2 + 1}\,[\mathrm{S_1}] - k_\mathrm{T}\,[\mathrm{T_1}]$$

$$= 2k_\mathrm{fis}\,(B)\,[\mathrm{S_1}] - k_\mathrm{T}\,[\mathrm{T_1}] = 0$$

$$(2.7)$$

where we have defined an overall rate constant $k_\mathrm{fis}(B)$ for the process of going from $\mathrm{S_1}$ to $\mathrm{T_1} + \mathrm{T_1}$ (i.e. singlet fission):

$$k_\mathrm{fis}\,(B) = k_1 \sum_{l=1}^{9} \frac{|S_l|^2}{\frac{k_{-1}}{k_2}|S_l|^2 + 1} \tag{2.8}$$

Note that the expression for $k_\mathrm{fis}(B)$ in Equations (2.6)–(2.8) is identical to the one the Merrifield theory (see Equation (1.31).[80] Our kinetic scheme can thus be simplified to Figure 2.1 and the following scheme:

$$h\nu$$

$$S_0 + S_1 \xrightarrow{k_{\text{fis}}(B)} T_1 + T_1$$

$$\downarrow k_S \qquad\qquad \downarrow k_T \qquad \downarrow k_T$$

$$1e^- \qquad\qquad 1e^- \qquad 1e^-$$
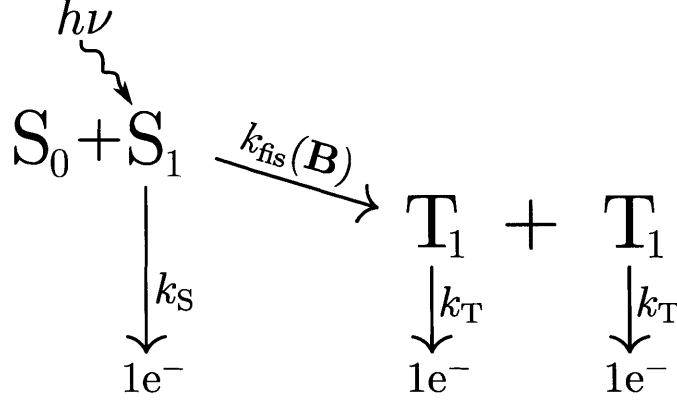
Combining Equations (2.4)–(2.7) gives an expression relating the photocurrent $I(B)$ to the rate constants:

$$I\left(B\right) \propto \frac{k_{\text{out}}}{\phi}\left[e^-\right] = \frac{k_S}{k_{\text{fis}}\left(B\right) + k_S} + 2\frac{k_{\text{fis}}\left(B\right)}{k_{\text{fis}}\left(B\right) + k_S} \tag{2.9}$$

For convenience, we write $\chi\left(B\right) = k_{\text{fis}}\left(B\right)/k_{\text{fis}}^0$, where $\chi(B)$ is the modulation of the zero-field fission rate k_{fis}^0 due to an external magnetic field [Equation (1.21)]. Using $\chi(B)$ in Equation (2.9), we can express the normalized

$$\delta = \frac{I\left(B\right) - I\left(0\right)}{I\left(0\right)} = \frac{k_S k_{\text{fis}}^0\left(\chi - 1\right)}{\left(2k_{\text{fis}}^0 + k_S\right)\left(\chi k_{\text{fis}}^0 + k_S\right)} \tag{2.10}$$

dissociation of the singlet exciton directly into charge is only likely to compete with fission for pentacene molecules directly adjacent to the acceptor. Indeed, reductions in the singlet exciton lifetime of pentacene have been observed in very thin pentacene films (0.6 monolayer) adjacent to a C_{60} layer.[55] Thus, we can approximately model pentacene films of varying thickness by changing the effective rate of singlet dissociation in Equation (2.10).

Analytically, we can solve for χ at a given value of the magnetic field by noting that the magnitude of δ is maximized when $k_S = k_{\text{fis}}^0\sqrt{2\chi}$. This yields Equation (2.11):

$$\chi = \frac{2\delta_{\text{max}}^2 + \delta_{\text{max}} + 1 + 2\sqrt{2}\delta_{\text{max}}\sqrt{\delta_{\text{max}} + 1}}{\left(\delta_{\text{max}} - 1\right)^2} \tag{2.11}$$

The result for χ can be used to directly obtain the triplet yield of singlet fission from the magnetic field modulation in photocurrent at zero field (note: $\chi(0) = 1$):

$$\eta_{\text{fis}} = \frac{2}{1 + k_{\text{S}}/k_{\text{fis}}^0} = \frac{(1 - \delta)\chi - 1 \pm \sqrt{(\delta(\chi + 2) - \chi + 1)^2 - 8\delta^2\chi}}{(\delta + 1)(\chi - 1)} \tag{2.12}$$

We note that while Merrifield's theory allows one to calculate $\chi(B) = k_{\text{fis}}(B)/k_{\text{fis}}^0$ from first principles, it requires knowledge of the triplet exciton zero-field-splitting parameters D and E in the Hamiltonian Equation (1.22) and also the ratio branching ratio k_{-1}/k_2. These were fitting parameters in Merrifield's work.[80] Equation (2.11) enables us to, instead, obtain an expression for $\chi(B = 0.4\text{T})$, requiring only the experimental values of δ_{max} at $B = 0.4$ T. Once δ_{max} is obtained for a material, the fission yield of a device can be determined simply by measuring the change in photocurrent at $B = 0.4$ T. This procedure does not require calculating or fitting the line shapes of MFE.

To obtain an independent measure of the yield of singlet fission, multiple devices were fabricated while varying the thickness of pentacene, see Figure 2.4. For thin layers of pentacene ($d < 5$ nm) the optical absorption was increased by employing the multilayer photodetector architecture.[49,88] Photodetectors were measured in reverse bias to improve charge extraction. As a test of generality, both C_{60} and 3,4,9,10-perylene tetracarboxylic bisbenzimidazole (PTCBI) were used as acceptor molecules and found to yield similar results. Devices with thicker layers of pentacene employed the same device architecture as in Figure 2.2A. The magnetic field modulation of photocurrent at 0.4 T is shown in Figure 2.4. It peaks at $\delta_{\text{max}} = -(2.7 \pm 0.1)\%$ in 2-nm-thick layers of pentacene sandwiched between acceptor layers. From Equation (2.11), we obtain $\chi = 0.85$, identical to the value assumed in Reference 49 based on tetracene measurements.[90]

In Figure 2.4, we apply Equation (2.12) to transform the magnetic field modulation data into the expected yield of triplet excitons from singlet fission. We find that singlet fission is incomplete in pentacene films with thickness $d < 5$ nm, accounting for the

70
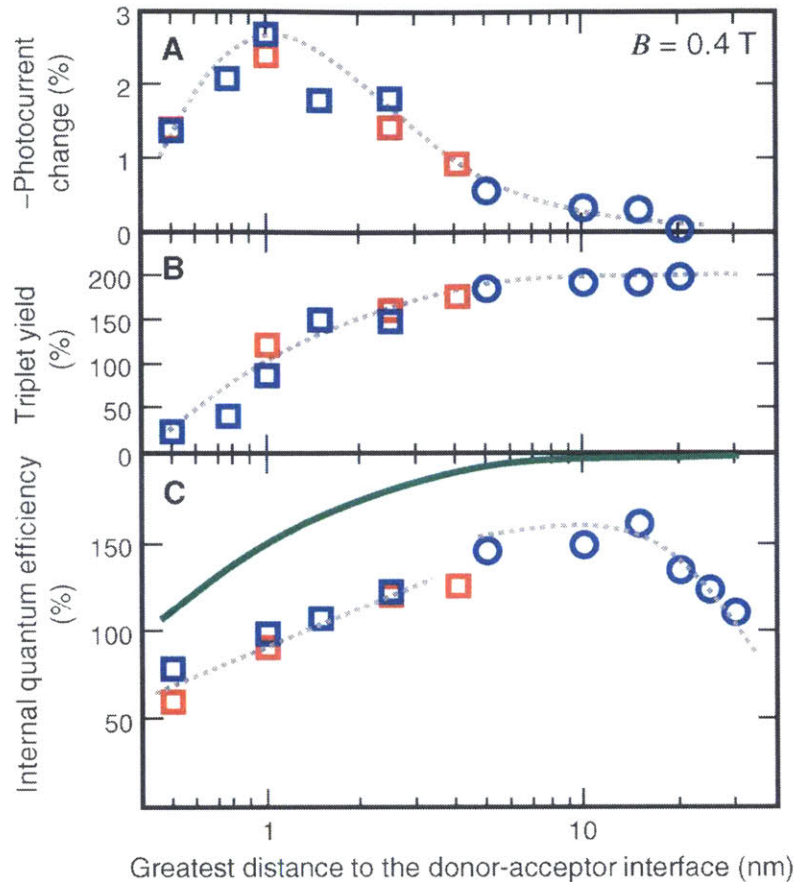
Figure 2.4: (A) The magnetic field dependent change in photocurrent measured at $B = 0.4$ T as a function of pentacene layer thickness. Square symbols are measured in photodetector structures, and each pentacene layer is sandwiched between C_{60} (blue squares) or PTCBI (red squares) acceptor films. Measurements in the solar cell architecture of Figure 2.2A are circles. (B) The triplet yield from singlet exciton fission as obtained from Equation (2.12). (C) A comparison of the maximum achievable quantum yield determined from the magnetic field effect (green line) with the internal quantum efficiency as determined from EQE measurements and the calculated optical absorption. The reduction in quantum efficiency observed in thin layers of pentacene is found to originate in incomplete singlet exciton fission. Gray dashed lines are a guide to the eye.

relatively low IQE in the photodetector structures. The triplet yield approaches 200% in thicker films, providing independent confirmation of the high IQE calculated for the device structure shown in Figure 2.2A.

The IQE, as evaluated with optical modeling,[88] is shown in Figure 2.4C and compared to predictions based on the magnetic field effect. The IQE is suppressed in thin layers of pentacene, increases to a maximum for $d \sim 15$ nm, and then is reduced in

71

thicker films. Decreases in IQE for thicker films are presumably due to triplet exciton diffusion limitations and lower-than-unity charge collection efficiency. There are two important conclusions from this IQE comparison. First, the yield of singlet fission can be conveniently determined directly from the normalized change in photocurrent under a magnetic field. A high yield is characterized by a vanishing modulation of photocurrent under a magnetic field. Second, singlet fission in pentacene requires a relatively thick film to minimize losses due to singlet exciton dissociation. Fission is not effective in fine-grained blends of pentacene and fullerene or perylene-based acceptors.

The observation of external quantum yields exceeding 100% in the visible spectrum represents a notable advance in the application of singlet fission to solar cells. To increase the device efficiency fission should be paired with a low-bandgap material that harvests photons below the singlet exciton energy. This could be an organic material,[56] inorganic semiconductor nanocrystal,[1,57,58] or a conventional inorganic semiconductor.[59] High-quality contemporary silicon solar cells show an AM1.5 efficiency of $\sim$ 25%;[91] singlet fission materials such as tetracene or rubrene could be integrated with silicon cells to double the photocurrent from high-energy solar photons ($\lambda < 550$ nm), ultimately boosting the efficiency of the silicon cell to more than 30%.

2.1.2 Tetracene-C_{60} devices

When paired in a solar cell with suitable low energy gap materials, fission increases the power efficiency by enhancing photocurrent in the visible spectrum.[56,92] Tetracene, for example, absorbs blue and green photons; exciton fission then generates two triplet excitons, each with energy ~ 1.25 eV.[93] This energy match to the bandgap of silicon (1.1 eV) provides special motivation for studying.[92,94–98] It is the most efficient fission material yet identified that can partner with the predominant material of modern solar cells.
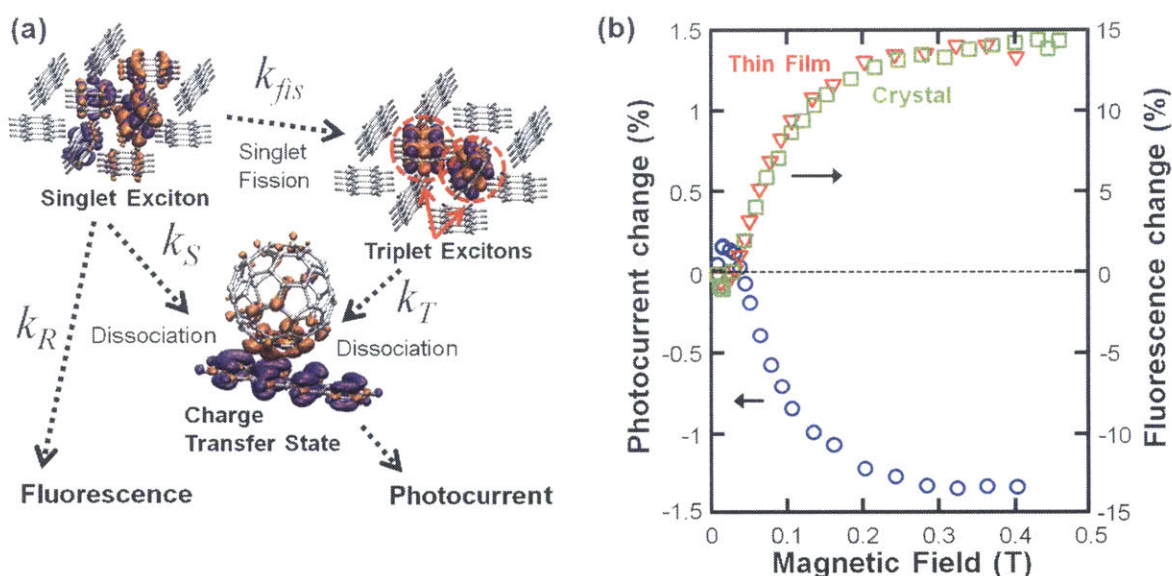
Figure 2.5: Dynamics of singlet fission and the magnetic field effect in tetracene. (a) A kinetic model including fluorescence as a possible singlet decay channel. (b) Fluorescence from a tetracene crystal (square) and thin film solar cells (triangle) as a function of magnetic field. The photocurrent from a solar cell with a 30-nm-thick tetracene layer exhibits the opposite sign to the measured changes in fluorescence.

Energy conservation during exciton fission requires that the initial exciton has approximately twice the energy of the product states. In tetracene, the fission process is thought to be slightly endothermic, resulting in a significant retardation of the rate.[93] Nevertheless, the yield of triplet excitons is aided by spin conservation, which eliminates a thermalization loss pathway.[7] The initial exciton is a singlet with total spin $S = 0$ and it cannot rapidly decay into one lower-energy triplet exciton with total spin $S = 1$. Only the generation of two triplets is allowed.[8,31,48,55] Thus, sin-

73

glet exciton fission in neat films of tetracene competes only with the relatively slow processes of singlet exciton fluorescence and non-radiative decay to the ground state. Indeed, multiple studies have shown or suggested a near unity efficiency for the fission process in neat films of tetracene.[54,99]

The determination of the IQE is especially challenging for tetracene devices, since its optical absorption overlaps with the usual acceptor material C_{60}. Alternative approaches for measuring triplet yield based on the temperature dependence of fission in tetracene[56] are also suspect given conflicting reports of the temperature dependence of the fission rate,[54,100] and the magnetic field effect in tetracene.[101] In this work we couple measurements of the internal quantum efficiency in tetracene solar cells with analysis of the magnetic field dependence of photocurrent generation and tetracene fluorescence. When combined, these techniques address the weaknesses of previous measurements of triplet yield in tetracene.[56]

In §2.1.1, the ultrafast fission rate in pentacene preempted triplet yield losses due to fluorescence. Due to tetracene's slower fission rate fluorescence losses must also be included when determining the triplet yield; see Figure 2.5(a).[102] Figure 2.5(b)[102] is a plot of fluorescence from a tetracene single crystal as a function of magnetic field. It is compared to the fluorescence and photocurrent from tetracene photovoltaic cells under an applied magnetic field. The fluorescence trends are identical in single crystals and thin films incorporated in solar cells, but both are opposite to the photocurrent dependence. Fluorescence monitors the singlet exciton population, which increases as fission is slowed under a magnetic field. Conversely, the negative sign of the magnetic field effect on photocurrent demonstrates that charge formation mostly originates in triplet excitons, which decrease under the magnetic field due to a slower fission rate.

The magnetic field effects in Figure 2.5(b) can provide a quantitative model of the yield of singlet exciton fission when they are combined with a kinetic model as described in Figure 2.5(a).[7] A photon is first absorbed by the fission material, creating a singlet exciton. The singlet exciton dynamics are modeled by three rates: the com-

bined radiative, k_R; the rate of singlet exciton dissociation into charge, k_S; and the effective singlet exciton fission rate, $k_{fis}(B)$. It is notable that charge generation occurs at donor-acceptor interfaces, so k_S can be tuned by adjusting the greatest exciton diffusion distance, d, as was done in §2.1.1.[7] Very thick tetracene layers have negligible charge generation rates. Normalizing by the rate of fission under zero applied magnetic field, $k_{fis}(0) = k_{fis}^0$, we define

$$\chi_{fis}(B) = \frac{k_{fis}(B)}{k_{fis}^0},$$

$$\chi_S(d) = \frac{k_S(d)}{k_{fis}^0},$$

$$\chi_R = \frac{k_R}{k_{fis}^0}.$$

The magnetic field-induced modulation, $\delta_I(B, d)$, of photocurrent, I, as a function of magnetic field B, and greatest exciton diffusion distance, d, is

$$\delta_I(B, d) = \frac{I(B, d) - I(0, d)}{I(0, d)} = \frac{(\chi_{fis}(B) - 1)(\chi_S(d) + 2\chi_R)}{(\chi_S(d) + \chi_{fis}(B) + \chi_R)(\chi_S(d) + 2)}.$$

Similarly, the magnetic field-induced modulation, $\delta_F(B, d)$, of fluorescence, F, is

$$\delta_F(B, d) = \frac{F(B, d) - F(0, d)}{F(0, d)} = \frac{1 - \chi_{fis}(B)}{\chi_S(d) + \chi_{fis}(B) + \chi_R}$$

For large magnetic fields $B > 0.4$ T, the normalized fission rate χ_{fis} converges to a constant value χ_{fis}^m. Under $B > 0.4$ T, both $\delta_I(B, d)$ and $\delta_F(B, d)$ have a limiting case for $d \to \infty$ when $\chi_S \to 0$:

$$\delta_I(B > 0.4 \text{ T}, d \to \infty) = \frac{(\chi_{fis}^m - 1)\chi_R}{\chi_{fis}^m + \chi_R},$$

$$\delta_F(B > 0.4 \text{ T}, d \to \infty) = \frac{1 - \chi_{fis}^m}{\chi_{fis}^m + \chi_R}.$$

The photocurrent change also has an additional minimum value at a particular value

75

of χ_S and d:

$$\delta_I \left(B > 0.4 \text{ T}, d_{max} \right) = \frac{\chi_{fis}^m - 1}{\left(\sqrt{2 \left(1 - \chi_R \right)} + \sqrt{\chi_{fis}^m - \chi_R} \right)^2}.$$

Any two of the three potential experimental measurements: $\delta_I \left(B > 0.4 \text{ T}, d \to \infty \right)$, $\delta_F \left(B > 0.4 \text{ T}, d \to \infty \right)$, or $\delta_I \left(B > 0.4 \text{ T}, d_{max} \right)$ allows us to solve for χ_{fis}^m and χ_R and then obtain $\chi_S(d)$ by measuring $\delta_I \left(B > 0.4 \text{ T}, d \right)$ or $\delta_F \left(B > 0.4 \text{ T}, d \right)$. But both photocurrent modulation measurements are complicated by additional photocurrent generation from C_{60} at overlapping wavelengths,[102] forcing us to also estimate the IQE of tetracene and C_{60}. Thus, obtaining the triplet yield from the magnetic field effect on photocurrent is hampered by the same problem that obstructs direct measurements of the IQE in tetracene. We can, however, correct a δ_I measurement at a tetracene thickness for which we expect the IQE to be most accurate, in this case $\delta_I \left(B > 0.4 \text{ T}, d \to \infty \right)$, and then rely on the δ_F measurement to predict the yield at varying thickness. Alternatively, we can find an approximate solution from the δ_F measurement alone.[102] We explore both approaches below.

Due to increasing photocurrent contributions from C_{60}, the IQE of thin tetracene layers is extremely sensitive to small errors in optical modeling parameters. Devices with thick layers of tetracene have lesser contributions from C_{60} to the photocurrent. Therefore, in Figure 2.6(a)[102] and 2.6(b),[102] we use : $\delta_I \left(B > 0.4 \text{ T}, d \to \infty \right)$ and $\delta_F \left(B > 0.4 \text{ T}, d \to \infty \right)$ to determine the normalized fission rate under a magnetic field, χ_{fis}^m, and radiative loss rates, χ_R. For tetracene under strong magnetic fields of ~ 0.4 T, we find $\chi_{fis}^m = 84.5\%$ and $\chi_R = 5.07\%$. From our measurement of fluorescence modulation under a magnetic field $\delta_F \left(B > 0.4 \text{ T}, d \right)$,[102] we then calculate the normalized singlet loss rate $\chi_S(d)$ as a function of tetracene thickness, which allows us to determine the triplet yield:

$$\text{triplet exciton yield} = 2\frac{\chi_{fis}^0}{\chi_{fis}^0 + \chi_S + \chi_R}.$$

Recall that these values are normalized by the zero field fission rate $k_{fis}^0 \cong 10 \text{ ns}^{-1}$.[48,95,99,103]
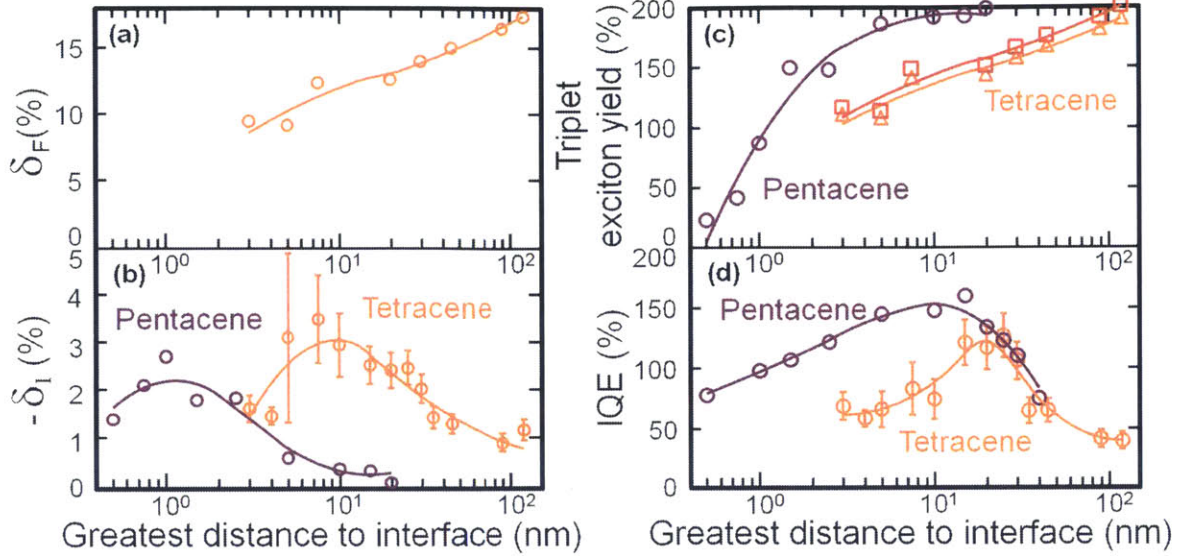
Figure 2.6: (a) and (b) The tetracene fluorescence change δ_F and photocurrent change δ_I under a magnetic field in both tetracene and pentacene. The tetracene fluorescence changes are measured in the same device used to determine the photocurrent change. (c) Tetracene and pentacene triplet exciton yields modeled from fluorescence and photocurrent changes, respectively. The red squares represent the triplet exciton yield approximated by the δ_F-only-approach. Orange triangles represent the full calculation based on both δ_F and the photocurrent change δ_I as corrected by the IQE. (d) The IQEs of thin layers of pentacene and tetracene reflect the changes in triplet yield, and triplet diffusion losses in thick films. Pentacene data are from Ref. 7, and tetracene IQE data are from Ref. 8.

We also test a δ_F-only-approach to estimating χ_S and the triplet yield. For most singlet fission materials, the radiative loss rates, χ_R, are significantly smaller than χ_{fis}. Under this assumption, we can simplify the magnetic field-induced modulation of fluorescence to

$$\delta_F\left(B, d\right) \approx \frac{1 - \chi_{fis}\left(B\right)}{\chi_S\left(d\right) + \chi_{fis}\left(B\right)}.$$

Solving at $\delta_F\left(B > 0.4\text{ T}, d \to \infty\right)$ we find $\chi_{fis}^m = 85.2\%$. We then calculate $\chi_S(d)$ and the triplet exciton yield from $\delta_F\left(B > 0.4\text{ T}, d\right)$. In Figure 2.6(c),[102] we show that this estimate of the triplet exciton yield agrees well with the full model. The δ_F-only-approach requires a quenching interface, but does not require a device structure engineered to extract photocurrent or measurement of the IQE, while still producing a good estimation of χ_{fis}^m, χ_S, and triplet exciton yield. The accuracy of this approach could be further improved by including the ratio of fluorescence and fission rates

as obtained from the photoluminescence transients in monomeric solutions and thin films; see Fig. 3 of Burdett et al.[99]

The triplet exciton yield of tetracene is plotted together with the triplet yield of pentacene in Figure 2.6(c). The IQEs of solar cells are also plotted for comparison in Figure 2.6(d).[102] The data show similar trends as a function of fission material thickness, but the overall photovoltaic performance is significantly worse in tetracene with a peak IQE of 127% ± 18% as compared to 160% ± 10% in pentacene.[7] Tetracene exhibits a relatively slow fission rate and hence it is less competitive with singlet exciton dissociation for thin tetracene layers. Consequently, the peak IQE in tetracene occurs for thicker layers where triplet diffusion losses are already significant. As demonstrated by the residual magnetic field modulation of photocurrent from thick tetracene layers, there are also losses due to fluorescence in tetracene, which is notably stronger than pentacene but still weaker than other losses. Subtracting from the maximum possible efficiency of 200%, we estimate that 20% of the potential photocurrent in our best device is lost due to singlet exciton dissociation (collecting one charge per singlet exciton instead of two), 8% to fluorescence, and the remaining 45% due to triplet exciton diffusion limitations, yielding the final IQE value of 127% ± 18%.

As additional verification for the determination of triplet yield, in Figure 2.7,[102] we compare our estimates of the singlet loss rate to measurements. As expected, the average rate of the extracted direct singlet exciton dissociation loss increases as the tetracene layer thickness decreases. In our thinnest photodetector, we determine $k_S = 0.8 k^0_{fis}$, which is consistent with the measured rate of $k_S \sim k^0_{fis} \sim 8.3$ ns^{-1} for a tetracene-C_{60} blended thin film featured in Fig. 5(a) of Yost et al.[8]

In conclusion, we find that the slow rate of singlet exciton fission in tetracene lowers its triplet yield within a 20 nm radius of a C_{60} interface. Pentacene exhibits faster exciton fission and higher yields at similar distances (singlet dissociation lossless nearly eliminated beyond 15 nm radius of C_{60}),[7] highlighting the importance of designing exothermic rather than endothermic fission materials. Nevertheless, tetracene can yield internal quantum efficiencies that exceed 100%. In optimized organic so-
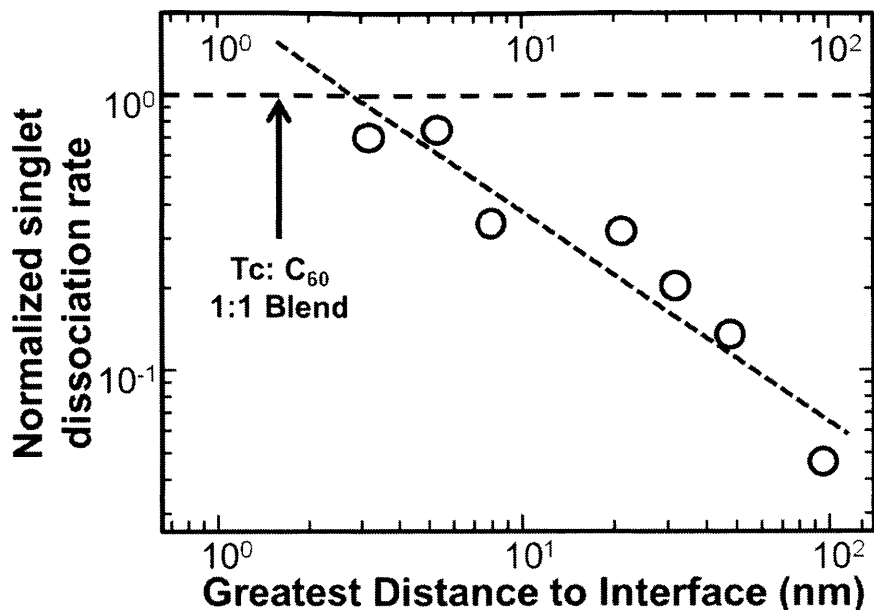
Figure 2.7: The normalized singlet dissociation rate, χ_S, as obtained from modeling the fluorescence change with a function of the greatest distance to a donor-acceptor interface. The χ_S of tetracene:C_{60} blend in Yost et al. 14 was included as a comparison and test of our method.

lar cells, we find a peak triplet yield of 153% ± 5% with an IQE of 127% ± 18%. These results agree with prior work,[56] although we find here that thicker layers of tetracene are required to optimally compete with singlet exciton dissociation. We have also demonstrated that the exciton yield in tetracene can be determined simply from the magnetic field modulation of fluorescence without measuring photocurrent or IQE.

2.2 Capturing photon energy between $E(\mathrm{T_1})$ and $E(\mathrm{S_1})$

As mentioned in §1.2.4, singlet fission sensitizers require a support from a conventional sensitizer that absorbs the photons with $E(\mathrm{T_1}) \leq E \leq E(\mathrm{S_1})$, because the dark $\mathrm{T_1}$ state will not absorb energy above $E(\mathrm{T_1})$. In this section we explore two approaches to integrating this conventional sensitizer into a PV structure. Magnetic field effects allow us to determine if the triplets produced from fission are contributing to the photocurrent, providing a simple method to evaluate various device compositions and architectures. The photocurrent of a device that benefits from the triplet products will be proportional to the rate of fission, while the photocurrent of a device that doesn't benefit from the triplet products will be inversely proportional to the rate of fission. These proportionalities are directly probed by the magnetic field effect on the fission rate.

2.2.1 Using long-wavelength acceptors

Organic devices may be able to narrow the gap in efficiency by incorporating multiple donor-acceptor junctions, thereby harnessing additional incident photons with wavelengths beyond the absorption cutoff of the first cell.[104] It is not clear, however, how organic multijunction cells will be manufactured. Many modern organic photovoltaics rely on solvent annealing to optimize morphology, leading to challenging solvent incompatibilities in the fabrication of the multijunction stack.[105]

Singlet exciton fission offers an alternative path to higher efficiencies. Because it does not require the addition of extra junctions in a stack, it is especially promising for single-layer solution-processed photovoltaic blends. As discussed above, however, realizing the benefits of fission requires pairing with a suitable low energy gap material. One route to this pairing is through the acceptor material. Since the fission materials identified to date are typically electron donors, we need electron acceptors with very deep unoccupied states, and appreciable optical absorption in the vicinity of $\lambda = 1 \ \mu\mathrm{m}$.[106]
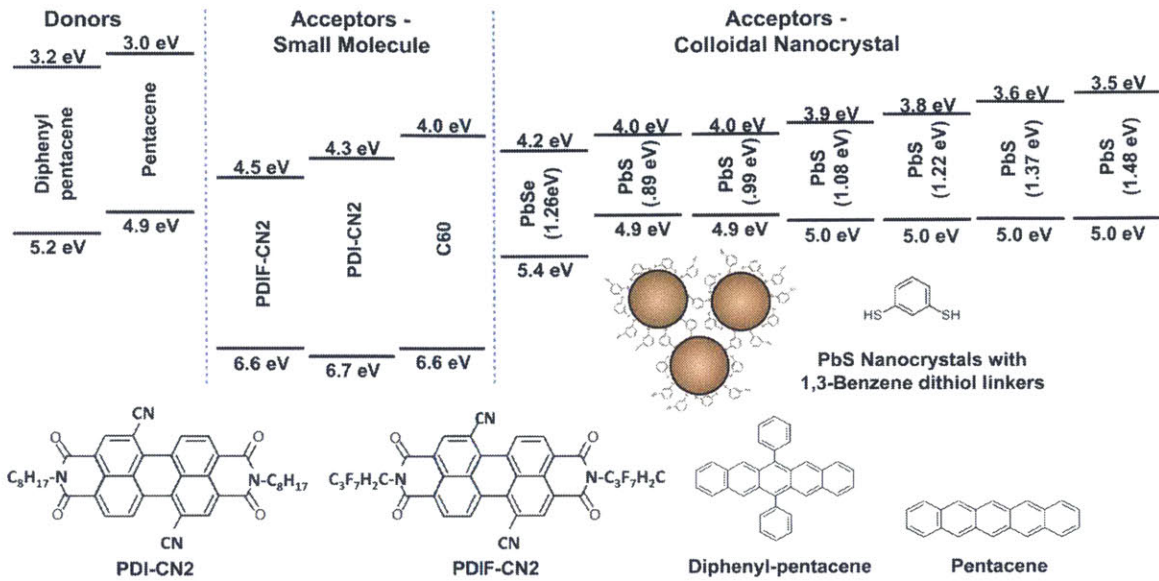
Figure 2.8: Energy levels and molecular structures of the materials used in this work, and representation of nanocrystals with 1,3-benzene dithiol linkers and chemical structure of the linker. The energy levels are taken from the literature.[5,9–15]

Here, we examine three classes of acceptors for compatibility with singlet fission donors: fullerenes,[49,56] perylene diimides,[9] and PbS and PbSe nanocrystals (NC).[57] Collectively, the lowest unoccupied molecular orbital (LUMO) levels of these acceptors span a range of approximately 1 eV, as seen from the energy levels in Figure 2.8.[1] We also vary the singlet fission donor, using either pentacene or its derivative 6,13-diphenyl-pentacene (DPP), in which we also demonstrate singlet fission. DPP has a highest occupied molecular orbital (HOMO) energy of 5.2 ± 0.1 eV,[10] which is slightly deeper than that of pentacene at 4.9 ± 0.1 eV.[5,11]

A singlet exciton that does not undergo fission yields one charge carrier pair at the donor-acceptor junction. However, if the singlet exciton does undergo fission, it splits into two triplet excitons and potentially forms two charge carrier pairs. Thus, in a device where triplets can dissociate at the donor/acceptor interface, the application of a magnetic field results in fewer generated charges and has a negative effect on the photocurrent. Conversely, in a device that can dissociate singlet excitons but not triplet excitons, the application of a magnetic field increases the photocurrent since the reduction in the fission rate increases the singlet exciton density.
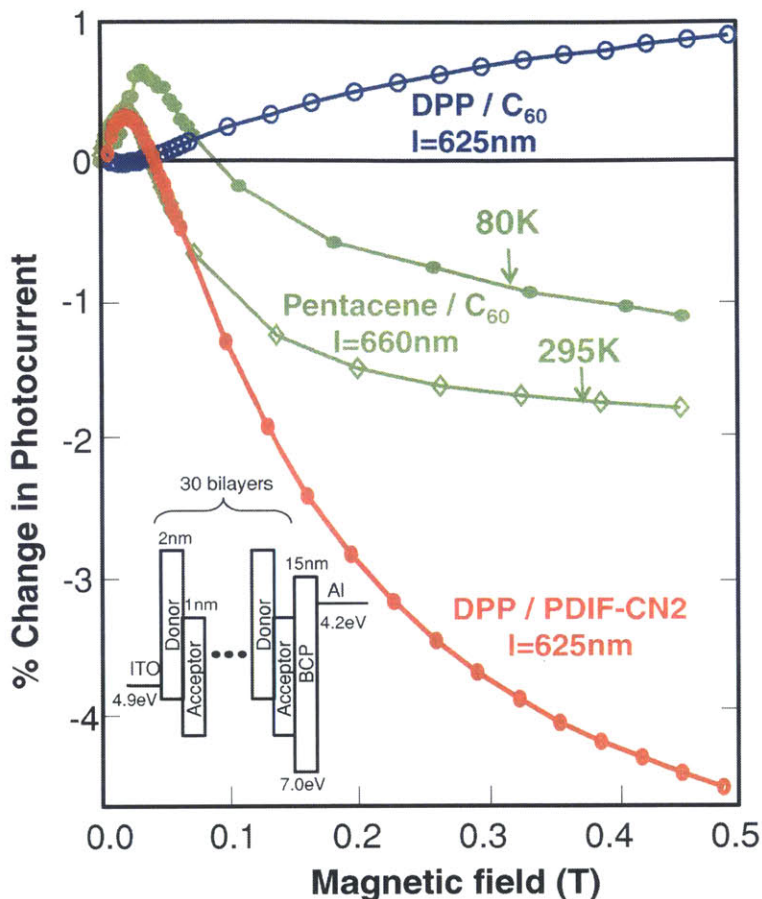
Figure 2.9: Magnetic field effect on the photocurrent for various donor/acceptor combinations in a multilayer structure. The DPP-C_{60} device was biased at -9.0 V, pentacene-C_{60} at -2.5 V and DPP-PDIF-CN2 at 0 V. The wavelengths of excitation as indicated on the plot are absorption peaks for the singlet fission material. Inset: device structure.

Figure 2.9 shows the photocurrent of three different donor/acceptor pairs as a function of applied magnetic field. Here our collaborators utilize multilayer photodetectors consisting of 1–2-nm-thick layers of the singlet fission donors combined with fullerene or perylene diimide-based acceptors as shown in the inset of Figure 2.9.[1] The magnetic field effect results from the competition between fission and singlet exciton dissociation into charge.[49] Thus, the effect of magnetic field on the photocurrent is strongest in thin layers of pentacene. Singlets formed deep within a pentacene film will all form triplets without any competition from exciton dissociation.

We find that the magnetic field effect is negative when the device generates substantial

current from pentacene or DPP, confirming that DPP performs singlet exciton fission. Positive magnetic field effects should be obtained when triplets cannot be dissociated, and indeed DPP/C_{60}, which generates very little current from photoexcitation of DPP, does exhibit an increase in the photocurrent with applied magnetic field. It is also notable that the negative trend in photocurrent with applied magnetic field for pentacene/C_{60} is still evident at low temperature, confirming that the triplet dissociation pathway is not endothermic.

We summarize our results in Figure 2.10.[1] Donor-acceptor junctions that demonstrate a triplet contribution to the photocurrent are colored in blue, while those that generate no photocurrent from triplets are colored in red. The ordinate is the difference in energy between the acceptor's LUMO and the donor's HOMO.[10,12] This HOMO-LUMO offset is an estimate of the CT state energy at the donor-acceptor junction; however, it neglects the binding energy of the CT state, which can be a few tenths of an eV.[107,108] The binding energy of a triplet exciton in pentacene is signified by the horizontal dashed line at 0.86 eV.[109] It is likely that the triplet energy in DPP is similar to that in pentacene since the triplet exciton is localized on the acene core, which is common to both molecules.

Overall, we find reasonable agreement between our observations of triplet exciton dissociation and our estimates of the CT energy at the donor-acceptor junctions, where donor/acceptor combinations with a CT state energy less than the pentacene/DPP triplet energy are able to dissociate the triplet excitons, and those with a significantly greater CT state energy are not. However, there are two notable discrepancies. When we exclude the binding energy of the CT state, we find that exciton dissociation at pentacene/C_{60} junctions is expected to be slightly endothermic. The temperature dependence of the magnetic field effect displayed in Figure 2.9 confirms this is not the case, suggesting that triplet exciton dissociation may rely on Columbic stabilization of the CT state. However, this conclusion is not definitive given the large uncertainty in the C_{60} LUMO measurement.

In conclusion, we have investigated the process of triplet dissociation in singlet fission-
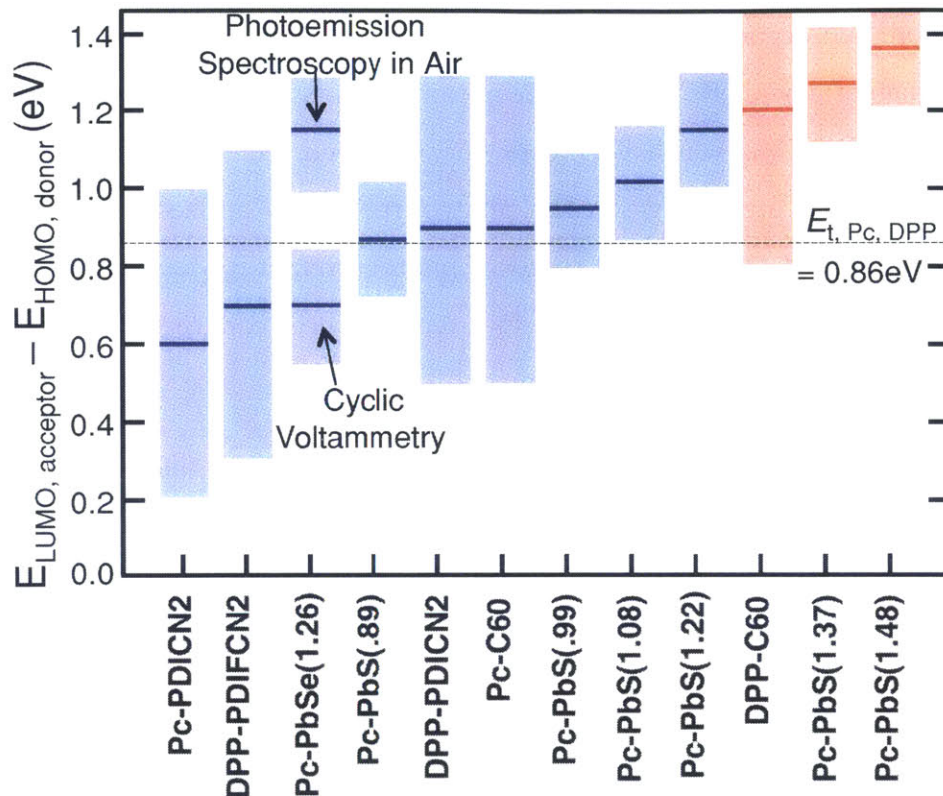
Figure 2.10: $E_{\text{LUMO, acceptor}} - E_{\text{HOMO, donor}}$ is shown for various junctions (solid lines). Blue indicates that photocurrent and/or magnetic field measurements confirm that the device can dissociate the triplets of the singlet fission material, while red lines indicate that triplets cannot be dissociated. The light blue regions and the pink regions indicate the error bars due to uncertainty in the values of $E_{\text{LUMO, acceptor}}$ and $E_{\text{HOMO, donor}}$. The pentacene(Pc)-PbSe(1.26 eV) device is indicated by two different levels which represent $E_{\text{LUMO, acceptor}}$ determined from literature values measured through cyclic voltammetry[14] and PESA.[13] The $E_{\text{LUMO, acceptor}}$ of PbS reported from the two measurements agree to within the experimental error.

sensitized donor-acceptor junctions through measurement of the EQE[1] and the magnetic field-dependence of the photocurrent. The magnetic field dependence provides a clear probe of triplet dissociation in thin layers of a singlet fission material. We find that interfaces with the archetype small molecular weight acceptor C_{60} are sensitive to small changes in the donor and acceptor energy levels. For example, the use of the pentacene derivative DPP instead of pentacene prevents the dissociation of triplet excitons at the interface. The most technologically promising acceptor is PbSe(1.26 eV). It efficiently dissociates pentacene triplet excitons and also absorbs

long wavelength light, thereby satisfying both characteristics of an effective acceptor in a singlet exciton fission-based solar cell.

2.2.2 Incorporating additional, long-wavelength donors

Singlet fission molecules, including acenes, often exhibit low absorption coefficients ($<$ 10^5 cm^{-1}), which limits the efficiency of singlet-fission-based solar cells. To overcome this problem, Reusswig et al. devised a solar cell architecture where a singlet fission sensitizer is inserted between a singlet donor and an acceptor, see Figure 2.11a for the device operation principle.[16] Excitons created by photon absorption of singlet donors migrate to a singlet fission sensitizer, where the number of excitons doubles. In this device, the process of singlet exciton fission is decoupled from photon absorption, exciton diffusion, and charge transport.[16] This architecture can convert a variety of highly light-absorbing molecules to effective singlet fission materials.[16]

Reusswig et al. built a tris[4-(5-phenylthiophen-2-yl)phenyl]amine (TPTPA)/PDI-CN2 planar heterojunction device with rubrene as the singlet fission sensitizer (see Figure 2.11b).[16] Figure 2.11c presents the boost in the efficiency of singlet donor photoexcitations by the singlet fission sensitizer. The EQEs at $\lambda < 450$ nm, where TPTPA absorption dominates, double as a thin layer of rubrene is inserted.

The magnetic field effect on photocurrent confirms that the EQE enhancement owes to energy transfer from TPTPA to rubrene and consequent singlet fission in rubrene; see Figure 2.11d.[16] The singlet fission sensitizer device shows reduction in photocurrent down to -14% upon photoexcitation of TPTPA under applied magnetic field, meaning that TPTPA absorption undergoes singlet fission. The control device shows almost no magnetic field effect. This study shows the possibility to overcome the typically poor optical absorption of singlet fission materials by utilizing energy transfer from a good light absorber to singlet fission sensitizers.[110]
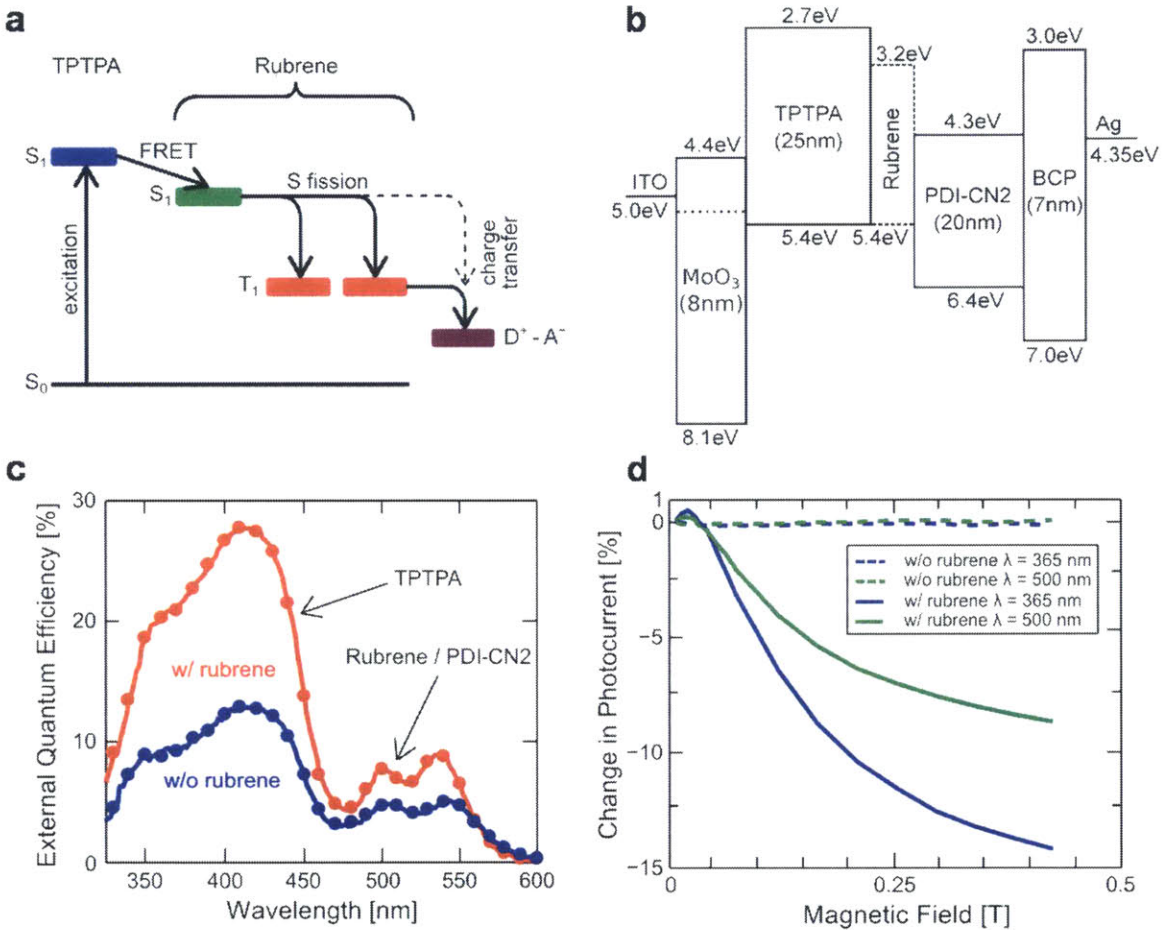
Figure 2.11: [Reference 16] (a) Energy flow in photovoltaic devices that exploit a singlet exciton fission sensitizer. Optical excitation populates singlets on TPTPA. The singlet excitons are transferred to rubrene, a singlet fission sensitizer, where they undergo singlet fission, followed by charge transfer at the donor-acceptor interface. (b) A device structure of TPTPA/PDI-CN2 bilayer photovoltaic cells incorporating a singlet fission sensitizer. (c) EQE spectra of the TPTPA/rubrene/PDI-CN2 photovoltaic device compared with the control device. (d) Comparison of magnetic field dependence of photocurrent for TPTPA/PDI-CN2 devices without rubrene (dashed) and with rubrene (solid). The illuminations at $\lambda = 365$ nm (blue) and $\lambda = 500$ nm (green) photoexcite TPTPA and rubrene, respectively.

2.3 Determining the impact of PV device design on triplet annihilation losses

Previous work has demonstrated that triplet excitons produced by singlet fission can be dissociated at the pentacene-C_{60} interface,[1,2,7,49,111] suggesting device quantum efficiencies could approach 200%. As was demonstrated in §2.1, the external quantum efficiency (EQE) of and solar cells can meet or exceed 100%. Unfortunately, we also found that pentacene-based singlet fission photovoltaics suffer from pentacene's low absorption coefficient and short triplet diffusion length. Use of pentacene in a bulk heterojunction (BHJ) solar cell should lessen absorption and triplet diffusion losses. However, previous pentacene BHJ devices have low EQEs.[112] Even the best performing blend[113] has neither an EQE nor an IQE[114] greater than 100%.

Here, we identify an important and characteristic loss mechanism in singlet-fission-based solar cells: triplet-charge annihilation (TCA). Triplet-charge annihilation is the process of destroying a triplet exciton during its interaction with a charge, represented in Figure 2.12a. Nanostructured layers enhance triplet-charge interactions by confining the triplet and the charge to a small volume. This becomes additionally important in singlet-fission-based devices, because singlet fission forms two triplets in close proximity to each other and potentially near the donor-acceptor interface. The charge resulting from dissociation of one triplet could possibly annihilate the remaining and subsequently formed triplet excitons, thereby negating the benefits of singlet fission. Thus, it is important to identify and engineer against TCA when building singlet-fission-based and, more generally, triplet-exciton-based solar cells.

Triplet-charge annihilation is also known as triplet-doublet[78] or triplet-polaron[115] annihilation, where the charge is characterized by its doublet spin multiplicity, or more accurately described as a polaron–a localized charge surrounded by its polarization field.
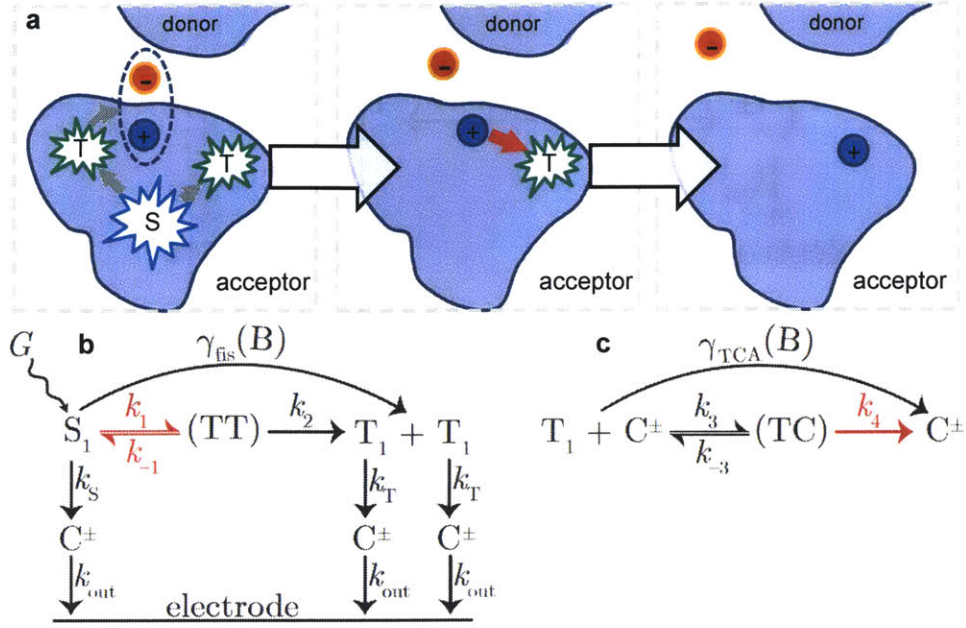
Figure 2.12: (a) Schematic diagram of singlet fission, exciton dissociation, and triplet-charge annihilation occurring in a bulk heterojunction photovoltaic device. The blue shading represents a donor material such as pentacene. The white region is the acceptor. The morphology of the bulk heterojunction structure encourages interactions between triplets and charges. Rate model diagrams of the processes of singlet fission (b) and triplet-charge annihilation (c) with the rates necessary for calculating the yield of singlet fission and loss due to triplet-charge annihilation labeled. Processes shown in red depend on the spin-character of the pair state.

Modeling the combined magnetic field effects of singlet fission and TCA

Changes in the rate of singlet fission and/or TCA change the yield of triplet excitons, which is reflected as a change in solar cell photocurrent from pentacene/C_{60}-based devices.[1,7,49] Using a magnetic field, our collaborators are able to modulate the rates of singlet fission and TCA and measure the changes in the photocurrent, a technique termed magnetic field photocurrent spectroscopy (MFPS). The MFPS signal, the normalized change in photocurrent, is defined as:

$$\delta = \frac{I\left(\lambda, B\right) - I\left(\lambda, B=0\right)}{I\left(\lambda, B=0\right)} \tag{2.13}$$

89

$$G \rightsquigarrow$$

$$C^{\pm} \xleftarrow{k_S} S_1 \xrightarrow{\gamma_{\text{fis}}(\mathbf{B})} T_1 + T_1$$

$$\downarrow k_{\text{out}} \qquad\qquad\qquad \downarrow k_T \qquad \downarrow k_T$$

$$\text{electrode} \qquad\qquad C^{\pm} \qquad C^{\pm}$$

$$\downarrow k_{\text{out}} \qquad \downarrow k_{\text{out}}$$

$$\text{electrode} \quad \text{electrode}$$

$$T_1 + C^{\pm} \xrightarrow{\gamma_{\text{TCA}}(\mathbf{B})} C^{\pm}$$

Figure 2.13: Diagram of the kinetic scheme used to incorporate the magnetic field-dependent rates of singlet fission and TCA within the setting of an operating solar cell.

where is the illumination wavelength λ used to generate the photocurrent I, and B is the magnetic field strength.

We can determine the contributions of triplet-charge annihilation (TCA) and singlet fission to a device's MFPS signals using a steady-state kinetic scheme that incorporates the magnetic field dependent rates of singlet fission and TCA within the setting of an operating solar cell. Our kinetic scheme is diagrammed in Figure 2.13.

Under steady-state conditions, the concentrations are constant with time:

$$\frac{d\left[S_1\right]}{dt} = G - \gamma_{\text{fis}}(\mathbf{B})\left[S_1\right] - k_S\left[S_1\right] = 0 \tag{2.14}$$

$$\frac{d\left[T_1\right]}{dt} = 2\gamma_{\text{fis}}(\mathbf{B})\left[S_1\right] - k_T\left[T_1\right] - \gamma_{\text{TCA}}(\mathbf{B})\left[T_1\right]\left[C^{\pm}\right] = 0 \tag{2.15}$$

$$\frac{d\left[C^{\pm}\right]}{dt} = k_S\left[S_1\right] + k_T\left[T_1\right] - k_{\text{out}}\left[C^{\pm}\right] = 0 \tag{2.16}$$

where the magnetic field dependence of the rate constants γ_{fis} and γ_{TCA} are indicated.

Combining Equations (2.14) through (2.16), the steady state concentration of charges is

$$\left[\mathrm{C}^{\pm}\right] = \frac{1}{2}\frac{G}{k_{\mathrm{out}}} \left(\frac{1}{K_{\mathrm{fis}}+1} - \frac{1}{K_{\mathrm{TCA}}} + \sqrt{\left(\frac{1}{K_{\mathrm{fis}}+1} - \frac{1}{K_{\mathrm{TCA}}}\right)^2 + 4\frac{1}{K_{\mathrm{TCA}}}\frac{2K_{\mathrm{fis}}+1}{K_{\mathrm{fis}}+1}} \right)$$

(2.17)

where

$$K_{\mathrm{fis}} = \frac{\gamma_{\mathrm{fis}}}{k_{\mathrm{S}}}$$

(2.18)

and

$$K_{\mathrm{TCA}} = \frac{\gamma_{\mathrm{TCA}}}{k_{\mathrm{T}}}\frac{G}{k_{\mathrm{out}}}$$

(2.19)

The zero-field values of K_{fis} and K_{TCA} are the two free parameters in our model used to fit the MFPS curves.

Since photocurrent, I, is proportional to the concentration of charge (i.e. $I = k_{\mathrm{out}}\left[\mathrm{C}^{\pm}\right]$), Equation (2.17), may be used to calculate the MFPS (the normalized change in photocurrent), δ:

$$\delta\left(\mathbf{B}\right) = \frac{I\left(\mathbf{B}\right) - I\left(0\right)}{I\left(0\right)} = \frac{\left[\mathrm{C}^{\pm}\right]^{\mathbf{B}} - \left[\mathrm{C}^{\pm}\right]^{0}}{\left[\mathrm{C}^{\pm}\right]^{0}}$$

(2.20)

Note that the value of G/k_{out} in Equation (2.17) cancels when calculating the MFPS; only the values of K_{fis} and K_{TCA} are needed for Equation (2.20).

The two fit parameters, K_{fis}^{0} and K_{TCA}^{0}, used to fit Equation (2.20) to the measured MFPS signals enter into Equation (2.17) through

$$K_{\mathrm{fis}} = K_{\mathrm{fis}}^{0}\frac{K_{\mathrm{fis}}}{K_{\mathrm{fis}}^{0}} = K_{\mathrm{fis}}^{0}\frac{\gamma_{\mathrm{fis}}}{\gamma_{\mathrm{fis}}^{0}} = K_{\mathrm{fis}}^{0}\chi_{\mathrm{fis}}$$

(2.21)

and

$$K_{\mathrm{TCA}} = K_{\mathrm{TCA}}^{0}\frac{K_{\mathrm{TCA}}}{K_{\mathrm{TCA}}^{0}} = K_{\mathrm{TCA}}^{0}\frac{\gamma_{\mathrm{TCA}}}{\gamma_{\mathrm{TCA}}^{0}} = K_{\mathrm{TCA}}^{0}\chi_{\mathrm{TCA}}$$

(2.22)

where the superscript "0" indicates the value at $B = 0$.

It is important to emphasize that changes in photocurrent for TCA or singlet fission

91

are only observed if there is a competing process present in the device. For example, K_{fis}^0 is determined by the ratio of the zero-field fission rate constant to the rate constant of the competing process of singlet exciton dissociation into charge k_{S}. In the limit of $k_{\text{S}} \to 0$, Equation (2.21) shows that χ_{fis} also goes to zero. On the other hand, triplet-charge annihilation depends on the density of triplets and charge. Consequently, its parameter, K_{TCA}^0, is the ratio of the zero field TCA rate constant to the rate constant of triplet dissociation into charge (k_{T}) and the generation rate of excitons (G) to the rate of charge extraction from the device (k_{out}). In the limit of $k_{\text{out}} \to 0$, Equation (2.22) shows that χ_{TCA} also goes to zero. Next we show that K_{fis}^0 and K_{TCA}^0 can be re-expressed as the key device parameters: singlet fission triplet yield and TCA triplet loss efficiency, η_{fis} and η_{TCA} .

Singlet Fission Yield

The fission yield, η_{fis}, is given by 2× the ratio of the fission rate to the total S_1 consumption rate, and we can simplify as follows.

$$\eta_{\text{fis}} = 2 \frac{\gamma_{\text{fis}}^0 [S_1]^0}{\gamma_{\text{fis}}^0 [S_1]^0 + k_{\text{S}} [S_1]^0} = 2 \frac{\frac{\gamma_{\text{fis}}^0}{k_{\text{S}}}}{1 + \frac{\gamma_{\text{fis}}^0}{k_{\text{S}}}} = 2 \frac{K_{\text{fis}}^0}{1 + K_{\text{fis}}^0} \tag{2.23}$$

Note: By convention, the factor of 2 is included to give a maximum fission yield of 200%.

Since K_{fis}^0 is one of our fitting parameters, we use the fit value and Equation (2.23) to calculate the reported yield value.

TCA Efficiency

The TCA efficiency, η_{TCA}, is given by the ratio of the TCA rate to the total T_1 consumption rate, and we can simplify as follows.

$$\eta_{\text{TCA}} = \frac{\gamma_{\text{TCA}}^0 [T_1]^0 [C^{\pm}]^0}{k_T [T_1]^0 + \gamma_{\text{TCA}}^0 [T_1]^0 [C^{\pm}]^0} = \frac{\gamma_{\text{TCA}}^0 [C^{\pm}]^0}{k_T + \gamma_{\text{TCA}}^0 [C^{\pm}]^0} = \frac{\frac{\gamma_{\text{TCA}}^0}{k_T} [C^{\pm}]^0}{1 + \frac{\gamma_{\text{TCA}}^0}{k_T} [C^{\pm}]^0} \quad (2.24)$$

where $[C^{\pm}]$ is given by Equation (2.17).

Using Equation (2.17), we have that

$$\frac{\gamma_{\text{TCA}}^0}{k_T} [C^{\pm}]^0 = \frac{1}{2} \left(\frac{K_{\text{TCA}}^0}{K_{\text{fis}}^0 + 1} - 1 + \sqrt{\left(\frac{K_{\text{TCA}}^0}{K_{\text{fis}}^0 + 1} - 1 \right)^2 + 4 K_{\text{TCA}}^0 \frac{2 K_{\text{fis}}^0 + 1}{K_{\text{fis}}^0 + 1}} \right) \quad (2.25)$$

Since K_{fis}^0 and K_{TCA}^0 are our fitting parameters, we use their fit values and Equations (2.24) and (2.25) to calculate the reported efficiency value.

Note: Our estimates of the TCA efficiency are most likely upper bounds, because our model neglects loss processes other than TCA (eg. ground state recombination of singlets and triplets, charge traps, etc.), which would reduce the number of charges at steady state and, therefore, decrease the right hand side of Equation (2.24).

Magnetic field modulation factors

The modulation factors $\chi_{\text{fis}}(B)$ and $\chi_{\text{TCA}}(B)$ are determined by the steady state density matrices of Equations (1.29) and (1.35) that enter into Equations (1.28) and (1.32). In the case of singlet fission, the calculation of ρ requires knowledge of the branching ratio, k_{-1}/k_2, and the rate constant, k_2. Figure 2.14 shows how k_2 and k_{-1}/k_2 affect χ_{fis}. We adjusted k_2 to match the smallest low-field rise of our MFPS signals and then adjusted the branching ratio until $\chi_{\text{fis}}(0.4 \text{ T})$ matched the experimentally determined value of 0.85 from §2.1.[7] The values used are $k_{-1}/k_2 = 0.7$ and $k_2 = 1 \times 10^9 \text{ s}^{-1}$, and they are *fixed* throughout the process of fitting each of the 9
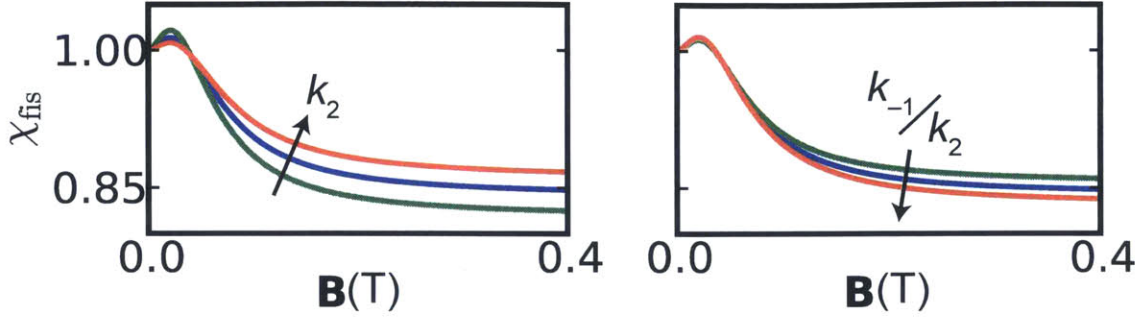
Figure 2.14: The effect of independently varying the rate constant, k_2, and branching ratio, k_{-1}/k_2, of Equation (1.29) on the magnetic field modulation factor of the singlet fission rate, χ_{fis}. To make the left subfigure, k_2 was varied through the series, $\{0.8, 1.0, 1.2\} \times 10^9$ s^{-1}, while holding k_{-1}/k_2 fixed at 0.7. To make the right subfigure, k_{-1}/k_2 was varied through the series, $\{0.6, 0.7, 0.8\}$, while holding k_2 fixed at 1×10^9 s^{-1}.

MFPS curves across the 5 different devices.

We note that the backward rate constant from the (TT) manifold to the singlet, k_{-1}, obtained from our fitting is, in fact, significantly smaller than the forward rate from the singlet to the (TT) manifold ($\sim 1/(100 \text{ fs}) = 1 \times 10^{13}$ s^{-1}).[50-55] However, the value of $k_2 = 1 \times 10^9$ s^{-1} obtained from our fitting is comparable to the value found for tetracene by[81] (2.8×10^9 s^{-1}) and results in a ratio of $k_{-1}/k_2 = 0.7$, which gives rise to a zero-to-high-field modulation of the overall fission rate constant of 0.85. We initially tried fitting the MFPS data using the simpler Merrifield model,[79] but we found it unable to describe the magnetic field dependence at low field. Specifically, the simple theory predicted too large an increase in the fission rate at low field. Only the Johnson and Merrifield density matrix description[81] proved to be adequate in describing low-field modulation of the fission rate and is the theory to calculate all MFEs throughout this study.

In the case of TCA, the calculation of ρ requires knowledge of the branching ratio, k_4/k_{-3}, and the rate constant, k_{-3}. Figure 2.15 shows the how k_{-3} and k_4/k_{-3} affect χ_{TCA}. We adjusted k_{-3} to match the MPFS signal of the 40 nm PV device (which is presumably due entirely to TCA), obtaining $k_{-3} = 9.5 \times 10^7$ s^{-1}, and then adjusted k_4/k_{-3} until $\chi_{\text{TCA}}(0.4 \text{ T})$ equaled 0.78, obtaining $k_4/k_{-3} = 0.47$. This value
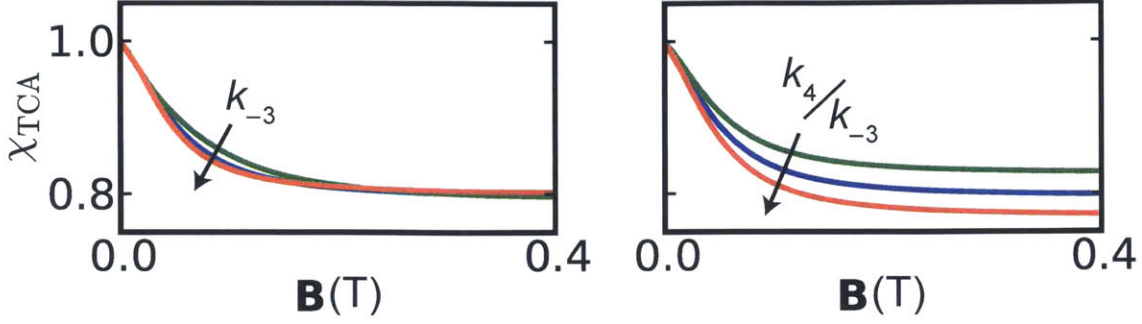
Figure 2.15: The effect of independently varying the rate constant, k_{-3}, and branching ratio, k_4/k_{-3}, of Equation (1.35) on the magnetic field modulation factor of the TCA rate, χ_{TCA}. To make the left subfigure, k_{-3} was varied through the series, $\{6.7, 9.5, 12\} \times 10^7$ s^{-1}, while holding k_4/k_{-3} fixed at 0.47. To make the right subfigure, k_4/k_{-3} was varied through the series, $\{0.38, 0.47, 0.56\}$, while holding k_{-3} fixed at 9.5×10^7 s^{-1}.

of $\chi_{\text{TCA}}(0.4$ T$)$ was determined by considering the limiting case where $K_{\text{fis}}^0 \to \infty$ (i.e. 100% singlet fission and maximum possible density of triplets) and $K_{\text{TCA}}^0 \to \infty$. This limiting case realizes the maximum possible positive MPFS signal, $\delta_{\max}$. Using Equations (2.17), (2.20), and (2.22) under these limiting conditions, $\delta_{\max}$ is

$$\delta_{\max} = \lim_{\substack{K_{\text{fis}}^0 \to \infty \\ K_{\text{TCA}}^0 \to \infty}} \delta(0.4 \text{ T}) = \frac{\sqrt{\chi_{\text{TCA}(0.4 \text{ T})}}}{\chi_{\text{TCA}(0.4 \text{ T})}} - 1$$

which can be used to determine $\chi_{\text{TCA}}(0.4$ T$)$ through

$$\chi_{\text{TCA}}(0.4 \text{ T}) = \frac{1}{(1 + \delta_{\max})^2} \tag{2.26}$$

The largest positive MPFS signal we measured was 13%, which gives $\chi_{\text{TCA}}(0.4$ T$) = 0.78$. The values of k_4/k_{-3} and k_{-3} are also *fixed* throughout the process of fitting each of the 9 MFPS curves across the 5 different devices.

Results

In Figure 2.16 we plot the measured MFPS signals and our fits for two solar cells with differing pentacene thickness, which changes the mechanism dominating the
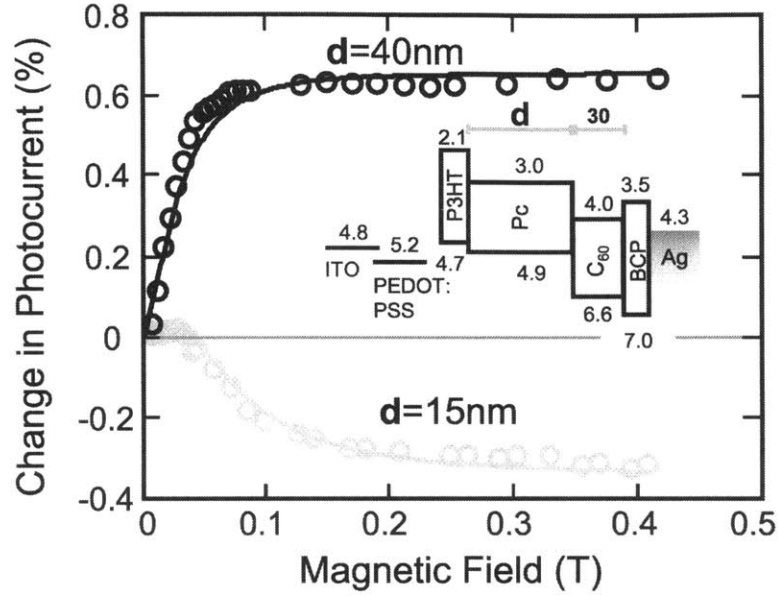
Figure 2.16: Bilayer pentacene photovoltaic device structures and energy levels for a 15-nm-thick and 40-nm-thick pentacene (Pc) layer, demonstrating the typical magnetic field photocurrent spectroscopy signatures of (a) singlet fission and (b) triplet-charge annihilation. Solid lines are fits from the steady state kinetic model and device thicknesses are in nanometers.

MFPS lineshape. The device with a 15-nm-thick pentacene active layer has a MFPS signature which shows no evidence of TCA and is characteristic of singlet fission's MFPS signature.[1,7,116] Note especially the negative value at high magnetic fields of ~ 0.4 T and the zero-crossing at low magnetic field ~ 0.04 T. In contrast, the change in photocurrent for a 40-nm-thick pentacene layer matches the characteristic positive monotonic modulation of TCA as a function of magnetic field.[78,87] This result was expected, because the 40-nm-thick device was designed to eliminate competition with singlet fission (i.e. $k_S \approx 0$) and, therefore, turn off the singlet fission MFE in the photocurrent. This device's MFPS therefore only reflects TCA. (Note: The change in photocurrent for the 40-nm-thick solar cell is proportional to χ_{TCA}^{-1}, because photocurrent is inversely proportional to loss processes.)
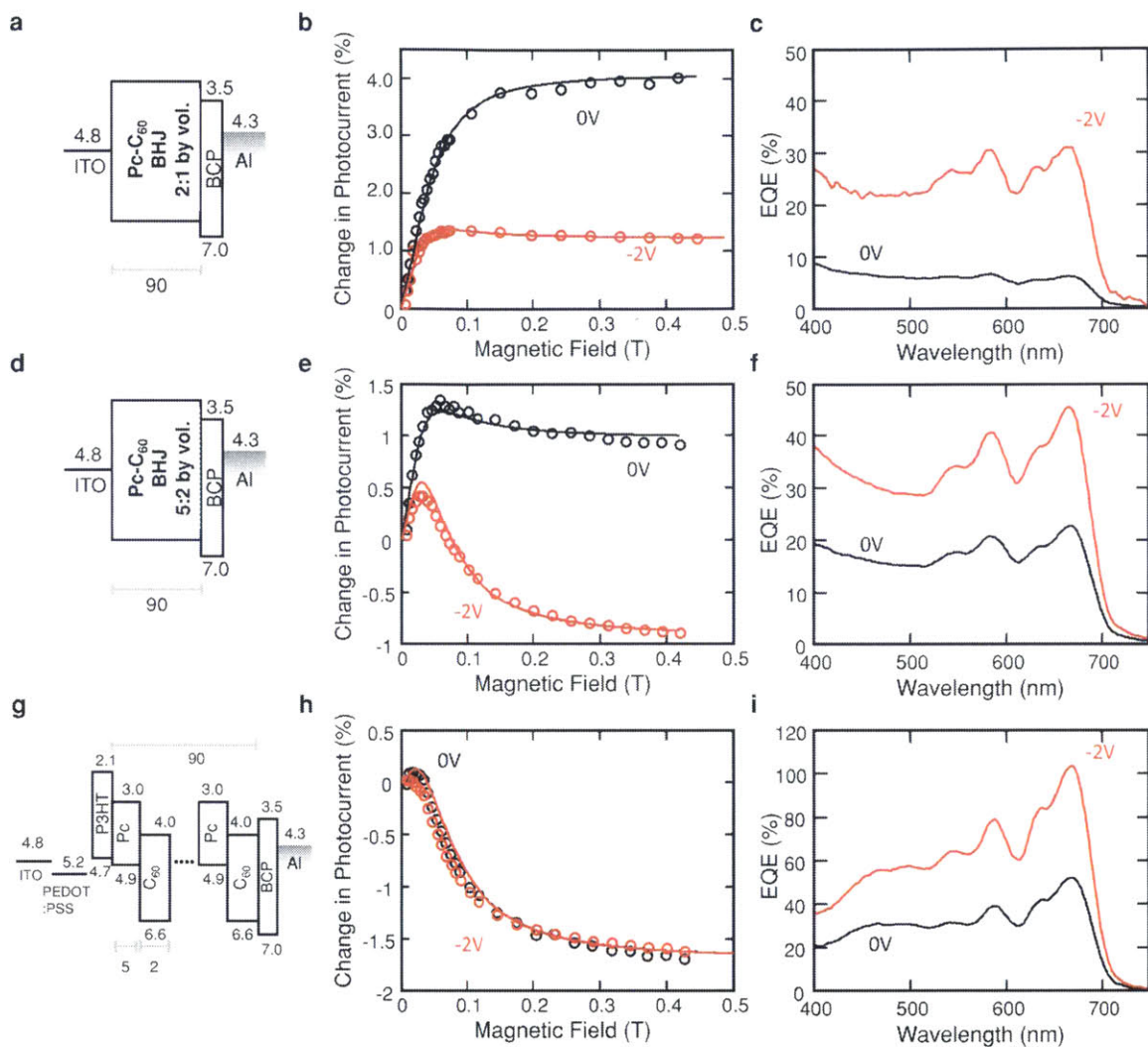
Figure 2.17: Devices used to study the effect of nanostructuring on TCA. (a) a pentacene-C_{60} 2:1 by volume BHJ, (d) a pentacene-C_{60} 5:2 by volume BHJ, and (g) a multilayer pentacene-C_{60} photodetector with 5 nm pentacene and 2 nm C_{60} layers. Bulk heterojunction devices under $\lambda = 670$ nm illumination and application of a magnetic field produce large positive changes in photocurrent (b,e) which is reduced with the application of a reverse bias. Short circuit and reverse bias EQEs (c,f) of the BHJ structures show improved device performance under a bias of $V = -2V$. The MFPS signal of the photodetector at 0 and -2 V bias (h) demonstrates the lack of TCA in the device. Short circuit and reverse biased EQE of the photodetector device (i) also shows improved performance with a peak EQE of 102%. Solid lines are fits from the steady state kinetic model and device thicknesses are in nanometers.

In Figure 2.17, we compare the performance of bulk heterojunction devices to a nanostructured photodetector built from thin alternating layers of pentacene and C_{60}. From the MFPS signals of each device we clearly see that TCA dominates the

97

MFPS in the bulk heterojunction structures. Application of a reverse bias to extract charges reduces the MFPS of TCA, as expected. The TCA signature is also weaker in the multilayer photodetector.

The results of Figures 2.16 and 2.17 demonstrate that the magnitude of TCA is strongly related to the ease of charge extraction in each device. Charge extraction is worst in finely-mixed blends, but can be improved by applying a bias to pull out the charges or fabricating larger aggregates of the donor and acceptor materials to facilitate percolation pathways within the device. Comparing the MFPS trends to the corresponding external quantum efficiency (EQE) measurement in Figure 2.17, we find that TCA is unsurprisingly correlated with very poor device efficiency. Our peak quantum efficiency of 103%, for $V = -2$ V, is observed in devices where TCA is not apparent even under short circuit conditions.

To further confirm the effect of poor charge extraction on increasing TCA, we added a N,N,N',N'-tetrakis(4-Methoxy-phenyl)benzidine (MeO-TPD) hole-blocking layer to the BHJ device of Figure 2.17a. Our largest measured positive MFPS signal increased from 4% to 13%; compare Figures 2.17b and 2.18b. The wavelength dependence of the high magnetic field MFPS signal traces the calculated pentacene thin film absorption spectrum, Figure 2.18b, and has a maximum change in photocurrent at pentacene's peak absorption wavelength, due to a maximum triplet exciton population at this wavelength. There is zero contribution to the MFPS from the C_{60} region of absorption, 425 to 450 nm, which leads us to conclude that TCA is solely a result of excitons that are created on pentacene. This also indicates that there are no polaron-pair-originating magnetic field effects on the photocurrent in these devices.

The device structure in Figure 2.18a exhibits the largest positive MFPS signal measured from TCA and can be used to empirically estimate the number of triplets lost due to TCA: The device EQE is 2.1% at pentacene's peak absorption wavelength. Optical modeling predicts 65% absorption by pentacene.[117] Assuming a 200% fission yield gives a peak possible EQE of 130%. If the reduction in EQE from 130% to 2.1% is entire due to TCA, then we can correlate the 13% MFPS signal with a loss
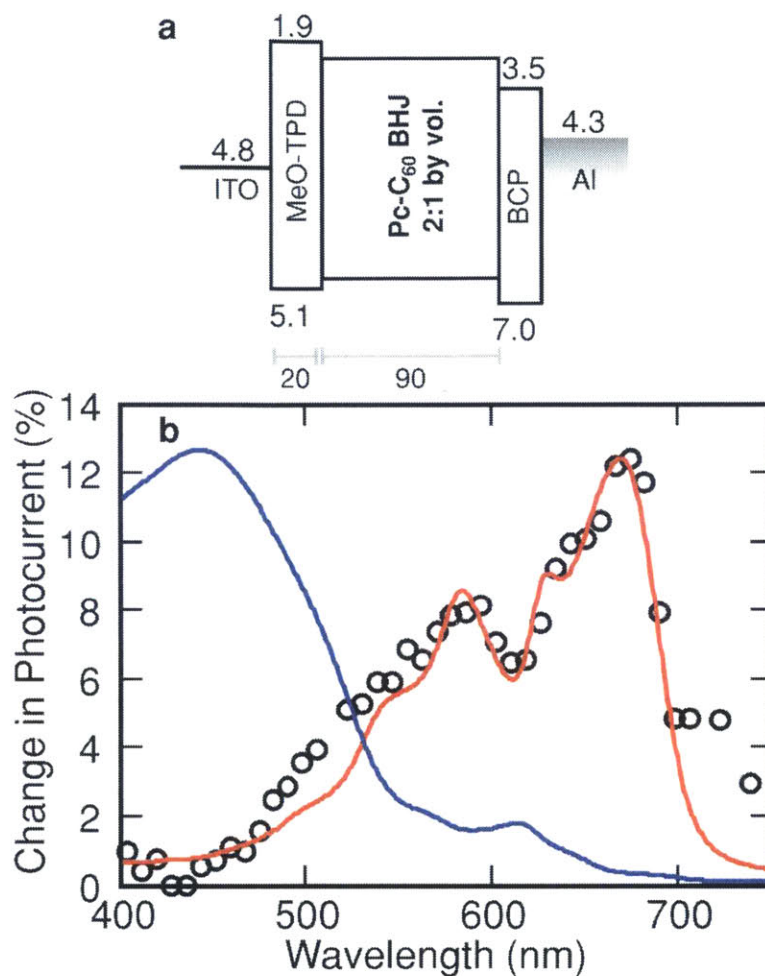
Figure 2.18: The device structure and energy levels of a BHJ solar cell with a MeO-TPD hole blocking layer (a) and the corresponding TCA MFPS signal (b) at short circuit. The solid lines trace out calculated absorption spectrums of pentacene (red) and C_{60} (blue) in the device, scaled equally so that the pentacene absorption matches the peak change in photocurrent. The match between pentacene absorption and the MFPS signal demonstrates that TCA is solely due to triplets produced by pentacene. Device thicknesses are in nanometers.

of approximately all of the triplet excitons. This represents an upper bound on the EQE loss due to TCA, as it assumes that under short circuit conditions all the loss in the device is due to TCA, e.g. no loss in EQE from poor charge extraction. As seen in Figure 2, a thick PV typically measures around 0.6% change in photocurrent due to TCA, corresponding to a maximum loss of 5% of the pentacene triplets due to TCA, if EQE and the MFPS change in photocurrent are linearly related.
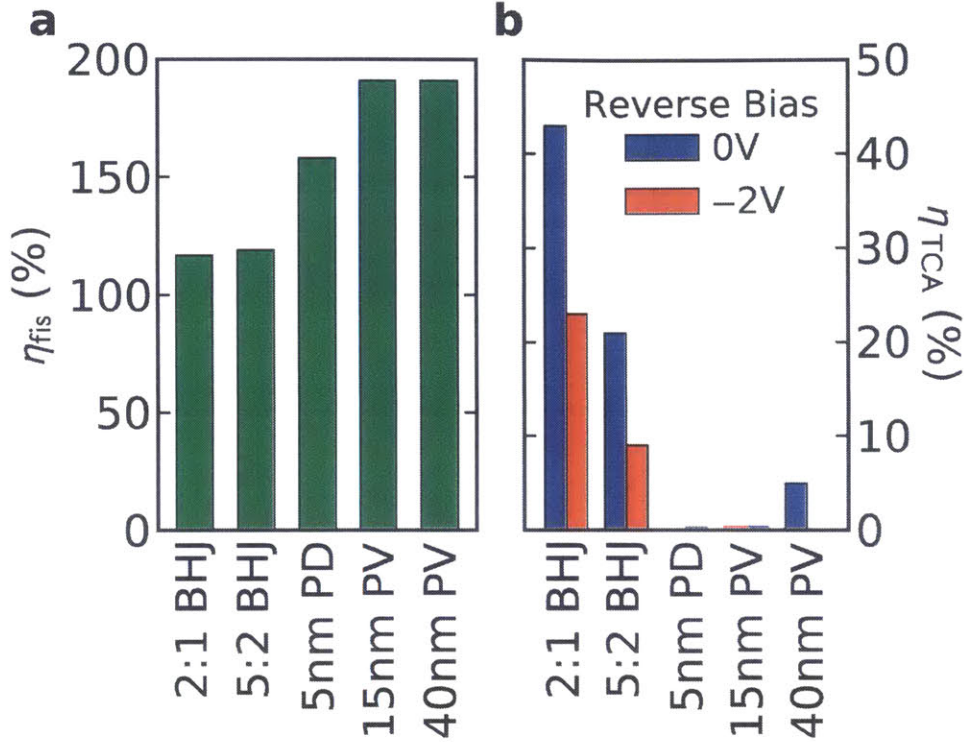
Figure 2.19: Singlet fission yield (a) and TCA efficiency (b) as determined from the two adjustable fit parameters [see Equations (2.23) and (2.24)] of the steady-state kinetic model for the bulk heterojunction (BHJ), nanostructured multilayer photodetector (PD), and photovoltaic (PV) devices of Figures 2.16 and 2.17. The red and blue bars in (b) correspond to the TCA yield at $V = 0$ V and $V = -2$ V, respectively.

The fit parameters of our steady-state kinetic scheme provide additional estimates of the singlet fission triplet yield and TCA efficiency, η_{fis} and η_{TCA}. A 200% singlet fission yield corresponds to 100% of the excited singlet excitons undergoing fission, and a 100% TCA efficiency corresponds to 100% of the triplets being annihilated before forming free charges. Figure 2.19 displays the results for the devices of Figures 2.16 and 2.17. The kinetic analysis finds a 5% efficiency for TCA in the 40-nm-thick PV, in agreement with the estimate above. The kinetic analysis also shows that singlet fission is nearly complete for pentacene layers greater than ~ 15 nm and that TCA is most prevalent in finely-blended BHJ structures. Triplet-charge annihilation decreases as the donor and acceptor layers become more structured in the photodetector, where greater continuity in the horizontal plane appears to benefit charge extraction, in

turn reducing TCA. Applying a bias to BHJ devices increases charge extraction, decreasing the TCA loss, with the singlet fission efficiency remaining unchanged. Because a TCA efficiency of 50% means that half of all triplets are annihilated before forming free charges, the 2:1 BHJ device (Figure 2.17a) is barely benefitting from singlet fission.

Through measurements of various pentacene singlet fission photovoltaic devices and modeling based on a steady-state kinetic scheme, we have identified an important loss process present in pentacene-based singlet fission solar cells, TCA. Different device architectures result in varying amounts of TCA, with pentacene-C_{60} BHJ solar cells having the largest prevalence of TCA. This is a result of poor charge extraction, likely due to a lack of percolation pathways. We conclude that obtaining a benefit from singlet fission is especially difficult in fine-grained BHJ photovoltaics. While TCA is observed in all singlet-fission-based solar cells, the magnitude of the MFPS signal can be decreased through device engineering, as was observed here for both bilayer solar cells and optimized nanostructured photovoltaic cells with improved phase separation and percolation pathways for charge extraction. The methods used here to quantify the loss due to TCA should apply equally well to other devices where triplet excitons and charges are contained spatially, such as triplet exciton based organic solar cells and phosphorescent emitting layers in organic light emitting diodes.

THIS PAGE INTENTIONALLY LEFT BLANK

Chapter 3

Magnetic field effects as a tool for studying charge-transfer-related processes in organic electronics

3.1 The role of electron-hole separation in thermally activated delayed fluorescence in donor-acceptor blends

Organic light emitting diodes (OLEDs) are a quickly evolving technology. The existing state of the art for these devices involves using phosphorescent organometallic complexes to extract light from otherwise dark triplet states that comprise the overwhelming majority of excitons formed in OLEDs.[61-63] In addition to the high cost associated with the precious metals found in many of these phosphors, empirical evidence suggests there is a practical lower limit to the phosphorescence lifetime of commonly used phosphors, which has stagnated somewhere in the vicinity of 1 microsecond.[64] This limit imposes a major roadblock to device design, because as the charge injection rate is increased to drive the OLED brighter, long lived excitons
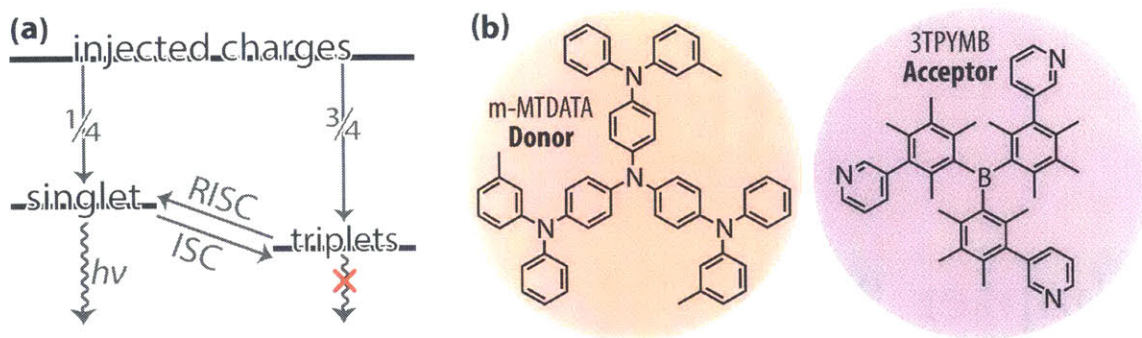
Figure 3.1: (a) Illustration of TADF in an OLED: 3/4 of the injected charges form non-emissive triplets, which can then undergo RISC and fluoresce from the singlet. (b) Chemical structures of the donor, m-MTDATA, and acceptor, 3TPYMB, of the exciplex system studied.

result in substantial energy build-up in the device, which ultimately leads to lower efficiency—a phenomenon often referred to as "roll-off."[65–67] To obtain high-efficiency, low-cost OLEDs, recent work has proposed thermally assisted delayed fluorescence (TADF) as an alternative mechanism to phosphorescence for harvesting triplet excitons.[69–71] TADF relies on efficient thermal upconversion from the triplet state to an emissive singlet state,[72] a process termed reverse intersystem crossing (RISC); see Figure 3.1(a). Because TADF does not rely on phosphorescence, it offers a fresh set of electronic parameters to optimize that could lead to faster energy conversion and higher efficiencies than phosphorescent OLEDs (pOLEDs).[118]

In the quest to engineer organic systems with efficient RISC, the main focus has been placed on decreasing the energy gap ΔE_{ST} between the triplet (T_1) and excited singlet (S_1) states.[119] Because ΔE_{ST} is the result of exchange interaction between the unpaired electrons of an exciton, one way to shrink ΔE_{ST} is to spatially separate the electron (e) and hole (h), creating a charge transfer (CT) state. Increasing the separation results in a tradeoff, however, because the oscillator strength that determines the fluorescence rate also decreases with e-h distance.[120,121]

In order to provide a more detailed perspective on how e-h separation influences device performance, here we study TADF in a blend of 4,4',4"-tris[3-methylphenyl(phenyl) amino]triphenylamine (m-MTDATA) donors and tris-[3-(3-pyridyl)mesityl]borane

(3TPYMB) acceptors; see Figure 3.1(b).[122,123] In this case, the luminescence comes from exciplex emission: the electron in the LUMO of the acceptor relaxes directly to the HOMO of the donor, so that the donor-acceptor spacing directly determines the electron hole distance. By measuring magnetic field effects (MFEs) on the time resolved photoluminescence, we discover rather complex dynamics—the MFE is negligible at short times (< 100 ns), becomes positive at intermediate times (~ 1 µs) and then changes sign at long times (> 5 µs). We are able to explain these observations using a quantum mechanical rate model in which the distance between the electron and hole *fluctuates* as a function of time. The photogenerated electron-hole pair begin on near neighbors and have a large exchange splitting that mutes the MFE. After some time, the electron and hole separate to a distance beyond the exchange radius, at which point ΔE_{ST} is on the order of the Zeeman energy of the applied field (~ 50 µeV), and MFE is large.[124,125] The conclusion is that the bound electron and holes in these blends are significantly more dynamic than previously appreciated, suggesting new avenues for controlling TADF efficiency.

Background

Before presenting the results, we review the fundamental ideas that govern magnetic field effects in these systems.

Energies of Spin States and Transitions Between Them

In a simple molecular orbital picture, singlet (S) and triplet (T) states with the same orbital configuration are separated by the exchange energy ($2J$), where

$$J = \iint \phi_n^* \left(\mathbf{r}_1\right) \phi_k \left(\mathbf{r}_1\right) \frac{1}{|\mathbf{r}_1 - \mathbf{r}_2|} \phi_n^* \left(\mathbf{r}_2\right) \phi_k \left(\mathbf{r}_2\right) d^3\mathbf{r}_1 d^3\mathbf{r}_2 \tag{3.1}$$

with ϕ_n and ϕ_k corresponding the electron and hole orbitals involved in the transition, respectively. Often ϕ_n is the LUMO and ϕ_k the HOMO. If the electron and hole

orbitals are localized and spatially separated, J decays rapidly (typically exponentially) with electron-hole separation. J is therefore an extremely sensitive measure of the proximity of the electron and hole. For typical bright states, J can be as large as several hundred meV. For typical TADF single molecule emitters J is $\lesssim 100$ meV.

In the absence of magnetic fields and relativistic effects, spin is a good quantum number and singlet and triplet states never interconvert. This approximation is generally good for organic molecules, where S-T interconversion times are typically long compared to fluorescence lifetimes.[34] There are, however, two terms that can mix S and T states in organic systems. The first is spin-orbit coupling (SOC). SOC is a relativistic effect that arises from a coupling between the spin angular momentum of the electron and its orbital motion. It is the dominant mechanism for intersystem crossing in small molecules,[34,126,127] with typical values as large as a few meV. However, SOC decays rapidly with the electron-hole distance, making it insignificant for electron-hole pairs on non-neighboring molecules.[128-131].

At larger electron-hole distances, S-T transitions are driven by the hyperfine interaction (HFI). HFI arises from interactions between an electron's spin S and the magnetic nuclei of its molecule, with a Hamiltonian of the form

$$H_{\mathrm{HFI}} = \mathbf{S} \cdot \left[\sum_N^{\mathrm{nuclei}} a_N \mathbf{I}_N \right] \tag{3.2}$$

where the a_N are the hyperfine coupling constants of the Nth magnetic nucleus with nuclear spin $\mathbf{I}_N$. For small molecules, HFI is typically negligible compared to SOC, with values as small as 10^{-4} meV. But for large electron hole separations, HFI dominates because it is completely local. The electron or hole experiences a field due to the nuclei in its own molecule, and this field is *independent* of the distance between the electron and hole. Because of the relatively large electron-hole spacing required for TADF, HFIs are gaining attention in the OLED community.[119,132-135]

For single-molecule TADF, the conclusion then is that ISC and RISC are driven

by SOC between S and T states that are relatively widely separated in energy. This energetic separation is responsible for the observed thermally activated behavior.[72,136] However, when the electron-hole separation is large (a so-called radical pair or polaron-pair (PP) state) the RISC mechanism is somewhat different.[125,137-141] During the formation of a PP, the exponential decrease of J and SOC eventually results in E_{SOC}, $\Delta E_{ST} < E_{HFI}$, and H_{HFI} becomes increasingly important. Most importantly, H_{HFI} does not conserve spin (i.e. $[H_{HFI}, S^2] \neq 0$). Thus, in the presence of HFI, an initially S or T state will evolve into an admixture of S, T_+, T_0, and T_-. Therefore, when the PP state recombines, it may form an S, T_+, T_0, or T_- exciplex, with the probability being proportional to the admixture of that state at the time of recombination.

Magnetic Field Effect of ISC and RISC of Polaron Pairs

Under application of an external magnetic field $\mathbf{B}_{ext}$ of magnitude B_{ext}, the T_+ and T_- triplet substates are increased and decrease in energy, respectively, by $E_{Zeeman} = g\mu_B B_{ext}$; see Fig. 3.2(a). Now, E_{Zeeman} is only approximately $4.5 \times 10^{-3} k_B T$ in a relatively strong magnetic field of 1 T, so the Zeeman effect will not appreciably affect the thermodynamic singlet/triplet equilibrium ratio or the RISC activation energy. However, the Zeeman splitting will influence the unitary evolution of states that are coupled by an interaction on the order of E_{Zeeman} by changing the oscillation frequencies and amplitudes. In the case of PPs, all four of the S, T_+, T_0, and T_- spin states will be mixed by H_{HFI} at zero field. As the external field increases, the mixing of T_+ and T_- with S and T_0 is decreased at a rate roughly proportional to B_{ext}^{-2}, resulting in a monotonic decrease in the overall rate of S-T transitions within the PP state.

To model HFI from the relatively large number of magnetic nuclei, we employ the model of Schulten and Wolynes.[142] Within this semiclassical approximation, the sum over nuclear spins $\sum a_N \mathbf{I}_N$ of Equation 3.2 is replaced with a static, classical "hyperfine field" $\mathbf{B}_{HF}$ representing the effective magnetic field experienced by the electron
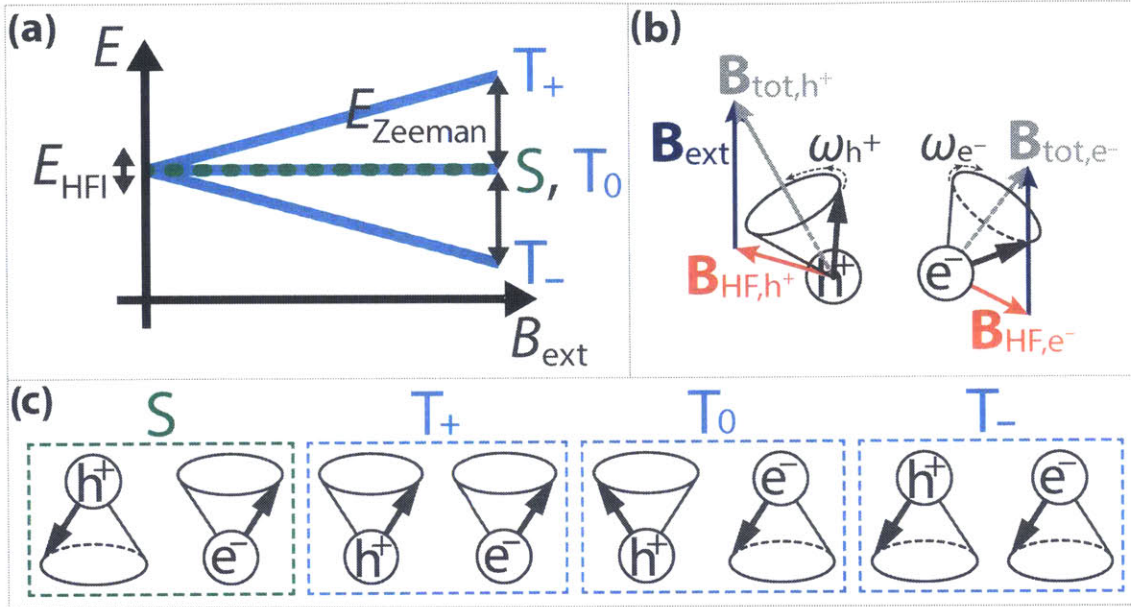
Figure 3.2: (a) Zeeman effect of an external magnetic field of strength B_{ext} on the energies of the spin states of a PP. At zero-field, all four states are degenerate and can be mixed by HFI; at high-field, only S and T_0 are mixed. (b) Spin-vector representation of singlet-triplet mixing in a PP. The electron e^- and hole h^+ spins (black vectors) precess about different total magnetic field vectors and at different Larmor frequencies, resulting in oscillations between various linear combinations of the mutual orientations corresponding to S, T_+, T_0, and T_- depicted in (c).

due to HFI with the molecule's magnetic nuclei. Because it is the sum of a large number of independent nuclear fields, $\mathbf{B}_{HF}$ can be reasonably approximated by a Gaussian distribution with a standard deviation, σ_{HF}, on the order of 1 mT for most organics.[143] The total effective field of the ith polaron spin of the ensemble is then $\mathbf{B}_{tot,i} = \mathbf{B}_{ext} + \mathbf{B}_{HF,i}$ observables are calculated by averaging over random samples of $\mathbf{B}_{HF}$ fields.

The interplay of $\mathbf{B}_{HF}$ and $\mathbf{B}_{ext}$ can be visualized using the vector representation of spin angular momentum. Each spin precesses at the Larmor frequency

$$\omega_i = g\mu_B \left| \mathbf{B}_{tot,i} \right| / \hbar$$

about a cone oriented along the total field vector it experiences, as shown in Figure 3.2(b). Within the standard spin-vector model, the pure spin states of S, T_+, T_0,
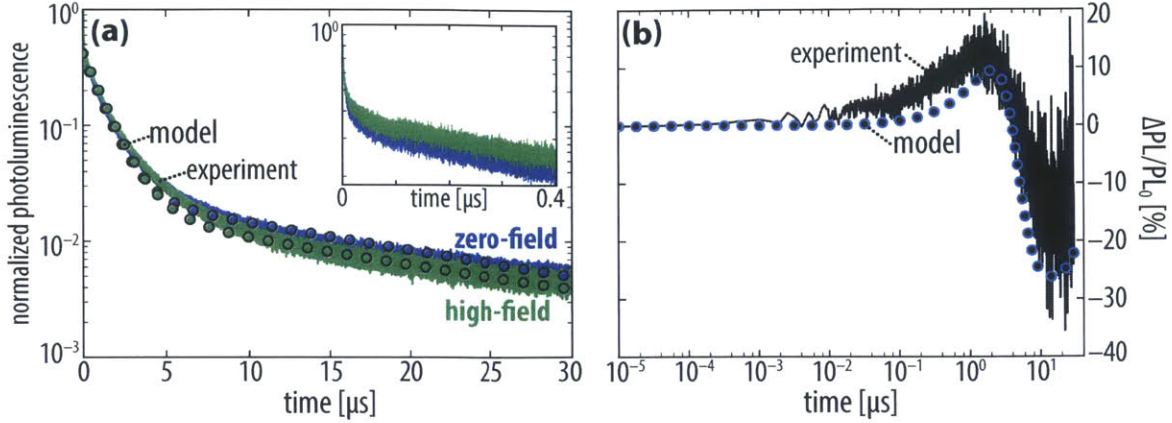
Figure 3.3: Experimental and fitted model t-PLMFE of the a 1:1 blend film of m-MTDATA:3TPYMB at zero- and high-field (0.2 T). Inset: Rapid short time decay of ∼ 60% of PL signal (see discussion in text). (b) The ΔPL/PL$_0$ [Equation (3.3)] based on the experimental and fitted model transient decays.

and T$_-$ are represented as drawn in Figure 3.2(c). To remain in one of these mutual orientations, the two spins must precess about the same axis at the same frequency. At zero-field, the hyperfine fields experienced by each polaron of a pair are randomly oriented and have different magnitudes. Therefore, the electron and hole precess about different axes and at different frequencies, resulting in time-dependent mutual orientations that are (in general) linear combinations of those corresponding to S, T$_+$, T$_0$, and T$_-$ (see Figure 3.2(b)). At high-field ($B_{ext} \ll \sigma_{HF}$), $\mathbf{B}_{e-}$ and $\mathbf{B}_{h+}$ are effectively parallel, precluding mixing of S, T$_+$, and T$_-$. Only the difference in precession frequency—due to components of $\mathbf{B}_{e-}$ and $\mathbf{B}_{h+}$ along $\mathbf{B}_{ext}$—causes oscillations between S and T$_0$. Therefore, pure spin states are more long-lived at high-field.

Results

The transient PL MFE (t-PLMFE) for a 1:1 blend film of m-MTDATA:3TPYMB is shown in Fig. 3(a). To better visualize the magnetic field effect over the PL decay, we have also plotted the normalized magnetic field induced change in the transient

PL, which is defined as

$$\Delta PL/PL_0 = \frac{PL\left(t; \mathbf{B}_{\text{ext}}\right) - PL\left(t; 0\right)}{PL\left(t; 0\right)} \tag{3.3}$$

Based on the $\Delta PL/PL_0$, the t-PLMFE of this system can be divided into three time periods: I. For $t \lesssim 100$ ns, there is little to no MFE. II. For 100 ns $\lesssim t \lesssim 1$ μs the MFE rises and becomes significantly positive III. For 1 μs $\lesssim t \lesssim 30$ μs the MFE drops, eventually becoming significantly negative. Based on the discussion of S-T transitions in the previous sections, the following explanation suggests itself:

- During period I, most of the electron-hole pairs remain on near neighbors within the exchange radius. At these close separations, the magnetic field is insufficient to influence the rate of S-T transitions and there is little to no MFE.

- During period II, a large fraction of the surviving electron-hole pairs separate beyond the exchange radius, forming PPs that are initially spin-singlet. At these distances, the MFE is significant and suppresses hyperfine-induced mixing with the T_+, and T_- PP spin states. The decreased mixing in the PP manifold increases the number of PPs that recombine in with singlet spin, resulting in increased PL.

- During period III, the luminescence comes almost entirely from TADF of long-lived triplet states. In the presence of the field, the number of surviving triplets is reduced (because fewer triplets were formed during the recombination events in period II) resulting in a negative MFE.

Some of the PL dynamics can be explained by the classic picture of SOC-induced ISC and RISC within the exciplex states. However, the important point is that the presence of an MFE requires a significant amount of indirect ISC and RISC, where the electron and hole must separate beyond the exchange radius (forming a PP) and geminately recombine on the timescale of the PL. Thus, the electron-hole separation is dynamic.

This qualitative picture is further supported by examining the PL decay itself. At times $t > 40$ ns the PL decay is fit well by a biexponential function, $I_\mathrm{p}e^{-t/\tau_\mathrm{p}} + I_\mathrm{d}e^{-t/\tau_\mathrm{d}}$, with two timescales: a 'prompt' signal with $\tau_\mathrm{p} \sim 1$ μs and a 'delayed' signal with $\tau_\mathrm{d} \sim 20$ μs. It is natural to associate the prompt signal with TADF from singlets that never underwent ISC to form triplets (and thus relax to the ground state more quickly), while the delayed signal originates from singlets that underwent ISC to form triplets, followed by RISC to the singlet manifold. The delayed states then have longer lifetimes, because the triplets relax slower and are longer lived, resulting in the larger τ_d.

In the presence of the magnetic field, the prompt PL signal increases in both intensity ($I_\mathrm{p} = 0.40 \rightarrow I_{\mathrm{p},B} = 0.43$), which suggests that, with the field on, there are more singlets that relax without ever undergoing ISC to triplets. At the same time, the magnetic field also increases the lifetime ($\tau_\mathrm{p} = 1.15$ μs $\rightarrow \tau_{\mathrm{p},B} = 1.22$ μs), which is also to be expected, as the reduced ISC rate will increase the lifetime of singlet CT states. Meanwhile, the delayed signal has a lower intensity with the field on ($I_\mathrm{d} = 0.019 \rightarrow I_{\mathrm{d},B} = 0.016$) which is again consistent with fewer singlets undergoing ISC to form triplets that would contribute to the delayed signal. The field slows down the delayed signal, as well ($\tau_\mathrm{d} = 21$ μs $\rightarrow \tau_{\mathrm{d},B} = 22$ μs) consistent with the reduced RISC rate in the presence of field.

We should note that there is a significant drop in the PL signal for $t < 10$ ns, during which time $\sim 60\%$ of the initial signal decays away; see the inset of Figure 3.2(b). This decay is not magnetic field dependent and it is not entirely clear what leads to this drop. It also appears to be absent from another transient PL measurement in the literature [see Supplementary Figures 1(b), 1(c) and 3 of Reference 123]. Possible sources include: 1) Radiative decay of the initial population of exciplexes, which never underwent charge separation and, therefore, never formed a magnetic field sensitive PP. 2) PL decay of overlapping 3TPYMB exciton emission in the range of 450-650 nm [see Figure 6 of Reference 123] 3) Limitations of the instrumental response function.[144,145] Due to the uncertainty about this initial signal, we focus our
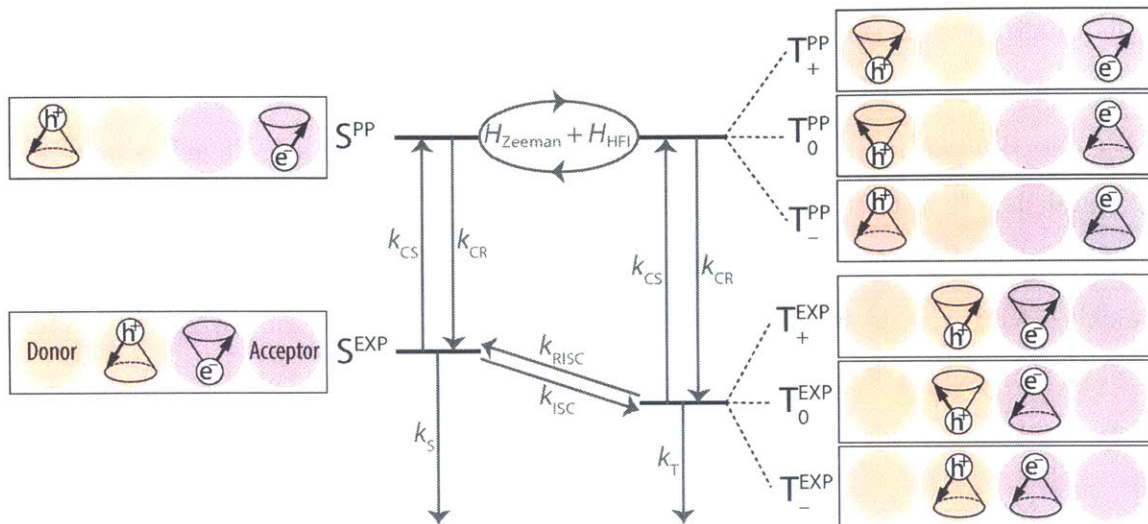
Figure 3.4: Jablonski-type diagram depiction of our theoretical model. The electron and hole are on neighboring donor and acceptor molecules (illustrated as circles) in the exciplex (EXP) configuration and on non-neighboring molecules (separated beyond the exchange radius) in the polaron pair (PP) configuration. The spin-vector representations of Figure 3.2(c) are used to depict the spins states within the EXP and PP configurations. The stochastic transitions are indicated by straight arrows and are labeled with the corresponding phenomenological rate constant (fit parameter), while the HFI-induced coherent evolution within the PP configuration in indicated as a cycling.

attention on explaining the dynamics for $t > 40$ ns.

The picture above seems qualitatively plausible, but lacks any qualitative or predictive power. In the next section, we construct a theoretical model that allows us to quantitatively test this picture and make predictions about the underlying microscopic rates.

Two-configuration model

To lend credence to our proposed set of dynamical processes underlying these three distinct time periods of the t-PLMFE, we developed a simplified model (drawing inspiration from the work of Frankevich and coworkers,[137,138] and Kersten and coworkers[146]), in which an excited electron-hole pair can exist in one of two "spatial" configurations: an exciplex (EXP) configuration or a PP configuration (see Figure 3.4).

While the spatial degrees of freedom are course-grained into the two discrete EXP and PP configurations, the electronic spins of the pair are treated explicitly and evolve according to interactions relevant to the spatial configuration they occupy. To treat both the coherent spin evolution in the PP configuration and the incoherent transitions throughout the model, we used the Lindblad quantum master equation to solve for the time dependent density matrix of our system:

$$\frac{d\rho}{dt} = -\frac{i}{\hbar} [H, \rho] + \sum_n \left(\Gamma_n \rho \Gamma_n^\dagger - \frac{1}{2} \{ \Gamma_n^\dagger \Gamma_n, \rho \} \right) - \frac{1}{2} \{ \Lambda, \rho \}, \qquad (3.4)$$

where $\{A, B\} = AB + BA$ is the anticommutator.

The density matrix ρ of our system is comprised of the 8 states labeled next to their spin-vector representation in Figure 3.4 and is expressed in the pure-spin basis as

$$\rho = \sum_\lambda p_\lambda^{\mathrm{EXP}} \left| \lambda^{\mathrm{EXP}} \right\rangle \left\langle \lambda^{\mathrm{EXP}} \right| + \sum_\lambda p_\lambda^{\mathrm{PP}} \left| \lambda^{\mathrm{PP}} \right\rangle \left\langle \lambda^{\mathrm{PP}} \right|. \qquad (3.5)$$

where λ represents a member of the set of 4 spin substates $\{S, T_-, T_0, T_+\}$.

The process of composing the basis states in Equation (3.5) is as follows. We start with the S_z spin-$^1/_2$ eigenstates

$$|\alpha\rangle = \begin{pmatrix} 1 \\ 0 \end{pmatrix},$$

$$|\beta\rangle = \begin{pmatrix} 0 \\ 1 \end{pmatrix}.$$

Next, we form the spin-coupled basis for the electron-hole pair using the Kronecker product $\otimes$:

$$|\alpha\alpha\rangle = |\alpha\rangle \otimes |\alpha\rangle,$$

$$|\alpha\beta\rangle = |\alpha\rangle \otimes |\beta\rangle,$$

$$|\beta\alpha\rangle = |\beta\rangle \otimes |\alpha\rangle,$$

$$|\beta\beta\rangle = |\beta\rangle \otimes |\beta\rangle.$$

Then, we compose the singlet and triplet substates (in the Zeeman representation: T_-, T_0 and T_+) from the spin coupled states:

$$|S\rangle = 2^{-1/2} \left(|\alpha\beta\rangle - |\beta\alpha\rangle \right), \tag{3.6}$$

$$|T_0\rangle = 2^{-1/2} \left(|\alpha\beta\rangle + |\beta\alpha\rangle \right), \tag{3.7}$$

$$|T_-\rangle = |\beta\beta\rangle, \tag{3.8}$$

$$|T_+\rangle = |\alpha\alpha\rangle. \tag{3.9}$$

Finally, we use the following two rotation matrices

$$Q_{\mathrm{PP}} = \begin{pmatrix} 1 & 0 & 0 & 0 \\ 0 & 1 & 0 & 0 \\ 0 & 0 & 1 & 0 \\ 0 & 0 & 0 & 1 \\ 0 & 0 & 0 & 0 \\ 0 & 0 & 0 & 0 \\ 0 & 0 & 0 & 0 \\ 0 & 0 & 0 & 0 \end{pmatrix} \tag{3.10}$$

$$Q_{\mathrm{EXP}} = \begin{pmatrix} 0 & 0 & 0 & 0 \\ 0 & 0 & 0 & 0 \\ 0 & 0 & 0 & 0 \\ 0 & 0 & 0 & 0 \\ 1 & 0 & 0 & 0 \\ 0 & 1 & 0 & 0 \\ 0 & 0 & 1 & 0 \\ 0 & 0 & 0 & 1 \end{pmatrix} \tag{3.11}$$

to generate generate the 8-state vectors of Equation (3.5):

$$\left|\lambda^{\mathrm{PP}}\right\rangle = Q_{\mathrm{PP}}\left|\lambda\right\rangle,$$

$$\left|\lambda^{\mathrm{EXP}}\right\rangle = Q_{\mathrm{EXP}}\left|\lambda\right\rangle,$$

where λ represents a member of the set of 4 spin substates $\{S, T_-, T_0, T_+\}$.

The first term on the right-hand side of Equation (3.5) describes the unitary evolution under the influence of the system Hamiltonian,

$$H = H^{\mathrm{EXP}} + H^{\mathrm{PP}}.$$

Within our model, we assume the relatively large exchange interaction prevents unitary evolution in the EXP manifold; the $\left|\lambda\right\rangle^{\mathrm{EXP}}$ states are eigenfunctions of the exchange Hamiltonian. Therefore, we can simply take $H^{\mathrm{EXP}} = 0$. The Hamiltonian for HFIs was discussed above within the semiclassical approximation, so the PP states experience a Hamiltonian:

$$H^{\mathrm{PP}} = \frac{g\mu_{\mathrm{B}}}{\hbar}\left(\mathbf{B}_{\mathrm{tot,e^-}}\cdot\mathbf{S}_{\mathrm{e^-}}^{\mathrm{PP}} + \mathbf{B}_{\mathrm{tot,h^+}}\cdot\mathbf{S}_{\mathrm{h^+}}^{\mathrm{PP}}\right), \tag{3.12}$$

where the spin-$^1/_2$ operator components—S_q, $q \in \{x, y, z\}$—of $\mathbf{S}_{\mathrm{e^-}}^{\mathrm{PP}}$ and $\mathbf{S}_{\mathrm{h^+}}^{\mathrm{PP}}$ are given by

$$S_{q,\mathrm{e^-}}^{\mathrm{PP}} = Q_{\mathrm{PP}}\left(S_q \otimes \mathbf{1}_2\right)Q_{\mathrm{PP}}^{\top},$$

$$S_{q,\mathrm{h^+}}^{\mathrm{PP}} = Q_{\mathrm{PP}}\left(\mathbf{1}_2 \otimes S_q\right)Q_{\mathrm{PP}}^{\top}.$$

The second term of Equation (3.4) describes the stochastic, incoherent transitions between the states of ρ. For each of the vertical transitions indicated between the states of Figure 3.4, there is a corresponding Γ (Lindblad or quantum-jump) operator of the form

$$\Gamma_{b\leftarrow a} = \sqrt{k_{b\leftarrow a}}\left|b\right\rangle\left\langle a\right|.$$

115

For example, the Γ operator corresponding to the charge separation of S^{EXP} is

$$\Gamma_{S^{PP} \leftarrow S^{EXP}} = \sqrt{k_{CS}} \left| S^{PP} \right\rangle \left\langle S^{EXP} \right|.$$

The complete set of Γ operators are

$$\Gamma_{S^{PP} \leftarrow S^{EXP}} = \sqrt{k_{CS}} \left| S^{PP} \right\rangle \left\langle S^{EXP} \right|,$$

$$\Gamma_{S^{EXP} \leftarrow S^{PP}} = \sqrt{k_{CR}} \left| S^{EX} \right\rangle \left\langle S^{PP} \right|,$$

$$\Gamma_{T_+^{PP} \leftarrow T_+^{EXP}} = \sqrt{k_{CS}} \left| T_+^{PP} \right\rangle \left\langle T_+^{EXP} \right|,$$

$$\Gamma_{T_+^{EXP} \leftarrow T_+^{PP}} = \sqrt{k_{CR}} \left| T_+^{EXP} \right\rangle \left\langle T_+^{PP} \right|,$$

$$\Gamma_{T_-^{PP} \leftarrow T_-^{EXP}} = \sqrt{k_{CS}} \left| T_-^{PP} \right\rangle \left\langle T_-^{EXP} \right|,$$

$$\Gamma_{T_-^{EXP} \leftarrow T_-^{PP}} = \sqrt{k_{CR}} \left| T_-^{EXP} \right\rangle \left\langle T_-^{PP} \right|,$$

$$\Gamma_{T_0^{PP} \leftarrow T_0^{EXP}} = \sqrt{k_{CS}} \left| T_0^{PP} \right\rangle \left\langle T_0^{EXP} \right|,$$

$$\Gamma_{T_0^{EXP} \leftarrow T_0^{PP}} = \sqrt{k_{CR}} \left| T_0^{EXP} \right\rangle \left\langle T_0^{PP} \right|.$$

The final term on the right hand side of Equation (3.4) describes population decay. In our case, this occurs (mainly) via photon emission from S^{EXP} and nonradiative decay from T^{EXP}, so we take

$$\Lambda = k_S \left| S^{EXP} \right\rangle \left\langle S^{EXP} \right| + k_T \left| T^{EXP} \right\rangle \left\langle T^{EXP} \right|. \tag{3.13}$$

The rate constants in this model ($k_{CS}, k_T, k_S, \ldots$) are treated as parameters and used to reproduce the experimental data.

To solve Equation (3.4) we write it as a superoperator equation

$$\frac{d}{dt} \left| \rho \right) = \mathcal{M} \left| \rho \right). \tag{3.14}$$

Here, ρ is treated as a super vector $\left| \rho \right)$ (with $8 \times 8 = 64$ elements) composed by

stacking the columns of ρ:

$$|\rho) = \begin{pmatrix} \rho_{1,1} \\ \vdots \\ \rho_{8,1} \\ \rho_{1,2} \\ \vdots \\ \rho_{8,2} \\ \vdots \end{pmatrix}.$$

$\mathcal{M}$ is a superoperator (a 64×64 matrix), which using the vectorization relation for the multiplication of matrices A, B, and C,

$$\mathrm{vec}\,(ABC) = \left(C^\top \otimes A\right)\mathrm{vec}\,(B),$$

is given by

$$\mathrm{vec}\left(\frac{d\rho}{dt}\right) = \mathrm{vec}\left(-\frac{i}{\hbar}\,[H,\rho] + \sum_n \left[\Gamma_n \rho \Gamma_n^\dagger - \frac{1}{2}\left\{\Gamma_n^\dagger \Gamma_n, \rho\right\}\right] - \frac{1}{2}\left\{\Lambda, \rho\right\}\right)$$

$$= \begin{pmatrix} -\dfrac{i}{\hbar}\left[\mathbf{1}_8 \otimes H - H^\top \otimes \mathbf{1}_8\right] \\[2mm] +\displaystyle\sum_n \left[\Gamma_n^{\,*} \otimes \Gamma_n - \dfrac{1}{2}\left(\mathbf{1}_8 \otimes \Gamma_n^\dagger \Gamma_n + \Gamma_n^\top \Gamma_n^* \otimes \mathbf{1}_8\right)\right] \\[2mm] -\dfrac{1}{2}\left[\mathbf{1}_8 \otimes \Lambda + \Lambda^\top \otimes \mathbf{1}_8\right] \end{pmatrix} \mathrm{vec}\,(\rho)$$

$$= \mathcal{M}\,|\rho).$$

Equation (3.14) is then solved as

$$|\rho(t)) = e^{\mathcal{M}t}\,|\rho(0)) \tag{3.15}$$

using the eigendecomposition of $\mathcal{M}$:

$$|\rho(t)) = e^{\mathcal{M}t}\,|\rho(0)) = U e^{Lt} U^{-1}\,|\rho(0)).$$

Finally, to obtain the normalized photoluminescence at time t, we start with the $t = 0$ density matrix corresponding to a unit population of S^{EXP} states after a pulse:

$$\rho(0) = \left|S^{EXP}\right\rangle \left\langle S^{EXP}\right| \tag{3.16}$$

We then evolve the density matrix using Equation (3.15) and evaluate the expectation value for the population of S^{EXP} states, which gives the normalized PL signal:

$$PL(t) = \text{Tr}\left[\left|S^{EXP}\right\rangle \left\langle S^{EXP}\right| \rho(t)\right] \tag{3.17}$$

Equation (3.17) is then averaged over 1000 random pairs of the hyperfine fields $\mathbf{B}_{e^-}$ and $\mathbf{B}_{h^+}$, sampled from a 3-dimensional Gaussian distribution with $\sigma_{HF} = 1$ mT, per the above discussion (Note: $\sigma_{HF} = 1$ mT was not treated as an adjustable parameter).

Modeling results

In order to obtain the model parameters, we performed a brute-force optimization search use a root-mean-square deviation metric, with the calculated $PL(t)$ scaled by 0.42 to match the experimental PL magnitude at $t = 10$ ns (i.e. after the ambiguous initial drop discussed above). There are 6 parameters: (k_S, k_T, k_{CS}, k_{CR}, k_{ISC}, and k_{RISC}). In fitting the data, we found that k_S was very important to fitting the overall decay magnitude without overshooting the prompt and delayed decay rates. k_{CS} and k_{CR} were important for fitting the onset of the MFE, because an MFE will only be present once a population of PPs begins to influence the S^{EXP} population. k_{ISC} was important for fitting the transition from the prompt and delayed components and the transition from positive to negative MFE. Both k_{CR} and k_{RISC} were important for fitting the magnitude of the MFE, with larger values of k_{CR} decreasing both the positive and negative MFE components and larger values of k_{RISC} decreasing the negative MFE in the vicinity of $\tau_{RISC} = k_{RISC}^{-1}$. And as expected, k_T was important for fitting the delayed lifetime.

The final rate constants we arrived at were as follows:

- $k_S = 320$ ms^{-1} [$\tau_S = 3.1$ μs]. This is a physically reasonable value when compared to the range of fluorescence and radiationless decay rates, $\sim$ 1-10 μs^{-1}, measured and calculated for various tetracyanobenzene singlet exciplex complexes in PMMA ridged solutions.[147] Also, In combination with the values of k_{CS} and k_{RISC}, the prompt PL quantum yield

$$\Phi_p = \frac{k_S}{k_S + k_{CS} + k_{ISC}} = 27\%$$

corresponds well with the literature PL quantum yield of 26%.[123]

- $k_T = 27$ ms^{-1} [$\tau_T = 37$ μs]. While we were unable to find a literature estimate for this parameter, this value appears too high to be entirely due to triplet non-radiative recombination, which is spin-forbidden. It is possible that this parameter is artificially high due to compensation for a lack of processes omitted from the model, such as charge or exciplex trap states, for instance. Another possibility is triplet quenching by oxygen contaminant. It as also possible an unexplored set of parameters would yield a similar fit with a smaller k_T (and a necessarily higher value for k_{RISC}).

- $k_{CS} = 720$ ms^{-1} [$\tau_{CS} = 1.4$ μs] and $k_{CR} = 530$ μs^{-1} [$\tau_{CR} = 1.9$ ns]. These values are physically reasonable when considering the energy required for detailed-balance between charge separation and recombination:

$$\frac{k_{CS}}{k_{CR}} = \exp\left(-\frac{E(PP) - E(EXP)}{k_B T}\right) \quad \Rightarrow \quad E(PP) - E(EXP) = 170 \text{ meV}$$

which is comparable to the literature estimate of the same energy gap for poly(1,4-phenylene-1,2-dimethoxyphenyl vinylene) (150 meV).[138] We note that, in reality, there are different rates k_{CS} and k_{CR} and energy gaps for the singlet and triplet states, but we ignored this fact in order to minimize the number of adjustable parameters.

- $k_{ISC} = 140$ ms^{-1} [$\tau_{ICS} = 7.1$ μs] and $k_{RISC} = 36$ ms^{-1} [$\tau_{RICS} = 28$ μs]. These values also yield a physically reasonable energy gap $E(S^{EXP}) - E(T^{EXP}) = 35$ meV, which is comparable to the Poole-Frankel model estimate of 51 meV.[148]

The results of this theoretical model are shown in Figure 3.2. As can be seen from the data, the rate model quantitatively reproduces the experimental results. Most importantly the model reproduces the distinct line shape of the $\Delta PL/PL_0$, yielding an initial latency period followed by a positive MFE and then a negative MFE. The magnitude of the MFE is also well reproduced, because the fast k_{CR} rate results in incomplete spin mixing within the PP manifold,[146] and because some of the ISC and RISC occurs through the field-insensitive, SOC-induced mechanism.

Discussion

These findings have a significant impact on our understanding of how charge recombination occurs in OLEDs. In the simplest picture, charge recombination occurs when two charges diffuse onto near neighbor molecules, at which point they become bound by Coulomb attraction and cannot escape one another. From this trapped CT state, they either emit (if the spin is a singlet) or recombine non-radiatively (if the spin is triplet). Our results show that this simple model is incorrect. Instead, even while the electron and hole are on near neighbors immediately after photoexcitation, the distance between them continues to thermally fluctuate.[149] The separation must routinely exceed the exchange radius of ~ 1 nm to generate the observed MFE. But the electron and hole must remain bound, because only geminate recombination is sensitive to the magnetic field. Thus the separation cannot exceed ~ 10 nm: an e-h pair separated by ≥ 10 nm in a dielectric medium with $\epsilon \sim 2.8$ (typical for organic semicondutors) are unbound at room temperature. Thus this picture of dynamically fluctuating bound electron-hole pairs in OLED materials is both physically reasonable and strongly supported by the experimental data and theoretical modeling presented above.

This picture has a significant impact on the design principles for OLEDs. First, we note that in these TADF blends, the electron hole pairs look much more like excitons in a traditional semiconductor. In those materials, the electron-hole pair binding energy is very small (only slightly more than $k_B T$) and the distance between the electron and hole is very large. Thus, many of the design principles used in creating inorganic LEDs could potentially be translated to the design of TADF-based OLEDs. In addition, it is interesting to speculate whether the same dynamics might be happening for intramolecular TADF materials or even traditional OLED systems. It is easy to verify that these systems do not typically show a MFE on the PL but a recent transient EPR study indicates that HFIs contribute to the ISC process in high-EQE single-molecule emitters.[134] Thus, if the bound electron and hole are moving, they must not be separating beyond the exchange radius, or at least not long enough for HFI mixing to be effective. This is likely due to the fact that the electron-hole pair binding energy is larger in these systems, creating a larger thermodynamic barrier to long range charge separation. To maximize energy efficiency, devices are moving more and more toward chromophores with small binding energies.[150,151] The work here suggests that as that occurs, one may also see the beneficial effect that more weakly bound excitons will be in equilibrium with PP states where singlet-triplet interconversion is facile. The fluctuations in the bound CT distance will thus provide a second, TADF-like mechanism for harvesting energy from bound triplet excitons in which $T^{EXP} \to T^{PP} \to S^{PP} \to S^{EXP}$.

Conclusions and future work

In this work we demonstrate that the electron-hole pair separation in the 1:1 blend film of m-MTDATA:3TPYMB is a dynamic variable, fluctuating on the 1 μs timescale and leading to complex time- and magnetic-field-dependent dynamics in the photoluminescence spectrum. Through careful theoretical modeling of the underlying dynamics, we are able to conclude that a significant portion of the delayed photoluminescence is due to an indirect mechanism in which the initially bound electron and hole separate

beyond the exchange radius ($\sim$ 1 nm) before eventually rejoining one another and emitting light.

The implications for this discovery are twofold. First, in designing OLEDs, our results suggest that thinking about CT states as static objects is not appropriate. Rather they should be seen as dynamically evolving states in which the electron and hole independently can move between multiple molecules before recombining. Secondly, the fact that the bond between electron and hole is apparently much weaker than previously assumed suggests that many of the design principles for inorganic LEDs could be useful in generating the next generation of OLED materials.

In the future, it will be interesting to study the morphology dependence of these characteristics. Do these observations persist in a host-guest architecture? In particular, spectroscopic probes of the spatial dynamics coupled with microscopic models of charge hopping could give us a much more fine-grained picture of how disorder in these materials affects the timescale for recombination.

3.2 Determining the spin of charge-transfer states that most efficiently generate photocurrent

Charge transfer (CT) states are bound combinations of an electron and a hole located on separate molecules.[152–154] They are formed on neighboring molecules at donor-acceptor interfaces in organic photovoltaics (OPVs) after dissociation of excitons or during recombination of free charge.[155–157] Modern OPVs demonstrate ultrafast formation of CT states from excitons, and efficient dissociation of CT states into charge under short circuit conditions.[158] Indeed, internal quantum efficiencies of many OPVs now commonly approach 100% (Ref. 159). But charge recombination losses mediated by CT states remain a problem in even the best devices,[160–164] increasing markedly at weaker internal electric fields, reducing open circuit voltage and power efficiency.

Synthetic control over donor and acceptor OPV materials enables us to engineer the physical separation of the electron and hole at the donor-acceptor interface. This prompts an important question in OPV: What is the effect of the CT state size? On one hand, separated CT states have smaller Coulombic binding energies, which should improve the photocurrent yield. But large separations are also expected to possess weaker coupling to the initial exciton, potentially reducing the exciton dissociation rate at donor-acceptor interfaces.[165] In addition, increased charge separation significantly reduces exchange splitting between singlet and triplet CT states. When the two are nearly degenerate, intersystem crossing between the two is fast, facilitating spin engineering that could improve the efficiency of OPVs. For example, spin-1 triplet CT states are forbidden from recombining to the ground state, which is typically a spin-0 singlet. Traditional OPV designs demand, however, that the CT state energy be as high as possible to maximize the open circuit voltage.[166,167] Typically, this pushes the CT energy above the energy of the triplet exciton on the donor or acceptor. As the lowest energy excited state in the system, the triplet exciton traps the energy originally contained in the CT state until it eventually recombines with the ground state, creating a crucial loss pathway or 'triplet drain.'[154,161]
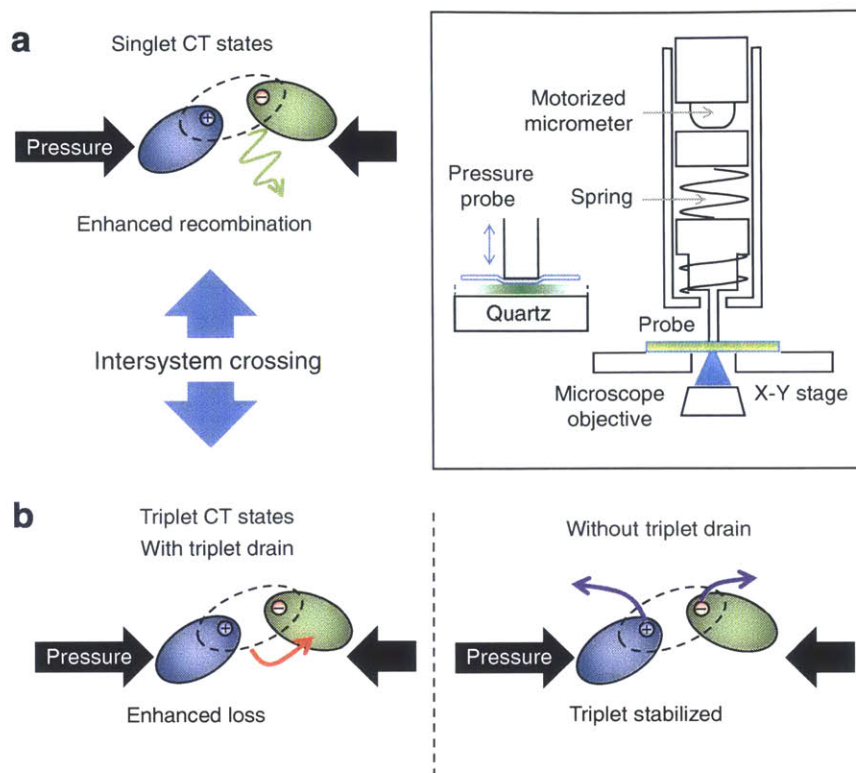
Figure 3.5: Schematic of expected changes in (a) singlet and (b) triplet charge transfer (CT) states as a function of their size. The possible triplet dynamics are dependent on the presence of a triplet quenching state or 'drain' on the donor or the acceptor. (inset) The measurement apparatus used to apply pressure to the films.

Summary of pressure-related results

To investigate the impact of CT state size on a complex set of tradeoffs for singlet and triplet states, our collaborators constructed an apparatus that allowed them to measure a material's transient photoluminescence (PL) under external pressure; see inset of Figure 3.5.[149,168,169] Singlet and triplet CT states were monitored as a function of size using a set of exciplex emitters originally designed for thermally activated delayed fluorescence (TADF) in organic light-emitting devices. Two specific TADF thin film donor:acceptor blends were selected: (1) the same m-MTDATA:3TPYMB blend studied in §3.1; (2) an m-MTDATA:t-Bu-PBD blend, which replaces the acceptor of the blend from §3.1 with 2-(biphenyl-4-yl)-5-(4-tert-butylphenyl)-1,3,4-oxadiazole (t-Bu-PBD). These materials have been demonstrated to fluoresce from the exciplex CT
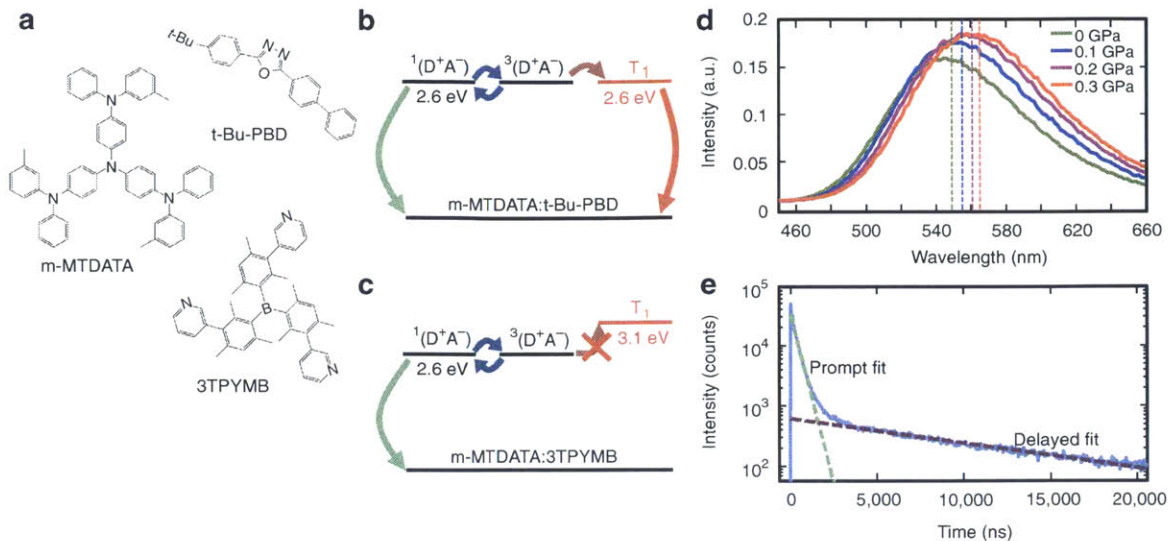
Figure 3.6: (a) Chemical structures of m-MTDATA, t-Bu-PBD and 3TPYMB. (b) The crucial energy levels and rates for the m-MTDATA:t-Bu-PBD and (c) m-MTDATA:3TPYMB systems. The excitonic triplet state T_1 state is for the acceptor; the excitonic triplet of m-MTDATA is $\sim$ 2.7 eV (not shown). (d) Measured m-MTDATA:3TPYMB film PL under pressure. Vertical line indicates the peak wavelength. (e) Transient PL for the m-MTDATA:t-Bu-PBD system. Green and purple dashed lines indicate fitted prompt and delay lifetimes, respectively.

state with efficiencies of $\sim$ 20%, and they exhibit the bi-exponential transient fluorescence decays and temperature-dependence characteristic of single-molecule TADF emitters (see Figure 3.6e).[123]

The dynamics of both the systems are shown in the rate diagrams of Figure 3.6b,c. Three critical states define the system: singlet CT state $^1(D^+A^-)$, triplet CT state $^3(D^+A^-)$, and excitonic triplet states T_1. In both the systems, the singlet CT state lies at $\sim$ 2.6 eV as determined by exciplex CT state fluorescence.[149] The triplet CT state is nearly isoenergetic with the singlet CT state; the triplet CT for the t-Bu-PBD acceptor system is estimated to be between 5 and 50 meV lower than that of the singlet CT state.[123,170] Note that the observed CT state emission in these systems is due to the exciplex singlet CT state between the nearest neighbor donor-acceptor molecules. Of particular importance to these systems are the excitonic triplet energies (see Figure 3.6b,c). The triplet back transfer is blocked in the m-MTDATA:3TPYMB system, due to the high energies of the triplet excitons, while the m-MTDATA:t-Bu-

PBD system has potentially significant triplet back transfer.

The pressure-induced changes to the transient PL provided insight into the principle spin-dependent loss pathways in an OPV, as illustrated in Figures 3.5 and 3.6.[149] The major findings from their pressure experiments were:[149]

1. Singlet CT states recombine directly to the singlet ground state of the donor and acceptor; this loss pathway is exacerbated as the CT state is physically constrained. This is due to an increased transition dipole moment under pressure.

2. Applied pressure also enhances the back transfer from triplet CT states to low-lying triplet exciton drains present on either the donor or acceptor.[160,164] This is due to an increased exchange splitting in the CT states, which decreases $E\left(^3(\mathrm{D^+A^-})\right)$, resulting in better coupling to the triplet drain.

Insights from magnetic field effects

Spin-orbit coupling- induced intersystem crossing (ISC) and reverse intersystem crossing modulates the interaction between singlet and triplet exciplex CT states. As revealed in §3.1, donor/acceptor systems like this may also contain another intersystem crossing mechanism, in which temporary delocalization of a CT state to form a polaron pair (PP) results in degeneracy of the singlet and triplet states, which are then interconverted through hyperfine coupling with the local magnetic nuclei. This mechanism is affected by an external magnetic field.

The CT state populations and resulting changes in photocurrent were probed by applying an external magnetic field to the device and simultaneously monitoring fluorescence and photocurrent.[149] The magnetic fields used in the experiments split two of the three triplet levels by up to ~ 50 meV. This Zeeman splitting is inconsequential to the intersystem crossing between the tightly bound CT states, because the exchange splitting between the singlet and triplet states is much larger than 50 meV. Instead, the magnetic field only modulates intersystem crossing between singlet and triplet states of larger CT states (PPs) whose exchange splitting is $\ll 50$ meV. Indeed,
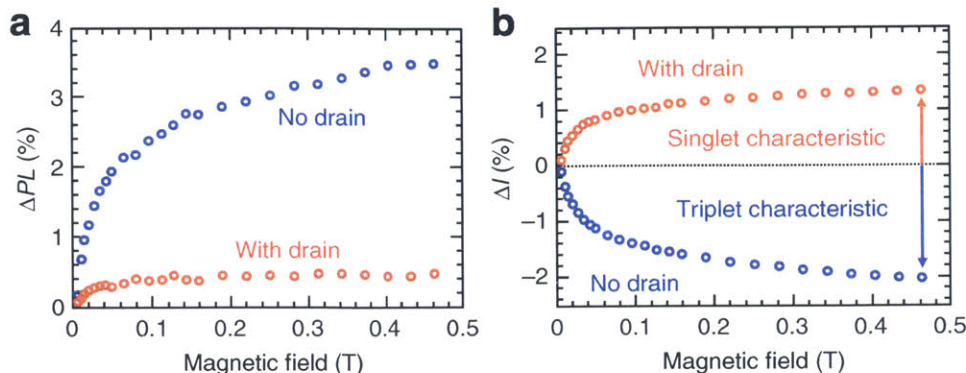
Figure 3.7: (a) Magnetic field effect on fluorescence for the m-MTDATA:t-Bu-PBD (red) and m-MTDATA:3TPYMB (blue) systems. Increases in PL from both the systems demonstrate that the applied magnetic field increases the population of singlet CT states. (b) The magnetic field effect on photocurrent for the m-MTDATA:t-Bu-PBD (red) and m-MTDATA:3TPYMB (blue) systems. The positive magnetic field effect with the t-Bu-PBD acceptor indicates that current is most efficiently collected from the singlet CT state, while the negative magnetic field effect with the 3TPYMB acceptor indicates that current is more efficiently collected from the triplet CT state.

as explained in §3.1, the magnetic field effect is due to an initial population of singlet CT states that temporarily separate beyond their exchange radius, forming Coulombically bound polaron pair states with zero effective exchange splitting. Such an extended singlet state may undergo intersystem crossing to a triplet mediated by hyperfine interactions. Otherwise, if the state remains as a singlet, it may collapse back and radiatively recombine within the spin-relaxation time.[125,138,171,172] Therefore, we expected the magnetic-induced increase in the probability of geminately recombining to singlet CT state to lead to an increase in the fluorescence quantum yield. Indeed, an increase in fluorescence under magnetic field was observed in both the material systems; see Figure 3.7a.

However, there is a striking difference between these material systems when we examine the magnetic field effect on photocurrent measured simultaneously with the fluorescence in Figure 3.7b. In the m-MTDATA:t-Bu-PBD system, the magnetic field effect on the photocurrent is also positive, that is, as the singlet CT population increases with the applied field, the photocurrent simultaneously increases. This signifies that the photocurrent is more efficiently generated from the singlet CT state, confirming

our observation of significant back transfer loss processes quenching the triplet CT states in this material system. Photocurrent from the m-MTDATA:3TPYMB system, however, shows the opposite effect, decreasing with applied magnetic field. As the singlet CT population increases with an applied external magnetic field the triplet CT population must correspondingly decrease. Because the change in the photocurrent is negative with increasing applied field, we conclude that photocurrent must be more effectively collected through the triplet CT state in the m-MTDATA:3TPYMB system. We also note that there was no measurable magnetic field effect on dark conductivity of our devices, indicating the absence of complicating magnetoresistance phenomena.[149]

Given the increase in the system's triplet CT state lifetime on pressure,[149] the magnetic field effect suggests that m-MTDATA:3TPYMB is spin protected in the triplet state. This direct measurement of CT state fluorescence and photocurrent generation under magnetic field indicates that triplet CT is more efficient in photocurrent generation in this system, since recombination to the ground state is spin forbidden, and recombination to a triplet exciton is energetically unfavourable. These results are reminiscent of recent studies of the P3HT:PCBM OPV system, where alternative methods showed evidence that the spin protection of triplet CT states can lead to longer lifetimes and greater probability of dissociation to free charges.[173,174]

In summary, applying a magnetic field to decrease the conversion of singlet CT states to triplet CT states allowed us to identify the spin of the CT states responsible for the efficient generation of photocurrent. We found that when a triplet drain is present, singlet CT states are responsible for the efficient generation of photocurrent, but in the absence of a triplet drain, photocurrent is more efficiently generated from the triplet CT states. Future organic solar cell designs should focus on raising the energy of triplet excitons to better utilize triplet charge transfer mediated photocurrent generation or increasing the donor-acceptor spacing to minimize recombination losses.

3.3 Nanoscale transport of charge transfer states in organic donor-acceptor blends

As a crucial transitional excited state in nanostructured optoelectronic devices, charge transfer (CT) states mediate both light emission in organic light emitting devices and charge generation in organic photovoltaics.[107,152,167] At the same time, much controversy surrounds the dynamics of CT states. Previous reports have described CT state dissociation into free charge that is both dependent[153,158,175] and independent[33,155,156] of the initial energy of the CT state. A particular puzzle is the apparent efficient generation of photocurrent from relaxed and tightly bound CT states.[108,176] Here, we report the dynamics of tightly bound CT states in the same donor-acceptor blend of m-MTDATA:3TPYMB investigated in §3.1 and §3.2 (shown in Figure 3.8), offering new insight in CT transport mechanism. The heterostructure under study is amorphous, with localized, highly fluorescent CT states, thus allowing direct observation of CT state dynamics.[123,149] As discussed in §3.2, this system is also notable because the triplet exciton energy levels are higher than that of the CT states, preventing "back transfer" loss to an otherwise typically lower energy triplet exciton.[149,164] Consequently, the CT states are long-lived, and the external quantum yield of photocurrent generation in m-MTDATA:3TPYMB is as high as 34%.[70] Thus, the blend is representative of the most perplexing of the donor-acceptor compositions, with tightly bound fluorescent CT states that are also an efficient source of photocurrent.

3.3.1 Collective motion of geminate charge-transfer states

By modeling the photoluminescence (PL) spatial profile obtained from an optical microscope with a scanning detector, our collaborators were able to obtain direct spatial and temporal visualization of CT state motion in the m-MTDATA:3TPYMB blend.[148] From their analysis of this donor-acceptor system, they drew the following conclusions:[148]
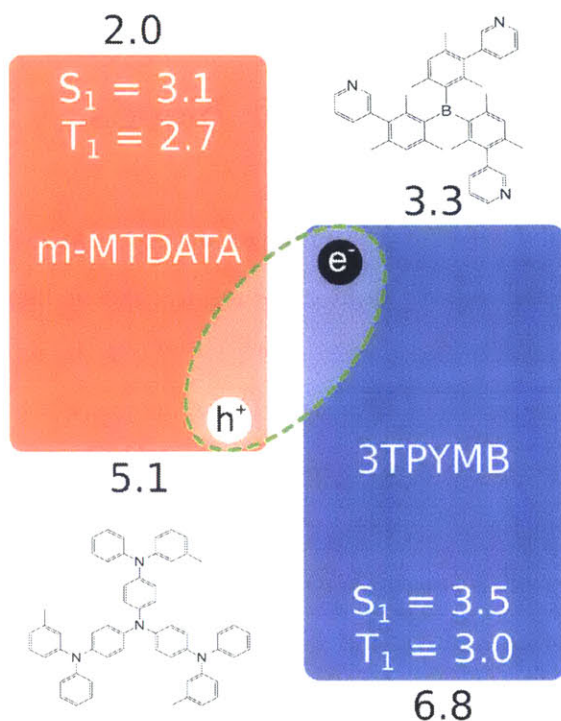
Figure 3.8: Energy diagram and chemical structures of the donor-acceptor material system. The energy levels of HOMO and LUMO states are in eV and are referenced to the vacuum level. The energies in eV of the lowest singlet (S_1) and triplet (T_1) excitons of m-MTDATA and 3TPYMB are also indicated.

1. CT state move over 5–10 nm in space.

2. The overall spectral redshift of ~ 60 meV is associated with either diffusion to lower-energy sites or solvation effects. (Note: This redshift is within the order of binding energies expected for tightly bound, geminate excitations.)

3. Excitation power and electric field dependencies confirm that CT states in this system behave as tightly bound particles with geminate characteristics.

The geminate nature of the CT state PL, in conjunction with the observed spatial broadening, indicates that both the photo-generated electron and hole are being displaced collectively. However, their optical analysis lacked information regarding the mechanism of CT state transport. The optical absorption of the CT state is negligibly low, suggesting that Förster transfer is not likely to be effective. Although the Dexter mechanism is feasible, CT states are weakly bound compared to most intra-

130

molecular excitonic states. More efficient transport may be possible, if CT motion occurs via asynchronous electron and hole motion. The CT state may stretch and contract as it moves through the blend. This 'inchworm'-type mechanism of CT state transport is probed by magnetic field studies, which are capable of examining the relative displacement of the electron and the hole.

3.3.2 Probing the CT state diffusion mechanism with a magnetic field

As explained in §3.1 and §3.2, magnetic field effects if CT states stretch, forming polaron-pair (PP) states, in which the exchange splitting is comparable to the Zeeman splitting induced by the field. The m-MTDATA:3TPYMB system, however, does exhibit magnetic field effects on both PL and photocurrent,[149] suggesting that the CT states can stretch while remaining bound. The magnetic field slows intersystem crossing in the PP states, preserving the population of the luminescent singlet CT states and increasing the fluorescence, as shown in Figures 3.7 and 3.9a.

The shape of the magnetic field dependence also provides insight into the dynamics of the electron and hole, specifically regarding any spin relaxation effect. According to the model of Schulten and Wolynes, the saturation of the magnetic field effect is determined by the applied magnetic field, the strength of the hyperfine field at each molecule, and the rate at which a charge hops to neighboring molecules.[177,178] The effective hyperfine field at each molecule is randomly oriented, with a standard deviation of ~ 1 mT. As a charge hops from molecule to molecule, it experiences a fluctuating local magnetic field, which induces transitions between spin states, leading to spin relaxation of the stretched CT state.[76] (In §3.3.3, we show how this hopping-induced relaxation effect can be incorporated into the two-configuration model of §3.1.) Consequently, stronger magnetic fields are required to suppress intersystem crossing when the charges are more mobile and visit more sites. Thus, the saturation of the magnetic field effect serves as a probe of the charge hopping rate in the
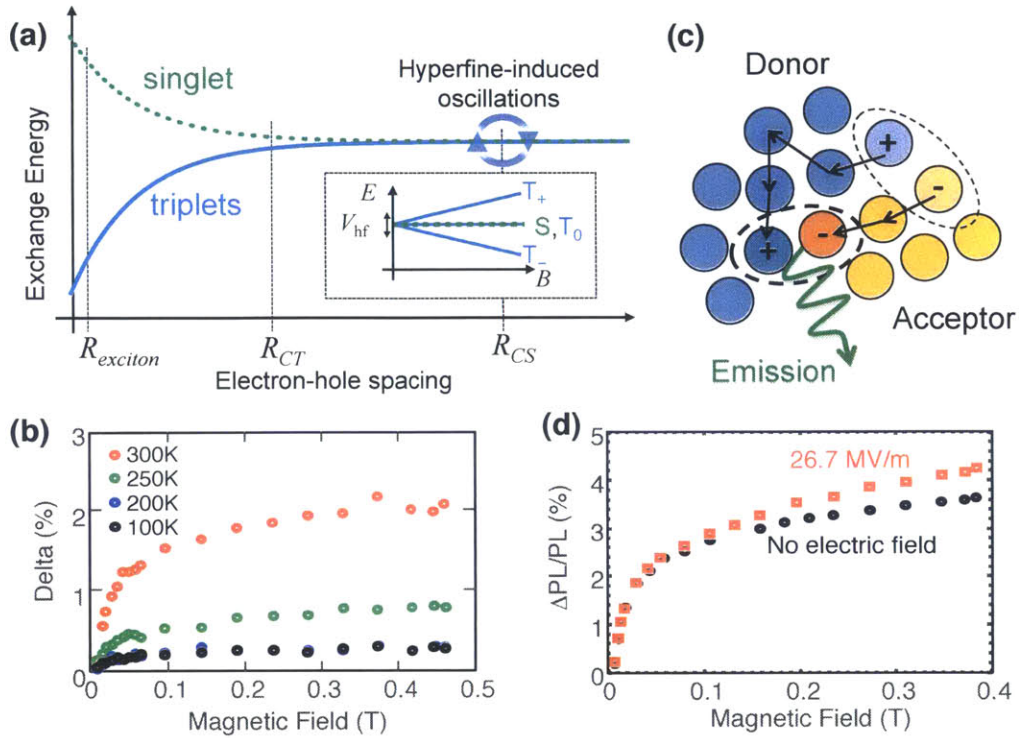
Figure 3.9: (a) Energy schematic of singlet-triplet energy splitting as a function of electron-hole spacing. (inset) Schematic of Zeeman splitting due to external magnetic field in relation to hyperfine coupling V_{hf}. (b) The temperature dependence of the magnetic field modulation of CT state PL. The magnitude of the change in PL decreases at lower temperature, indicating magnetic field-dependent hyperfine mediated intersystem crossing decreases with lower thermal energy. However, change in the shape of the magnetic field dependence is not observed over this range of temperatures. (c) Illustration of stretching effect on CT state dynamics and spectral diffusion. (d) Bulk heterojunction device sample under magnetic field at open-circuit and closed-circuit, demonstrating that application of an electric field distorts the size of the CT state.

stretched-CT configuration.

The magnetic field effect can occur only if the CT state can stretch, thus we probe it by examining the temperature dependence of the CT state PL. As shown in Figure 3.9b, we find the magnitude of the magnetic field effect on PL to be thermally activated, which is consistent with expectations that fewer CT states should stretch at lower
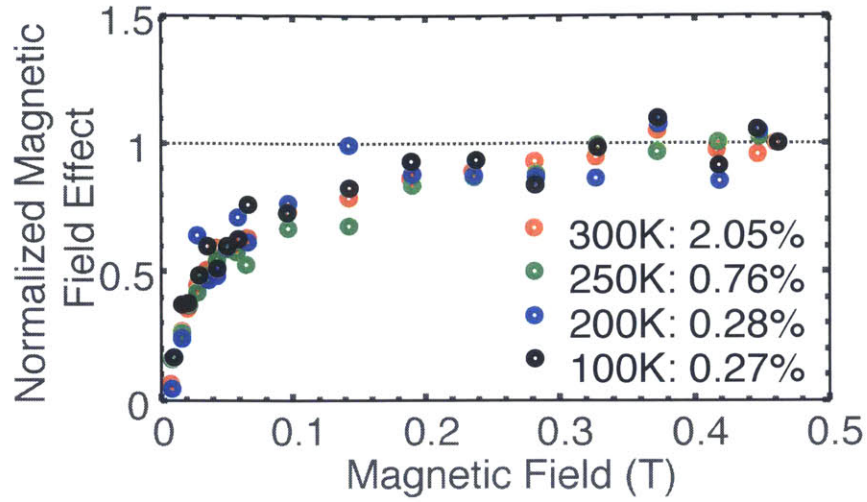
Figure 3.10: Temperature dependence of the normalized PL magnetic field effect. The line-shape invariance within the measured range of temperatures is rationalized in §3.3.3.

temperatures. The line shape of the *normalized* MFE shows no change as a function of temperature above 100 K (see Figure 3.10). This line-shape invariance within the measured range of temperatures is rationalized in §3.3.3. Instead, the more significant effect of lower temperature is to decrease the number of CT states that stretch beyond the exchange radius, thus decreasing the magnitude of the observed change.

Notable change in spin relaxation is observed, however, under the application of an electric field as shown in Figure 3.9d. An external field increases the hopping rate of the charges in stretched CT states beyond a threshold value (see §3.3.3), increasing the spin relaxation and producing a slower saturation of the magnetic field effect. Overall, the magnetic field studies show that transport via asynchronous electron and hole hopping is plausible; there is fluctuation in the electron-hole spacing during the lifetime of the CT states, but the relative displacement is sufficiently small that the electron-hole pair remains bound.

3.3.3   Including spin relaxation in the two-configuration model

As an electron (or hole) hops from one molecule to another, it experiences a rapid change its hyperfine interactions (HFIs), which are due to local interactions with a molecule's magnetic nuclei (see §3.1). This fluctuating HFI causes spin relaxation.[76] For a system with an average charge hopping time τ_{hop} much greater than the hyperfine spin evolution time $\tau_{\text{HFI}} \sim 10^{-8}$ s, the following Block-Redfield treatment can be used to describe the spin relaxation.[76,179]

We start by assuming the same correlation function

$$\Phi\left(t\right) = e^{-t/\tau_{\text{hop}}}$$

for the HFI fluctuations of both the electron and hole. The spectral density at the Zeeman Larmor frequency $\omega = g\mu_{\text{B}}B_{\text{ext}}$ is then

$$J\left(\omega\right) = \int\limits_0^\infty \Phi\left(t\right)\cos\left(\omega t\right) dt = \frac{\tau_{\text{hop}}}{1 + \left(\tau_{\text{hop}}\omega\right)^2}.$$

Within the semiclassical approximation described in §3.1, the mean square HFI frequency in each direction, $1/3(g\mu_{\text{B}}\sigma_{\text{HF}})^2$, results in spin-lattice and spin-spin relaxation times T_1 and T_2 given by.[179]

$$\frac{1}{T_1} = 2\frac{1}{3}(g\mu_{\text{B}}\sigma_{\text{HF}})^2 J\left(\omega\right), \tag{3.18}$$

and

$$\frac{1}{T_2} = \frac{1}{3}(g\mu_{\text{B}}\sigma_{\text{HF}})^2 J\left(0\right) + \frac{1}{2T_1}. \tag{3.19}$$

These relaxation transitions can be treated within the Lindblad formalism.   For a

single spin-1/2 system, the Γ operators describing relaxation are

$$\Gamma_- = \sqrt{k_{\mathrm{pop}}}\,|\beta\rangle\,\langle\alpha|$$

$$\Gamma_+ = \sqrt{k_{\mathrm{pop}}}\,|\alpha\rangle\,\langle\beta|$$

$$\Gamma_z = \sqrt{k_{\mathrm{phase}}}\,(|\alpha\rangle\,\langle\alpha| - |\beta\rangle\,\langle\beta|)$$

were the population and phase relaxation rate constants are given by

$$k_{\mathrm{pop}} = \frac{1}{3}(g\mu_{\mathrm{B}}\sigma_{\mathrm{HF}})^2 J(\omega),$$

and

$$k_{\mathrm{phase}} = \frac{1}{2}\left[\frac{1}{3}(g\mu_{\mathrm{B}}\sigma_{\mathrm{HF}})^2 J(0)\right].$$

To treat relaxation within the polaron pair manifold in the eight-state basis of the two-configuration model of §3.1, we append the following set of Γ operators:

$$\Gamma_{-,1} = Q_{\mathrm{PP}}\left[\Gamma_- \otimes \mathbf{1}_2\right]Q_{\mathrm{PP}}{}^\top,$$

$$\Gamma_{-,2} = Q_{\mathrm{PP}}\left[\mathbf{1}_2 \otimes \Gamma_-\right]Q_{\mathrm{PP}}{}^\top,$$

$$\Gamma_{+,1} = Q_{\mathrm{PP}}\left[\Gamma_+ \otimes \mathbf{1}_2\right]Q_{\mathrm{PP}}{}^\top,$$

$$\Gamma_{+,2} = Q_{\mathrm{PP}}\left[\mathbf{1}_2 \otimes \Gamma_+\right]Q_{\mathrm{PP}}{}^\top,$$

$$\Gamma_{z,1} = Q_{\mathrm{PP}}\left[\Gamma_z \otimes \mathbf{1}_2\right]Q_{\mathrm{PP}}{}^\top,$$

$$\Gamma_{z,2} = Q_{\mathrm{PP}}\left[\mathbf{1}_2 \otimes \Gamma_z\right]Q_{\mathrm{PP}}{}^\top,$$

where Q_{PP} is the rotation matrix given in Equation (3.10).

The MFE line shape above ~ 0.1 T is determined almost entirely from spin relaxation. Therefore, $k_{\mathrm{hop}} = \tau_{\mathrm{hop}}^{-1}$ is parameter that determines the line shape. We obtained excellent agreement with the experimental line shape using $k_{\mathrm{hop}} = 3.57 \times 10^9$ s^{-1}, as shown in Figure 3.11.

Finally, we rationalize the temperature-independence of the PL MFE lineshape by examining the influence of k_{hop} on the normalized change in the magnetic field dependent relaxation time T_1; plotted in Figure 3.12. [Note: T_1 is the only magnetic
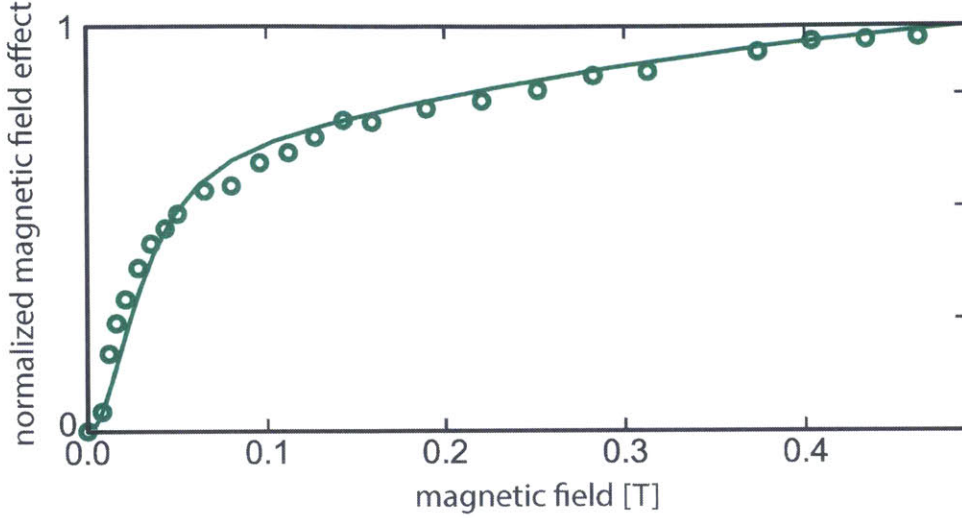
Figure 3.11: Fit of theory (line) to the experimental (dots) normalized PL magnetic field effect. The lineshape was obtained using $k_{hop} = 3.57 \times 10^9$ s^{-1}.
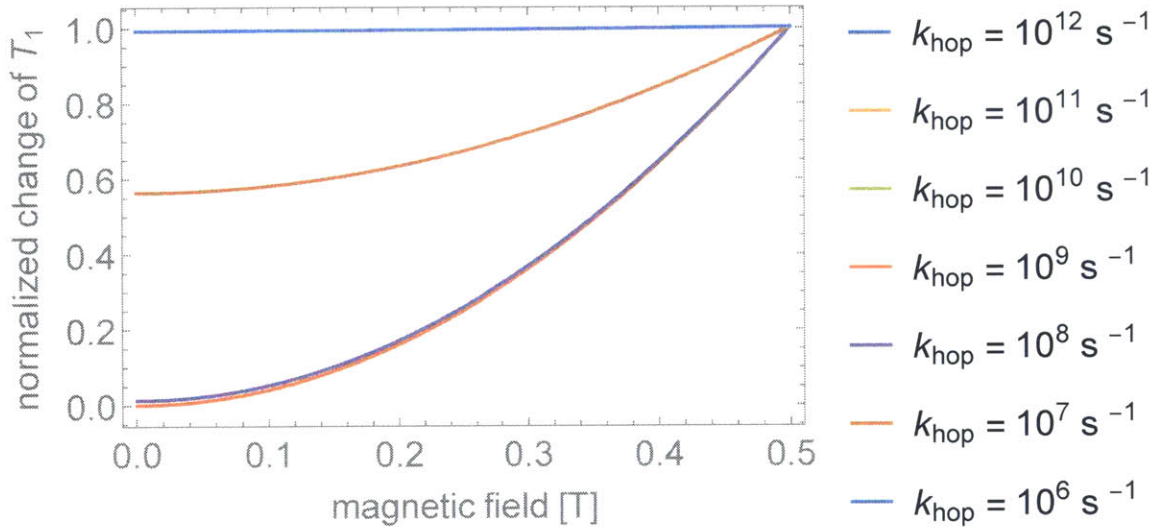
Figure 3.12: Normalized change in the magnetic field dependent relaxation time T_1 calculated with different hopping rates; see Equation (3.18).

field dependent component of T_2, see Equations (3.18) and (3.19).] Changes in the lineshape only emerge above $k_{hop} \sim 10 \times 10^{10}$ s^{-1}, which could only be obtained by *increasing* the temperature, if our fitted room-temperature value of $k_{hop} = 3.57 \times 10^9$ s^{-1} is correct within approximately an order of magnitude. It is, however, reasonable to argue that application of an external field could increase k_{hop} to a value in the range at which the line shape changes.

3.3.4 Implications of CT transport for organic electronics

We conclude by considering the implications of CT transport for organic optoelectronic devices. Arguably, the evidence of CT diffusion to lower energy traps only deepens the mystery concerning the origin of efficient photocurrent generation from tightly bound CT states in organic photovoltaics. Consequently, we offer some insight as to other potential ramifications of the diffusion of CT states. First, it is well known from exciton dissociation models that the probability of charge separation is significantly higher if the CT state is aligned with the electric field.[180] The ability of the CT state to move is expected to help reorient the CT states, since the aligned donor-acceptor pairs are lower energy sites. Second, constraining the percolation networks in phase-separated donor-acceptor blends, where CT states can only diffuse along the grain boundaries, would significantly reduce the diffusion distances, while still allowing the states to orient optimally for charge separation. Imaging measurements in different morphologies coupled to simulations should help resolve the mechanism of the transport as well as identify the optimum tradeoff between diffusion and trapping.

In summary, direct imaging of blends of m-MTDATA:3TPYMB coupled with magnetic field studies demonstrate the presence of tightly bound CT states that diffuse 5–10 nm before settling into lower energy CT states. Since donor-acceptor blends typically exhibit rapid conversion from excitons to CT states, it is possible that CT state diffusion distances in many organic devices exceed that of the initial exciton, highlighting the potential importance and impact of CT state transport on device performance.

THIS PAGE INTENTIONALLY LEFT BLANK

Chapter 4

Electronic structure of metal-organic frameworks

4.1 Charge transfer or J-coupling? Assignment of an unexpected red-shifted absorption band in a naphthalenediimide-based metal-organic framework

The ability to define the packing of organic chromophores in molecular aggregates is paramount for understanding and controlling the photophysical processes in artificial light-harvesting constructs such as organic photovoltaics (OPVs). Inspiration toward this goal is often drawn from photosynthetic organisms, which efficiently trap photons and coherently transport excitons to a charge-separating center by using supramolecular architectures of light-absorbing chromophores such as chlorophylls and carotenes.[181–183] The challenge in mimicking the natural light-harvesting systems is to apply the photophysical and supramolecular organizational principles refined by nature in developing artificial materials that can harvest visible light and guide excitation energy transfer in a unidirectional manner. Many elegant synthetic solutions
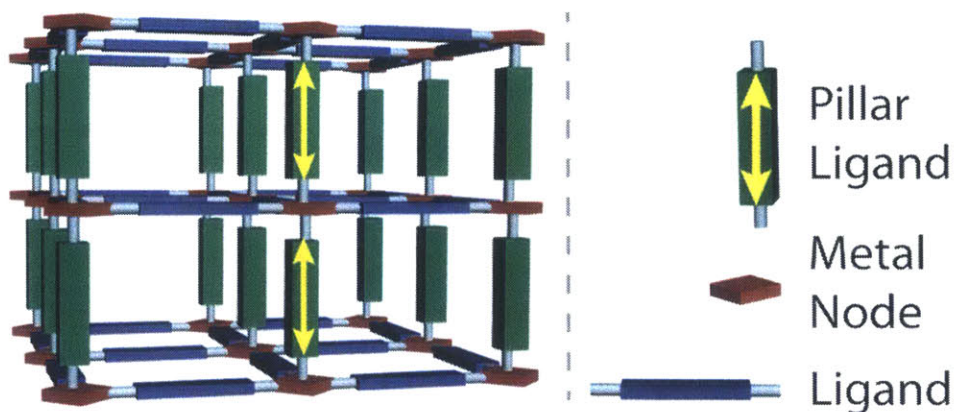
Figure 4.1: Schematic of a pillared MOF, with two types of organic ligands including the pillar. Yellow arrows indicate the transition dipoles and their expected head-to-tail arrangement within the chains defined by the pillar molecules.

have been elaborated toward this goal. Dendrimers,[184–187] hyperbranched conjugated polymers,[188] and oligomeric porphyrin arrays,[189] for instance, show evidence of the electronic cooperativity necessary for efficient energy transfer. One particular architecture that has received attention to this end is that of J-aggregates. These are molecular constructs in which individual light-absorbing molecules are arranged such that their excitation dipole moments couple to promote delocalization of the excited state over many chromophores.[190] Whereas no single model for J-aggregate structure has been universally accepted, one widely acknowledged criterion is that such excitonic coupling occurs when the primary transition dipoles of the dye molecules are aligned head-to-tail.[190,191] J-aggregates are characterized by a red-shifted, narrow band with a high extinction coefficient that is frequently coupled to a fluorescence peak separated by only a very small Stokes shift. The interest in such aggregates from an OPV perspective stems from the advantages presented by this highly absorbing band: deliberate engineering of organic chromophores into J-aggregates could significantly reduce the required thickness of the light-absorbing layer, thereby reducing the likelihood of charge recombination losses. However, it is currently very difficult to control the solid-state packing of molecular chromophores, and J-aggregates historically have mostly been discovered by serendipity.

One class of materials that allows exquisite control over the intermolecular distances

and angles between organic molecules is metal-organic frameworks (MOFs). These are crystalline hybrid materials made from inorganic and organic building blocks whose topologies, and implicitly the intermolecular distances between various building blocks, can be controlled by design using the principles of reticular chemistry. Although MOFs have traditionally been used for gas separation and storage, their highly ordered nature has also made them attractive targets for studying photophysical phenomena related to energy transfer[38-40] for light harvesting and luminescence for sensing.[41-45] The structure-function relationship of MOFs in relation to luminescence properties has also been the focus of recent careful studies.[41-43] Along the same lines, we envisioned that the inherent ordered structure of MOFs could be conducive to J-aggregate formation in chromophores that do not normally exhibit this behavior if such chromophores could be aligned in the typical head-to-tail arrangement within MOFs. Furthermore, we surmised that given the extraordinary variety of MOF structures reported to date, J-coupling behavior may have gone unnoticed in some of the existing materials. We initially set out to investigate the possibility of J-coupling in the class of materials known as pillared MOFs. As shown in Figure 4.1, these are made from 2-D lattices containing one type of ligand and one type of secondary building unit and are connected in the third dimension by a second type of ligand—the pillar. Because the pillars are naturally aligned head-to-tail, we searched for materials in this class wherein the pillars were made of light-absorbing molecules. One promising candidate was quickly identified as $Zn_2(NDC)_2(DPNI)$ (**1**, NDC = 2,6-naphthalenedicarboxylate; DPNI = dipyridyl naphthalenediimide). Originally reported by Hupp et al., **1** was described as having an unexpected yellow color and weak luminescence despite the colorless nature of the individual building blocks: Zn^{2+} ions, NDC^{2-}, and DPNI.[192] Encouragingly, the supramolecular structure of **1**, shown in Figure 4.2a, reveals linear chains of DPNI pillars, a chromophore class well known to possess a primary transition dipole moment aligned with the long axis of the molecule.[190] Coupled to the reported unexpected yellow color and weak luminescence, it seemed feasible that J-coupling was occurring in **1**.
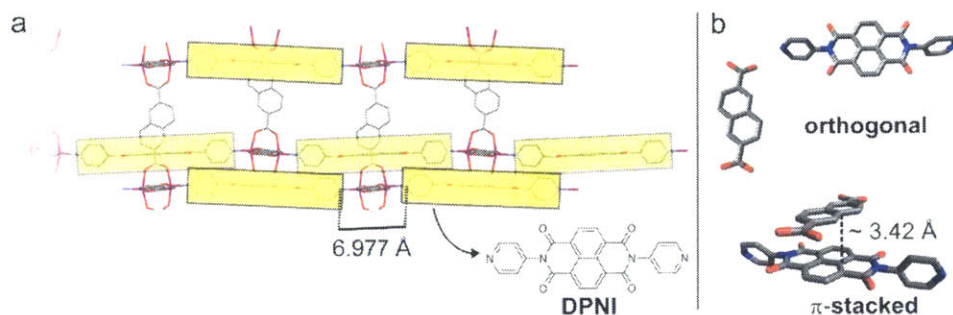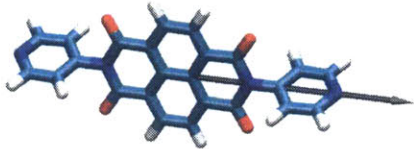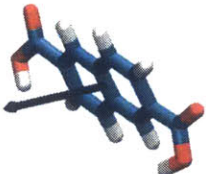
Figure 4.2: Partial crystal structure of **1**. Outlined yellow boxes represent DPNI units. Faded yellow boxes indicate DPNI units located behind the first set due to framework interpenetration. (b) Two dimer pairs, orthogonal and π-stacked, of DPNI and NDC^{2-}. Gray, blue, red, and pink spheres represent C, N, O, and Zn atoms, respectively. Hydrogen atoms were omitted for clarity.

4.1.1 Ruling out J-coupling

Although J-coupling in **1** seemed possible, it was clear that whereas numerous studies on MOFs exist, very few focus on explicitly interpreting bulk photophysical properties, and little established methodology is dedicated exclusively to interpreting the photophysical properties of MOFs. For instance, although many reports of photophysical properties of MOFs focus on fluorescence or luminescence, little effort has been devoted on understanding the influence of the supramolecular environment on the optical transitions. Additionally, whereas computational studies often help to elucidate the origins of photophysical properties in molecular species, little precedent exists for how such studies should be tuned for MOFs. Herein, we investigate the photophysical properties of **1** and present a theoretical framework for understanding its red-shifted absorption band, with a particular emphasis of modeling charge-transfer interactions in these intensively studied materials.

To facilitate the interpretation of the origin of the red-shifted band giving rise to the yellow color of **1**, a portion of its crystal structure is shown in Figure 4.2. Viewed along the a or c axes, linear chains of DPNI units, marked with yellow boxes in Figure 4.2a, are clearly visible. Each DPNI unit is separated from the next by 6.977 Å, which includes a $(Zn^{2+})_2$ cluster. Contrasting its arrangement with neighboring

142

Table 4.1: Primary transition moment dipoles, transition energies, and oscillator strengths for studied ligands.

Organic moiety	primary transition moment dipole	$S_0 \rightarrow S_1$ (nm)[a]	oscillator strength
DPNI		313 – 349	0.4941
2,6-H$_2$NDC		301 – 334	0.0528

[a] Given 0.2 eV error bars

DPNI molecules, DPNI forms two distinct spatial relationships with NDC^{2-}. Within a single unit cell, DPNI is oriented orthogonal to the neighboring NDC^{2-} ligand with which it shares a $(Zn^{2+})_2$ cluster (Figure 4.2b). Two-fold interpenetration of **1** results in a second DPNI-NDC^{2-} interaction, in which the naphthalene core of a DPNI molecule in one framework π-stacks with a NDC^{2-} molecule of the second interpenetrated framework (Figure 4.2b).

Importantly, because the primary transition dipole of non core-substituted naphthalene diimides (NDIs) frequently lies directly along the long molecular axis,[193] and given the literature precedent for solution NDI J-aggregates,[194–197] it seemed feasible that J-coupling could occur along the chains of DPNI units observed in **1** and that such coupling is responsible for the red-shifted absorption band. Additionally, the DPNI–DPNI separation of 6.977 Å is within the range of interchromophore distances that are conducive of such coupling; for instance, reported J-aggregates of pyronine observed within channels of zeolite L are characterized by estimated interpyronine distances of 7.0 Å.[198] Furthermore, a calculation of the primary transition dipole of molecular DPNI confirmed that it lay directly along the long intermolecular axis (as discussed in §4.1.3; see Table 4.1), confirming the head-to-tail transition dipole

143

arrangement that we hypothesized.

With J-coupling seemingly feasible by this structural analysis, compound 1 was synthesized and obtained as yellow needle-like crystals. Spectroscopic analysis[199] suggested that the originally reported weak fluorescence arose from a small amount of impurity in the crystal but that the red-shifted absorption band indeed originated from 1 itself. Importantly, the lack of fluorescence in 1, which is atypical of J-aggregation, was a first indication that this material may not in fact exhibit J-coupling. Furthermore, although J-aggregates with broad red-shifted features have been previously reported,[195–197,200] the broadness and relative weakness of the red-shifted band in 1 prompted us to evaluate alternative interpretations for the novel photophysical features in this material.

4.1.2 Assignment as charge-transfer band

With J-coupling likely ruled out and the full d manifold of Zn^{2+} eliminating the possibility of d–d transitions, CT interactions were considered as a possible explanation instead. CT interactions could be envisioned to occur between any of the components of 1 (DPNI, NDC^{2-}, and/or the paddlewheel $Zn_2(O_2C-)_4$ cluster), or even across building blocks from the two interpenetrated frameworks. Ligand-to-metal or metal-to-ligand CT was deemed unlikely because it would result in a formal reduction or oxidation of the very stable d^{10} Zn^{2+} ion. Another possible CT interaction could occur between the framework and dimethylamine (DMA) formed by thermal decomposition of the DMF solvent during synthesis.[43] Because the synthesis of 1 is carried out at a relatively low temperature (100 °C), little DMA is expected to have been formed. Recently, CT interactions between DPNI linkers and donor aromatic solvents were reported for a MOF similar to 1.[201,202] To simplify the CT analysis, the two organic components, DPNI and 2,6-H_2NDC, were considered first.

Comparison of the MOF absorption spectra with that of a charge transfer (CT) complex formed by manual grinding of DPNI and H_2NDC 2 led to the tentative

144

Table 4.2: Effect of dielectric constant on CT energy for π-stacked DPNI/2,6-NDC^{2-} model system (cc-PVTZ).

ε	$S_0 \to CT$ (eV)	$S_0 \to CT$ range (nm)[a]
2	3.41	344 – 386
2.5	3.30	354 – 400
3	3.23	362 – 410
3.5	3.18	367 – 416
4	3.13	373 – 424
4.5	3.10	376 – 428

[a] Given 0.2 eV error bars

assignment of the new band in **1** as arising from an CT interaction between 2,6-H$_2$NDC and DPNI.[199]

To investigate the assignment of the new band in **1** as a CT interaction instead of J-coupling, computational methods were utilized. The first excited singlet state of a DPNI monomer was found to have a considerable transition dipole moment of 13.6 D (with an oscillator strength of 0.49); see §4.1.3. However, the centers of mass of DPNI monomers within **1** are separated by ~ 22 Å, which yields an estimated dipole-dipole coupling of only 2 meV. Because the spacing between the lowest energy electronic transition of DPNI and the middle of the broad band of **1** is about 450–500 meV, this estimated dipole-dipole coupling of 2 meV is too small to support assignment of the band as J-coupling.

With J coupling experimentally and theoretically ruled out, CT excitation energies were calculated for various dimer systems to support assignment of the new transition observed in **1** to an interligand CT. The π-stacked and orthogonal dimer systems shown in Figure 4.2b were considered. To account for the stabilization energy of the CT state due to the polarization of the surrounding molecules in the MOF, the dimer systems were embedded in a polarizable continuum with dielectric constant $\epsilon = 2.0$ (a sample input file is included in §A). The CT state energy was found to scale with ϵ, with larger ϵ values further stabilizing the CT state and lowering the excitation
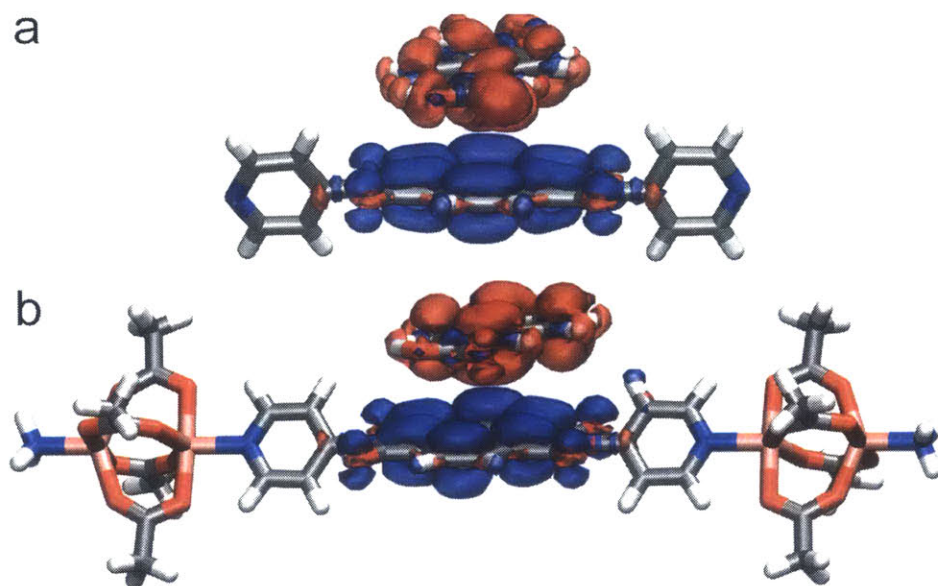
Figure 4.3: Two calculated charge-transfer states of dimers consisting of NDC^{2-} and DPNI (**2a**) and DPNI with capped $Zn_2(O_2CCH_3)_3$ linkage groups (**2b**). The electron and hole density changes are plotted as isosurfaces with the electron density in blue and the hole density in red.

energy (Table 4.2). The few reported dielectric constants for MOFs range from 4.6 to over 100,[203–205] but these simulations need to mimic the dielectric response at optical frequencies, which is typically much smaller. Thus, the dielectric constant was conservatively set to 2 but is possibly larger. Comparison of the oscillator strength for the π-stacked versus orthogonal dimer geometries suggested that CT happens predominantly within π-stacked dimers because the orthogonal geometry calculation yielded a very low oscillator strength (2.3×10^{-5}), whereas the π-stacked dimer gave a higher oscillator strength of 0.019.

Although basis set convergence for the CT energy of the simplified π-stacked system **2a** (Figure 4.3a) was reached with cc-PVTZ, the calculated energy range for the excitation (Table 4.3) remained higher than the experimentally observed band for **1**. To simulate the effect of the local charges on the CT energy, a model system dimer **2b** was built containing Zn^{2+} clusters on either end of the DPNI ligand truncated by acetate ions and ammonia molecules and is shown in Figure 4.3b. Indeed, the calculated energy for **2b** was lower than that of the dimer **2a**, but the use of the

Table 4.3: CT Excitation energy ranges of dimer systems (a) and (b) of Figure 4.3 calculated using CDFT with a custom long-range-corrected functional

dimer system	basis set	CT energy $(nm)^a$
(a)	6-31g*	337–378
(a)	cc-PVTZ	344–386
(b)	6-31g*	363–411
(b)	cc-PVTZ (estimated)	374–435

^{a}Given 0.2 eV error bars.

cc-PVTZ basis set was computationally prohibitive in this case. Consequently, the cc-PVTZ CT energy for **2b** was estimated from the difference in CT energy between the two basis sets for **2a**, ~ 0.1 eV, as shown in Table 4.3. This resulted in a CT excitation energy within the range observed experimentally for **1** and suggests that the presence of the positively charged Zn^{2+} ions facilitates stabilization of the accepted electron density on DPNI.

4.1.3 Computational details

Tuning long-range-corrected functionals to Koopman's theorem

Typical functionals are known to yield inaccurate energies for CT excitation energies,[206,207] especially when using time-dependent density functional theory (TDDFT).[208] For this reason, a customized version of the LC-ωPBE long-range-corrected[209] hybrid functional known to obtain accurate CT excitation energies[210] was used in all calculations. The range separation parameter ω and the amount of short-range Hartree-Fock exchange C_{HF} were tuned to match Koopman's theorem for the ionization potential of the neutral molecule and the anion[211–214] of DPNI.

A long-range-corrected (LRC) hybrid functional[209] splits the Coulomb repulsion term into short-range and long-range parts and calculates the short-range correlation energy using both generalized gradient approximations (GGAs) and Hartree-Fock (HF)

and the long-range correlation energy using only HF:

$$\frac{1}{r_{12}} = \underbrace{\frac{1 - \text{erf}\left(\omega r_{12}\right)}{r_{12}}}_{\substack{\text{short - range} \\ \text{GGAs \& HF}}} + \underbrace{\frac{\text{erf}\left(\omega r_{12}\right)}{r_{12}}}_{\substack{\text{long - range} \\ \text{HF only}}}$$

$$\frac{1}{r_{12}}$$

$$\frac{\text{erf}\left(\omega r_{12}\right)}{r_{12}}$$

$$\frac{1 - \text{erf}\left(\omega r_{12}\right)}{r_{12}}$$

$$r_{12}$$
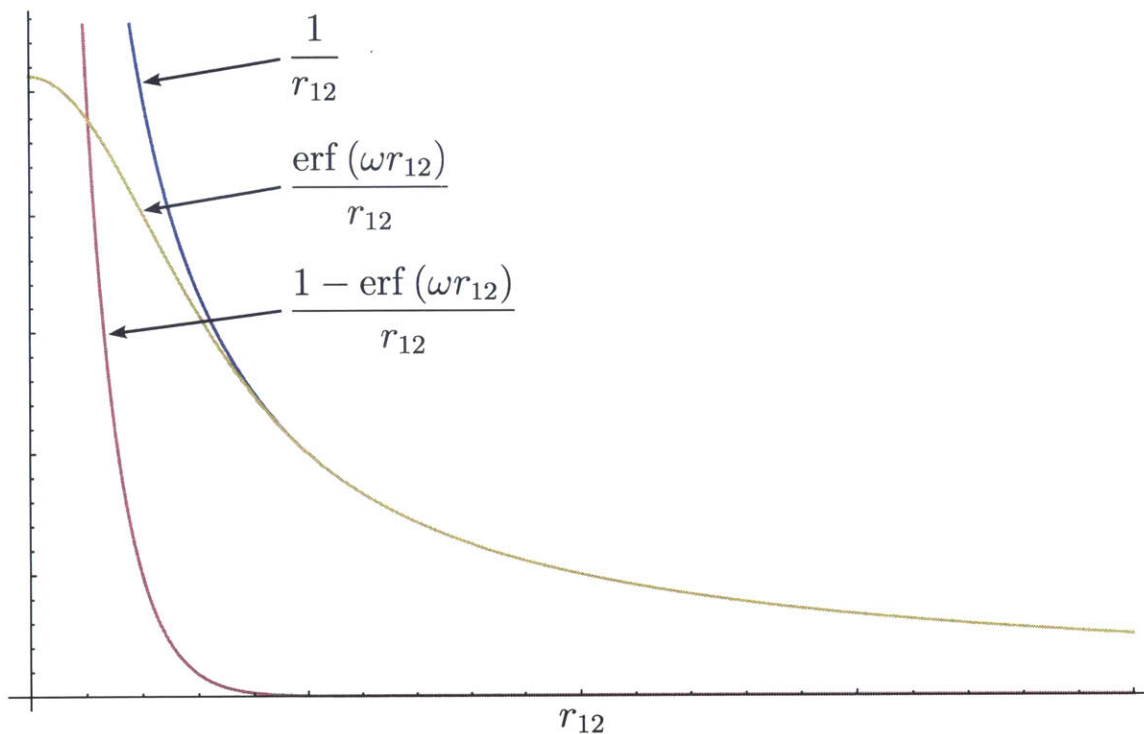
The exchange energy of the system is thus given by

$$E_{\text{exchange}}^{\text{LRC}} = \left(1 - C_{\text{HF}}\right) E_{\text{GGA exchange}}^{\text{short - range}} + C_{\text{HF}} E_{\text{HF exchange}}^{\text{short - range}} + E_{\text{HF exchange}}^{\text{long - range}},$$

where the exchange energies are evaluated using the components of $1/r_{12}$ above.

We optimized 2 parameters:

- ω: determines where the transition from a hybrid functional (GGAs and HF) to pure HF exchange takes place

- C_{HF}: determines the amount of HF exchange included at short-range

Our objective function to minimize J is based on matching Koopman's Theorem for

the neutral and anion species and is given by

$$J\left(\omega, C_{\mathrm{HF}}\right) = \left| \varepsilon_{\mathrm{HOMO}}^{\omega, C_{\mathrm{HF}}}\left(\text{neutral}\right) - \mathrm{IP}\left(\text{neutral}\right) \right| + \left| \varepsilon_{\mathrm{HOMO}}^{\omega, C_{\mathrm{HF}}}\left(\text{anion}\right) - \mathrm{IP}\left(\text{anion}\right) \right|,$$

where $\varepsilon_{\mathrm{HOMO}}^{\omega, C_{\mathrm{HF}}}$ is the homo energy and IP is the ionization potential.

To find the optimal values of ω and C_{HF}, we perform a series of single-point energy calculations on the species of interest over a grid of values of ω and C_{HF}:
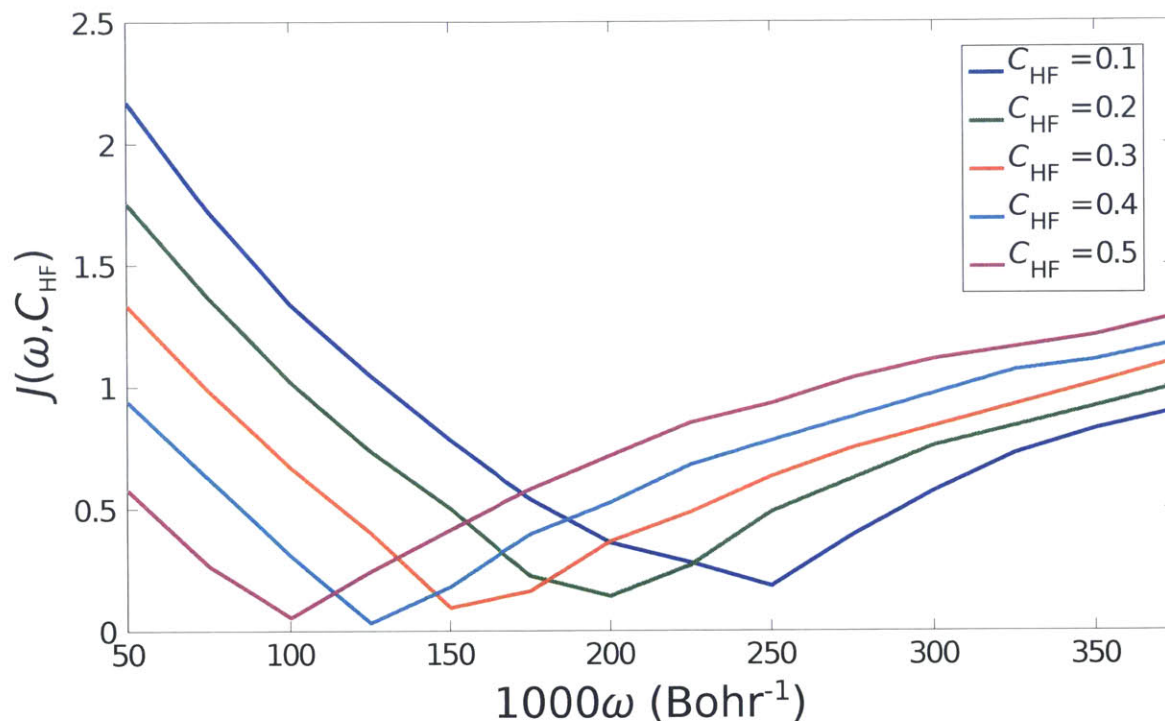
We then choose the set of parameters $\{\omega, C_{\mathrm{HF}}\}_{\mathrm{best}}$ that yield the lowest value of J.

The calculations necessary to calculate J for a give set $\{\omega, C_{\mathrm{HF}}\}$ are

- single-point energy calculation on **neutral species**

- single-point energy calculation on **anion**

- single-point energy calculation on **cation**

The values in the objective function J are then obtained as follows:

- $\varepsilon_{\mathrm{HOMO}}^{\omega, C_{\mathrm{HF}}}$ is the larger of the alpha and beta occupied molecular orbital energies

149

- IP (neutral) = E (cation) − E (neutral)

- IP (anion) = E (anion) − E (neutral)

Example Q-Chem input files templates necessary to tune a LRC hybrid functional can be found in §A.

Excition and charge-transer transition properties

The transition dipole of the DPNI monomer unit was obtained from a TDDFT calculation using the 6-31G* basis set.[215] The first 10 singlet excited states were calculated in all TDDFT calculations. The CT calculations were performed on dimer systems using constrained density function theory (CDFT)[216] by constraining an additional electron and spin on the acceptor molecule (the DPNI unit). For CT calculations, the dimers were embedded in a polarizable continuum[217] with a dielectric constant $\epsilon = 2.0$ (this choice of dielectric constant is discussed in the previous section). CDFT with configuration interaction (CDFT-CI)[218] between the ground and CT states was used to obtain the transition dipole for the CT excitation. All calculations were performed using the Q-Chem 3.1 computational package.[219]

An example input file for a CDFT-CI calculation, from which the CT state and it's transition dipole moment are obtained can be found in §A.

4.1.4 Conclusions

Accordingly, the unexpected new red-shifted transition of **1** was assigned to an interligand DPNI/NDC^{2-} CT based on comparison with the CT complex **2**, an assignment that was supported computationally. Theoretical models also support the fact that the majority of the CT responsible for the new transition in **1** arises from π-stacked DPNI/NDC^{2-} units rather than orthogonal dimers. The lack of fluorescence from the MOF also lends credence to excitation of a CT state because nonradiative recombination of the CT states is often a very rapid process.[220] Although the more

desirable J-coupling behavior was not observed in **1**, we have gained practical knowledge in what should be avoided in the design of MOFs with J-coupling and in how to accurately model these materials computationally. It is possible that the presence of the $(Zn^{2+})_2$ clusters directly between DPNI units interrupts coupling or, as our calculations suggest, that the inter-DPNI distance is too great for strong coupling. Interestingly, an analogous but noninterpenetrated MOF, $Zn_2(1,4-NDC)_2(DPNI)$, was reported to possess an orange color[221] despite the colorless nature of the ligands involved and a lack of π-stacking between $1,4-NDC^-$ and DPNI. Efforts to cleanly duplicate the synthesis of this material and check the absorption spectrum for J-band or CT features were nevertheless unsuccessful. Additionally, a calcium MOF with NDI ligands was reported to have features in the visible region; these were attributed to intermolecular CT.[222]

The assignment of the new band in **1** to a CT interaction may have implications for prior reports of J-aggregation in NDIs that are also characterized by broad tailing bands rather than sharp transitions. Intriguingly, some of these reported NDI-based J-aggregates have side chains containing potential donating groups[196] that may participate in CT interactions. Efforts to design supramolecular J-aggregates in MOFs or other assemblies should be carried out with careful consideration of other potential interactions including CT, and this study underscores the importance of analyzing the extended structure for interpreting photophysical data. In the case of **1**, framework interpenetration resulted in well-aligned π-stacked donor/acceptor pairs. Whereas this structural motif did not lead to J-coupling, it could be used to facilitate energy transfer between π-stacked ligands in new MOFs. This report also highlights the utility of coupling synthetic design with computational studies, especially when targeting complex interchromophore interactions such as J-coupling in MOFs.

THIS PAGE INTENTIONALLY LEFT BLANK

Chapter 5

Reaction pathfinding

5.1   A simple method for generating approximate reaction paths:

The Harmonic Interpolating Path

Knowledge of reaction paths and transition states of a chemical reaction is important, since they can be used to calculate kinetic rate information and offer insight into the mechanism by which a reaction occurs.[223-228] Chemical reactions of particular interest in the field of OLEDs are believed to be activated by the energy released during the bimolecular recombination events responsible for the efficiency decrease at high driving power and have been found to result in structural defects that degrade the lifetime of the OLED structure.[29,65-68] But reaction path are hard to find, and the efficient identification of transition states and minimum energy paths (MEPs) on potential energy surfaces (PESs) is an active area of research, with a variety of pathfinding methods available.[226,229-235] The existing methods can be broken down into two main categories: transition state optimization and pathway optimization.[223] Transition state methods require prior knowledge of the reaction's transition state and then use that information to find paths to the reactant and product. For pathway
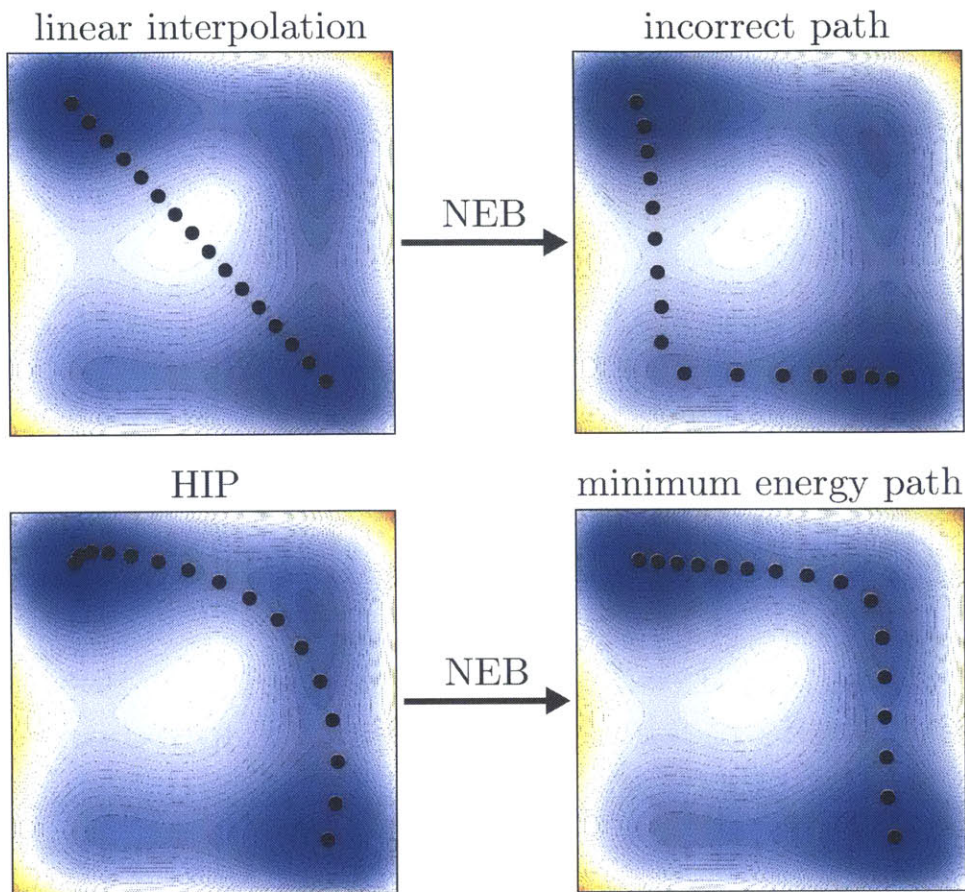
Figure 5.1: Results of running the Nudged Elastic Band (NEB) algorithm with two different initial guess paths. Linear interpolation between the reactant and product states leads to convergence to an incorrect reaction path that transverses a higher-energy reaction barrier, while a Harmonic Interpolated Path (HIP) leads to convergence to the minimum energy path that traverses the lower energy reaction barrier.

optimization, however, no prior knowledge of the transition state is assumed. While some single-minimum methods—those that require knowledge of only the reactant *or* product configuration—exist, two-minima methods are most commonly used.[236–238] Specifically, chain-of-states methods are perhaps the most efficient and widely used today.[226,227,229,239–248]

In chain-of-states methods, a chain of system configurations is generated between the reactant and product by selecting a number of states along an initial guess path. The intermediate states are are then iteratively relaxed until convergence to a lower-energy path. The nudged elastic band (NEB) method is an example of a chain-of-states

method and has been shown to be effective for finding transition states.[239-243,245,249,250] In the NEB method, some initially specified states are are connected by springs. Each of the states are then "nudged" by the force tangent to the path in order to relax the path until convergence.

Chain-of-states methods typically require some guess path. For example, a linear interpolation path (or some modified form of one) between reactant and product is often used.[229,243-245,247,249,251-253] But with a poor guess path, there is no guarantee that the right reaction path will be found (see Fig. 5.1). In particular, it is widely acknowledged that the energy landscape for transition paths is very rough,[227,235,254,255] so that global optimization is impossible.[256] Is it possible to propose good approximate reaction paths based solely on knowledge of information about the reactant and product? Such a path might be useful as an initial guess for a more sophisticated calculation, increasing the chances of converging to the correct reaction path and decreasing the number of cycles to convergence. Furthermore, in some cases, it might be enough to have a qualitative idea of possible ways the reaction could progress, so that an approximate path might be sufficient.

In this work, we develop a method for generating an initial guess path, which we refer to as a Harmonic Interpolated Path (HIP). We first introduce the properties of a HIP and then apply the method to four test systems: two analytical, 2-dimensional PESs and two multi-particle cluster rearrangements. In all cases, the optimal HIP proves to be better than linear interpolation, in some cases even semi-qualitatively matching the MEP, supporting the idea that such a path may be useful in obtaining both qualitative insight into a reaction mechanism and a superior initial guess for subsequent use in more sophisticated solvers.

5.1.1   Theory

Before introducing the HIP, it is instructive to first discuss some properties of the MEP. The MEP is series of system configurations $\{q^\star(s)\}$ whose energies $V(q^\star)$ lie

on a PES $V([x_1, \ldots, x_n])$, where $x_1, \ldots, x_n$ represent the independent variables of the system. Here, s represents a progress variable ranging from zero to one, and since MEP begins at the reactant configuration $\mathbf{q_r}$ and ends at the product configuration $\mathbf{q_p}$, we know that $\mathbf{q^\star}(0) = \mathbf{q_r}$ and $\mathbf{q^\star}(1) = \mathbf{q_p}$. Additionally, since the MEP follows the path of steepest decent between transition states, the derivative of the MEP $d\mathbf{q^\star}/ds$ is (by definition) parallel to the gradient of the PES ∇V for all points between the reactant and product. Additionally, a particular useful property of the MEP is highlighted by the following theorem.

Theorem 1. *If a step $\boldsymbol{\delta}\mathbf{q}$ is taken from a local minimum $\mathbf{q_0}$ of a potential V along one of the eigenvectors $\boldsymbol{\psi}^{(i)}$ of the Hessian $\nabla^2 V\big|_{\mathbf{q_0}}$, then the gradient ∇V is parallel to $\boldsymbol{\delta}\mathbf{q}$.*

Proof. Consider an infinitesimal step $\boldsymbol{\delta}\mathbf{q}$ from $\mathbf{q_0}$ along the ith eigenvector: $\boldsymbol{\delta}\mathbf{q} = \epsilon\boldsymbol{\psi}^{(i)}$. Expanding the gradient to first order in $\boldsymbol{\delta}\mathbf{q}$ about $\mathbf{q_0}$, we have

$$\begin{aligned}
\nabla V\big|_{\mathbf{q_0}+\boldsymbol{\delta}\mathbf{q}} &= \nabla V\big|_{\mathbf{q_0}} + \nabla^2 V\big|_{\mathbf{q_0}}\boldsymbol{\delta}\mathbf{q} = \epsilon\nabla^2 V\big|_{\mathbf{q_0}}\boldsymbol{\psi}^{(i)} \\
&= \lambda_i\epsilon\boldsymbol{\psi}^{(i)} = \lambda_i\boldsymbol{\delta}\mathbf{q}.
\end{aligned}$$

Therefore, $\nabla V\big|_{\mathbf{q_0}+\boldsymbol{\delta}\mathbf{q}}$ is simply a multiple of $\boldsymbol{\psi}^{(i)}$. $\qquad\square$

Theorem 1 allows us to make the HIP, which we denote $\mathbf{q}(s)$, follow the gradient at the reactant and product by forcing it to leave the reactant following an eigenvector of the reactant Hessian $\boldsymbol{\psi}_{\mathbf{r}}^{(i)}$ and end at the product following an eigenvector of the product Hessian $\boldsymbol{\psi}_{\mathbf{p}}^{(j)}$ This is useful, because the reactant and product are typically trivial to locate, as compared to a transition state or other point along the path, which can be very tricky to optimize. The hope is that by retaining some of the local gradient and Hessian information at the reactant and product, a HIP may be a good first-order approximation to the MEP. It is these Hessian-eigenvector-following conditions that lead to the "Harmonic" part of "Harmonic Interpolating Path."

Summarizing the properties of a HIP, we have four conditions:

Starts at reactant configuration

$$\mathbf{q}(s = 0) = \mathbf{q}_\mathrm{r},$$

Ends at product configuration

$$\mathbf{q}(s = 1) = \mathbf{q}_\mathrm{p},$$

Begins parallel to a Hessian e.vector at reactant

$$\left.\frac{d\mathbf{q}}{ds}\right|_{s=0} = a\boldsymbol{\psi}_\mathrm{r}^{(i)},$$

Ends parallel to a Hessian e.vector at product

$$\left.\frac{d\mathbf{q}}{ds}\right|_{s=1} = a\boldsymbol{\psi}_\mathrm{p}^{(j)},$$

where a and b are arbitrary constants.

Finally, we consider the interpolation between $\mathbf{q}_\mathrm{r}$ and $\mathbf{q}_\mathrm{p}$. At a minimum, four vectors must be involved. Additionally, we need to assume some functional dependence on the path parameter s. For the the simplest model, it makes sense to use only the minimal number of vectors. Meanwhile, for the interpolation, we could choose from any number of interpolation schemes: polynomial, Gaussian, trigonometric, etc. If we use a trig expansion, we can construct a path that satisfies the above conditions as

$$
\begin{aligned}
\mathbf{q}(s) = {}& \frac{1}{2}\left(1 + \cos \pi s\right)\mathbf{q}_\mathrm{r} + \frac{1}{2}\left(1 - \cos \pi s\right)\mathbf{q}_\mathrm{p} \\
& + \left(\sin \pi s + \frac{1}{2}\sin 2\pi s\right)\frac{a\boldsymbol{\psi}_\mathrm{r}^{(i)}}{2\pi} \\
& + \left(\sin \pi s - \frac{1}{2}\sin 2\pi s\right)\frac{b\boldsymbol{\psi}_\mathrm{p}^{(j)}}{2\pi}. \quad (5.1)
\end{aligned}
$$

Eq. (5.1) obeys all four of our conditions, and the trigonometric basis functions ensure a smooth path between the reactant and product states. A HIP is constructed by selecting a pair of eigenvectors $\{\boldsymbol{\psi}_\mathrm{r}^{(i)}, \boldsymbol{\psi}_\mathrm{p}^{(j)}\}$ and optimizing the scalar parameters a and b as desired. The scalar parameters a and b essentially determine how long the path follows the eigenvectors, as will be demonstrated in the following section. We note that the requirement of knowing the eigenvectors of the Hessian is something of

a limitation. While many methods have accurate gradients (as are required for molecular dynamics) relatively few have analytic Hessians.[257-275] However, as Theorem 1 above shows, it is not possible to make a path locally follow the MEP without at least some knowledge of the Hessian eigenvectors. Thus, this difficulty is unavoidable. For very large systems it may be possible to compute the lowest few Hessian eigenvectors without explicitly calculating the entire Hessian.[276-282]

5.1.2   Computational strategy

To illustrate the strengths and weaknesses of HIPs, we present a few illustrative applications. We restrict our attention to relatively small systems so that that computing and scanning all $\{\psi_r^{(i)}, \psi_p^{(j)}\}$ is feasible. Our test systems also have analytical PESs, so we are able to optimize our HIPs by minimizing the path's reaction barrier (largest transition-state energy). Of course, other strategies for finding HIPs will be necessary for large, complicated systems, as will be discussed in the conclusion.

The process of finding the optimal HIP for each system is as follows. $1)$ Compute all reactant $\psi_r^{(i)}$ and product $\psi_p^{(i)}$ Hessian eigenvectors.; $2)$ for every pair of eigenvectors $\{\psi_r^{(i)}, \psi_p^{(j)}\}$, minimize the HIP's transition state energy $\max_{0 \le s \le 1} V(\mathbf{q}(s))$ using the parameters a and b of Eq. (5.1); $3)$ select the HIP with the lowest transition state energy; this is termed the "optimal HIP" and will be plotted as a dashed black line in each of the following figures. In the first two test systems, we will also plot a few suboptimal HIPs, in order to demonstrate the flexibility imparted by the parameters a and b and the impact of selecting different eigenvector pairs $\{\psi_r^{(i)}, \psi_p^{(j)}\}$ for the interpolation.

5.1.3 Applications

Müller-Brown potential energy surface

The Müller-Brown PES[17] is given by

$$V(x,y) = \sum_{i=0}^{3} A_i e^{a_i(x-x_i^0)^2 + b_i(x-x_i^0)(y-y_i^0) + c_i(y-y_i^0)^2}, \qquad (5.2)$$

where $A = [-200, -100, -170, 15]$; $a = [-1, -1, -6.5, 0.7]$; $b = [0, 0, 11, 0.6]$; $c = [-10, -10, -6.5, 0.7]$; $x^0 = [1, 0, -0.5, -1]$; and $y^0 = [0, 0.5, 1.5, 1]$.

This PES has been used extensively as a benchmark for previous path finding methods, because it provides a simple example of the stable intermediates and nonlinear reaction coordinates that appear in chemical reactions.[283-288]

Fig. 5.2 serves to demonstrate how choosing different entrance and exit vectors to follow leads to physically distinct reaction paths from each HIP. This is a good thing, as it means the method can obtain several candidates, and path(s) can then be selected by considering which are most chemically reasonable for an initial guess. For each $\{\psi_r^{(i)}, \psi_p^{(j)}\}$, we optimized a and b to give the lowest reaction barrier along each HIP. Since there are four sets of $\{\psi_r^{(i)}, \psi_p^{(j)}\}$, there are four HIPs. The optimal HIP—the one with the lowest reaction barrier—is plotted as a black, dashed line in Fig. 5.2. It interpolates using the eigenvectors $\{\psi_r^{(2)}, \psi_p^{(1)}\}$, as labeled in Fig. 5.2. Also plotted in Fig. 5.2 are the three other (suboptimal) HIPs that interpolate using one of the three remaining sets of eigenvectors.

The optimal HIP is qualitatively the right path, whereas the others, to varying degrees, are wrong. For a real chemical reaction, one would need some intuition (or a higher level refinement) to discard the lower quality HIPs, but the method provides at least one really good guess path for this complicated 2-dimensional potential. We note that the ability of the optimal HIP to nearly reproduce the MEP's transition state is likely an artifact of the low dimensionality of the problem. A HIP is formed by a two-parameter optimization of the path, so in two dimensions, it becomes possible to
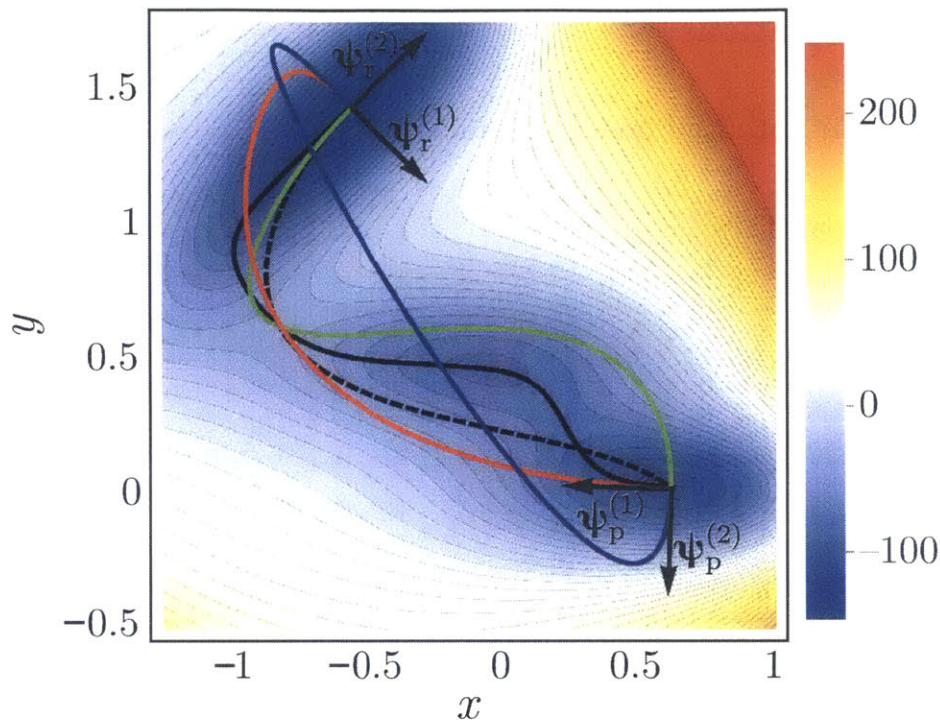
MEP $\quad \left\{ \psi_r^{(2)} \psi_p^{(1)} \right\} \quad \left\{ \psi_r^{(2)} \psi_p^{(2)} \right\} \quad \left\{ \psi_r^{(1)} \psi_p^{(2)} \right\} \quad \left\{ \psi_r^{(1)} \psi_p^{(1)} \right\}$

Figure 5.2: Four different HIPs, each using one of the four possible pairs of reactant and product Hessian eigenvectors $\{\psi_r^{(i)}, \psi_p^{(j)}\}$ on the Müller-Brown potential energy surface.[17] The minimum energy path is plotted in solid black, the optimal HIP is plotted in dashed black, and the arrows indicate the direction of the Hessian eigenvectors. The scalar a and b parameters of each of the four HIPs were determined by minimizing the path's reaction barrier. Choosing different sets of eigenvectors to follow leads to physically distinct reaction paths from each HIP, from which the most chemically reasonable path(s) can be selected for an initial guess.

force the "wrong" path to still go through the "right" transition state in some cases. In higher dimensions, such as those treated below, there will be a more clear distinction between the optimal and suboptimal HIPs. In this low-dimensionality example, however, it is easy to see that following the intuitive Hessian modes leads to the optimal HIP, while using chemically irrelevant modes leads to suboptimal HIPs.

Modified Wolfe-Quapp potential energy surface

We begin from the Wolfe-Quapp PES[18,289–291] and modify it slightly in order to demonstrate how performing NEB with a poor guess path can lead to convergence to a path drastically different from the MEP (see Fig. 5.1). To do so, we added two small exponential terms to the Wolfe-Quapp surface, which serve to shift the center peak such that a linearly-interpolated path is to the bottom-left of it. Our modified PES is plotted in Figures 5.1 and 5.3 and is given by

$$
\begin{aligned}
V(x,y) = x^4 + y^4 - 2x^2 - 4y^2 + xy + 0.3x + 0.1y \\
- 3.9e^{-\left((x-1.1)^2 + (y-0.28)^2\right)} \\
+ 1.61e^{-5\left((x-0.23)^2 + (y-0.49)^2\right)}. \quad (5.3)
\end{aligned}
$$

With Fig. 5.2 we demonstrate how the HIP varies when different sets of Hessian eigenvectors are scanned. In Fig. 5.3 we demonstrate how a HIP between a specific $\{\psi_r^{(i)}, \psi_p^{(j)}\}$ changes with the parameters, a and b. To construct Fig. 5.3, we found the optimal HIP using the process described in §5.1.3, and then we *manually varied* the scalar parameters a and b of this path in order to produce two suboptimal HIPs, one of which transverses the alternate and suboptimal set of transition states. The magnitude of a and b determine how long $\psi_r^{(i)}$ and $\psi_p^{(j)}$ are followed, while the signs determine which direction they are followed. In some cases, a HIP may follow an eigenvector for a very short length, as indicated by a small value of a or b. Note that for this low-degree-of-freedom system, the flexibility offered by the a and b parameters allows the HIP to search out different transition states on the PES, even without varying $\{\psi_r^{(i)}, \psi_p^{(j)}\}$.

The optimal HIP of Fig. 5.2 is the same HIP input used as input to the NEB method in Fig. 5.1. Due to the location of the center peak of the potential, the linearly interpolated path causes the NEB method to converge to the incorrect reaction path, which differs both qualitatively and quantitatively from the MEP. The optimal HIP,
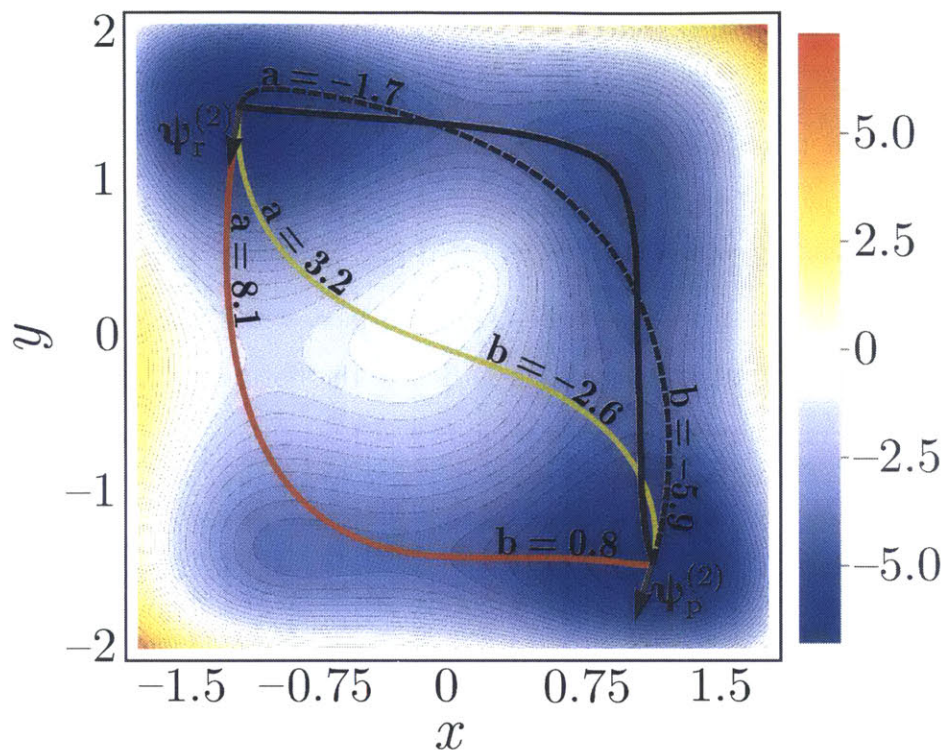
Figure 5.3: Three different HIPs on the modified Wolfe-Quapp potential energy surface[18] of Eq. (5.3). The optimal HIP was found by optimizing a and b to minimize the reaction barrier for all sets of Hessian eigenvectors, $\{\boldsymbol{\psi}_r^{(i)}, \boldsymbol{\psi}_p^{(j)}\}$. The suboptimal HIPs use the same $\{\boldsymbol{\psi}_r^{(2)}, \boldsymbol{\psi}_p^{(2)}\}$ as the optimal HIP, but they use different values of a and b. The magnitudes of a and b determine how long the eigenvectors are followed, while the signs determine which direction they are followed. The minimum energy path is plotted in solid black, and the arrows indicate the direction of the Hessian eigenvectors used for both HIPs. This figure demonstrates what happens during the optimization of the scalar HIP parameters a and b for a set of Hessian eigenvectors.

however, causes the NEB method to converge to the MEP, and as the optimal HIP is already qualitatively very similar to the MEP, the number of steps to convergence is reduced. Although they are not displayed in Fig. 5.2, the a- and b-optimized HIPs following the remaining three pairs of eigenvectors also transverse around the correct side of the center peak and will lead to correct convergence of the NEB. We note that not all the HIPs generated for more complex potentials will lead to correct NEB convergence, but performing NEB using the most chemically probable HIPs may
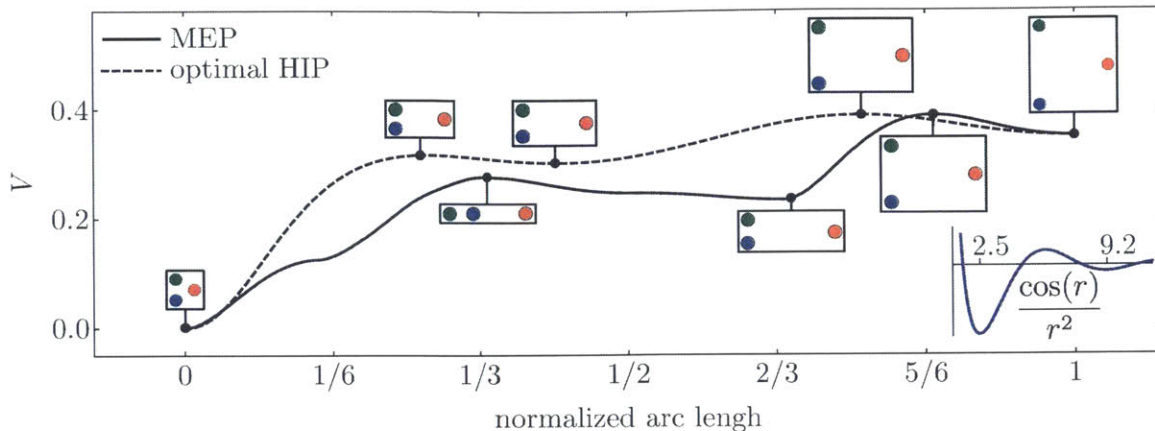
Figure 5.4: The optimal HIP for a three-particle expansion reaction, where pairwise $\cos r/r^2$ interactions (inset) define the potential, V, of Eq. (5.4). The potential-energy profiles of the optimal HIP and the MEP are plotted, and the particle positions along the paths are shown in the boxes. In this three-dimensional system, the optimal HIP still nearly reproduces the exact barrier height and also has a intermediate state.

prevent missing the MEP or, at the least, increase ones confidence in their reported results. This result is a clear demonstration of the benefit of a quality initial guess path.

Three-particle expansion reaction

In addition to the analytic 2-dimensional surfaces, we also tested the HIP method on two particle-rearrangement reactions. The first of these is a three-particle expansion reaction that mimics a trimer going from an energetically favorable double-bond-type configuration to a less favorable single-bond-type configuration. A simple $\cos r/r^2$ interaction potential defines the pairwise interactions between the three particles as they expand from $r = 2.5$ to $r = 9.2$:

$$V = \sum_{i<j} \frac{\cos\left(r_{ij}\right)}{r_{ij}^{2}}. \tag{5.4}$$

Fig. 5.4 compares the optimal HIP for this reaction to the MEP. This system has one greater degree of freedom than the two-dimensional test systems of §5.1.3 and §5.1.3, and yet the optimal HIP has a reaction barrier near that of the MEP and also recov-

163

ers an important quality of the MEP, namely the presence of two transition states. Comparing the particle motions along the optimal HIP to those of the MEP: the HIP fails to qualitatively reproduce the configuration resulting in the first transition state of the MEP, but it does quantitively reproduce the configuration of the second transition state. For this three-dimensional system, it is not too difficult to deduce the MEP mentally, so it serves as a bridge between the previous two-dimensional test systems, where the MEP can be discerned by visual inspection of the PES, and the following six-dimensional test system, where even a rather complicated human guess leads to a path quite different from the MEP.

Seven-particle Lennard-Jones cluster rearrangement

Our final test system consists of a seven-particle cluster with pairwise Lennard-Jones interactions in two dimensions, resulting in the potential

$$V = 4\varepsilon \sum_{i<j} \left[\left(\frac{\sigma}{r_{ij}} \right)^{12} - \left(\frac{\sigma}{r_{ij}} \right)^{6} \right], \tag{5.5}$$

where we set $\sigma = 2^{5/6}$ and $r_{ij} = \|\mathbf{r}_i - \mathbf{r}_j\|$.

In the rearrangement, the black, center particle moves to the outer ring and is replaced by the red, outer particle. Dellago et al. successfully applied their transition path sampling method to this cluster rearrangement and found three reaction paths, each with distinct particle trajectories and intermediate states.[19] Perhaps the most interesting thing about this reaction is that a linear path from the reactant to product state completely fails, since the two particles exchanging places will overlap, resulting in $r_{ij} = 0$. In addition, this cluster rearrangement is difficult to simulate with a conventional dynamics simulation at low temperatures, because very few transitions—inner particle moving the outside—occur within the limited time scales of computer simulations.[19] A human guess at the path is also rather difficult, because the collective motion of many particles at once makes this reaction difficult to understand and predict. A simple human guess path in which only the red and black particles rotate

164
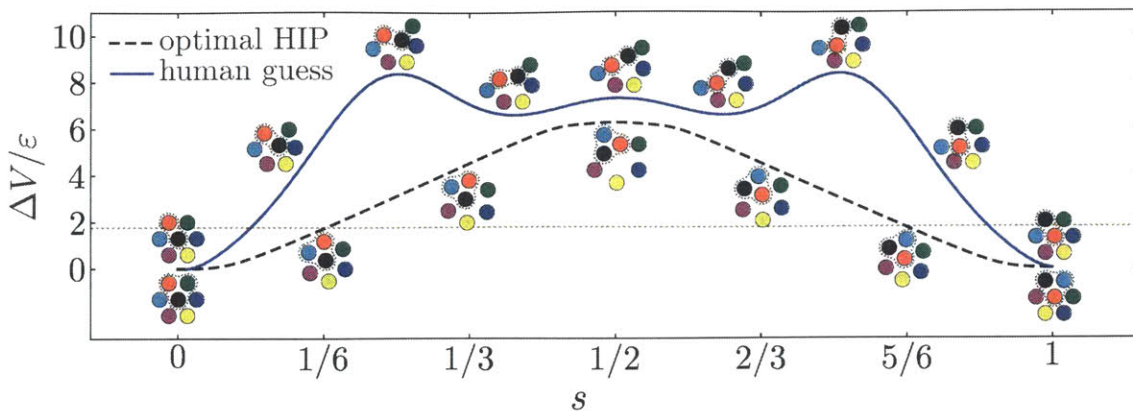
Figure 5.5: The optimal HIP for a seven-particle Lennard-Jones cluster rearrangement, where the system potential energy is given by Eq. (5.5). In the rearrangement, the black, center particle exchanges places with the red particle. The potential-energy profile of the optimal HIP is plotted, and the particle positions along the path are shown below the curve. The dotted lines around the particles are simply a guide to the eye. Standard linear interpolation between reactant and product states cannot be performed for this rearrangement (due to the r_{12}^{-1} in V), so we include a human guess path, in which only four of the seven particles are moved. The particle positions along this path are shown above the curve. While the HIP does not qualitatively reproduce the Transition Path Sampling result,[19] it is considerably better than a rather complicated human guess and has a barrier $\sim$4 units above the lowest known barrier.

about their center of mass results in a barrier of more than $3.4 \times 10^5 \varepsilon$ (not shown in Fig. 5.5). We came up with a fairly sophisticated human guess path, in which the red and black particles rotate about their center-of-mass as the green and cyan particles move outward to make room for the rotation (see Fig. 5.5), but even the barrier to this path is nearly 50% worse than the optimal HIP.

The potential-energy profile of the optimal HIP is plotted in Fig. 5.5, along with the particle positions over the progression of the rearrangement. Interestingly, we found that optimal HIPs with different reaction barriers and potential profiles are generated for the $6! = 720$ possible final arrangements of the outer particles. The major difference between the best optimal HIPs is the presence of a rotation of the system of particles. It is important to note, however, that the rotation of the system does not affect the potential energy. In fact, the outer particles are completely indistinguishable as far as potential energy is concerned. Instead, the 720 possible final arrangements of the outer particles result in changes to the product Hessian eigenvectors relative

to those of the reactant, which offers a further degree of freedom to the HIPs. In the event that a set of energy-equivalent reactant/product permutations exist, one must be aware that different permutations may result in different optimal HIPs.

While there was basically no need to refine the HIP in the previous sections, as it was qualitatively correct from the outset, here the HIP does not qualitatively reproduce the Transition Path Sampling result[19] and would need to be used as an initial guess for something more sophisticated. But having a reasonable initial guess is already an achievement here, especially in light of the impossibility of a linearly interpolated initial guess path, and the HIP's outperformance of even a rather complicated human-guess path shows its utility.

5.1.4 Discussion

In this work, we presented and tested a new type of initial guess path, named a HIP, and demonstrated its utility with four test systems. A HIP is a guess path based only on information about the reactant and product states. It interpolates between the two states by following eigenvectors of their Hessians, which ensures the gradient is followed in the immediate vicinity. The utility a HIP is two-fold: Commonly used chain-of-states methods require an initial guess for the reaction path but may fail to converge to the correct path if a poor initial guess is provided, making a method for a generating quality initial guess paths invaluable. In some cases, one may only be interested in obtaining qualitative reaction paths for insight into the possibles mechanisms through which a reaction could proceed. The HIP is provides a relatively straightforward way to achieve such paths using only local information of the reactant and product states.

Our results from application of our method to four test systems support the idea that a HIP may serve as a quality initial guess path. The optimal HIPs for three of the test systems had nearly identical reaction barriers to those of the MEPs, and sometimes the HIP reproduced other features of the MEPs. For the seven-particle

Lenard-Jones cluster rearrangement, the optimal HIP's reaction barrier wasn't great, and it did not qualitatively resemble the Transition Path Sampling result,[19] but it was considerably better than even a rather sophisticated human guess. The bottom line is that having another way to generate initial guess paths is a valuable tool for any path finding method, since it could help one locate the right reaction path in cases where a linear interpolated initial guess path leads to an incorrect one (as was the case in Fig. 5.1) or is unfeasible (as was the case in §5.1.3). In addition, a HIP may be useful even on its own as a qualitative measure of the barrier height or the possible reaction mechanisms.

We note that our test systems were of relatively low-dimensionality and had analytical potential energy surfaces, allowing us to find optimal HIPs by scanning all sets of Hessian eigenvectors and use the HIP's reaction barrier to optimize the scalar parameters, a and b. Of course, other strategies for finding HIPs will be necessary for the large, complicated real-world systems of chemical significance. For instance, the N^2 eigenvector pairs of a large system will make scanning all possible pairs prohibitive. In these cases, one expects that the MEP should typically follow only the low frequency modes near reactant and product, thus reducing the search space.[276-282,292] The validity of this assumption needs to be tested, but the results of §5.1.3 support this idea by illustrating how following the intuitive Hessian modes leads to the optimal HIP. Additionally, most systems of real-world interest will not have analytical PESs, so one would like to avoid the repeated evaluating of $V(\mathbf{q})$ that was used here to optimize a and b. Is it possible to use the Hessian information to approximate a and b? This could be performed, for instance, utilizing the quadratic or image gradient approximations developed by Ruedenberg and coworkers.[293,294] Or, could a lower level of theory be used to to approximate $V(\mathbf{q})$ during the optimization? This would significantly simplify the method. Finally, we note that only a handful of techniques have analytical Hessians.[257-275] For other methods, is it sufficient to use an approximate Hessian (say, from a lower level of theory) or to compute only a few eigenvectors of the Hessian?[292,295-302] Answering these questions will be the focus of future work and will enhance the practical application of the HIP to more chemically interesting

systems.

Chapter 6

Conclusions

As the need for clean energy and efficient energy consumption increases, OPVs and OLEDs offer a number of solutions to the energy landscape. In §2, we explored magnetic field effects as a tool for studying singlet-fission-based organic photovoltaics. In §2.1, we showed how MFEs can be used to quantify triplet yields and provide independent conformation of IQE evaluations. By determining the triplet yield of devices with different thicknesses of the singlet fission material, the minimum thickness required to prevent singlet exciton dissociation can be determined. Our observation of external quantum yields exceeding 100% in the visible spectrum represents a notable advance in the application of singlet fission to solar cells. We found that the slow rate of singlet exciton fission in tetracene lowers its triplet yield within a 20 nm radius of a C_{60} interface. Pentacene exhibits faster exciton fission and higher yields at similar distances (singlet dissociation lossless nearly eliminated beyond 15 nm radius of C_{60}),[7] highlighting the importance of designing exothermic rather than endothermic fission materials.

Singlet fission sensitizers require a support from a conventional sensitizer that absorbs the photons with $E(T_1) \leq E \leq E(S_1)$, because the dark T_1 state will not absorb energy above $E(T_1)$. In §2.2, we explored two approaches to integrating this conventional sensitizer into a PV structure. Magnetic field effects allowed us to de-

169

termine if the triplets produced from fission are contributing to the photocurrent, providing a simple method to evaluate various device compositions and architectures. The photocurrent of a device that benefits from the triplet products will be proportional to the rate of fission, while the photocurrent of a device that doesn't benefit from the triplet products will be inversely proportional to the rate of fission. These proportionalities are directly probed by the magnetic field effect on the fission rate. We found that interfaces with the archetype small molecular weight acceptor C_{60} are sensitive to small changes in the donor and acceptor energy levels. We also showed the possibility to overcome the typically poor optical absorption of singlet fission materials by utilizing energy transfer from a good light absorber to singlet fission sensitizers.[110]

In §2.3 we identified an important and characteristic loss mechanism in singlet-fission-based solar cells: triplet-charge annihilation (TCA). Triplet-charge annihilation is the process of destroying a triplet exciton during its interaction with a charge. Through measurements of various pentacene singlet fission photovoltaic devices and modeling based on a steady-state kinetic scheme, we found that nanostructured layers enhance triplet-charge interactions by confining the triplet and the charge to a small volume. This becomes additionally important in singlet-fission-based devices, because singlet fission forms two triplets in close proximity to each other and potentially near the donor-acceptor interface. We concluded that obtaining a benefit from singlet fission is especially difficult in fine-grained BHJ photovoltaics, but TCA can be decreased through device engineering, as was observed for both bilayer solar cells and optimized nanostructured photovoltaic cells with improved phase separation and percolation pathways for charge extraction.

In the future, singlet fission materials such as tetracene or rubrene could be integrated with silicon cells to double the photocurrent from high-energy solar photons ($\lambda < 550$ nm), ultimately boosting the efficiency of the silicon cell to more than 30%.[303]

As a crucial transitional excited state in nanostructured optoelectronic devices, charge transfer (CT) states mediate both light emission in organic light emitting devices1

and charge generation in organic photovoltaics.[107,152,167]. In §3.2, applying a magnetic field to decrease the conversion of singlet CT states to triplet CT states allowed us to identify the spin of the CT states responsible for the efficient generation of photocurrent. We fond that when a triplet drain is present, singlet CT states are responsible for the efficient generation of photocurrent, but in the absence of a triplet drain, photocurrent is more efficiently generated from the triplet CT states. Future organic solar cell designs should focus on raising the energy of triplet excitons to better utilize triplet charge transfer mediated photocurrent generation or increasing the donor-acceptor spacing to minimize recombination losses.

In an addition study of CT states in OPVs, we used direct imaging of blends of m-MTDATA:3TPYMB coupled with magnetic field studies in §3.3 demonstrated the presence of tightly bound CT states that diffuse 5–10 nm before settling into lower energy CT states. Since donor-acceptor blends typically exhibit rapid conversion from excitons to CT states, it is possible that CT state diffusion distances in many organic devices exceed that of the initial exciton, highlighting the potential importance and impact of CT state transport on device performance.

In §3.1 we demonstrated that the electron-hole pair separation in an exciplex blend of m-MTDATA:3TPYMB is a dynamic variable, fluctuating on the 1 μs timescale and leading to complex time- and magnetic-field-dependent dynamics in the photoluminescence spectrum. Through theoretical modeling of the underlying dynamics, we were able to conclude that a significant portion of the delayed photoluminescence is due to an indirect mechanism in which the initially bound electron and hole separate beyond the exchange radius (~ 1 nm) before eventually rejoining one another and emitting light. Our results suggest that thinking about CT states as static objects is not appropriate. Rather they should be seen as dynamically evolving states in which the electron and hole independently can move between multiple molecules before recombining. The fact that the bond between electron and hole is apparently much weaker than previously assumed suggests that many of the design principles for inorganic LEDs could be useful in generating the next generation of OLED materi-

als.

We also used electronic structure methods to determine the nature of an unexpected red-shifted absorption band in a metal-organic framework (MOF) in §4.1. MOFs may one day serve as frameworks to improve energy transport and charge extraction in OPVs, so it is important to correctly identify underlying photophysics.

In addition, we developed the HIP, a novel method for generating approximate reaction paths in §5.1. Our results from application of our method to four test systems support the idea that a HIP may serve as a quality initial guess path for more advance algorithms or as a qualitative reaction path from which insight into the possible mechanisms through which a reaction could proceed. The HIP method could be used to investigate the reactions leading to degradation in OLEDs.[68]

Appendix A

Example input files for tuning LRC functionals and for CDFT-CI

Example Input File — Neutral Sample, Qchem format

```
$rem
EXCHANGE          gen
LRC_DFT           true
OMEGA             **n** [omega=n/1000/bohr; sugstd. range: 50-375]
BASIS             6-31G
MEM_TOTAL        8000
MEM_STATIC       2000
SYMMETRY          false
SYM_IGNORE        true
INCDFT            false
MAX_SCF_CYCLES   150
UNRESTRICTED      true
$end


$xc_functional
```

```
        C       PBE       1.00
        X       wPBE      **(1-C_HF)**
        X       HF        **C_HF**
$end


$molecule
0  1
C          -7.094846     0.501463    -0.983261
H          -7.683371     0.918014    -1.798475
C          -5.701571     0.528436    -1.046879
H          -5.190406     0.963806    -1.898302
C          -4.988684    -0.009588     0.020957
C          -5.685285    -0.551322     1.097716
H          -5.161040    -0.983570     1.942820
C          -7.079314    -0.531592     1.051985
H          -7.655256    -0.951177     1.874610
C          -2.895889     1.250407     0.069619
C          -1.409281     1.229090     0.069133
C          -0.712306    -0.001300     0.003223
C          -1.405263    -1.234121    -0.060007
C          -2.891734    -1.260672    -0.053439
C          -0.700987    -2.426083    -0.127406
H          -1.255600    -3.357010    -0.177364
C           0.706205    -2.423641    -0.129725
H           1.263905    -3.352633    -0.181286
C           1.406491    -1.229162    -0.065047
C           0.709403     0.001148     0.000449
C           1.402474     1.233875     0.063547
C           0.698292     2.425905     0.130909
H           1.252958     3.356806     0.180691
```

```
C        -0.708896     2.423507     0.133584

H        -1.266545     3.352517     0.185410

C         2.888959     1.260494     0.057037

C         2.893126    -1.250617    -0.064115

C         4.986170     0.008744    -0.007236

C         5.694055    -0.545855     1.055574

H         5.178939    -0.993889     1.897964

C         7.087563    -0.518832     0.998690

H         7.672040    -0.948242     1.810148

C         7.081829     0.544672    -1.020793

H         7.661676     0.976357    -1.834365

C         5.688060     0.566161    -1.072591

H         5.168121     1.012245    -1.913060

N        -7.785660    -0.016829     0.038808

N        -3.543261    -0.006378     0.013004

N         3.540908     0.006073    -0.005046

N         7.783385     0.014238    -0.012337

O        -3.535186     2.285820     0.119891

O        -3.527876    -2.297904    -0.104842

O         3.524618     2.297965     0.109799

O         3.532126    -2.286173    -0.114100

$end
```

Example Input File — Neutral Sample, Qchem format

```
$rem

EXCHANGE        gen

LRC_DFT         true

OMEGA           **n** [omega=n/1000/bohr; sugstd. range: 50-375]

BASIS           6-31G
```

```
MEM_TOTAL         8000

MEM_STATIC        2000

SYMMETRY          false

SYM_IGNORE        true

INCDFT            false

MAX_SCF_CYCLES    150

UNRESTRICTED      true

$end


$xc_functional

        C       PBE       1.00

        X       wPBE      **(1-C_HF)**

        X       HF        **C_HF**

$end


$molecule

1 2

C          -7.094846      0.501463     -0.983261

H          -7.683371      0.918014     -1.798475

C          -5.701571      0.528436     -1.046879

H          -5.190406      0.963806     -1.898302

C          -4.988684     -0.009588      0.020957

C          -5.685285     -0.551322      1.097716

H          -5.161040     -0.983570      1.942820

C          -7.079314     -0.531592      1.051985

H          -7.655256     -0.951177      1.874610

C          -2.895889      1.250407      0.069619

C          -1.409281      1.229090      0.069133

C          -0.712306     -0.001300      0.003223

C          -1.405263     -1.234121     -0.060007
```

C	-2.891734	-1.260672	-0.053439
C	-0.700987	-2.426083	-0.127406
H	-1.255600	-3.357010	-0.177364
C	0.706205	-2.423641	-0.129725
H	1.263905	-3.352633	-0.181286
C	1.406491	-1.229162	-0.065047
C	0.709403	0.001148	0.000449
C	1.402474	1.233875	0.063547
C	0.698292	2.425905	0.130909
H	1.252958	3.356806	0.180691
C	-0.708896	2.423507	0.133584
H	-1.266545	3.352517	0.185410
C	2.888959	1.260494	0.057037
C	2.893126	-1.250617	-0.064115
C	4.986170	0.008744	-0.007236
C	5.694055	-0.545855	1.055574
H	5.178939	-0.993889	1.897964
C	7.087563	-0.518832	0.998690
H	7.672040	-0.948242	1.810148
C	7.081829	0.544672	-1.020793
H	7.661676	0.976357	-1.834365
C	5.688060	0.566161	-1.072591
H	5.168121	1.012245	-1.913060
N	-7.785660	-0.016829	0.038808
N	-3.543261	-0.006378	0.013004
N	3.540908	0.006073	-0.005046
N	7.783385	0.014238	-0.012337
O	-3.535186	2.285820	0.119891
O	-3.527876	-2.297904	-0.104842
O	3.524618	2.297965	0.109799

```
O               3.532126    -2.286173   -0.114100
$end
```

Example Input File — Anion Sample, Qchem format

```
$rem
EXCHANGE            gen
LRC_DFT            true
OMEGA              **n** [omega=n/1000/bohr; sugstd. range: 50-375]
BASIS              6-31G
MEM_TOTAL          8000
MEM_STATIC         2000
SYMMETRY           false
SYM_IGNORE         true
INCDFT             false
MAX_SCF_CYCLES     150
UNRESTRICTED       true
$end


$xc_functional
        C       PBE      1.00
        X       wPBE     **(1-C_HF)**
        X       HF       **C_HF**
$end


$molecule
-1 2
C           -7.094846    0.501463   -0.983261
H           -7.683371    0.918014   -1.798475
C           -5.701571    0.528436   -1.046879
```

H	-5.190406	0.963806	-1.898302
C	-4.988684	-0.009588	0.020957
C	-5.685285	-0.551322	1.097716
H	-5.161040	-0.983570	1.942820
C	-7.079314	-0.531592	1.051985
H	-7.655256	-0.951177	1.874610
C	-2.895889	1.250407	0.069619
C	-1.409281	1.229090	0.069133
C	-0.712306	-0.001300	0.003223
C	-1.405263	-1.234121	-0.060007
C	-2.891734	-1.260672	-0.053439
C	-0.700987	-2.426083	-0.127406
H	-1.255600	-3.357010	-0.177364
C	0.706205	-2.423641	-0.129725
H	1.263905	-3.352633	-0.181286
C	1.406491	-1.229162	-0.065047
C	0.709403	0.001148	0.000449
C	1.402474	1.233875	0.063547
C	0.698292	2.425905	0.130909
H	1.252958	3.356806	0.180691
C	-0.708896	2.423507	0.133584
H	-1.266545	3.352517	0.185410
C	2.888959	1.260494	0.057037
C	2.893126	-1.250617	-0.064115
C	4.986170	0.008744	-0.007236
C	5.694055	-0.545855	1.055574
H	5.178939	-0.993889	1.897964
C	7.087563	-0.518832	0.998690
H	7.672040	-0.948242	1.810148
C	7.081829	0.544672	-1.020793

```
H              7.661676      0.976357     -1.834365

C              5.688060      0.566161     -1.072591

H              5.168121      1.012245     -1.913060

N             -7.785660     -0.016829      0.038808

N             -3.543261     -0.006378      0.013004

N              3.540908      0.006073     -0.005046

N              7.783385      0.014238     -0.012337

O             -3.535186      2.285820      0.119891

O             -3.527876     -2.297904     -0.104842

O              3.524618      2.297965      0.109799

O              3.532126     -2.286173     -0.114100

$end
```

Example Input File — CDFT-CI calculation, Qchem format

```
$rem
jobtype              sp
basis                cc-PVDZ
exchange             gen
lrc_dft              true
omega                125
symmetry             off
mem_total         8000
mem_static        2000
unrestricted         true
cdftci               true
cdftci_skip_promolecules        true
cdftci_print                    1
$end
```

```
$xc_functional
        C       PBE        1.00
        X       wPBE       **(1-C_HF)**
        X       HF         **C_HF**
$end


$cdft
1.0
1.0 1  44
1.0
1.0 1  44  s
-----------
0.0
0.0  1  44
0.0
0.0  1  44  s
$end


$molecule
0  1
C          -7.094846     0.501463    -0.983261
H          -7.683371     0.918014    -1.798475
C          -5.701571     0.528436    -1.046879
H          -5.190406     0.963806    -1.898302
C          -4.988684    -0.009588     0.020957
C          -5.685285    -0.551322     1.097716
H          -5.161040    -0.983570     1.942820
C          -7.079314    -0.531592     1.051985
H          -7.655256    -0.951177     1.874610
C          -2.895889     1.250407     0.069619
```

C	-1.409281	1.229090	0.069133
C	-0.712306	-0.001300	0.003223
C	-1.405263	-1.234121	-0.060007
C	-2.891734	-1.260672	-0.053439
C	-0.700987	-2.426083	-0.127406
H	-1.255600	-3.357010	-0.177364
C	0.706205	-2.423641	-0.129725
H	1.263905	-3.352633	-0.181286
C	1.406491	-1.229162	-0.065047
C	0.709403	0.001148	0.000449
C	1.402474	1.233875	0.063547
C	0.698292	2.425905	0.130909
H	1.252958	3.356806	0.180691
C	-0.708896	2.423507	0.133584
H	-1.266545	3.352517	0.185410
C	2.888959	1.260494	0.057037
C	2.893126	-1.250617	-0.064115
C	4.986170	0.008744	-0.007236
C	5.694055	-0.545855	1.055574
H	5.178939	-0.993889	1.897964
C	7.087563	-0.518832	0.998690
H	7.672040	-0.948242	1.810148
C	7.081829	0.544672	-1.020793
H	7.661676	0.976357	-1.834365
C	5.688060	0.566161	-1.072591
H	5.168121	1.012245	-1.913060
N	-7.785660	-0.016829	0.038808
N	-3.543261	-0.006378	0.013004
N	3.540908	0.006073	-0.005046
N	7.783385	0.014238	-0.012337

```
O           -3.535186     2.285820     0.119891
O           -3.527876    -2.297904    -0.104842
O            3.524618     2.297965     0.109799
O            3.532126    -2.286173    -0.114100
$end
```

THIS PAGE INTENTIONALLY LEFT BLANK

Bibliography

[1] Priya J Jadhav, Patrick R Brown, Nicholas Thompson, Benjamin Wunsch, Aseema Mohanty, Shane R Yost, Eric Hontz, Troy Van Voorhis, Moungi G Bawendi, Vladimir Bulovä, and Marc A Baldo. Triplet exciton dissociation in singlet exciton fission photovoltaics. *Adv. Mater.*, 24(46):6169–6174, December 2012. ISSN 09359648. doi: 10.1002/adma.201202397. URL http://www.ncbi.nlm.nih.gov/pubmed/22968762.

[2] S Yoo, B Domercq, and B Kippelen. Efficient thin-film organic solar cells based on pentacene/C60 heterojunctions. *Appl. Phys. Lett.*, 85(22):5427–5429, 2004. ISSN 0003-6951. doi: 10.1063/1.1829777.

[3] Ze-Lei Guan, Jong-Bok Kim, He Wang, Cherno Jaye, Daniel A Fischer, Yueh-Lin Loo, and Antoine. Kahn. Direct determination of the electronic structure of the poly(3-hexylthiophene):phenyl-[6,6]-C61 butyric acid methyl ester blend. *Org. Electron.*, 11(11):1779–1785, 2010. ISSN 1566-1199. doi: 10.1016/j.orgel.2010.07.023.

[4] Naoki Sato, Yahachi Saito, and Hisanori. Shinohara. Threshold ionization energy of fullerene C60 in the solid state. *Chem. Phys.*, 162(2-3):433–438, 1992. ISSN 0301-0104. doi: 10.1016/0301-0104(92)85020-U.

[5] Antoine Kahn, Norbert Koch, and Weiying. Gao. Electronic structure and electrical properties of interfaces between metals and π-conjugated molecular films. *J. Polym. Sci. Part B Polym. Phys.*, 41(21):2529–2548, 2003. ISSN 0887-6266. doi: 10.1002/polb.10642.

[6] Jaehyung Hwang, Alan Wan, and Antoine Kahn. Energetics of metalâĂŞorganic interfaces: New experiments and assessment of the field. *Mater. Sci. Eng. R Reports*, 64(1-2):1–31, March 2009. ISSN 0927796X. doi: 10.1016/j.mser. 2008.12.001. URL `http://www.sciencedirect.com/science/article/pii/S0927796X08001228`.

[7] Daniel N Congreve, Jiye Lee, Nicholas J Thompson, Eric Hontz, Shane R Yost, Philip D Reusswig, Matthias E Bahlke, Sebastian Reineke, Troy Van Voorhis, and Marc A Baldo. External quantum efficiency above 100% in a singlet-exciton-fission-based organic photovoltaic cell. *Science*, 340(6130):334–7, 2013. ISSN 1095-9203. doi: 10.1126/science. 1232994. URL `http://www.ncbi.nlm.nih.gov/pubmed/23599489http://www.sciencemag.org/content/340/6130/334.long`.

[8] Shane R Yost, Jiye Lee, Mark W B Wilson, Tony Wu, David P McMahon, Rebecca R Parkhurst, Nicholas J Thompson, Daniel N Congreve, Akshay Rao, Kerr Johnson, Matthew Y Sfeir, Moungi G Bawendi, Timothy M Swager, Richard H Friend, Marc A Baldo, and Troy. Van Voorhis. A transferable model for singlet-fission kinetics. *Nat. Chem.*, 6(6):492–7, 2014. ISSN 1755-4349. doi: 10.1038/nchem.1945. URL `http://www.ncbi.nlm.nih.gov/pubmed/24848234`.

[9] Brooks A Jones, Antonio Facchetti, Michael R Wasielewski, and Tobin J Marks. Tuning Orbital Energetics in Arylene Diimide Semiconductors. Materials Design for Ambient Stability of n-Type Charge Transport. *J. Am. Chem. Soc.*, 129(49): 15259–15278, 2007. ISSN 0002-7863. doi: 10.1021/ja075242e.

[10] L C Picciolo, H Murata, and Z H Kafafi. Organic light-emitting devices with saturated red emission using 6,13-diphenylpentacene. *Appl. Phys. Lett.*, 78(16): 2378–2380, 2001. ISSN 0003-6951. doi: 10.1063/1.1362259.

[11] Olga Lobanova Griffith, John E Anthony, Adolphus G Jones, and Dennis L Lichtenberger. Electronic properties of pentacene versus

triisopropylsilylethynyl-substituted pentacene: environment-dependent effects of the silyl substituent. *J. Am. Chem. Soc.*, 132(2):580–6, January 2010. ISSN 1520-5126. doi: 10.1021/ja906917r. URL http://dx.doi.org/10.1021/ja906917r.

[12] J H Weaver. Electronic structures of C60 and C70 fullerenes and the fullerides: photoemission and inverse photoemission studies. *J. Phys. Chem. Solids*, 53 (11):1433–1447, 1992. ISSN 0022-3697. doi: 10.1016/0022-3697(92)90237-8.

[13] Jacek Jasieniak, Marco Califano, and Scott E Watkins. Size-dependent valence and conduction band-edge energies of semiconductor nanocrystals. *ACS Nano*, 5(7):5888–5902, 2011. ISSN 1936-0851. doi: 10.1021/nn201681s.

[14] Joshua J Choi, Yee-Fun Lim, Mitk'El B Santiago-Berrios, Matthew Oh, Byung-Ryool Hyun, Liangfeng Sun, Adam C Bartnik, Augusta Goedhart, George G Malliaras, Hector D Abruna, Frank W Wise, and Tobias. Hanrath. PbSe Nanocrystal Excitonic Solar Cells. *Nano Lett.*, 9(11):3749–3755, 2009. ISSN 1530-6984. doi: 10.1021/nl901930g.

[15] Hakan Usta, Antonio Facchetti, and Tobin J Marks. n-Channel Semiconductor Materials Design for Organic Complementary Circuits. *Acc. Chem. Res.*, 44(7): 501–510, 2011. ISSN 0001-4842. doi: 10.1021/ar200006r.

[16] P D Reusswig, D N Congreve, N J Thompson, and M A Baldo. Enhanced external quantum efficiency in an organic photovoltaic cell via singlet fission exciton sensitizer. *Appl. Phys. Lett.*, 101(11):113304/1–113304/4, 2012. ISSN 0003-6951. doi: 10.1063/1.4752445.

[17] Klaus Müller and Leo D Brown. Location of saddle points and minimum energy paths by a constrained simplex optimization procedure. *Theor. Chim. Acta*, 53(1):75–93, 1979. ISSN 0040-5744. doi: 10.1007/BF00547608. URL http://link.springer.com/10.1007/BF00547608.

[18] Wolfgang Quapp. A growing string method for the reaction pathway defined by a Newton trajectory. *J. Chem. Phys.*, 122(17):174106, May 2005. ISSN 0021-9606. doi: 10.1063/1.1885467. URL `http://www.ncbi.nlm.nih.gov/pubmed/15910022`.

[19] Christoph Dellago, Peter G. Bolhuis, and David Chandler. Efficient transition path sampling: Application to Lennard-Jones cluster rearrangements. *J. Chem. Phys.*, 108(22):9236, 1998. ISSN 00219606. doi: 10.1063/1.476378. URL `http://link.aip.org/link/JCPSA6/v108/i22/p9236/s1&Agg=doihttp://scitation.aip.org/content/aip/journal/jcp/108/22/10.1063/1.476378`.

[20] Energy Information Administration. Annual Energy Outlook. Technical report, US Dept. of Energy, Washington, 2014. URL `http://www.eia.gov/forecasts/aeo/er/pdf/0383er(2012).pdf`.

[21] Ronald Lee. The outlook for population growth. *Science*, 333(6042):569–573, July 2011. ISSN 0036-8075. doi: 10.1126/science.1208859. URL `http://www.sciencemag.org/content/333/6042/569.full`.

[22] J. P. Holdren. PRESIDENTIAL ADDRESS: Science and Technology for Sustainable Well-Being. *Science*, 319(5862):424–434, January 2008. ISSN 0036-8075. doi: 10.1126/science.1153386. URL `http://www.sciencemag.org/content/319/5862/424.short`.

[23] John Meurig Thomas. Reflections on the topic of solar fuels. *Energy Environ. Sci.*, 7(1):19–20, December 2014. ISSN 1754-5692. doi: 10.1039/C3EE43197E. URL `http://pubs.rsc.org/en/Content/ArticleHTML/2014/EE/C3EE43197E`.

[24] Nathan S Lewis and Daniel G Nocera. Powering the planet: chemical challenges in solar energy utilization. *Proc. Natl. Acad. Sci. U. S. A.*, 103(43):15729–35, October 2006. ISSN 0027-8424. doi: 10.1073/pnas.0603395103. URL `http://www.pnas.org/content/103/43/15729.figures-only`.

[25] Oliver Morton. Solar energy: a new day dawning? Silicon Valley sunrise., 2006. ISSN 1476-4687.

[26] M Grätzel. Photoelectrochemical cells. *Nature*, 414(6861):338–344, 2001. ISSN 0028-0836. doi: 10.1038/35104607.

[27] Michael Grätzel. Photovoltaic and photoelectrochemical conversion of solar energy. *Philos. Trans. A. Math. Phys. Eng. Sci.*, 365(1853):993–1005, 2007. ISSN 1364-503X. doi: 10.1098/rsta.2006.1963.

[28] Kristen Ardani, Daniel Seif, Carolyn Davidson, Jesse Morris, Sarah Truitt, Roy Torbert, and Robert Margolis. Preliminary non-hardware ('soft') cost-reduction Roadmap for residential and small commercial solar photovoltaics, 2013-2020. Technical Report August, NREL, 2013.

[29] Committee on Assessment of Solid State Lighting, Board on Energy and Environmental Systems, and Division on Engineering and Physical Sciences. Assessment of Advanced Solid State Lighting. Technical report, National Research Council, Washington, DC, 2013.

[30] M. Knupfer. Exciton binding energies in organic semiconductors. *Appl. Phys. A Mater. Sci. Process.*, 77(5):623–626, 2003. ISSN 09478396. doi: 10.1007/s00339-003-2182-9.

[31] Martin Pope and Charles E Swenberg. *Electronic processes in organic crystals and polymers*, volume 74. Oxford University Press, New York and Oxford, 2 edition, 1999.

[32] Yuan-Chung Cheng and Graham R Fleming. Dynamics of light harvesting in photosynthesis. *Annu. Rev. Phys. Chem.*, 60:241–262, January 2009. ISSN 0066-426X. doi: 10.1146/annurev.physchem.040808.090259. URL http://www.annualreviews.org/doi/abs/10.1146/annurev.physchem.040808.090259.

[33] Shane Robert Yost. *Theoretical Investigations of the Electronic Processes in*

Organic Photovoltaics by. PhD thesis, Massachusetts Institute of Technology, 2013.

[34] NJ Turro. *Modern molecular photochemistry.* University Science Books, Mill Valley, CA, 1991. ISBN 0935702717.

[35] Shane R. Yost, Eric Hontz, Sina Yeganeh, and Troy Van Voorhis. Triplet vs singlet energy transfer in organic semiconductors: The tortoise and the hare. *J. Phys. Chem. C*, 116(33):17369–17377, August 2012. ISSN 19327447. doi: 10. 1021/jp304433t. URL http://pubs.acs.org/doi/abs/10.1021/jp304433t.

[36] Jiangeng Xue and Stephen R. Forrest. Carrier transport in multilayer organic photodetectors: II. Effects of anode preparation. *J. Appl. Phys.*, 95(4):1869–1877, 2004. ISSN 00218979. doi: 10.1063/1.1640454.

[37] Jiangeng Xue and Stephen R. Forrest. Carrier transport in multilayer organic photodetectors: I. Effects of layer structure on dark current and photoresponse. *J. Appl. Phys.*, 95(4):1859–1868, 2004. ISSN 00218979. doi: 10.1063/1.1640453.

[38] Caleb A Kent, Demin Liu, Liqing Ma, John M Papanikolas, Thomas J Meyer, and Wenbin. Lin. Light Harvesting in Microscale Metal-Organic Frameworks by Energy Migration and Interfacial Electron Transfer Quenching. *J. Am. Chem. Soc.*, 133(33):12940–12943, 2011. ISSN 0002-7863. doi: 10.1021/ja204214t.

[39] Zhigang Xie, Liqing Ma, Kathryn E de Krafft, Athena Jin, and Wenbin. Lin. Porous Phosphorescent Coordination Polymers for Oxygen Sensing. *J. Am. Chem. Soc.*, 132(3):922–923, 2010. ISSN 0002-7863. doi: 10.1021/ja909629f.

[40] Chang Yeon Lee, Omar K Farha, Bong Jin Hong, Amy A Sarjeant, Son Binh T Nguyen, and Joseph T Hupp. Light-Harvesting Metal-Organic Frameworks (MOFs): Efficient Strut-to-Strut Energy Transfer in Bodipy and Porphyrin-Based MOFs. *J. Am. Chem. Soc.*, 133(40):15858–15861, 2011. ISSN 0002-7863. doi: 10.1021/ja206029a.

[41] Yohei Takashima, Virginia Martínez Martínez, Shuhei Furukawa, Mio Kondo, Satoru Shimomura, Hiromitsu Uehara, Masashi Nakahama, Kunihisa Sugimoto, and Susumu Kitagawa. Molecular decoding using luminescence from an entangled porous framework. *Nat. Commun.*, 2:168, January 2011. ISSN 2041-1723. doi: 10.1038/ncomms1170. URL http://www.nature.com.libproxy.mit.edu/ncomms/journal/v2/n1/full/ncomms1170.html.

[42] John J Perry IV, Patrick L Feng, Scott T Meek, Kirsty Leong, F Patrick Doty, and Mark D Allendorf. Connecting structure with function in metal-organic frameworks to design novel photo- and radioluminescent materials. *J. Mater. Chem.*, 22(20):10235–10248, 2012. ISSN 0959-9428. doi: 10.1039/c2jm16627e.

[43] Patrick L Feng, Kirsty Leong, and Mark D Allendorf. Charge-transfer guest interactions in luminescent MOFs: implications for solid-state temperature and environmental sensing. *Dalt. Trans.*, 41(29):8869–8877, 2012. ISSN 1477-9226. doi: 10.1039/c2dt30649b.

[44] Natalia B Shustova, Brian D McCarthy, and Mircea. Dinca. Turn-On Fluorescence in Tetraphenylethylene-Based Metal-Organic Frameworks: An Alternative to Aggregation-Induced Emission. *J. Am. Chem. Soc.*, 133(50):20126–20129, 2011. ISSN 0002-7863. doi: 10.1021/ja209327q.

[45] Marcela M Wanderley, Cheng Wang, Chuan-De Wu, and Wenbin. Lin. A Chiral Porous Metal-Organic Framework for Highly Sensitive and Enantioselective Fluorescence Sensing of Amino Alcohols. *J. Am. Chem. Soc.*, 134(22):9050–9053, 2012. ISSN 0002-7863. doi: 10.1021/ja302110d.

[46] William Shockley and Hans J. Queisser. Detailed balance limit of efficiency of p-n junction solar cells. *J. Appl. Phys.*, 32(3):510–519, 1961. ISSN 00218979. doi: 10.1063/1.1736034. URL http://link.aip.org/link/JAPIAU/v32/i3/p510/s1&Agg=doi.

[47] Octavi E Semonin, Joseph M Luther, Sukgeun Choi, Hsiang-Yu Chen, Jianbo Gao, Arthur J Nozik, and Matthew C Beard. Peak External Photocurrent

Quantum Efficiency Exceeding 100% via MEG in a Quantum Dot Solar Cell. *Sci. (Washington, DC, United States)*, 334(6062):1530–1533, 2011. ISSN 0036-8075. doi: 10.1126/science.1209845.

[48] Millicent B. Smith and Josef. Michl. Singlet fission. *Chem. Rev.*, 110(11): 6891–6936, November 2010. ISSN 00092665. doi: 10.1021/cr1002613. URL http://www.ncbi.nlm.nih.gov/pubmed/21053979.

[49] J. Lee, P. Jadhav, and M. A. Baldo. High efficiency organic multilayer photodetectors based on singlet exciton fission. *Appl. Phys. Lett.*, 95 (3):033301, July 2009. ISSN 00036951. doi: 10.1063/1.3182787. URL http://link.aip.org/link/APPLAB/v95/i3/p033301/s1&Agg=doihttp:// scitation.aip.org/content/aip/journal/apl/95/3/10.1063/1.3182787.

[50] Mark W B Wilson, Akshay Rao, Jenny Clark, R. Sai Santosh Kumar, Daniele Brida, Giulio Cerullo, and Richard H. Friend. Ultrafast dynamics of exciton fission in polycrystalline pentacene. *J. Am. Chem. Soc.*, 133(31):11830–11833, August 2011. ISSN 00027863. doi: 10.1021/ja201688h. URL http://www. ncbi.nlm.nih.gov/pubmed/21755937.

[51] Justin C Johnson, Thomas H Reilly, Allison C Kanarr, and Jao. van de Lagemaat. The Ultrafast Photophysics of Pentacene Coupled to Surface Plasmon Active Nanohole Films. *J. Phys. Chem. C*, 113(16):6871–6877, 2009. ISSN 1932-7447. doi: 10.1021/jp901419s.

[52] C Jundt, G Klein, B Sipp, J Le Moigne, M Joucla, and A A Villaeys. Exciton dynamics in pentacene thin films studied by pump-probe spectroscopy. *Chem. Phys. Lett.*, 241(1,2):84–88, 1995. ISSN 0009-2614. doi: 10.1016/0009-2614(95) 00603-2.

[53] H Marciniak, M Fiebig, M Huth, S Schiefer, B Nickel, F Selmaier, and S Lochbrunner. Ultrafast exciton relaxation in microcrystalline pentacene films. *Phys. Rev. Lett.*, 99(17):176402, 2007. ISSN 0031-9007.

[54] V K Thorsmolle, R D Averitt, J Demsar, D L Smith, S Tretiak, R L Martin, X Chi, B K Crone, A P Ramirez, and A J Taylor. Morphology effectively controls singlet-triplet exciton relaxation and charge transport in organic semiconductors. *Phys. Rev. Lett.*, 102(1):17401, 2009. ISSN 0031-9007.

[55] W.-L. Chan, Manuel Ligges, Askat Jailaubekov, Loren Kaake, Luis Miaja-Avila, and X.-Y. Zhu. Observing the Multiexciton State in Singlet Fission and Ensuing Ultrafast Multielectron Transfer, December 2011. ISSN 0036-8075. URL http://www.ncbi.nlm.nih.gov/pubmed/22174249.

[56] Priya J Jadhav, Aseema Mohanty, Jason Sussman, Jiye Lee, and Marc A Baldo. Singlet exciton fission in nanostructured organic solar cells. *Nano Lett.*, 11 (4):1495–1498, April 2011. ISSN 15306984. doi: 10.1021/nl104202j. URL http://www.ncbi.nlm.nih.gov/pubmed/21355536.

[57] Bruno Ehrler, Mark W B Wilson, Akshay Rao, Richard H Friend, and Neil C Greenham. Singlet exciton fission-sensitized infrared quantum dot solar cells. *Nano Lett.*, 12(2):1053–1057, February 2012. ISSN 15306984. doi: 10.1021/nl204297u. URL http://www.ncbi.nlm.nih.gov/pubmed/22257168.

[58] Bruno Ehrler, Brian J. Walker, Marcus L Boehm, Mark W.B. B Wilson, Yana Vaynzof, Richard H. Friend, Neil C. Greenham, Marcus L. Böhm, Mark W.B. B Wilson, Yana Vaynzof, Richard H. Friend, and Neil C. Greenham. In situ measurement of exciton energy in hybrid singlet-fission solar cells. *Nat. Commun.*, 3(may):1019, August 2012. ISSN 2041-1723. doi: 10.1038/ncomms2012. URL http://www.nature.com/doifinder/10.1038/ncomms2012http://www.ncbi.nlm.nih.gov/pubmed/22910365.

[59] D L Dexter. Two ideas on energy transfer phenomena: ion-pair effects involving the hydroxyl group stretching mode, and sensitization of photovoltaic cells. *J. Lumin.*, 18-19(Pt. 2):779–784, 1979. ISSN 0022-2313. doi: 10.1016/0022-2313(79)90235-7.

[60] MC Hanna and AJ Nozik. Solar conversion efficiency of photovoltaic and pho-
toelectrolysis cells with carrier multiplication absorbers. *J. Appl. Phys.*, 100(7):
074510, 2006. ISSN 00218979. doi: 10.1063/1.2356795.

[61] Chihaya Adachi, Marc a. Baldo, Mark E. Thompson, and Stephen R. Forrest.
Nearly 100% internal phosphorescence efficiency in an organic light emitting
device. *J. Appl. Phys.*, 90(10):5048-5051, 2001. ISSN 00218979. doi: 10.1063/
1.1409582.

[62] M. a. Baldo, S. Lamansky, P. E. Burrows, M. E. Thompson, and S. R. For-
rest. Very high-efficiency green organic light-emitting devices based on elec-
trophosphorescence. *Appl. Phys. Lett.*, 75(1):4–6, 1999. ISSN 00036951. doi:
doi:10.1063/1.124258. URL http://apl.aip.org/resource/1/applab/v75/
i1/p4_s1.

[63] Simonas Krotkus, Fabian Ventsch, Daniel Kasemann, Alexander a. Zakhidov,
Simone Hofmann, Karl Leo, and Malte C. Gather. Photo-patterning of Highly
Efficient State-of-the-Art Phosphorescent OLEDs Using Orthogonal Hydrofluo-
roethers. *Adv. Opt. Mater.*, pages n/a–n/a, 2014. ISSN 21951071. doi: 10.1002/
adom.201400181. URL http://doi.wiley.com/10.1002/adom.201400181.

[64] Hartmut Yersin, Andreas F. Rausch, RafaÅĆ Czerwieniec, Thomas Hofbeck,
and Tobias Fischer. The triplet state of organo-transition metal compounds.
Triplet harvesting and singlet harvesting for efficient OLEDs, November 2011.
ISSN 00108545. URL http://linkinghub.elsevier.com/retrieve/pii/
S0010854511000403.

[65] N. C. Giebink and S. R. Forrest. Quantum efficiency roll-off at high brightness
in fluorescent and phosphorescent organic light emitting diodes. *Phys. Rev.
B - Condens. Matter Mater. Phys.*, 77(23):1–9, 2008. ISSN 10980121. doi:
10.1103/PhysRevB.77.235215.

[66] Sebastian Reineke and Marc a. Baldo. Recent progress in the understanding
of exciton dynamics within phosphorescent OLEDs. *Phys. Status Solidi*, 209

(12):2341–2353, December 2012. ISSN 18626300. doi: 10.1002/pssa.201228292. URL http://doi.wiley.com/10.1002/pssa.201228292.

[67] Daisaku Tanaka, Hisahiro Sasabe, Yan-Jun Li, Shi-Jian Su, Takashi Takeda, and Junji Kido. Ultra High Efficiency Green Organic Light-Emitting Devices. *Jpn. J. Appl. Phys.*, 46(1):L10–L12, 2006. ISSN 0021-4922. doi: 10.1143/JJAP. 46.L10.

[68] G. C. M. Silvestre, M. T. Johnson, A. Giraldo, and J. M. Shannon. Light degradation and voltage drift in polymer light-emitting diodes. *Appl. Phys. Lett.*, 78(11):1619, March 2001. ISSN 00036951. doi: 10.1063/1. 1355013. URL http://scitation.aip.org/content/aip/journal/apl/78/ 11/10.1063/1.1355013.

[69] Ayataka Endo, Keigo Sato, Kazuaki Yoshimura, Takahiro Kai, Atsushi Kawada, Hiroshi Miyazaki, and Chihaya Adachi. Efficient up-conversion of triplet excitons into a singlet state and its application for organic light emitting diodes. *Appl. Phys. Lett.*, 98(8):083302, 2011. ISSN 00036951. doi: 10.1063/1.3558906. URL http://link.aip.org/link/APPLAB/v98/i8/p083302/s1&Agg=doi.

[70] Hiroki Uoyama, Kenichi Goushi, Katsuyuki Shizu, Hiroko Nomura, and Chihaya Adachi. Highly efficient organic light-emitting diodes from delayed fluorescence. *Nature*, 492(7428):234–8, December 2012. ISSN 1476-4687. doi: 10.1038/nature11687. URL http://www.ncbi.nlm.nih.gov/pubmed/ 23235877http://www.nature.com/doifinder/10.1038/nature11687http: //dx.doi.org/10.1038/nature11687.

[71] Qisheng Zhang, Daniel Tsang, Hirokazu Kuwabara, Yasuhiro Hatae, Bo Li, Takehiro Takahashi, Sae Youn Lee, Takuma Yasuda, and Chihaya Adachi. Nearly 100% Internal Quantum Efficiency in Undoped Electroluminescent Devices Employing Pure Organic Emitters. *Adv. Mater.*, 27:2096, 2015. ISSN 09359648. doi: 10.1002/adma.201405474. URL http://doi.wiley.com/10. 1002/adma.201405474.

[72] Renie van der Werf, Dick Zevenhuijzen, and Joshua Jortner. Theory of delayed molecular fluorescence, 1978. ISSN 03010104.

[73] Abraham Nitzan. *Chemical Dynamics in Condensed Phases: Relaxation, Transfer and Reactions in Condensed Molecular Systems: Relaxation, Transfer and Reactions in Condensed Molecular Systems*. Oxford University Press, 2006.

[74] G. Lindblad. On the generators of quantum dynamical semigroups. *Commun. Math. Phys.*, 48(2):119–130, 1976. ISSN 00103616. doi: 10.1007/BF01608499.

[75] A. ISAR, A. SANDULESCU, H. SCUTARU, E. STEFANESCU, and W. SCHEID. Open Quantum Systems, 1994. ISSN 0218-3013. URL http://www.worldscientific.com/doi/abs/10.1142/S0218301394000164.

[76] A. Shushin. Magnetic field effects on electron-hole recombination in disordered organic semiconductors. *Phys. Rev. B*, 84(11):115212, September 2011. ISSN 1098-0121. doi: 10.1103/PhysRevB.84.115212. URL http://link.aps.org/doi/10.1103/PhysRevB.84.115212.

[77] D. Kohen, C. C. Marston, and D. J. Tannor. Phase space approach to theories of quantum dissipation. *J. Chem. Phys.*, 107(13):5236, 1997. ISSN 00219606. doi: 10.1063/1.474887. URL http://link.aip.org/link/JCPSA6/v107/i13/p5236/s1&Agg=doi.

[78] Charles E Swenberg and Nicholas E Geacintov. Exciton Interactions in Organic Solids. In J.B. Birks, editor, *Org. Mol. Photophysics*, volume 18, chapter 10, pages 489–564. Wiley, New York, 1973.

[79] R. E. Merrifield. Theory of Magnetic Field Effects on the Mutual Annihilation of Triplet Excitons. *J. Chem. Phys.*, 48(9):4318, 1968. ISSN 00219606. doi: 10.1063/1.1669777. URL http://link.aip.org/link/?JCP/48/4318/1&Agg=doihttp://scitation.aip.org/content/aip/journal/jcp/48/9/10.1063/1.1669777.

[80] R. E. Merrifield. Magnetic effects on triplet exciton interactions, 1971. ISSN 0033-4545. URL http://iupac.org/publications/pac/27/3/0481/.

[81] R. Johnson and R. Merrifield. Effects of Magnetic Fields on the Mutual Annihilation of Triplet Excitons in Anthracene Crystals. *Phys. Rev. B*, 1(2):896–902, January 1970. ISSN 0556-2805. doi: 10.1103/PhysRevB.1.896. URL http://link.aps.org/doi/10.1103/PhysRevB.1.896.

[82] Himan Sternlicht and Harden M. McConnell. Paramagnetic Excitons in Molecular Crystals. *J. Chem. Phys.*, 35(5):1793, 1961. ISSN 00219606. doi: 10.1063/1.1732146. URL http://scitation.aip.org/content/aip/journal/jcp/35/5/10.1063/1.1732146http://link.aip.org/link/?JCPSA6/35/1793/1http://link.aip.org/link/JCPSA6/v35/i5/p1793/s1&Agg=doi.

[83] Jonathan J Burdett, Geoffrey B Piland, and Christopher J Bardeen. Magnetic field effects and the role of spin states in singlet fission. *Chem. Phys. Lett.*, 585:1–10, 2013. ISSN 0009-2614. doi: 10.1016/j.cplett.2013.08.036.

[84] M. Chabr and D. F. Williams. Fission of singlet excitons into triplet-exciton pairs in molecular crystals. *Phys. Rev. B*, 16(4):1685–1693, 1977. ISSN 01631829. doi: 10.1103/PhysRevB.16.1685. URL http://prb.aps.org/abstract/PRB/v16/i4/p1685_1.

[85] C.E. Swenberg, R. van Metter, and M. Ratner. Comments on exciton fission and electron spin resonance in tetracene single crystals, 1972. ISSN 00092614. URL http://linkinghub.elsevier.com/retrieve/pii/0009261472804056.

[86] A. Suna. Kinematics of Exciton-Exciton Annihilation in Molecular Crystals. *Phys. Rev. B*, 1(4):1716, 1970. URL http://onlinelibrary.wiley.com/doi/10.1002/cbdv.200490137/abstracthttp://prb.aps.org/abstract/PRB/v1/i4/p1716_1.

[87] V Ern and R. E. Merrifield. Magnetic field effect on triplet exciton quenching in organic crystals. *Phys. Rev. Lett.*, 21(9):609–611, 1968. ISSN 00319007. doi: 10.1103/PhysRevLett.21.609.

[88] Peter Peumans, Aharon Yakimov, and Stephen R. Forrest. Small molecular weight organic thin-film photodetectors and solar cells, March 2003. ISSN 00218979. URL http://scitation.aip.org/content/aip/journal/jap/93/7/10.1063/1.1534621.

[89] George F Burkhard, Eric T Hoke, and Michael D McGehee. Accounting for interference, scattering, and electrode absorption to make accurate internal quantum efficiency measurements in organic and other thin solar cells. *Adv. Mater.*, 22(30):3293–3297, August 2010. ISSN 09359648. doi: 10.1002/adma.201000883. URL http://www.ncbi.nlm.nih.gov/pubmed/20517871.

[90] H. Bouchriha, V. Ern, J.L. L Fave, C. Guthmann, and M. Schott. Magnetic field dependence of singlet exciton fission and fluorescence in crystalline tetracene at 300 K, 1978. ISSN 0302-0738. URL http://www.edpsciences.org/10.1051/jphys:01978003903025700.

[91] Martin A Green. The path to 25% silicon solar cell efficiency: history of silicon cell evolution. *Prog. Photovoltaics*, 17(3):183–189, 2009. ISSN 1062-7995. doi: 10.1002/pip.892.

[92] D. L. Dexter. A Theory of Sensitized Luminescence in Solids. *J. Chem. Phys.*, 21(5):836, December 1953. ISSN 00219606. doi: 10.1063/1.1699044. URL http://link.aip.org/link/JCPSA6/v21/i5/p836/s1&Agg=doihttp://scitation.aip.org.libproxy.mit.edu/content/aip/journal/jcp/21/5/10.1063/1.1699044.

[93] Y Tomkiewicz, R P Groff, and P Avakian. Spectroscopic approach to energetics of exciton fission and fusion in tetracene crystals. *J. Chem. Phys.*, 54(10):4504–4507, 1971. ISSN 0021-9606. doi: 10.1063/1.1674702.

[94] Chih-Wei Chu, Yan Shao, Vishal Shrotriya, and Yang. Yang. Efficient photovoltaic energy conversion in tetracene-C60 based heterojunctions. *Appl. Phys. Lett.*, 86(24):243506/1–243506/3, 2005. ISSN 0003-6951. doi: 10.1063/1. 1946184.

[95] Jonathan J Burdett, David Gosztola, and Christopher J Bardeen. The dependence of singlet exciton relaxation on excitation density and temperature in polycrystalline tetracene thin films: Kinetic evidence for a dark intermediate state and implications for singlet fission. *J. Chem. Phys.*, 135(21):214508/1–214508/10, 2011. ISSN 0021-9606. doi: 10.1063/1.3664630.

[96] Nicholas Geacintov, Martin Pope, and Frank E Vogel III. Effect of magnetic field on the fluorescence of tetracene crystals: exciton fission. *Phys. Rev. Lett.*, 22(12):593–596, 1969. ISSN 0031-9007. doi: 10.1103/PhysRevLett.22.593.

[97] RE Merrifield, P. Avakian, and RP Groff. Fission of singlet excitons into pairs of triplet excitons in tetracene crystals, June 1969. ISSN 00092614. URL http: //www.sciencedirect.com/science/article/pii/0009261469801442http: //linkinghub.elsevier.com/retrieve/pii/0009261469801442.

[98] Z R Hong, R Lessmann, B Maennig, Q Huang, K Harada, M Riede, and K Leo. Antenna effects and improved efficiency in multiple heterojunction photovoltaic cells based on pentacene, zinc phthalocyanine, and C60. *J. Appl. Phys.*, 106(6): 064511/1–064511/6, 2009. ISSN 0021-8979. doi: 10.1063/1.3187904.

[99] Jonathan J Burdett, Astrid M Mueller, David Gosztola, and Christopher J Bardeen. Excited state dynamics in solid and monomeric tetracene: The roles of superradiance and exciton fission. *J. Chem. Phys.*, 133(14):144506/1–144506/12, 2010. ISSN 0021-9606. doi: 10.1063/1.3495764.

[100] RP Groff, P. Avakian, and R. E. Merrifield. Coexistence of Exciton Fission and Fusion in Tetracene Crystals. *Phys Rev B*, 1(2):815, 1970.

[101] Mark W B Wilson, Akshay Rao, Kerr Johnson, Simon Gelinas, Riccardo di Pietro, Jenny Clark, and Richard H Friend. Temperature-Independent Singlet Exciton Fission in Tetracene. *J. Am. Chem. Soc.*, 135(44):16680–16688, 2013. ISSN 0002-7863. doi: 10.1021/ja408854u.

[102] Shuanghong Wu, Masaki Aonuma, Qisheng Zhang, Shuping Huang, Tetsuya Nakagawa, Kazuhiro Kuwabara, and Chihaya Adachi. High-efficiency deep-blue organic light-emitting diodes based on a thermally activated delayed fluorescence emitter. *J. Mater. Chem. C*, 2(3):421, 2014. ISSN 2050-7526. doi: 10.1039/c3tc31936a. URL http://xlink.rsc.org/?DOI=c3tc31936a.

[103] S Arnold, RR Alfano, M Pope, W Yu, P Ho, R Selsby, J Tharrats, and CE Swenberg. Triplet exciton caging in two dimensions. *J. Chem. Phys.*, 64(12):5104, 1976. ISSN 00219606. doi: 10.1063/1. 432184. URL http://link.aip.org/link/?JCP/64/5104/1&Agg=doihttp://link.aip.org/link/?JCPSA6/64/5104/1.

[104] Srinivas Sista, Mi-Hyae Park, Ziruo Hong, Yue Wu, Jianhui Hou, Wei Lek Kwan, Gang Li, and Yang. Yang. Highly Efficient Tandem Polymer Photovoltaic Cells. *Adv. Mater. (Weinheim, Ger.*, 22(3):380–383, 2010. ISSN 0935-9648. doi: 10.1002/adma.200901624.

[105] Guangjin Zhao, Youjun He, and Yongfang. Li. 6.5% Efficiency of Polymer Solar Cells Based on poly(3-hexylthiophene) and Indene-C60 Bisadduct by Device Optimization. *Adv. Mater. (Weinheim, Ger.*, 22(39):4355–4358, 2010. ISSN 0935-9648. doi: 10.1002/adma.201001339.

[106] Richard R Lunt, Timothy P Osedach, Patrick R Brown, Jill A Rowehl, and Vladimir. Bulovic. Practical Roadmap and Limits to Nanostructured Photovoltaics. *Adv. Mater. (Weinheim, Ger.*, 23(48):5712–5727, 2011. ISSN 0935-9648. doi: 10.1002/adma.201103404.

[107] XY Y. Zhu, Q Yang, and M Muntwiler. Charge-transfer excitons at organic semiconductor surfaces and interfaces. *Acc. Chem. Res.*, 42(11):1779–1787,

2009. ISSN 00014842. doi: 10.1021/ar800269u. URL http://pubs.acs.org/doi/abs/10.1021/ar800269u.

[108] Matthias Muntwiler, Qingxin Yang, William A. Tisdale, and X.-Y. Zhu. Coulomb Barrier for Charge Separation at an Organic Semiconductor Interface. *Phys. Rev. Lett.*, 101(19):196403, November 2008. ISSN 0031-9007. doi: 10.1103/PhysRevLett.101.196403. URL http://link.aps.org/doi/10.1103/PhysRevLett.101.196403.

[109] J Burgos, M Pope, and CE Swenberg. Heterofission in pentaceneâĂŘdoped tetracene single crystals. *Phys. status solidi (*, 83:249, 1977. URL http://onlinelibrary.wiley.com/doi/10.1002/pssb.2220830127/abstract.

[110] Jiye Lee, Priya Jadhav, Philip D Reusswig, Shane R Yost, Nicholas J Thompson, Daniel N Congreve, Eric Hontz, Troy Van Voorhis, and Marc A Baldo. Singlet exciton fission photovoltaics. *Acc. Chem. Res.*, 46(6):1300–1311, 2013. ISSN 00014842. doi: 10.1021/ar300288e. URL http://pubs.acs.org/doi/abs/10.1021/ar300288e.

[111] Akshay Rao, Mark W B Wilson, Justin M Hodgkiss, Sebastian Albert-Seifried, Heinz Bassler, and Richard H Friend. Exciton Fission and Charge Generation via Triplet Excitons in Pentacene/C60 Bilayers. *J. Am. Chem. Soc.*, 132(36):12698–12703, 2010. ISSN 0002-7863. doi: 10.1021/ja1042462.

[112] Ajay K Pandey, K N N Unni, and Jean-Michel. Nunzi. Pentacene/perylene co-deposited solar cells. *Thin Solid Films*, 511-512:529–532, 2006. ISSN 0040-6090. doi: 10.1016/j.tsf.2005.12.015.

[113] Ajay K. Pandey, Sylvie Dabos-Seignon, and Jean-Michel Nunzi. Pentacene: PTCDI-C13H27 molecular blends efficiently harvest light for solar cell applications. *Appl. Phys. Lett.*, 89(11):113506, September 2006. ISSN 00036951. doi: 10.1063/1.2352800. URL http://scitation.aip.org/content/aip/journal/apl/89/11/10.1063/1.2352800.

[114] Florent Monestier, Ajay K Pandey, Jean-Jacques Simon, Philippe Torchio, Ludovic Escoubas, and Jean-Michel. Nunzi. Optical modeling of the ultimate efficiency of pentacene:N,N'-ditridecylperylene-3,4,9,10-tetracarboxylic diimide-blend solar cells. *J. Appl. Phys.*, 102(3):034512/1–034512/6, 2007. ISSN 0021-8979. doi: 10.1063/1.2767619.

[115] D Hertel and K Meerholz. Triplet-polaron quenching in conjugated polymers. *J. Phys. Chem. B*, 111(42):12075–12080, 2007. ISSN 1520-6106.

[116] Geoffrey B. Piland, Jonathan J. Burdett, Dharmalingam Kurunthu, and Christopher J. Bardeen. Magnetic field effects on singlet fission and fluorescence decay dynamics in amorphous rubrene. *J. Phys. Chem. C*, 117(3): 1224–1236, January 2013. ISSN 19327447. doi: 10.1021/jp309286v. URL http://pubs.acs.org/doi/abs/10.1021/jp309286v.

[117] Nicholas J Thompson. *Singlet Exciton Fission: Applications to Solar Snergy Harvesting.* PhD thesis, Massachusetts Institute of Technology, 2014.

[118] Sebastian Reineke. Organic light-emitting diodes: Phosphorescence meets its match. *Nat. Photonics*, 8(4):269–270, 2014. ISSN 1749-4885. doi: 10. 1038/nphoton.2014.78. URL http://www.nature.com/doifinder/10.1038/nphoton.2014.78.

[119] Fernando B. Dias, Konstantinos N. Bourdakos, Vygintas Jankus, Kathryn C. Moss, Kiran T. Kamtekar, Vandana Bhalla, José Santos, Martin R. Bryce, and Andrew P. Monkman. Triplet harvesting with 100% efficiency by way of thermally activated delayed fluorescence in charge transfer OLED emitters. *Adv. Mater.*, 25(27):3707–3714, July 2013. ISSN 09359648. doi: 10.1002/adma. 201300753. URL http://www.ncbi.nlm.nih.gov/pubmed/23703877.

[120] Thomas Hofbeck, Uwe Monkowius, and Hartmut Yersin. Highly Efficient Luminescence of Cu(I) Compounds: Thermally Activated Delayed Fluorescence Combined with Short-Lived Phosphorescence. *J. Am. Chem. Soc.*, 137

(1):399–404, 2015. ISSN 0002-7863. doi: 10.1021/ja5109672. URL `http://pubs.acs.org/doi/abs/10.1021/ja5109672`.

[121] Yuyu Pan, Weijun Li, Shitong Zhang, Liang Yao, Cheng Gu, Hai Xu, Bing Yang, and Yuguang Ma. High Yields of Singlet Excitons in Organic Electroluminescence through Two Paths of Cold and Hot Excitons. *Adv. Opt. Mater.*, pages n/a–n/a, March 2014. ISSN 21951071. doi: 10.1002/adom.201300467. URL `http://doi.wiley.com/10.1002/adom.201300467`.

[122] Kenichi Goushi and Chihaya Adachi. Efficient organic light-emitting diodes through up-conversion from triplet to singlet excited states of exciplexes. *Appl. Phys. Lett.*, 101(2):023306, 2012. ISSN 00036951. doi: 10.1063/1.4737006. URL `http://link.aip.org/link/APPLAB/v101/i2/p023306/s1&Agg=doi`.

[123] Kenichi Goushi, Kou Yoshida, Keigo Sato, and Chihaya Adachi. Organic light-emitting diodes employing efficient reverse intersystem crossing for triplet-to-singlet state conversion, March 2012. ISSN 1749-4885. URL `http://dx.doi.org/10.1038/nphoton.2012.31http://www.nature.com/doifinder/10.1038/nphoton.2012.31http://links.ealert.nature.com/ctt?kn=138&ms=Mzg5NDQxNTQS1&r=ODkwMTM2NjI2NgS2&b=0&j=MTM1NzczMDYxS0&mt=1&rt=0`.

[124] Christopher T. Rodgers. Magnetic field effects in chemical systems. *Pure Appl. Chem.*, 81(1):19–43, 2009. ISSN 0033-4545. doi: 10.1351/PAC-CON-08-10-18.

[125] Ulrich E. Steiner and Thomas Ulrich. Magnetic Field Effects in Chemical Kinetics and Related Phenomena. *Chem. Rev.*, 89(1):51–147, January 1989. ISSN 0009-2665. doi: 10.1021/cr00091a003. URL `http://pubs.acs.org/doi/abs/10.1021/cr00091a003http://dx.doi.org/10.1021/cr00091a003`.

[126] Martin Klessinger and Josef Michl. *Excited states and photochemistry of organic molecules*. VCH Publishers Inc., New York, 1995. ISBN 1560815884.

[127] SP McGlynn, T Azumi, and M Kinoshita. *Molecular Spectroscopy of the Triplet State*. Prentice-Hall, Englewood Cliffs, NJ, 1969.

[128] Louis Carlacci, C. Doubleday Jr, T.R. Furlani, H.F. King, and J.W. McIver Jr. Spin-orbit coupling in biradicals. Ab initio MCSCF calculations on trimethylene and the methyl-methyl radical pair. *J. Am. Chem. Soc.*, 109(18):5323–5329, 1987. ISSN 0002-7863. doi: 10.1021/ja00252a004. URL http://pubs.acs. org/doi/abs/10.1021/ja00252a004.

[129] C. J. Doubleday, N. J. Turro, and J.-W. Wang. Dynamics of Flexible Triplet Biradicals. *Accounts Chem.*, 22(6):199–205, 1989. ISSN 0001-4842. doi: 10.1021/ ar00162a001. URL http://pubs.acs.org/doi/abs/10.1021/ar00162a001.

[130] K Bhattacharyya and M Chowdhury. Environmental and magnetic field effects on exciplex and twisted charge transfer emission. *Chem. Rev.*, pages 507–535, 1993. ISSN 0009-2665. doi: 10.1021/cr00017a022. URL http://pubs.acs. org/doi/abs/10.1021/cr00017a022.

[131] Matthew B. Zimmt, Charles Doubleday, Ian R. Gould, and Nicholas J. Turro. Nanosecond flash photolysis studies of intersystem crossing rate constants in biradicals: structural effects brought about by spin-orbit coupling. *J. Am. Chem. Soc.*, 107(23):6724–6726, November 1985. ISSN 0002-7863. doi: 10.1021/ ja00309a059. URL http://pubs.acs.org/doi/abs/10.1021/ja00309a059.

[132] Carlos Baleizão and Mário N Berberan-Santos. The brightest fullerene: a new isotope effect in molecular fluorescence and phosphorescence. *Chemphyschem*, 12(7):1247–50, May 2011. ISSN 1439-7641. doi: 10.1002/cphc.201100156. URL http://www.ncbi.nlm.nih.gov/pubmed/21433243.

[133] Ping Chen, Li-Ping Wang, Wan-Yi Tan, Qi-Ming Peng, Shi-Tong Zhang, Xu-Hui Zhu, and Feng Li. Delayed Fluorescence in a Solution-Processable Pure Red Molecular Organic Emitter Based on Dithienylbenzothiadiazole: A Joint Optical, Electroluminescence, and Magnetoelectroluminescence Study. *ACS*

Appl. Mater. Interfaces, 7(4):2972–2978, 2015. ISSN 1944-8244. doi: 10.1021/ am508574m. URL http://pubs.acs.org/doi/abs/10.1021/am508574m.

[134] Toshinari Ogiwara, Yusuke Wakikawa, and Tadaaki Ikoma. Mechanism of Intersystem Crossing of Thermally Activated Delayed Fluorescence Molecules. *J. Phys. Chem. A*, page 150326072831000, 2015. ISSN 1089-5639. doi: 10.1021/ acs.jpca.5b02253. URL http://pubs.acs.org/doi/abs/10.1021/acs.jpca. 5b02253.

[135] Qiming Peng, Aiwu Li, Yunxia Fan, Ping Chen, and Feng Li. Studying the influence of triplet deactivation on the singletâĂŞtriplet inter-conversion in intra-molecular charge-transfer fluorescence-based OLEDs by magneto-electroluminescence. *J. Mater. Chem. C*, 2(31):6264, 2014. ISSN 2050-7526. doi: 10.1039/C4TC00885E. URL http://xlink.rsc.org/?DOI=C4TC00885E.

[136] Gregory D Gillispie and E.C. Lim. Some related aspects of sequential coupling, 1980. ISSN 00092614.

[137] E.L. Frankevich, G.E. Zoriniants, A.N. Chaban, M.M. Triebel, S. Blumstengel, and V.M. Kobryanskii. Magnetic field effects on photoluminescence in PPP. Investigation of the influence of chain length and degree of order, 1996. ISSN 00092614.

[138] EL L Frankevich, A. A. Lymarev, I Sokolik, F. E. Karasz, S. Blumstengel, R. H. Baughman, and H. H. Hörhold. Polaron-pair generation in poly(phenylene vinylenes). *Phys. Rev. B*, 46(15):9320–9324, 1992. ISSN 01631829. doi: 10. 1103/PhysRevB.46.9320. URL http://dx.doi.org/10.1103/PhysRevB.46. 9320http://prb.aps.org/abstract/PRB/v46/i15/p9320_1.

[139] Ken-ichi Okamoto, Norikazu Oda, Akira Itaya, and Shigekazu Kusabayashi. Magnetic field effect on the photoconductivity of poly-n-vinylcarbazole, 1975. ISSN 00092614.

[140] I a Sokolik and E L Frankevich. The effect of magnetic fields on photoprocesses in organic solids. *Sov. Phys. Uspekhi*, 16(5):687–701, May 1974. ISSN 0038-5670. doi: 10.1070/PU1974v016n05ABEH004131. URL `http://stacks.iop.org/0038-5670/16/i=5/a=R07?key=crossref.6d310ac36eb4ba831b683c905d568461`.

[141] Masahuro Okazaki, Yutaka Tai, Keichi Nunome, Kazumi Toriyama, and Saburo Nagakura. Hyperfine versus relaxation mechanisms of the magnetic field effect on recombination fluorescence of geminate pairs, 1992. ISSN 03010104.

[142] Klaus Schulten and Peter G. Wolynes. Semiclassical description of electron spin motion in radicals including the effect of electron hopping. *J. Chem. Phys.*, 68 (7):3292, 1978. ISSN 00219606. doi: 10.1063/1.436135. URL `http://link.aip.org/link/JCPSA6/v68/i7/p3292/s1&Agg=doi`.

[143] N. J. Harmon and M. E. Flatté. Spin-flip induced magnetoresistance in positionally disordered organic solids. *Phys. Rev. Lett.*, 108(18):186602, May 2012. ISSN 00319007. doi: 10.1103/PhysRevLett.108.186602. URL `http://link.aps.org/doi/10.1103/PhysRevLett.108.186602`.

[144] Tobias Gokus, Laurent Cognet, Juan G. Duque, Matteo Pasquali, Achim Hartschuh, and Brahim Lounis. Mono-and biexponential luminescence decays of individual single-walled carbon nanotubes. *J. Phys. Chem. C*, 114(33):14025–14028, 2010. ISSN 19327447. doi: 10.1021/jp1049217.

[145] Dirk Veldman, Özlem Ipek, Stefan C J Meskers, Jörgen Sweelssen, Marc M Koetse, Sjoerd C. Veenstra, Jan M Kroon, Svetlana S. Van Bavel, Joachim Loos, and René a J Janssen. Compositional and electric field dependence of the dissociation of charge transfer excitons in alternating polyfluorene copolymer/fullerene blends. *J. Am. Chem. Soc.*, 130(24):7721–7735, 2008. ISSN 00027863. doi: 10.1021/ja8012598.

[146] S.P. P. Kersten, a.J. J. Schellekens, B. Koopmans, and P.a. a. Bobbert. Effect of hyperfine interactions on exciton formation in or-

206

ganic semiconductors. *Synth. Met.*, 161(7-8):613–616, April 2011. ISSN 03796779. doi: 10.1016/j.synthmet.2010.11.040. URL `http://linkinghub.elsevier.com/retrieve/pii/S0379677910004935http://dx.doi.org/10.1016/j.synthmet.2010.11.040`.

[147] Takayoshi Kobayashi, Keitaro Yoshihara, and Saburo Nagakura. Charge-Transfer Interaction and Fluorescence in Some Tetracyanobenzene Complexes. *Bull. Chem. Soc. Jpn.*, 44(10):2603–2610, 1971. ISSN 0009-2673. doi: 10.1246/bcsj.44.2603.

[148] PB Deotare, W Chang, E Hontz, DN Congreve, PD Reusswig, B Modtland, Vladimir Bulović, Troy Van Voorhis, and MA Baldo. Nanoscale Transport of Charge Transfer States in Organic Donor-Acceptor Blends. *Manuscr. Submitt. Publ.*, 2015.

[149] Wendi Chang, Daniel N. Congreve, Eric Hontz, Matthias E. Bahlke, David P. McMahon, Sebastian Reineke, Tony C. Wu, Vladimir Bulović, Troy Van Voorhis, and Marc a. Baldo. Spin-dependent charge transfer state design rules in organic photovoltaics. *Nat. Commun.*, 6:6415, 2015. ISSN 2041-1723. doi: 10.1038/ncomms7415. URL `http://www.nature.com/doifinder/10.1038/ncomms7415`.

[150] Weijun Li, Yuyu Pan, Ran Xiao, Qiming Peng, Shitong Zhang, Dongge Ma, Feng Li, Fangzhong Shen, Yinghui Wang, Bing Yang, and Yuguang Ma. Employing âLij100% excitons in OLEDs by utilizing a fluorescent molecule with hybridized local and charge-transfer excited state. *Adv. Funct. Mater.*, 24(11):1609–1614, March 2014. ISSN 1616301X. doi: 10.1002/adfm.201301750. URL `http://doi.wiley.com/10.1002/adfm.201301750`.

[151] Xiaguang Zhang, Wei Shen, Dongmei Zhang, Yongzhen Zheng, Rongxing He, and Ming Li. Theoretical investigation of dihydroacridine- and diphenylsulphone- derivatives as thermally activated delayed fluorescence emitters for organic light-emitting diodes. *RSC Adv.*, 2015. ISSN 2046-

2069. doi: 10.1039/C5RA04929F. URL http://pubs.rsc.org/en/Content/ArticleLanding/2015/RA/C5RA04929F.

[152] Carsten Deibe, Thomas Strobe, and Vladimir Dyakonov. Role of the charge transfer state in organic donor-acceptor solar cells. *Adv. Mater.*, 22(37):4097–4111, October 2010. ISSN 09359648. doi: 10.1002/adma. 201000376. URL http://www.ncbi.nlm.nih.gov/pubmed/20803527http://dx.doi.org/10.1002/adma.201000376.

[153] Tracey M Clarke and James R Durrant. Charge photogeneration in organic solar cells. *Chem. Rev.*, 110(11):6736–6767, November 2010. ISSN 00092665. doi: 10.1021/cr900271s. URL http://www.ncbi.nlm.nih.gov/pubmed/20063869http://dx.doi.org/10.1021/cr900271s.

[154] Jean Luc Brédas, Joseph E Norton, Jérôme Cornil, and Veaceslav Coropceanu. Molecular understanding of organic solar cells: The challenges. *Acc. Chem. Res.*, 42(11):1691–1699, 2009. ISSN 00014842. doi: 10.1021/ar900099h. URL http://pubs.acs.org/stoken/campaign/acs/full/10.1021/ar900099hhttp://dx.doi.org/10.1021/ar900099h.

[155] J Lee. Charge transfer state versus hot exciton dissociation in polymer-fullerene blended solar cells. *J. Am. Chem. Soc.*, 132:11878–11880, 2010. URL http://dx.doi.org/10.1021/ja1045742.

[156] Koen Vandewal, Steve Albrecht, Eric T Hoke, Kenneth R Graham, Johannes Widmer, Jessica D Douglas, Marcel Schubert, William R Mateker, Jason T Bloking, George F Burkhard, Alan Sellinger, Jean M J Fréchet, Aram Amassian, Moritz K Riede, Michael D McGehee, Dieter Neher, and Alberto Salleo. Efficient charge generation by relaxed charge-transfer states at organic interfaces. *Nat. Mater.*, 13(1):63–8, 2014. ISSN 1476-1122. doi: 10.1038/nmat3807. URL http://dx.doi.org/10.1038/nmat3807http://www.ncbi.nlm.nih.gov/pubmed/24240240.

[157] Arne C Morteani, Paiboon Sreearunothai, Laura M Herz, Richard H Friend, and Carlos Silva. Exciton regeneration at polymeric semiconductor heterojunctions. *Phys. Rev. Lett.*, 92(24):247402–1, June 2004. ISSN 00319007. doi: 10.1103/ PhysRevLett.92.247402. URL `http://dx.doi.org/10.1103/PhysRevLett. 92.247402http://link.aps.org/doi/10.1103/PhysRevLett.92.247402`.

[158] S. Gelinas, A. Rao, A. Kumar, S. L. Smith, A. W. Chin, J. Clark, T. S. van der Poll, G. C. Bazan, and R. H. Friend. Ultrafast Long-Range Charge Separation in Organic Semiconductor Photovoltaic Diodes. *Science*, 343(6170):512–516, 2013. ISSN 0036-8075. doi: 10.1126/science. 1246249. URL `http://dx.doi.org/10.1126/science.1246249http://www. sciencemag.org/cgi/doi/10.1126/science.1246249`.

[159] S H S Park. Bulk heterojunction solar cells with internal quantum efficiency approaching 100%. *Nat. Photonics*, 3:297–302, 2009. URL `http://dx.doi. org/10.1038/nphoton.2009.69`.

[160] P C Y Chow, S Gélinas, A Rao, and R H Friend. Quantitative bimolecular recombination in organic photovoltaics through triplet exciton formation. *J. Am. Chem. Soc.*, 136:3424–3429, 2014.

[161] S Westenhoff. Charge recombination in organic photovoltaic devices with high open-circuit voltages. *J. Am. Chem. Soc.*, 130:13653–13658, 2008. URL `http: //dx.doi.org/10.1021/ja803054g`.

[162] Artem A Bakulin, Akshay Rao, Vlad G Pavelyev, Paul H M van Loosdrecht, Maxim S Pshenichnikov, Dorota Niedzialek, Jérôme Cornil, David Beljonne, and Richard H Friend. The Role of Driving Energy and Delocalized States for Charge Separation in Organic Semiconductors. *Science*, 335(6074):1340–1344, March 2012. ISSN 0036-8075. doi: 10.1126/science. 1217745. URL `http://www.ncbi.nlm.nih.gov/pubmed/22362882http://dx. doi.org/10.1126/science.1217745`.

[163] F Etzold. Ultrafast exciton dissociation followed by nongeminate charge recombination in PCDTBT: PCBM photovoltaic blends. *J. Am. Chem. Soc.*, 133:9469–9479, 2011. URL http://dx.doi.org/10.1021/ja201837e.

[164] Akshay Rao, Philip C Y Chow, Simon Gélinas, Cody W Schlenker, Chang-Zhi Li, Hin-lap Yip, Alex K-y Jen, David S Ginger, and Richard H Friend. The role of spin in the kinetic control of recombination in organic photovoltaics. *Nature*, 500(7463):435–9, August 2013. ISSN 1476-4687. doi: 10.1038/nature12339. URL http://dx.doi.org/10.1038/nature12339http://www.ncbi.nlm.nih.gov/pubmed/23925118.

[165] Jean Luc Brédas, David Beljonne, Veaceslav Coropceanu, and JérÇŠme Cornil. Charge-transfer and energy-transfer processes in π-conjugated oligomers and polymers: A molecular picture. *Chem. Rev.*, 104(11):4971–5003, November 2004. ISSN 00092665. doi: 10.1021/cr040084k. URL http://www.ncbi.nlm.nih.gov/pubmed/15535639.

[166] K Vandewal, K Tvingstedt, A Gadisa, O Inganas, and J V Manca. On the origin of the open-circuit voltage of polymer-fullerene solar cells. *Nat. Mater.*, 8:904–909, 2009. URL http://dx.doi.org/10.1038/nmat2548.

[167] D Veldman, S C J Meskers, and R A J Janssen. The energy of charge-transfer states in electron donorâĂŞacceptor blends: insight into the energy losses in organic solar cells. *Adv. Funct. Mater.*, 19:1939–1948, 2009. URL http://dx.doi.org/10.1002/adfm.200900090.

[168] J P Schmidtke, J.-S. Kim, J Gierschner, C Silva, and R H Friend. Optical spectroscopy of a polyfluorene copolymer at high pressure: intra- and intermolecular interactions. *Phys. Rev. Lett.*, 99:167401, 2007. URL http://dx.doi.org/10.1103/PhysRevLett.99.167401.

[169] S Albert-Seifried. Pressure-induced delocalization of photoexcited states in a semiconducting polymer. *Phys. Rev. Lett.*, 105:195501, 2010.

[170] David Graves, Vygintas Jankus, Fernando B. Dias, and Andrew Monkman. Photophysical Investigation of the Thermally Activated Delayed Emission from Films of m-MTDATA: PBD Exciplex, December 2013. ISSN 1616301X. URL http://doi.wiley.com/10.1002/adfm.201303389.

[171] Bin Hu, Liang Yan, and Ming Shao. Magnetic-Field Effects in Organic Semiconducting Materials and Devices. *Adv. Mater.*, 21(14-15):1500–1516, April 2009. ISSN 09359648. doi: 10.1002/adma.200802386. URL http://doi.wiley.com/10.1002/adma.200802386.

[172] E L Frankevich, A A Lymarev, and I A Sokolik. CT-excitons and magnetic field effect in polydiacetylene crystals. *Chem. Phys.*, 162:1–6, 1992.

[173] Fujian Wang, Ferran Macià, Markus Wohlgenannt, Andrew D. Kent, and Michael E. Flatté. Magnetic Fringe-Field Control of Electronic Transport in an Organic Film. *Phys. Rev. X*, 2(2):021013, June 2012. ISSN 2160-3308. doi: 10.1103/PhysRevX.2.021013. URL http://link.aps.org/doi/10.1103/PhysRevX.2.021013.

[174] Hideo Ohkita, Steffan Cook, Yeni Astuti, Warren Duffy, Steve Tierney, Weimin Zhang, Martin Heeney, Iain McCulloch, Jenny Nelson, Donal D C Bradley, and James R Durrant. Charge carrier formation in polythiophene/fullerene blend films studied by transient absorption spectroscopy. *J. Am. Chem. Soc.*, 130 (10):3030–3042, 2008. ISSN 00027863. doi: 10.1021/ja076568q. URL http://dx.doi.org/10.1021/ja076568q.

[175] Askat E Jailaubekov, Adam P Willard, John R Tritsch, Wai-Lun Chan, Na Sai, Raluca Gearba, Loren G Kaake, Kenrick J Williams, Kevin Leung, Peter J Rossky, and X-Y Zhu. Hot charge-transfer excitons set the time limit for charge separation at donor/acceptor interfaces in organic photovoltaics. *Nat. Mater.*, 12(1):66–73, January 2013. ISSN 1476-1122. doi: 10.1038/nmat3500. URL http://dx.doi.org/10.1038/nmat3500.

[176] Markus Hallermann, Enrico Da Como, Jochen Feldmann, Marta Izquierdo, Salvatore Filippone, Nazario MartiÌ\n, Sabrina JuÌLchter, and Elizabeth von Hauff. Correlation between charge transfer exciton recombination and photocurrent in polymer/fullerene solar cells. *Appl. Phys. Lett.*, 97(2):023301, July 2010. ISSN 00036951. doi: 10.1063/1.3462298. URL `http://scitation.aip.org.libproxy.mit.edu/content/aip/journal/apl/97/2/10.1063/1.3462298`.

[177] Ernst-Walter Knapp and Klaus Schulten. Magnetic field effect on the hyperfine-induced electron spin motion in radicals undergoing diamagneticâĂŞparamagnetic exchange. *J. Chem. Phys.*, 71(4):1878, 1979. ISSN 00219606. doi: 10.1063/1.438541. URL `http://scitation.aip.org/content/aip/journal/jcp/71/4/10.1063/1.438541`.

[178] Kazuo Kitahara, Hidetoshi Osakabe, Kenichiro Mori, and Urbaan M. Titulaer. The effect of a magnetic field on the recombination of a radical pair. *J. Mol. Liq.*, 86(1-3):53–59, June 2000. ISSN 01677322. doi: 10.1016/S0167-7322(99)00124-5. URL `http://www.sciencedirect.com/science/article/pii/S0167732299001245`.

[179] A Abragam. *The Principles of Nuclear Magnetism*. International series of monographs on physics. Clarendon Press, Oxford, 1961. URL `http://books.google.com/books?id=dyJRAAAAMAAJ`.

[180] Charles L. Braun. Electric field assisted dissociation of charge transfer states as a mechanism of photocarrier production. *J. Chem. Phys.*, 80(9):4157–4161, 1984. ISSN 00219606. doi: 10.1063/1.447243. URL `http://scitation.aip.org/content/aip/journal/jcp/80/9/10.1063/1.447243`.

[181] Rienk van Grondelle, Jan P. Dekker, Tomas Gillbro, and Villy Sundstrom. Energy transfer and trapping in photosynthesis. *Biochim. Biophys. Acta - Bioenerg.*, 1187(1):1–65, August 1994. ISSN 00052728. doi: 10.1016/0005-2728(94)90166-X. URL `http://www.sciencedirect.com/science/article/pii/000527289490166X`.

[182] Melih K Sener, John D Olsen, C Neil Hunter, and Klaus. Schulten. Atomic-level structural and functional model of a bacterial photosynthetic membrane vesicle. *Proc. Natl. Acad. Sci. U. S. A.*, 104(40):15723–15728, 2007. ISSN 0027-8424. doi: 10.1073/pnas.0706861104.

[183] G McDermott, S M Prince, A A Freer, A M Hawthornthwaite-Lawless, M Z Papiz, R J Cogdell, and N W Isaacs. Crystal structure of an integral membrane light-harvesting complex from photosynthetic bacteria. *Nat.*, 374(6522):517–521, 1995. ISSN 0028-0836. doi: 10.1038/374517a0.

[184] Dong-Lin Jiang and Takuzo. Aida. Photoisomerization in dendrimers by harvesting of low-energy photons. *Nat.*, 388(6641):454–456, 1997. ISSN 0028-0836. doi: 10.1038/41290.

[185] Pritam Mukhopadhyay, Yuya Iwashita, Michihiro Shirakawa, Shin-ichiro Kawano, Norifumi Fujita, and Seiji. Shinkai. Spontaneous colorimetric sensing of the positional isomers of dihydroxynaphthalene in a 1D organogel matrix. *Angew. Chemie, Int. Ed.*, 45(10):1592–1595, 2006. ISSN 1433-7851. doi: 10.1002/anie.200503158.

[186] Paola Ceroni, Giacomo Bergamini, Filippo Marchioni, and Vincenzo. Balzani. Luminescence as a tool to investigate dendrimer properties. *Prog. Polym. Sci.*, 30(3-4):453–473, 2005. ISSN 0079-6700. doi: 10.1016/j.progpolymsci.2005.01. 003.

[187] Roland E Bauer, Andrew C Grimsdale, and Klaus. Muellen. Functionalised polyphenylene dendrimers and their applications. *Top. Curr. Chem.*, 245 (Functional Molecular Nanostructures):253–286, 2005. ISSN 0340-1022. doi: 10.1007/b98171.

[188] Long Chen, Yoshihito Honsho, Shu Seki, and Donglin. Jiang. Light-harvesting conjugated microporous polymers: rapid and highly efficient flow of light energy with a porous polyphenylene framework as antenna. *J. Am. Chem. Soc.*, 132 (19):6742–6748, 2010. ISSN 0002-7863. doi: 10.1021/ja100327h.

[189] V S Lin, S G DiMagno, and M J Therien. Highly conjugated, acetylenyl bridged porphyrins: new models for light-harvesting antenna systems. *Science*, 264 (5162):1105–1111, 1994. ISSN 0036-8075.

[190] Frank Würthner, Theo E. Kaiser, and Chantu R. Saha-Möller. J-aggregates: From serendipitous discovery to supramolecular engineering of functional dye materials, 2011. ISSN 14337851.

[191] Kazuhiko Misawa and Takayoshi Kobayashi. Hierarchical Structure in Oriented J-aggregates. In Takayoshi Kobayashi, editor, *J-aggregates*. World Scientific, Singapore, 1996.

[192] Bao-Qing Ma, Karen L Mulfort, and Joseph T Hupp. Microporous Pillared Paddle-Wheel Frameworks Based on Mixed-Ligand Coordination of Zinc Ions. *Inorg. Chem.*, 44(14):4912–4914, 2005. ISSN 0020-1669. doi: 10.1021/ic050452i.

[193] Sheshanath V Bhosale, Chintan H Jani, and Steven J Langford. Chemistry of naphthalene diimides. *Chem. Soc. Rev.*, 37(2):331–342, 2008. ISSN 0306-0012. doi: 10.1039/B615857A.

[194] M B Avinash and T Govindaraju. Engineering Molecular Organization of Naphthalenediimides: Large Nanosheets with Metallic Conductivity and Attoliter Containers. *Adv. Funct. Mater.*, 21(20):3875–3882, 2011. ISSN 1616-301X. doi: 10.1002/adfm.201101001.

[195] Mohit Kumar and Subi J George. Spectroscopic Probing of the Dynamic Self-Assembly of an Amphiphilic Naphthalene Diimide Exhibiting Reversible Vapochromism. *Chem. - A Eur. J.*, 17(40):11102–11106, S11102/1–S11102/7, 2011. ISSN 0947-6539. doi: 10.1002/chem.201101642.

[196] Mijanur Rahaman Molla and Suhrit. Ghosh. Structural Variations on Self-Assembly and Macroscopic Properties of 1,4,5,8-Naphthalene-diimide Chromophores. *Chem. Mater.*, 23(1):95–105, 2011. ISSN 0897-4756. doi: 10.1021/cm102343r.

[197] Hui Shao, Tuan Nguyen, Natalie C Romano, David A Modarelli, and Jon R Parquette. Self-assembly of 1-D n-type nanostructures based on naphthalene diimide-appended dipeptides. *J. Am. Chem. Soc.*, 131(45):16374–16376, 2009. ISSN 0002-7863. doi: 10.1021/ja906377q.

[198] Michael Busby, Christian Blum, Marc Tibben, Sandra Fibikar, Gion Calzaferri, Vinod Subramaniam, and Luisa. De Cola. Time, Space, and Spectrally Resolved Studies on J-Aggregate Interactions in Zeolite L Nanochannels. *J. Am. Chem. Soc.*, 130(33):10970–10976, 2008. ISSN 0002-7863. doi: 10.1021/ja801178p.

[199] Brian D. McCarthy, Eric R Hontz, Shane R Yost, Troy Van Voorhis, and Mircea DincÇŐ. Charge transfer or J-coupling? Assignment of an unexpected red-shifted absorption band in a naphthalenediimide-based metal-organic framework. *J. Phys. Chem. Lett.*, 4(3):453–458, 2013. ISSN 19487185. doi: 10.1021/jz302076s.

[200] Michael Busby, Andre Devaux, Christian Blum, Vinod Subramaniam, Gion Calzaferri, and Luisa. De Cola. Interactions of Perylene Bisimide in the One-Dimensional Channels of Zeolite L. *J. Phys. Chem. C*, 115(13):5974–5988, 2011. ISSN 1932-7447. doi: 10.1021/jp1108625.

[201] Yohei Takashima, Shuhei Furukawa, and Susumu. Kitagawa. Control of the charge-transfer interaction between a flexible porous coordination host and aromatic guests by framework isomerism. *CrystEngComm*, 13(10):3360–3363, 2011. ISSN 1466-8033. doi: 10.1039/c1ce05201b. URL http://pubs.rsc.org/en/content/articlepdf/2011/ce/c1ce05201b?page=search.

[202] Virginia Martinez-Martinez, Shuhei Furukawa, Yohei Takashima, Inigo Lopez Arbeloa, and Susumu. Kitagawa. Charge transfer and exciplex emissions from a naphthalenediimide-entangled coordination framework accommodating various aromatic guests. *J. Phys. Chem. C*, 116(49):26084–26090, 2012. ISSN 1932-7447. doi: 10.1021/jp309784y.

[203] Da-Wei Fu, Jia-Zhen Ge, Jing Dai, Heng-Yun Ye, and Zhi-Rong. Qu. Synthesis, structure and dielectric constant properties of a novel 1D coordination polymer[K(2-PTA)(H2O)]n. *Inorg. Chem. Commun.*, 12(10):994–997, 2009. ISSN 1387-7003. doi: 10.1016/j.inoche.2009.08.002.

[204] Qiong Ye, Yu-Mei Song, Guo-Xi Wang, Kai Chen, Da-Wei Fu, Philip Wai Hong Chan, Jin-Song Zhu, Songping D Huang, and Ren-Gen. Xiong. Ferroelectric Metal-Organic Framework with a High Dielectric Constant. *J. Am. Chem. Soc.*, 128(20):6554–6555, 2006. ISSN 0002-7863. doi: 10.1021/ja060856p.

[205] Da-Wei Fu, Heng-Yun Ye, Qiong Ye, Ke-Ji Pan, and Ren-Gen. Xiong. Ferroelectric metal-organic coordination polymer with a high dielectric constant. *Dalton Trans.*, (7):874–877, 2008. ISSN 1477-9226. doi: 10.1039/b714293e.

[206] Jochen Autschbach. Charge-transfer excitations and time-dependent density functional theory: problems and some proposed solutions. *Chemphyschem*, 10 (11):1757–60, August 2009. ISSN 1439-7641. doi: 10.1002/cphc.200900268. URL http://www.ncbi.nlm.nih.gov/pubmed/19507206.

[207] Yoshihiro Tawada, Takao Tsuneda, Susumu Yanagisawa, Takeshi Yanai, and Kimihiko Hirao. A long-range-corrected time-dependent density functional theory. *J. Chem. Phys.*, 120(18):8425–33, May 2004. ISSN 0021-9606. doi: 10.1063/1.1688752. URL http://www.ncbi.nlm.nih.gov/pubmed/15267767.

[208] Erich Runge and EKU K. U. Gross. Density-functional theory for time-dependent systems. *Phys. Rev. Lett.*, 52(12):997–1000, March 1984. ISSN 00319007. doi: 10.1103/PhysRevLett.52.997. URL http://link.aps.org/doi/10.1103/PhysRevLett.52.997http://prl.aps.org/abstract/PRL/v52/i12/p997_1.

[209] Hisayoshi Iikura, Takao Tsuneda, Takeshi Yanai, and Kimihiko Hirao. A long-range correction scheme for generalized-gradient-approximation exchange functionals. *J. Chem. Phys.*, 115(8):3540, 2001. ISSN 00219606. doi: 10.1063/1.

1383587. URL http://link.aip.org/link/JCPSA6/v115/i8/p3540/s1&Agg=
doi.

[210] Mary a Rohrdanz, Katie M Martins, and John M Herbert. A long-range-
corrected density functional that performs well for both ground-state proper-
ties and time-dependent density functional theory excitation energies, including
charge-transfer excited states. *J. Chem. Phys.*, 130(5):054112, February 2009.
ISSN 1089-7690. doi: 10.1063/1.3073302. URL http://www.ncbi.nlm.nih.
gov/pubmed/19206963.

[211] Ester Livshits and Roi Baer. A well-tempered density functional theory of
electrons in molecules. *Phys. Chem. Chem. Phys.*, 9(23):2932–2941, June 2007.
ISSN 1463-9076. doi: 10.1039/b617919c. URL http://www.ncbi.nlm.nih.
gov/pubmed/17551616.

[212] Sivan Refaely-abramson, Roi Baer, and Leeor Kronik. Fundamental and excita-
tion gaps in molecules of relevance for organic photovoltaics from an optimally
tuned range-separated hybrid functional. *Potentials*, pages 1–8, 2011.

[213] Roi Baer and Daniel Neuhauser. Density Functional Theory with Correct Long-
Range Asymptotic Behavior. *Phys. Rev. Lett.*, 94(4):043002, February 2005.
ISSN 0031-9007. doi: 10.1103/PhysRevLett.94.043002. URL http://link.
aps.org/doi/10.1103/PhysRevLett.94.043002.

[214] Roi Baer, Ester Livshits, and Daniel Neuhauser. Avoiding self-repulsion
in density functional description of biased molecular junctions. *Chem.
Phys.*, 329(1-3):266–275, October 2006. ISSN 03010104. doi: 10.1016/j.
chemphys.2006.06.041. URL http://linkinghub.elsevier.com/retrieve/
pii/S0301010406003648.

[215] R. Ditchfield. Self-Consistent Molecular-Orbital Methods. IX. An Extended
Gaussian-Type Basis for Molecular-Orbital Studies of Organic Molecules. *J.
Chem. Phys.*, 54(2):724, September 1971. ISSN 00219606. doi: 10.1063/1.

1674902. URL http://scitation.aip.org/content/aip/journal/jcp/54/2/10.1063/1.1674902.

[216] Qin Wu and Troy Van Voorhis. Direct optimization method to study constrained systems within density-functional theory. *Phys. Rev. A*, 72(2):24502, 2005. ISSN 1050-2947. doi: 10.1103/PhysRevA.72.024502. URL http://link.aps.org/doi/10.1103/PhysRevA.72.024502.

[217] Jacopo Tomasi and Maurizio Persico. Molecular Interactions in Solution: An Overview of Methods Based on Continuous Distributions of the Solvent. *Chem. Rev.*, 94(7):2027–2094, November 1994. ISSN 0009-2665. doi: 10.1021/cr00031a013. URL http://pubs.acs.org/doi/abs/10.1021/cr00031a013.

[218] Yue Wu, Zhihua Xu, Bin Hu, and Jane Howe. Tuning magnetoresistance and magnetic-field-dependent electroluminescence through mixing a strong-spin-orbital-coupling molecule and a weak-spin-orbital-coupling polymer. *Phys. Rev. B*, 75(3):035214, January 2007. ISSN 1098-0121. doi: 10.1103/PhysRevB.75.035214. URL http://link.aps.org/doi/10.1103/PhysRevB.75.035214.

[219] Jing Kong, Christopher A White, Anna I Krylov, David Sherrill, Ross D Adamson, Thomas R Furlani, Michael S. Lee, Aaron M Lee, Steven R Gwaltney, Terry R Adams, Christian Ochsenfeld, Andrew T B Gilbert, Gary S Kedziora, Vitaly A Rassolov, David R Maurice, Nikhil Nair, Yihan Shao, Nicholas A Besley, Paul E Maslen, Jeremy P Dombroski, Holger Daschel, Weimin Zhang, Prakashan P Korambath, Jon Baker, Edward F C Byrd, Troy Van Voorhis, Manabu Oumi, So Hirata, Chao-ping Hsu, Naoto Ishikawa, Jan Florian, Arieh Warshel, Benny G Johnson, Peter M W Gill, Martin Head-Gordon, and John A Pople. Q-Chem 2.0: a high-performanceab initio electronic structure program package. *J. Comput. Chem.*, 21(16):1532–1548, 2000. ISSN 0192-8651. doi: 10.1002/1096-987X(200012)21:16<1532::AID-JCC10>3.0.CO;2-W. URL http://doi.wiley.com/10.1002/1096-987X(200012)21:16<1532::AID-JCC10>3.0.CO;2-W.

[220] Joseph R. Lakowicz, editor. *Principles of Fluorescence Spectroscopy*. Springer US, Boston, MA, 2006. ISBN 978-0-387-31278-1. doi: 10.1007/978-0-387-46312-4. URL http://www.springerlink.com/index/10.1007/978-0-387-46312-4.

[221] Shuhei Furukawa, Kenji Hirai, Yohei Takashima, Keiji Nakagawa, Mio Kondo, Takaaki Tsuruoka, Osami Sakata, and Susumu. Kitagawa. A block PCP crystal: anisotropic hybridization of porous coordination polymers by face-selective epitaxial growth. *Chem. Commun. (Camb).*, (34):5097–5099, 2009. ISSN 1359-7345. doi: 10.1039/b909993j.

[222] Lei Han, Lan Qin, Lanping Xu, Yan Zhou, Junliang Sun, and Xiaodong Zou. A novel photochromic calcium-based metal-organic framework derived from a naphthalene diimide chromophore. *Chem. Commun. (Camb).*, 49(4): 406–8, January 2013. ISSN 1364-548X. doi: 10.1039/c2cc37497h. URL http://pubs.rsc.org/en/content/articlehtml/2013/cc/c2cc37497h.

[223] H Bernhard Schlegel. Exploring potential energy surfaces for chemical reactions: An overview of some practical methods. *J. Comput. Chem.*, 24(12):1514–1527, September 2003. ISSN 01928651. doi: 10.1002/jcc.10231. URL http://www.ncbi.nlm.nih.gov/pubmed/12868114.

[224] B J Berne, Michal Borkovec, and J E Straub. Classical and modern methods in reaction rate theory. *J. Phys. Chem.*, 92(13):3711–3725, 1988. doi: 10.1021/j100324a007. URL http://pubs.acs.org/doi/abs/10.1021/j100324a007.

[225] David Chandler. Statistical mechanics of isomerization dynamics in liquids and the transition state approximation. *J. Chem. Phys.*, 68(6):2959, 1978. ISSN 00219606. doi: 10.1063/1.436049. URL http://scitation.aip.org/content/aip/journal/jcp/68/6/10.1063/1.436049.

[226] B J Berne, G Ciccotti, and D F Coker, editors. *Classical and Quantum Dynamics in Condensed Phase Simulations*. World Scientific, Singapore, 1998.

ISBN 9810234988. URL http://www.worldscientific.com/worldscibooks/10.1142/3816#t=aboutBook.

[227] Weinan E and Eric Vanden-Eijnden. Transition-path theory and path-finding algorithms for the study of rare events. *Annu. Rev. Phys. Chem.*, 61(1):391–420, January 2010. ISSN 0066-426X. doi: 10.1146/annurev.physchem.040808.090412. URL http://www.ncbi.nlm.nih.gov/pubmed/18999998http://dx.doi.org/10.1146/annurev.physchem.040808.090412.

[228] Peter Hänggi, Peter Talkner, and Michal Borkovec. Reaction-rate theory: fifty years after Kramers. *Rev. Mod. Phys.*, 62(2):251, April 1990. ISSN 0034-6861. doi: 10.1103/RevModPhys.62.251. URL http://link.aps.org/doi/10.1103/RevModPhys.62.251.

[229] G Henkelman, G Jóhannesson, and H Jónsson. Methods for Finding Saddle Points and Minimum Energy Paths. In Steven D. Schwartz, editor, *Theor. Methods Condens. Phase Chem.*, volume 5 of *Progress in Theoretical Chemistry and Physics*, pages 269–302. Kluwer Academic Publishers, Dordrecht, 2002. ISBN 0-7923-6687-5. doi: 10.1007/0-306-46949-9. URL http://link.springer.com/chapter/10.1007/0-306-46949-9_10.

[230] Graeme Henkelman and Hannes Jónsson. A dimer method for finding saddle points on high dimensional potential surfaces using only first derivatives. *J. Chem. Phys.*, 111(15):7010, 1999. ISSN 00219606. doi: 10.1063/1.480097. URL http://scitation.aip.org/content/aip/journal/jcp/111/15/10.1063/1.480097.

[231] Titus V. Albu, José C. Corchado, and Donald G. Truhlar. Molecular Mechanics for Chemical Reactions: A Standard Strategy for Using Multiconfiguration Molecular Mechanics for Variational Transition State Theory with Optimized Multidimensional Tunneling. *J. Phys. Chem. A*, 105(37):8465–8487, September 2001. ISSN 1089-5639. doi: 10.1021/jp011951h. URL http://pubs.acs.org/doi/abs/10.1021/jp011951h.

[232] Wolfgang Quapp. Reduced Gradient Methods and Their Relation To Reaction Paths. *J. Theor. Comput. Chem.*, 02(03):385–417, September 2003. ISSN 0219-6336. doi: 10.1142/S0219633603000604. URL http://www.worldscientific. com/doi/abs/10.1142/S0219633603000604.

[233] H Lee Woodcock, Milan Hodoscek, Andrew T B Gilbert, Peter M W Gill, Henry F Schaefer, and Bernard R Brooks. Interfacing Q-Chem and CHARMM to perform QM/MM reaction path calculations. *J. Comput. Chem.*, 28(9): 1485–502, July 2007. ISSN 0192-8651. doi: 10.1002/jcc.20587. URL http: //www.ncbi.nlm.nih.gov/pubmed/17334987.

[234] Joshua T Berryman and Tanja Schilling. Sampling rare events in nonequilibrium and nonstationary systems. *J. Chem. Phys.*, 133(24):244101, December 2010. ISSN 1089-7690. doi: 10.1063/1.3525099. URL http://www.ncbi.nlm.nih. gov/pubmed/21197970.

[235] Peter G Bolhuis, David Chandler, Christoph Dellago, and Phillip L Geissler. Transition path sampling: throwing ropes over rough mountain passes, in the dark. *Annu. Rev. Phys. Chem.*, 53:291–318, January 2002. ISSN 0066-426X. doi: 10.1146/annurev.physchem.53.082301.113146. URL http://www.ncbi. nlm.nih.gov/pubmed/11972010.

[236] Charles J. Cerjan and William H. Miller. On finding transition states. *J. Chem. Phys.*, 75(6):2800, 1981. ISSN 00219606. doi: 10.1063/1.442352. URL http:// scitation.aip.org/content/aip/journal/jcp/75/6/10.1063/1.442352.

[237] R. a. Olsen, G. J. Kroes, G. Henkelman, A. Arnaldsson, and H. Jónsson. Comparison of methods for finding saddle points without knowledge of the final states. *J. Chem. Phys.*, 121(20):9776–9792, November 2004. ISSN 00219606. doi: 10.1063/1.1809574. URL http://www.ncbi.nlm.nih.gov/ pubmed/15549851.

[238] Jon Baker. An algorithm for the location of transition states. *J. Comput. Chem.*,

7(4):385–395, August 1986. ISSN 0192-8651. doi: 10.1002/jcc.540070402. URL http://doi.wiley.com/10.1002/jcc.540070402.

[239] Graeme Henkelman and Hannes Jónsson. Improved tangent estimate in the nudged elastic band method for finding minimum energy paths and saddle points. *J. Chem. Phys.*, 113(22):9978, 2000. ISSN 00219606. doi: 10.1063/1.1323224. URL http://scitation.aip.org/content/aip/journal/jcp/113/22/10.1063/1.1323224.

[240] Graeme Henkelman, Blas P. Uberuaga, and Hannes Jónsson. A climbing image nudged elastic band method for finding saddle points and minimum energy paths. *J. Chem. Phys.*, 113(22):9901, 2000. ISSN 00219606. doi: 10.1063/1.1329672. URL http://scitation.aip.org/content/aip/journal/jcp/113/22/10.1063/1.1323224http://scitation.aip.org/content/aip/journal/jcp/113/22/10.1063/1.1329672.

[241] Enrique R. Batista and Hannes Jónsson. Diffusion and Island formation on the ice Ih basal plane surface. *Comput. Mater. Sci.*, 20(3-4):325–336, March 2001. ISSN 09270256. doi: 10.1016/S0927-0256(00)00190-7. URL http://www.sciencedirect.com/science/article/pii/S0927025600001907.

[242] Hannes Jónsson. Simulation of surface processes. *Proc. Natl. Acad. Sci. U. S. A.*, 108(3):944–9, January 2011. ISSN 1091-6490. doi: 10.1073/pnas.1006670108. URL http://www.pubmedcentral.nih.gov/articlerender.fcgi?artid=3024682&tool=pmcentrez&rendertype=abstract.

[243] Graeme Henkelman, Andri Arnaldsson, and Hannes Jónsson. Theoretical calculations of CH4 and H2 associative desorption from Ni(111): could subsurface hydrogen play an important role? *J. Chem. Phys.*, 124(4):044706, January 2006. ISSN 0021-9606. doi: 10.1063/1.2161193. URL http://www.ncbi.nlm.nih.gov/pubmed/16460199.

[244] Daniel Sheppard, Rye Terrell, and Graeme Henkelman. Optimization methods for finding minimum energy paths. *J. Chem. Phys.*, 128(13):134106, April 2008.

ISSN 0021-9606. doi: 10.1063/1.2841941. URL `http://www.ncbi.nlm.nih.gov/pubmed/18397052`.

[245] H Jónsson, Greg Mills, and K W Jacobsen. Nudged elastic band method for finding minimum energy paths of transitions. In B J Berne, G Ciccotti, and D F Coker, editors, *Class. quantum Dyn. Condens. phase simulations*, pages 385–404. World Scientific, Singapore, 1998. URL `http://citeseerx.ist.psu.edu/viewdoc/summary?doi=10.1.1.31.531http://scholar.google.com/scholar?hl=en&btnG=Search&q=intitle:Nudged+elastic+band+method+for+finding+minimum+energy+paths+of+transition+In+Classical+and+quantum+dynamics+in+condensed+phase+simulations#8`.

[246] E Weinan, Weiqing Ren, and Eric Vanden-Eijnden. String method for the study of rare events. *Phys. Rev. B*, 66(5):052301, August 2002. ISSN 0163-1829. doi: 10.1103/PhysRevB.66.052301. URL `http://link.aps.org/doi/10.1103/PhysRevB.66.052301`.

[247] E Weinan, Weiqing Ren, and Eric Vanden-Eijnden. Simplified and improved string method for computing the minimum energy paths in barrier-crossing events. *J. Chem. Phys.*, 126(16):164103, April 2007. ISSN 0021-9606. doi: 10.1063/1.2720838. URL `http://www.ncbi.nlm.nih.gov/pubmed/17477585`.

[248] Semen A Trygubenko and David J Wales. A doubly nudged elastic band method for finding transition states. *J. Chem. Phys.*, 120(5):2082–94, February 2004. ISSN 0021-9606. doi: 10.1063/1.1636455. URL `http://www.ncbi.nlm.nih.gov/pubmed/15268346`.

[249] Li Xie, Haiyan Liu, and Weitao Yang. Adapting the nudged elastic band method for determining minimum-energy paths of chemical reactions in enzymes. *J. Chem. Phys.*, 120(17):8039–52, May 2004. ISSN 0021-9606. doi: 10.1063/1.1691404. URL `http://www.ncbi.nlm.nih.gov/pubmed/15267723`.

[250] Gregory Mills and Hannes Jonsson. Reversible Work Transiton State Theory: Application to Dissociative Adsorption of Hydrogen. *Surf. Sci.*, 324(2-3):42, February 1994. ISSN 00396028. doi: 10.1016/0039-6028(94)00731-4. URL http://www.sciencedirect.com/science/article/pii/0039602894007314http://arxiv.org/abs/chem-ph/9411012.

[251] Frank Jensen. *Introduction to Computational Chemistry*. Wiley, 2 edition, 2006. ISBN 0470011874. URL http://www.amazon.com/Introduction-Computational-Chemistry-Frank-Jensen/dp/0470011874.

[252] T A Halgren and W N Lipscomb. The synchronous-transit method for determining reaction pathways and locating molecular transition states. *Chem. Phys. Lett.*, 49(2):225, 1977. doi: 10.1016/0009-2614(77)80574-5. URL http://www.sciencedirect.com/science/article/pii/0009261477805745.

[253] Sø ren Smidstrup, Andreas Pedersen, Kurt Stokbro, and Hannes Jónsson. Improved initial guess for minimum energy path calculations. *J. Chem. Phys.*, 140(21):214106, June 2014. ISSN 00219606. doi: 10.1063/1.4878664. URL http://scitation.aip.org/content/aip/journal/jcp/140/21/10.1063/1.4878664.

[254] E Vanden-Eijnden. Transition Path Theory. In Mauro Ferrario, Giovanni Ciccotti, and Kurt Binder, editors, *Comput. Simulations Condens. Matter Syst. From Mater. to Chem. Biol. Vol. 1*, pages 453–493. Springer Berlin Heidelberg, 2006. ISBN 9783540352709. doi: 10.1007/3-540-35273-2. URL http://link.springer.com/chapter/10.1007/3-540-35273-2_13.

[255] Jin Wang, Jose Onuchic, and Peter Wolynes. Statistics of Kinetic Pathways on Biased Rough Energy Landscapes with Applications to Protein Folding. *Phys. Rev. Lett.*, 76(25):4861–4864, June 1996. ISSN 0031-9007. doi: 10.1103/PhysRevLett.76.4861. URL http://link.aps.org/doi/10.1103/PhysRevLett.76.4861.

[256] Stefan Goedecker. Minima hopping: an efficient search method for the global minimum of the potential energy surface of complex molecular systems. *J. Chem. Phys.*, 120(21):9911–7, June 2004. ISSN 0021-9606. doi: 10.1063/1. 1724816. URL http://www.ncbi.nlm.nih.gov/pubmed/15268009.

[257] DanPing Chen, Jie Liu, Huili Ma, Qiao Zeng, and Wanzhen Liang. Analytical derivative techniques for TDDFT excited-state properties: Theory and application. *Sci. China Chem.*, 57(1):48–57, January 2014. ISSN 1674-7291. doi: 10.1007/s11426-013-5006-6. URL http://link.springer.com/10.1007/s11426-013-5006-6.

[258] Qiang Cui and Martin Karplus. Molecular properties from combined QM/MM methods. I. Analytical second derivative and vibrational calculations. *J. Chem. Phys.*, 112(3):1133, 2000. ISSN 00219606. doi: 10.1063/1.480658. URL http://scitation.aip.org/content/aip/journal/jcp/112/3/10.1063/1.480658.

[259] Peter Deglmann, Filipp Furche, and Reinhart Ahlrichs. An efficient implementation of second analytical derivatives for density functional methods. *Chem. Phys. Lett.*, 362(5-6):511–518, August 2002. ISSN 00092614. doi: 10.1016/S0009-2614(02)01084-9. URL http://linkinghub.elsevier.com/retrieve/pii/S0009261402010849.

[260] Douglas J Fox, Yoshihiro Osamura, Mark R Hoffmann, Jeffrey F Gaw, George Fitzgerald, Yukio Yamaguchi, and Henry F. Schaefer. Analytic energy second derivatives for general correlated wavefunctions, including a solution of the first-order coupled-perturbed configuration-interaction equations. *Chem. Phys. Lett.*, 102(1):17–19, November 1983. ISSN 00092614. doi: 10.1016/0009-2614(83)80648-4. URL http://linkinghub.elsevier.com/retrieve/pii/0009261483806484.

[261] Jürgen Gauss and Dieter Cremer. Analytical Energy Gradients in Møller-Plesset Perturbation and Quadratic Configuration Interaction Methods: Theory and Application. *Adv. Quantum Chem.*, 23:205–299, 1992. ISSN 00653276.

doi: 10.1016/S0065-3276(08)60031-3. URL http://www.sciencedirect.com/science/article/pii/S0065327608600313.

[262] Jürgen Gauss, John F. Stanton, and Rodney J. Bartlett. Analytic ROHF-MBPT(2) second derivatives. *J. Chem. Phys.*, 97(10):7825, 1992. ISSN 00219606. doi: 10.1063/1.463452. URL http://scitation.aip.org/content/aip/journal/jcp/97/10/10.1063/1.463452.

[263] N.C. Handy, R.D. Amos, J.F. Gaw, J.E. Rice, and E.D. Simandiras. The elimination of singularities in derivative calculations. *Chem. Phys. Lett.*, 120(2): 151–158, October 1985. ISSN 00092614. doi: 10.1016/0009-2614(85)87031-7. URL http://linkinghub.elsevier.com/retrieve/pii/0009261485870317.

[264] Mihály Kállay and Jürgen Gauss. Analytic second derivatives for general coupled-cluster and configuration-interaction models. *J. Chem. Phys.*, 120 (15):6841–8, April 2004. ISSN 0021-9606. doi: 10.1063/1.1668632. URL http://www.ncbi.nlm.nih.gov/pubmed/15267583.

[265] Henrik Koch, Hans Jo/rgen Aa. Jensen, Poul Jo̷rgensen, Trygve Helgaker, Gustavo E. Scuseria, and Henry F. Schaefer. Coupled cluster energy derivatives. Analytic Hessian for the closed-shell coupled cluster singles and doubles wave function: Theory and applications. *J. Chem. Phys.*, 92(8):4924, 1990. ISSN 00219606. doi: 10.1063/1.457710. URL http://scitation.aip.org/content/aip/journal/jcp/92/8/10.1063/1.457710.

[266] WanZhen Liang, Yi Zhao, and Martin Head-Gordon. An efficient approach for self-consistent-field energy and energy second derivatives in the atomic-orbital basis. *J. Chem. Phys.*, 123(19):194106, November 2005. ISSN 0021-9606. doi: 10.1063/1.2114847. URL http://www.ncbi.nlm.nih.gov/pubmed/16321075.

[267] Jie Liu and Wan Zhen Liang. Molecular-orbital-free algorithm for the excited-state force in time-dependent density functional theory. *J. Chem. Phys.*, 134 (4):044114, January 2011. ISSN 1089-7690. doi: 10.1063/1.3548063. URL http://www.ncbi.nlm.nih.gov/pubmed/21280694.

[268] Jie Liu and WanZhen Liang. Analytical Hessian of electronic excited states in time-dependent density functional theory with Tamm-Dancoff approximation. *J. Phemical Phys.*, 135(1):014113, July 2011. ISSN 1089-7690. doi: 10.1063/1. 3605504. URL http://www.ncbi.nlm.nih.gov/pubmed/21744894.

[269] David Maurice and Martin Head-Gordon. Analytical second derivatives for excited electronic states using the single excitation configuration interaction method: theory and application to benzo[a]pyrene and chalcone. *Mol. Phys.*, 96 (10):1533–1541, May 1999. ISSN 0026-8976. doi: 10.1080/00268979909483096. URL http://www.tandfonline.com/doi/abs/10.1080/00268979909483096.

[270] J. A. Pople, R. Krishnan, H. B. Schlegel, and J. S. Binkley. Derivative studies in hartree-fock and møller-plesset theories. *Int. J. Quantum Chem.*, 16(S13): 225–241, March 1979. ISSN 00207608. doi: 10.1002/qua.560160825. URL http://doi.wiley.com/10.1002/qua.560160825.

[271] H. Bernhard Schlegel. Optimization of equilibrium geometries and transition structures. *J. Comput. Chem.*, 3(2):214–218, 1982. ISSN 0192-8651. doi: 10. 1002/jcc.540030212. URL http://doi.wiley.com/10.1002/jcc.540030212.

[272] Michael Seth, Grzegorz Mazur, and Tom Ziegler. Time-dependent density functional theory gradients in the Amsterdam density functional package: geometry optimizations of spin-flip excitations. *Theor. Chem. Acc.*, 129(3-5): 331–342, June 2011. ISSN 1432-881X. doi: 10.1007/s00214-010-0819-2. URL http://link.springer.com/10.1007/s00214-010-0819-2.

[273] John F. Stanton and Jürgen Gauss. Many-body methods for excited state potential energy surfaces. II. Analytic second derivatives for excited state energies in the equation-of-motion coupled cluster method. *J. Chem. Phys.*, 103(20): 8931, 1995. ISSN 00219606. doi: 10.1063/1.470083. URL http://scitation. aip.org/content/aip/journal/jcp/103/20/10.1063/1.470083.

[274] Henryk A Witek, Stephan Irle, and Keiji Morokuma. Analytical second-order geometrical derivatives of energy for the self-consistent-charge density-

functional tight-binding method. *J. Chem. Phys.*, 121(11):5163–70, September 2004. ISSN 0021-9606. doi: 10.1063/1.1775786. URL http://www.ncbi.nlm.nih.gov/pubmed/15352808.

[275] Yokio Yamaguchi, John D Goddard, Yoshihiro Osamara, and Henry Schaefer. *A New Dimension to Quantum Chemistry: Analytic Derivative Methods in Ab Initio Molecular Electronic Structure Theory*. Oxford, New York, 1994. ISBN 0195070283. URL http://www.amazon.com/New-Dimension-Quantum-Chemistry-International/dp/0195070283.

[276] Thom. H Dunning, Lawrence B Harding, Raymond A Bair, Robert A Eades, and Ron L Shepard. Theoretical studies of the energetics and mechanisms of chemical reactions: abstraction reactions. *J. Phys. Chem.*, 90(3):344–356, January 1986. ISSN 0022-3654. doi: 10.1021/j100275a001. URL http://pubs.acs.org/doi/abs/10.1021/j100275a001.

[277] Samuel Glasstone, Keith James Laidler, and Henry Eyring. *The Theory of Rate Processes: The Kinetics of Chemical Reactions, Viscosity, Diffusion and Electrochemical Phenomena*. McGraw-Hill, New York; London, 1941. ISBN 0070233608. URL http://books.google.com/books/about/The_Theory_of_Rate_Processes.html?id=zb2GAAAAIAAJ&pgis=1.

[278] Richard F. Grote and James T. Hynes. Reactive modes in condensed phase reactions. *J. Chem. Phys.*, 74(8):4465, 1981. ISSN 00219606. doi: 10.1063/1.441634. URL http://scitation.aip.org/content/aip/journal/jcp/74/8/10.1063/1.441634.

[279] Gregory V. Hartland, Bryan F. Henson, Vincent A Venturo, and Peter M. Felker. Ionization-loss stimulated Raman spectroscopy of jet-cooled hydrogen-bonded complexes containing phenols. *J. Phys. Chem.*, 96(3):1164, February 1992. ISSN 0022-3654. doi: 10.1021/j100182a028. URL http://pubs.acs.org/doi/abs/10.1021/j100182a028.

[280] R. M. Levy, D Perahia, and M Karplus. Molecular dynamics of an alpha-helical polypeptide: Temperature dependence and deviation from harmonic behavior. *Proc. Natl. Acad. Sci.*, 79(4):1346–1350, February 1982. ISSN 0027-8424. doi: 10.1073/pnas.79.4.1346. URL http://www.pnas.org/content/79/4/1346.shorthttp://www.pnas.org/cgi/doi/10.1073/pnas.79.4.1346.

[281] Michael I Page and William P Jencks. Entropic Contributions to Rate Accelerations in Enzymic and Intramolecular Reactions and the Chelate Effect. *Proc. Natl. Acad. Sci.*, 68(8):1678–1683, August 1971. ISSN 0027-8424. doi: 10.1073/pnas.68.8.1678. URL http://www.pnas.org/cgi/doi/10.1073/pnas.68.8.1678.

[282] Efrat Rosenman and Michael L. McKee. Reaction-Path Dynamics and Theoretical Rate Constants for the CH3F + Cl –> HCl + CH2F Reaction by Direct Dynamics Method. *J. Am. Chem. Soc.*, 119(38):9033–9038, September 1997. ISSN 0002-7863. doi: 10.1021/ja971185l. URL http://pubs.acs.org/doi/abs/10.1021/ja971185l.

[283] Josep Maria Bofill, Wolfgang Quapp, and Marc Caballero. Locating transition states on potential energy surfaces by the gentlest ascent dynamics. *Chem. Phys. Lett.*, 583:203–208, September 2013. ISSN 00092614. doi: 10.1016/j.cplett.2013.07.074. URL http://linkinghub.elsevier.com/retrieve/pii/S0009261413009652.

[284] Paul Zimmerman. Reliable Transition State Searches Integrated with the Growing String Method. *J. Chem. Theory Comput.*, 9(7):3043–3050, July 2013. ISSN 1549-9618. doi: 10.1021/ct400319w. URL http://pubs.acs.org/doi/abs/10.1021/ct400319w.

[285] Yuli Liu, Steven K. Burger, and Paul W. Ayers. Newton trajectories for finding stationary points on molecular potential energy surfaces. *J. Math. Chem.*, 49(9):1915–1927, October 2011. ISSN 0259-9791. doi: 10.1007/s10910-011-9864-x. URL http://link.springer.com/10.1007/s10910-011-9864-x.

[286] Dhagash Mehta, Jonathan D Hauenstein, and David J Wales. Communication: Certifying the potential energy landscape. *J. Chem. Phys.*, 138(17):171101, May 2013. ISSN 1089-7690. doi: 10.1063/1.4803162. URL `http://www.ncbi.nlm.nih.gov/pubmed/23656107`.

[287] Andrew Behn, Paul M Zimmerman, Alexis T Bell, and Martin Head-Gordon. Efficient exploration of reaction paths via a freezing string method. *J. Chem. Phys.*, 135(22):224108, December 2011. ISSN 1089-7690. doi: 10.1063/1.3664901. URL `http://www.ncbi.nlm.nih.gov/pubmed/22168681`.

[288] Anthony Goodrow, Alexis T. Bell, and Martin Head-Gordon. A strategy for obtaining a more accurate transition state estimate using the growing string method. *Chem. Phys. Lett.*, 484(4-6):392–398, January 2010. ISSN 00092614. doi: 10.1016/j.cplett.2009.11.050. URL `http://linkinghub.elsevier.com/retrieve/pii/S0009261409014894`.

[289] Wolfgang Quapp and Josep Maria Bofill. A comment to the nudged elastic band method. *J. Comput. Chem.*, 31(13):2526–31, October 2010. ISSN 1096-987X. doi: 10.1002/jcc.21540. URL `http://www.ncbi.nlm.nih.gov/pubmed/20652994`.

[290] Josep Maria Bofill and Wolfgang Quapp. Variational nature, integration, and properties of Newton reaction path. *J. Chem. Phys.*, 134(7):074101, February 2011. ISSN 1089-7690. doi: 10.1063/1.3554214. URL `http://www.ncbi.nlm.nih.gov/pubmed/21341822`.

[291] Saul Wolfe, H. Bernhard Schlegel, Imre G. Csizmadia, and Fernando Bernardi. Chemical dynamics of symmetric and asymmetric reaction coordinates. *J. Am. Chem. Soc.*, 97(8):2020–2024, April 1975. ISSN 0002-7863. doi: 10.1021/ja00841a005. URL `http://pubs.acs.org/doi/abs/10.1021/ja00841a005http://dx.doi.org/10.1021/ja00841a005`.

[292] Philippe Durand, Georges Trinquier, and Y. H. Sanejouand. A new approach for determining low-frequency normal modes in macromolecules. *Biopoly-*

mers, 34(6):759–771, June 1994. ISSN 00063525. doi: 10.1002/bip. 360340608. URL http://yh.sanejouand.com/GT_biop1994.pdfhttp://doi. wiley.com/10.1002/bip.360340608.

[293] Klaus Ruedenberg and Jun-Qiang Sun. A simple prediction of approximate transition states on potential energy surfaces. *J. Chem. Phys.*, 101(3):2168, 1994. ISSN 00219606. doi: 10.1063/1.467722. URL http://scitation.aip. org/content/aip/journal/jcp/101/3/10.1063/1.467722.

[294] Jun-Qiang Sun and Klaus Ruedenberg. Locating transition states by quadratic image gradient descent on potential energy surfaces. *J. Chem. Phys.*, 101(3): 2157, 1994. ISSN 00219606. doi: 10.1063/1.467721. URL http://scitation. aip.org/content/aip/journal/jcp/101/3/10.1063/1.467721.

[295] Shaama Mallikarjun Sharada, Paul M. Zimmerman, Alexis T. Bell, and Martin Head-Gordon. Automated Transition State Searches without Evaluating the Hessian. *J. Chem. Theory Comput.*, 8(12):5166–5174, December 2012. ISSN 1549-9618. doi: 10.1021/ct300659d. URL http://pubs.acs.org/doi/abs/10. 1021/ct300659d.

[296] H. Bernhard Schlegel. Estimating the hessian for gradient-type geometry optimizations. *Theor. Chim. Acta*, 66(5):333–340, 1984. ISSN 0040-5744. doi: 10. 1007/BF00554788. URL http://link.springer.com/10.1007/BF00554788.

[297] María Fernández-Serra, Emilio Artacho, and José Soler. Model Hessian for accelerating first-principles structure optimizations. *Phys. Rev. B*, 67(10): 100101, March 2003. ISSN 0163-1829. doi: 10.1103/PhysRevB.67.100101. URL http://link.aps.org/doi/10.1103/PhysRevB.67.100101.

[298] Francesco Filippone, Simone Meloni, and Michele Parrinello. A novel implicit NewtonâĂŞRaphson geometry optimization method for density functional theory calculations. *J. Chem. Phys.*, 115(2):636, 2001. ISSN 00219606. doi: 10.1063/1.1377877. URL http://scitation.aip.org/content/aip/ journal/jcp/115/2/10.1063/1.1377877.

[299] Thomas H Fischer and Jan Almlof. General methods for geometry and wave function optimization. *J. Phys. Chem.*, 96(24):9768–9774, November 1992. ISSN 0022-3654. doi: 10.1021/j100203a036. URL `http://pubs.acs.org/doi/abs/10.1021/j100203a036`.

[300] Joanne M. Wittbrodt and H.Bernhard Schlegel. Estimating stretching force constants for geometry optimization. *J. Mol. Struct. THEOCHEM*, 398-399(96): 55–61, June 1997. ISSN 01661280. doi: 10.1016/S0166-1280(96)04928-7. URL `http://linkinghub.elsevier.com/retrieve/pii/S0166128096049287`.

[301] Liliane Mouawad and David Perahia. Diagonalization in a mixed basis: A method to compute low-frequency normal modes for large macromolecules. *Biopolymers*, 33(4):599–611, April 1993. ISSN 0006-3525. doi: 10.1002/bip. 360330409. URL `http://doi.wiley.com/10.1002/bip.360330409`.

[302] B Brooks and M Karplus. Normal modes for specific motions of macromolecules: application to the hinge-bending mode of lysozyme. *Proc. Natl. Acad. Sci.*, 82 (15):4995–4999, August 1985. ISSN 0027-8424. doi: 10.1073/pnas.82.15.4995. URL `http://www.pnas.org/cgi/doi/10.1073/pnas.82.15.4995`.

[303] Nicholas J Thompson, Mark W B Wilson, Daniel N Congreve, Patrick R Brown, Jennifer M Scherer, Thomas S Bischof, Mengfei Wu, Nadav Geva, Matthew Welborn, Troy Van Voorhis, Vladimir Bulović, Moungi G Bawendi, and Marc A Baldo. Energy harvesting of non-emissive triplet excitons in tetracene by emissive PbS nanocrystals. *Nat. Mater.*, 13(11):1039–43, November 2014. ISSN 1476-1122. doi: 10.1038/nmat4097. URL `http://dx.doi.org/10.1038/nmat4097`.